PROPAGATION AND EARLY GROWTH OF NORMAL FAULTS

Catherine Baudon

Submitted in partial fulfilment of the requirements for the degree of Ph.D.

Cardiff University

April 2007

ProQuest LLC
789 East Eisenhower Parkway
P.O. Box 1346
Ann Arbor, MI 48106-1346

SUMMARY

This research project used 3D seismic data located in the Levant Basin, eastern Mediterranean and in the Espirito Santo Basin, offshore Brazil, in order to investigate the early propagation of small normal faults and develop criteria to reconstruct fault kinematics. Detailed interpretation of the 3D geometry of faults, extensive mapping of the throw distribution and investigation of the ductile deformation in the volume surrounding the fault planes provided new insights into the propagation and early growth of normal faults.

The Levant survey was used to investigate a unique array of small blind normal faults that were then compared to neighbouring small growth faults in order to better understand their early growth history. Criteria for the recognition of blind faults were defined. Unrestricted blind faults were compared to those that underwent a subsequent mechanical interaction with a major lithological boundary or another structure. The results show that such restrictions affect the throw distribution on most of the fault plane and is not only limited to the proximal zone of interaction.

An analysis of growth faults that have recently made the transition from a blind stage to a syn-sedimentary stage suggests that most of the fault surface area formed during the blind propagation phase. A large proportion of the displacement was added during the syn-sedimentary phase as a result of interaction with the free surface. This led to a change in the position of the point of maximum displacement, as well as a shift of the entire vertical throw distribution. These results suggest that the dimensions of the faults were established early in the growth history and that displacement on and surrounding fault planes was added for a near constant dimension.

Crestal extensional faults that grew by blind propagation before reaching the surface were investigated from the Espirito-Santo survey. These faults were reactivated by blind propagation after a significant period of quiescence. A reconstruction of the 3D geometry of the fault network and detailed analysis of the throw distribution provided new insights into the kinematics of reactivation. Two distinct modes of reactivation are recognised: a typical reactivation by upward propagation and a reactivation by dip linkage. These are selective processes and factors controlling preferential reactivation are discussed.

All these results have wide implications for fault growth models and are applicable to many petroleum systems.

ACKNOWLEDGEMENTS

Firstly, I am deeply grateful to my supervisor, Joe Cartwright, who gave me the opportunity to undertake this research. I learned a lot through his passion for geology, numerous discussions about structural geology and invaluable advice for writing scientific papers. This project greatly benefited from his patience, knowledge and guidance through the years as well as the freedom necessary to such a research project that he gave me.

Thanks are due to BG group for funding and providing the seismic data from the Levant Basin. In particular, I would like to thank Paul Griffiths for helping with permission to publish the results. CGG Veritas is also acknowledged for providing the Brazil seismic data and Richard Davies for giving me full access to the data. Schlumberger Ltd is acknowledged for the use of Geoquest seismic interpretation software and Neil Ferguson and Gwen Pettigrew for technical support. Thanks are due to Jonathan Redfern for making it possible for me to finish this thesis in the best conditions.

This thesis benefited from very thought-provoking discussions, technical advices or proof-reading from David James, Jonathan Imber, John Walsh, Richard Lisle, Màiri Nelson, Simon Higgins and Päivi Heiniö along with Rob Evans, Tom Praeger and Aggeliki Georgiopoulou.

Thanks to my friends from the 3D Lab for a warm welcome when I first arrived: Andy R., Claudia, Jose, Simon S., Mads, Mike and especially Dorthe for continuous help and encouragements and Mairi for fantastic fieldwork in the Canyonlands and inspiration. I appreciated working in such a nice environment and this is mostly due to Mostyn, Rob, Aggie, William, Suzy, Tom and to my great officemates Simon H. and Päivi who provided the best coffee-breaks I've even had, for effort in speaking French to my mum when she rings and for fun procrastination time which I'm sure increased my efficiency at the end. I'll miss the black board, competitions and your craziness guys.

Very special thanks to all my friends in Cardiff who made me feel at home since my first day here. Nick, Simon S., Helena, Christian, Cesar, Martin W., Lizzie, Alan, Ruth, Dave, Jay, Bryan, Päivi, Julia, Wendy, Rich, Sarah, Cathal, Dan, Falko, Anna, Marcus, Lia, Adonis and many others... I know I'm lucky to have spend so much fun time with you all and thanks for enduring the smelly cheese, helping improving my English (although not much different from French as you keep telling me!) and my rants about the weather, British wine and trains.

I can not wait to thank my friends from Brittany and Tours for their friendship all these years and for the visit in Cardiff for most of them. Delphine (pour toutes ces années à grandir ensemble), Flo (pour m'avoir hébergée et chouchouttée quand j'en avais besoin), Katia et Stephanie (merci la BCBG team!), Ben et Erwan (mes Bretons partis loin), Charly, Alan le caribou, Sam (*Hiiiii*), Chrystelle, Nolween et mon Nico (toujours un plaisir de finir en retard avec toi, merci d'avoir supporté mes états d'âmes).

Thanks to Cédric for listening to my PhD stories, encouraging me, cooking nice meals and entertaining me through the writing up period and above all for wrapping me in a sweet and exciting cloud of happiness.

I would like to thank my family and especially my parents Marie-Claude and Gérard Baudon and my sister Christine Guého for their continuous advice and encouragement in all my decisions, for their emotional and financial support, for their patience and their unconditional love.

My time in Wales left me with many memories, friendships and stories; as for the written part, it goes like this...

Cette thèse est dédicacée à Lucienne Baudon

LIST OF FIGURES

Chapter 1: Introduction

Chapter 2 Blind normal faults in the Levant Basin, Eastern Mediterranean

Chapter 3: Early stage of evolution of growth faults located in the Levant Basin, Offshore Israel

Chapter 4: The kinematics of reactivation of normal faults; example from the Espirito Santo Basin

Chapter 5: Discussion

Appendices

LIST OF TABLES

TABLE OF CONTENT

Chapter I

Introduction

1 INTRODUCTION

1.1 Rationale

This PhD research project examines different types of extensional faults in various settings and using high quality 3D seismic data in order to improve our current understanding of the mechanics and kinematics of the growth of normal faults.

1.1.1 Mechanics of fault growth

Over the past 20 years, numerous authors have investigated the growth of faults based on field studies, numerical and analogue modelling along with 2D and 3D seismic data. Our contemporary understanding of the mechanics of fault growth derives from a wide range of studies exploring the initiation, the propagation and the linkage of faults.

The conceptual framework of fault analysis is based on the characteristics of a simple blind normal fault defined as a fault which does not intersect a free surface (Watterson 1986). An early model of fault growth was proposed from an ideal isolated normal fault that is characterised by an elliptical tip line that grows by radial propagation with no migration of the point of maximum displacement (Barnett et al. 1987). Subsequent to this model, numerous datasets of different types of faults, in varying contexts, have been published and used primarily to define a relationship between the maximum displacement and the dimension of faults (e.g. Muraoka & Kamata 1983, Watterson 1986, Dawers et al. 1993, Schlische et al. 1996). These studies provide insights into the mechanics of the initiation and the growth of faults and have been used to promote different fault growth models (e.g. Walsh & Watterson 1988, Cowie & Scholz 1992c, Cartwright et al. 1995). Several models predict a systematic increase in both the dimensions and displacement of faults through time (Walsh & Watterson 1988, Cowie & Scholz 1992b, Gillespie et al. 1992, Dawers et al. 1993, Schlische et al. 1996). However, a departure from this self-similarity has been observed and attributed to several factors such as segment linkage

occurring during the fault propagation (e.g. Peacock & Sanderson 1991, Cartwright et al. 1995), mechanical interaction with other structures (e.g. Nicol et al. 1996a) or with a major stratigraphic boundary (e.g. Gross et al. 1997). Reactivation processes have also been recently considered as an important controlling parameter in fault growth (e.g. Walsh et al. 2002a, Bellahsen & Daniel 2005). Reactivated faults have been shown to follow different growth paths than previously suggested by the conventional models (e.g. Meyer et al. 2002, Walsh et al. 2002a). Further research into the mechanisms of fault reactivation would greatly improve our understanding of fault propagation and growth.

1.1.2 Kinematics of fault growth

One of the most fundamental issues in structural geology and basin analysis is to date fault activity accurately in order to distinguish syn-sedimentary from post-sedimentary faults, and to correctly assign the magnitude of displacement on a fault segment and has accrued whilst a fault has been active at the surface.

Despite the importance of the blind fault concept to our current understanding of fault growth, there have been surprisingly few published descriptions of simple blind normal faults from seismic data. One possible explanation for this is the difficulty in making a positive identification based on the standard definition of a blind fault as one that does not intersect a free surface during its life span as an active fault. The lack of reliable criteria to identify blind faults on subsurface data such as 3D seismic might lead to serious misinterpretation of the mechanisms and kinematics of considered faults. Therefore, there is a clear scope for characterising blind propagation and providing tools enabling its recognition.

Furthermore, small syn-sedimentary faults can occasionally be extremely difficult to distinguish from post-sedimentary faults that grew by blind propagation (Petersen et al. 1992). Not only that the two different types of faults can bear striking similarities but different parts of a single fault can be attributed to syn- and post-sedimentary processes. As parts of the same fault can be active at different times, syn-sedimentary faults can also comprise a post-sedimentary component (Meyer et al. 2002, Childs et al. 2003). There is therefore a need to further understand the

characteristics of syn- and post-sedimentary propagation and the transition between these different mechanisms of faulting.

These questions have wide implications from both an academic and an applied point of view. Advances in the understanding of normal faults kinematics would significantly improve existing fault growth models. Determining accurately the timing of faults movements with respect to the sedimentation is essential to improve predictions of reservoir geology in many petroliferous basins such as the Niger Delta (Weber 1987) or the Gulf of Mexico (Rowan et al. 1998). The differentiation of the relative parts of blind propagation and syn-sedimentary growth and the characterisation of reactivation processes are necessary to predict important reservoir characterisation parameters such as seal quality, fluids circulation and net-to-gross of reservoir volume.

1.2 Aims of the thesis

This PhD research project aims to investigate in detail the propagation of various small extensional faults using 3D seismic data in order to improve our current understanding of the mechanisms and kinematics of fault growth. A series of key questions have been addressed in the thesis in an attempt to improve our understanding of early-stage propagation processes. The main aims of this thesis are to:

- Present several case studies of some small normal blind faults using 3D seismic data and analyse the throw distribution of the fault planes
- Devise criteria to enable the recognition of blind faults from 3D seismic data
- Investigate the effects of interaction of blind faults with other structures or major lithological boundary
- Investigate the transition from a blind stage to a syn-sedimentary stage and characterise the early stage of development of specific growth faults
- Develop criteria to differentiate blind propagation from syn-sedimentary growth and help assessing the kinematics of faults
- Investigate the strain in the volume surrounding the fault plane

- Investigate the transition from a growth faults to a fault propagating by blind propagation through reactivation processes
- Investigate the different modes of reactivation
- Examine the factors influencing selection of faults or fault segments for reactivation
- Evaluate previous model of fault growth and scaling relationship in the lights of the main findings herein

1.3 Background & Literature review

This section aims to review and summarise the background literature of the different traditional techniques for displacement analysis and the conceptual framework for fault propagation and growth. The proposed scaling laws and different fault growth models resulting from this are then summarised.

1.3.1 Displacement analysis of normal faults

The terminology used in this thesis is summarised in Figure 1.1. The along strike dimension of a fault plane between the two lateral tip is expressed as the length (L), the vertical distance from the upper tip line to the lower tip line is the height (H) and the thickness of the fracture zone normal to the fault strike direction is the width (W). When faults characteristics are compared within an array or different fault populations for instance, the dimensions of the faults are generally expressed as maximum values (Lmax, Hmax or Wmax). The same can apply to maximum throw value (Tmax) or maximum displacement (Dmax).

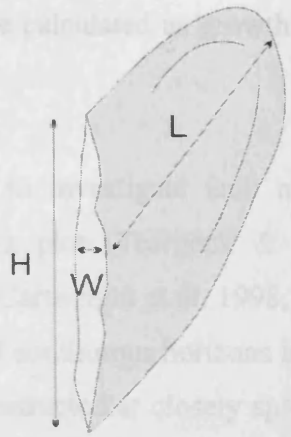

Fig. 1.1: (a) Schematic representation of half of a simple normal fault plane showing the terminology used in this thesis. The strike-slip, vertical and horizontal components are respectively the length (L), the height (H) and the width (W) of the fault plane.

1.3.1.1 Traditional methods of displacement analysis

The conceptual framework for the analysis of fault motion history was first undertaken on growth faults (Wadsworth 1953, Hardin & Hardin 1961, Ocamb 1961, Thorsen 1963). The expansion index (E.I.) has been commonly used to define periods of most significant growth on normal faults (Thorsen 1963, Gibbs 1983, Beach 1984, McCulloh 1988, Xiao & Suppe 1992, Bischke 1994, Edwards 1995). It is obtained by dividing the thickness of a unit in the downthrown block by the thickness of the corresponding unit in the upthrown block. However, as the expansion index is a ratio, it does not give information on the slip rate (Cartwright et al. 1998).

Numerous studies evaluate variations in displacement by gradient measurements. It is generally considered that gradients are obtained by dividing the amount of displacement over a distance by this distance although the measurement techniques are not systematically specified in the literature. These gradients can be calculated with throw values as well and are equivalent to what has been defined as growth indices (Childs et al. 2003). The growth index is calculated by the difference in thickness between the hanging wall and the footwall of an interval divided by the thickness of the interval in the footwall. This measurement expresses therefore the ratio between relative throw rates and sedimentation in the footwall. Gradients

presented along this thesis were calculated as growth indices and E.I. are sometimes provided as well.

An alternative method to investigate fault motion characteristics is to use throw versus depth called T-z plot (Tearpock & Bischke 1991, Bischke 1994, Mansfield & Cartwright 1996, Cartwright et al. 1998, Bouroullec 2001). This method consists of plotting the throw of continuous horizons immediately adjacent to the fault plane versus their depth. If constructed at closely spaced interval, this technique can provide extremely detailed information on the vertical throw distribution on a fault plane (Fig. 1.2).

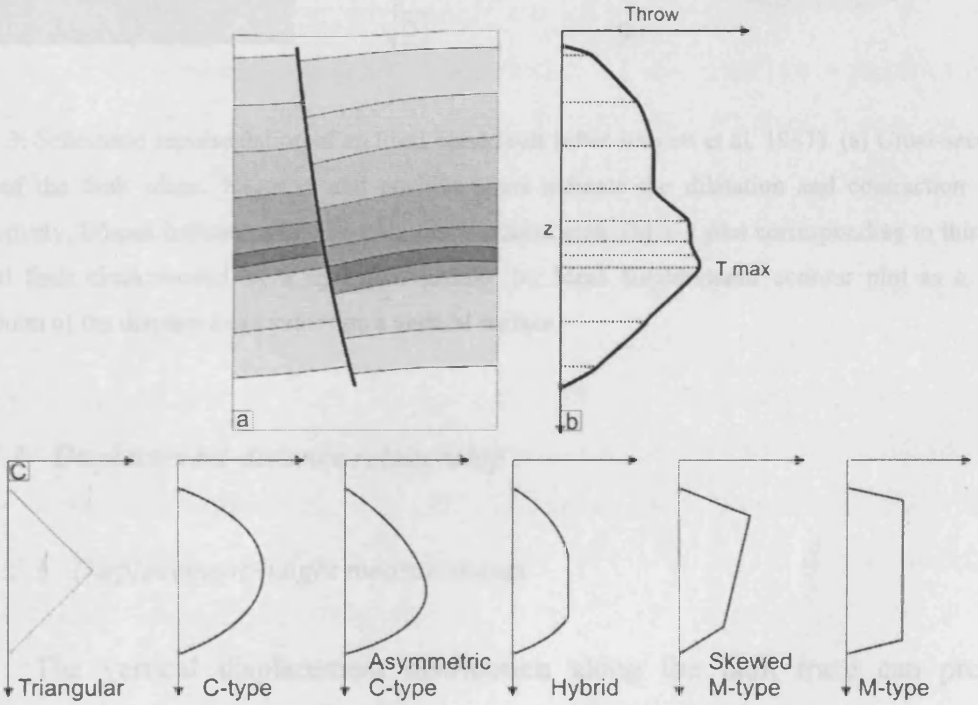

Fig. 1.2: (a) Schematic section across a normal fault offsetting a layered sedimentary succession. (b) Vertical throw distribution plot (T-z plot) obtained for this fault. Throw values (x axis) are plotted against the depth (z) along the y axis. (c) Schematic examples of vertical throw profiles and terminology used in the thesis.

Throw (or displacement) contour plots have also been largely used for throw (displacement) distribution analysis. Contoured fault plane projections of throw values derive from regularly spaced transects (such as T-z plots) across a single fault plane. The measurements are plotted on a projection of the fault plane before contouring with lines joining points of equal value (Fig. 1.3c). If the projection can

not be done on the fault plane itself, point can be projected on a vertical plane parallel to the fault strike or a horizontal plane for shallow dipping faults (Barnett et al. 1987).

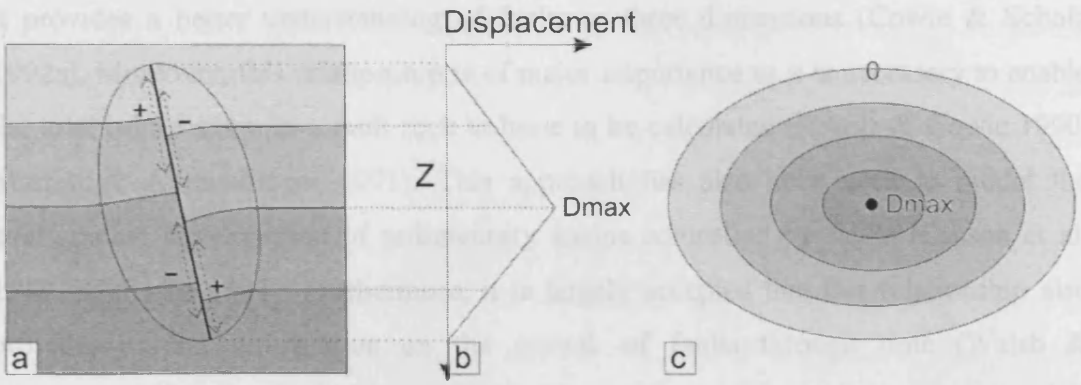

Fig. 1.3: Schematic representation of an ideal blind fault (after Barnett et al. 1987). (a) Cross-sectional view of the fault plane. Negative and positive signs indicate the dilatation and contraction zones respectively. Ellipse indicates the near-field displacement area. (b) T-z plot corresponding to this ideal normal fault characterised by a triangular profile. (c) Ideal displacement contour plot as a strike projection of the displacement values on a vertical surface.

1.3.1.2 Displacement-distance relationship

1.3.1.2.1 Displacement-height measurements

The vertical displacement distribution along the fault trace can provide important insights into fault formation and development. The fault trace is the line of intersection between the fault plane and a vertical outcrop or a seismic cross section. The most valuable measurements are those from cross section that are normal to the fault strike in order to obtain values as close as possible from the true dip slip of normal faults. This analysis consists in plotting the displacement versus the vertical distance along the fault trace in diagrams called (L-D) or (d-x) plots (Muraoka & Kamata 1983, Higgs & Williams 1987, Pollard & Segall 1987, Dawers & Anders 1995). This technique of displacement analysis has also been used on thrust fault (Ellis & Dunlap 1988), fold-thrust structures and linked-fault systems (Williams & Chapman 1983, Chapman & Williams 1984).

1.3.1.2.2 Displacement-length measurements

This relationship between the displacement and the length (or more accurately maximum displacement versus maximum length) has been largely used partly because it provides a better understanding of faults in three dimensions (Cowie & Scholz 1992a). Moreover, this relationship is of major importance as it is necessary to enable the total brittle strain in a fault rock volume to be calculated (Scholz & Cowie 1990, Marrett & Allmendinger 1991). This approach has also been used to model the stratigraphic development of sedimentary basins controlled by faults (Gibson et al. 1989, Schlische 1991). Furthermore, it is largely accepted that this relationship also provides crucial information on the growth of faults through time (Walsh & Watterson 1988, Cowie & Scholz 1992b). Most of the traditional fault growth models have been developed using displacement-length data (e.g. Walsh & Watterson 1988, Cowie & Scholz 1992c).

The first displacement-length relationship was published in a study on restored cross-sections on thrust faults in the Canadian Rockies (Elliott 1976). A displacement-geometry analysis was then conducted by on complete (both lateral tips visible) normal faults at Chimney Rock, Utah (Krantz 1988). Numerous other displacement-length analyses are detailed in a later section (as they are linked to the different fault growth models (Muraoka & Kamata 1983, Watterson 1986, Barnett et al. 1987, Walsh & Watterson 1988, Marrett & Allmendinger 1991, Cowie & Scholz 1992a, c, Gillespie et al. 1992, Dawers et al. 1993).

1.3.1.2.3 Displacement-width measurements

Relationship between the width and the displacement also provides information on the growth of the fault zone with time and has applications to fault zone growth model. A linear trend relationship obtained from logarithmic width-displacement data plots has been used to suggest that there is a systematic correlation between the width (or thickness) of fault zones and the maximum displacement (Otsuki 1978, Scholz 1987, Hull 1988, 1989). This would mean that as the fault displacement increases, the fault zone thickness also increases (Scholz 1987). It has also been proposed that in further detail, the width of the fault zone increases in a

non-continuous (or stepwise) shape, which could indicate a discontinuous growth of the fault zone (Knott 1994). In contrast, several authors have found no correlation between fault zone thickness and the displacement along the fault (Jamison & Stearns 1982, Blenkinsop & Rutter 1986, Woodward et al. 1988, Evans 1990). An explanation for this could be that the width of the fault zone can change in the dip direction or/and along the fault length whilst the displacement is nearly constant (Evans 1990, Childs et al. 1996b). It has been strongly suggested that further data would be necessary to infer a width-displacement relationship (Evans 1990). These data should present thickness-displacement measurements from different points on the same fault, from families of faults with the same lithology but different amount of displacement, and from faults in both similar structural settings and amounts of net slip.

1.3.2 Fault growth models and scaling laws

1.3.2.1 Blind fault model and growth by radial propagation

Fault propagation has been described as the increase in length, displacement and area of a fault from an initiated fracture nucleation (e.g. Segall & Pollard 1983, Walsh & Watterson 1987, Reches & Lockner 1994, Peacock & Sanderson 1996).

The early work on fault propagation was based on the characteristics of an idealised blind normal fault defined as a fault which does not intersect a free surface (Watterson 1986). This ideal blind fault would be characterised by displacement decreasing from a maximum at the centre of the fault plane to a tip line of zero displacement (Fig. 1.3). In the absence of mechanical heterogeneity, this tip line would be elliptical and would grow by radial propagation with no migration of the point of maximum displacement. This model for the growth of simple faults only applies to growth in which each slip event, or stable sliding, occurred over the entire fault plane (Watterson 1986). The displacement distribution on such a fault has been described as organised in concentric ellipses of equal value (Barnett et al. 1987). The point of maximum displacement could be taken to indicate the point of nucleation of the fault, ideally at the centre of the fault plane. This model also described the near-field displacements surrounding an ideal, single normal fault as characterised by

reverse drag folding in both hanging wall and footwall. The reverse drag folding is interpreted to develop to maintain compatibility between rocks on either side of the fault, and its variation is complementary to the systematic changes in displacements over the fault surface.

1.3.2.2 Scaling laws

Relationship between the displacement and length (D/L) of different types of faults, in varying contexts provide insight into the mechanics of the initiation of faults. This scaling of faults dimensions have been used to promote several fault growth models (e.g. Walsh & Watterson 1988, Cowie & Scholz 1992c, Cartwright et al. 1995). This section aims to detail the different fault growth models resulting from scaling laws derived from numerous extensive datasets.

1.3.2.2.1 Non-linear power-law

A combination of datasets compiling thrust data from the Canadian Rockies (Elliott 1976), various fault scarps in Iceland and several ocean floor areas along with data from British Coalfields (Rippon 1985) was used to suggest a model of fault growth by radial propagation (Watterson 1986, Walsh & Watterson 1988). The compilation of data is presented in a logarithmic plot of fault length versus maximum displacement (Fig. 1.4). Based on the ideal concept of an isolated blind fault with fault growth by elliptical slip events whose rupture dimensions encompass the entire fault surface, this model assumes that the fault dimensions increase by a constant increment at each slip event or stable sliding.

The power-law relationship between the maximum displacement (D) and the maximum trace length (L) suggested by this model can be expressed as:

$$D = c \cdot L^{n}$$

where c is a constant related to the material properties. The study concludes that the displacement is proportional to the square root of the length (n = 2). This suggests a power-law relationship by which faults grow by a systematic increase in both maximum displacement and length.

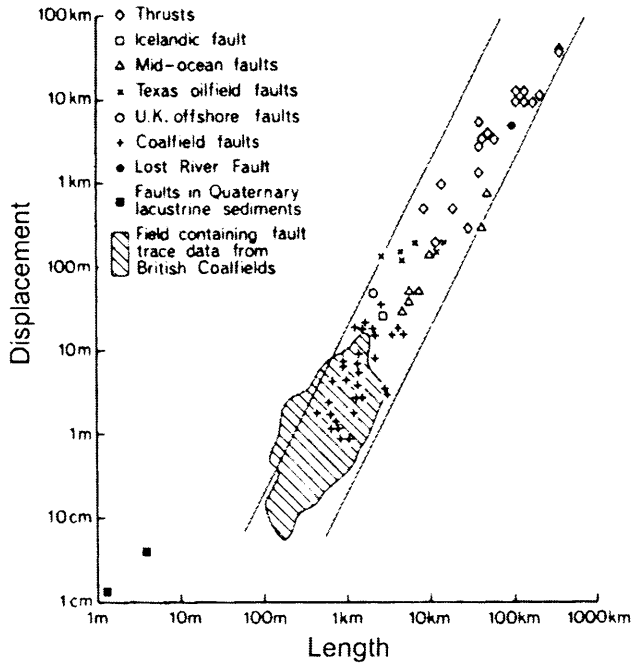

Fig. 1.4: Logarithmic plot of maximum displacement versus length (after Walsh and Watterson, 1988).

Other independent studies predict a non-linear relationship ($n > 1$) for fault growth. Various values of the exponent of proportionality n greater than 1 were suggested on the basis of combinations of individual datasets such as $n = 1.5$ (Marrett & Allmendinger 1992) or $1.5 < n < 2.0$ (Gillespie et al. 1992). Such values of the exponent implies that the difference between consecutive slip events on a fault is not a constant but is linearly related to the number of events which have occurred on the fault.

1.3.2.2.2 Linear power law and self-similar growth of faults

It has been suggested that the use of combined individual datasets for a displacement-length analysis could lead to serious misinterpretation (Cowie & Scholz 1992a). In opposition to the previous models and based on early work by Dugdale (1960), a linear relationship ($n=1$) between displacement and length was suggested (Cowie & Scholz 1992c). This model specifies that the scaling parameter depends on rock properties and tectonic settings. Such a model predicts displacement distribution following a self-similar behaviour. This can only be explained if the shape of the

displacement distribution profile as well as the magnitude of the displacement gradients is maintained during the growth of the fault.

Numerous studies predict or have been used to support the hypothesis of a self-similar relationship between the dimension and maximum displacement of fault (Elliott 1976, Villemin & Sunwoo 1987, Opheim & Gudmundsson 1989, Dawers et al. 1993, Scholz et al. 1993, Anders & Schlische 1994, Carter & Winter 1995, Dawers & Anders 1995, Clark & Cox 1996, Schlische et al. 1996). Various field based studies such as the database from the Volcanic Tableland, California (Dawers et al. 1993) or numerical modelling studies (e.g. Clark & Cox 1996) have suggested a linear relationship.

However, the linear displacement gradient commonly observed on faults sometimes differs from the inflexion in the shape of the profile observed in the earlier model (Cowie & Scholz 1992c). This variation in the profile shape can be explained if a change occurs in the fault growth geometry or in the material properties (Dawers et al. 1993).

1.3.2.2.3 Scatter in D-L data

Scatter is observed in all D-L datasets, and has been attributed to a number of factors:

(1) Changes in mechanical properties in the host rocks or the fault trace itself (Gudmundsson, 1992; Dawers et al., 1993; Cowie et al, 1992).

(2) Mechanical anisotropy and mechanical stratigraphy in the rock volume being offset by the faults (Burgmann et al. 1994, Wojtal 1994, 1996, Gross et al. 1997, Kim & Sanderson 2005).

(3) Sampling effects and measurement biases (Walsh & Watterson 1987, 1988, Gillespie et al. 1992).

(4) Some aspect of the variations might be partially masked by the nature of log-log plots in which the data are frequently presented (Marrett & Allmendinger 1991, Gillespie et al. 1992, Schlische et al. 1996, Gross et al. 1997).

(5) In addition to this, numerous workers have attributed a part of the scatter in displacement-length relationship to interaction with neighbouring faults, segment

linkage and change in structural style during fault evolution (e.g. Wojtal 1994, Cartwright et al. 1995, Willemse et al. 1996, Wojtal 1996). Indeed, the displacement- length ratio is expected higher in areas of overlapping faults segments (Peacock & Sanderson 1991, Dawers & Anders 1995). This gave rises to a new type of model for the evolution of faults in which faults grow by linkage between originally separated segments (e.g. Ellis & Dunlap 1988, Peacock & Sanderson 1991, Cartwright et al. 1995).

1.3.2.3 Growth by segment linkage

All models presented in the previous section considered faults as simple, isolated surfaces of slip. However, many authors have suggested a growth of faults resulting from the linkage of previously individual segments (e.g. Segall & Pollard 1980, 1983, Granier 1985, Ellis & Dunlap 1988, Martel et al. 1988, Peacock & Sanderson 1991, Anders & Schlische 1994, Peacock & Sanderson 1994, Trudgill & Cartwright 1994, Cartwright et al. 1995).

Most faults in the Earth's brittle upper crust are complex structures and often result from bifurcating slip surfaces, overlapping and coalescence or linkage of shorter sections called segments (e.g. Segall & Pollard 1980, Gudmundsson 1987, Walsh & Watterson 1991, Mansfield 1996). Faults exist across a wide range of scales, from brittle microstructures of centimetre scale in granite (Granier 1985) to oceanic ridge segments of 10s kilometres length (Pollard & Aydin 1984). The segmentation resulting from fault interactions and linkage affects the displacement distribution along the fault length (Gillespie et al. 1992, Dawers et al. 1993, Scholz et al. 1993, Cartwright et al. 1995). Therefore segmented fault geometries could be responsible for scatter in maximum displacement-length data that complicates the establishment of any single scaling law (Mansfield & Cartwright 2001).

Since the importance of linkage between individual fault segments in the evolution of fault zones has been highlighted, studies into transfer zone, en échelon segments, ramp and relay zones have been carried out extensively (e.g. Larsen 1988, Morley et al. 1990, Peacock & Sanderson 1991, Gawthorpe & Hurst 1993, Jackson & Leeder 1994, Peacock & Sanderson 1994, Trudgill & Cartwright 1994, Huggins et al. 1995, Walsh et al. 1999, Nicol et al. 2002, Imber et al. 2004). These studies help

improve greatly the understanding of fault linkages and provided insights into the growth of faults in general.

1.3.2.3.1 Fault growth by lateral tip linkage

Early displacement analyses carried out on thrust faults of different sizes suggest that segmented large faults formed by the linkage of smaller individual faults (Ellis & Dunlap 1988). The paper describes a hypothetical scenario by which three initially independent faults linked through their lateral tip regions (Fig. 1.5). The areas of nucleation of initial faults are suggested to be recognisable by displacement maxima and the point of potential linkage by displacement minima.

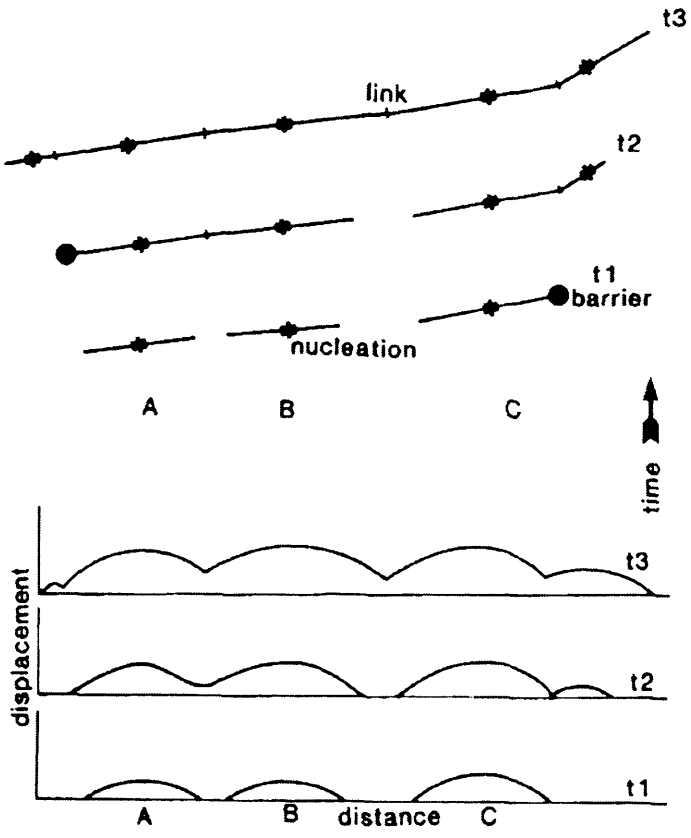

Fig. 1.5: Schematic representation of large thrust fault development (Ellis and Dunlap, 1988). The figure shows 3 initially independent faults (A, B and C) that subsequently linked by interaction of the lateral tips in map view (top of the figure) and on displacement-distance plots (bottom).

Studies on strike slip faults suggested similar growth evolution such as work in SW Scotland (Peacock 1991) or in California on granitic plutons (Martel et al. 1988). The fault zones are interpreted to grow in length as faults linked end-to-end with the displacement progressively localizing on the longer faults.

Research on segmentation and linkage processes have since been presented with further detail. A kinematic analysis of displacement variation due to segment linkage was conducted on a normal fault zone at Kilve, Sommerset, U.K. (Peacock & Sanderson 1991). The study, illustrated with normalized displacement-distance profiles, suggests a model of fault growth by nucleation of non-interacting faults (linear d-x profile), that then grow and overlap (Fig. 1.6). Rotations of bedding accommodate the displacement transfer between the faults segments, developing a relay ramp (steep displacement gradients at the offset tips) which is then faulted. The offset segments are connected by faults cutting the ramp (fault displacement decrease at the connection) which can be destroyed as faulting continues. It results in a composite fault with an along-strike bend. Therefore, the growth evolution of a fault can be read from the final displacement profile. Faults that propagated equi-dimensionally from the nucleation point (maximum displacement) have symmetric profiles and linked faults have asymmetric profiles with steep displacement gradients. Minima in total fault displacement are likely to be due to relay ramps at oversteps and linkage points (Peacock & Sanderson 1994).

A similar fault growth model was derived from a study based on inactive faults in the Triassic Newark Basin and active normal faults in the Basin and Range Province (Anders & Schlische 1994). The evolution of these large fault systems could be modelled as beginning with the nucleation of independent segments that linked. This was interpreted as occurring in regions where the strains are accommodated by growth of small faults in order to maintain the scaling relationship of the larger fault zone.

The several stages of segmentation have been suggested to correspond to order-of-magnitude variation in typical length scales of individual segments from a study on normal faults in Canyonlands, Utah, (Trudgill & Cartwright 1994). This suggests that mechanical anisotropies, such as the influence of basement structure, the thickness of brittle layer and joint length have a consequence on the different scales of segmentation.

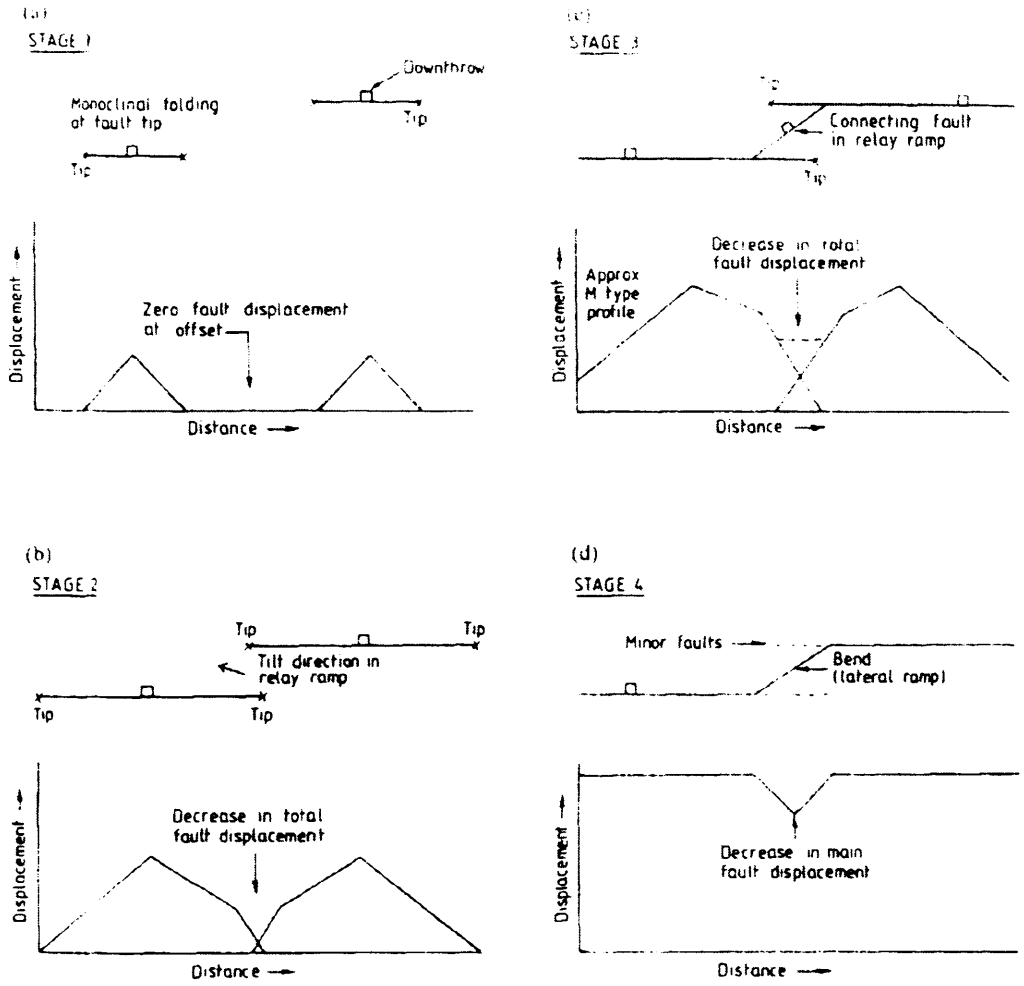

Fig. 1.6: Diagrams illustrating the different stages of development of linked fault segments through a relay zone and associated characteristics on displacement-distance plots (Peacock and Sanderson, 1991).

As large normal fault zones often result from the coalescence and linkage of smaller faults, a mode of fault growth by linkage induces a change in the displacement pattern described for simple isolated faults (Dawers & Anders 1995, Peacock & Parfitt 2002). The maximum displacement of a linked fault is expected to be the greatest value of the smaller faults whereas the length corresponds to the sum of the smaller faults. This suggests that the smaller faults grew during and after the linkage of the larger fault segments in order to accommodate large strains. These studies concluded that the scaling relationship observed for single faults is also

applicable for linked faults systems and maintained during the growth of the fault system (Dawers et al. 1993).

It has also been suggested that a fault resulting from the linkage of two different sized segments will have a maximum displacement in the centre of the larger segment (Anders & Schlische 1994).

A model of fault growth by segment linkage through lateral tip region was suggested using maximum displacement (D) and trace length (L) measurements of Canyonlands Grabens region faults in Utah (Cartwright et al. 1995). This study proposes fault growth by segment linkage as an explanation for scatter in the displacement-length relationship (Fig. 1.7). From this set of data, the displacement distribution near the fault termination was discussed and three types of lateral tip geometries were defined (Cartwright & Mansfield 1998). Following from this model, faults would grow by a combined process of radial propagation and linkage of precursor individual segments; relay structures developing in the overlap regions (Cartwright et al. 1996). Similar conclusions were obtained from analogue modelling analysis (Mansfield & Cartwright 2001). It was also suggested that segments from a fault can be characterised by independent kinematics although being physically linked.

The regions of linkages are represented by anomalies in the displacement variation along the fault plane. It has been largely recognised that lateral tips of fault segment within the overlap zone are characterised by steeper displacement gradients (e.g. Walsh & Watterson 1989, Peacock 1991, Huggins et al. 1995, Mansfield & Cartwright 1996, Willemse et al. 1996, Cartwright & Mansfield 1998). As two sub-parallel faults propagate towards each other, tip stress fields are altered (Segall & Pollard 1980) and fault propagation is inhibited and displacement begins to accumulate near interacting tips, and steep profiles develop on interaction ends (Gupta & Scholz 2000). Anomalous displacement increases the stress concentration at the interacting tip; this provides the additional strain energy necessary for tip propagation and fault tips exhibit steepen gradients as a result of this (Walsh & Watterson 1989, Peacock & Sanderson 1991, Cartwright et al. 1995, Nicol et al. 1996b, Gupta & Scholz 2000, Wilkins & Gross 2002).

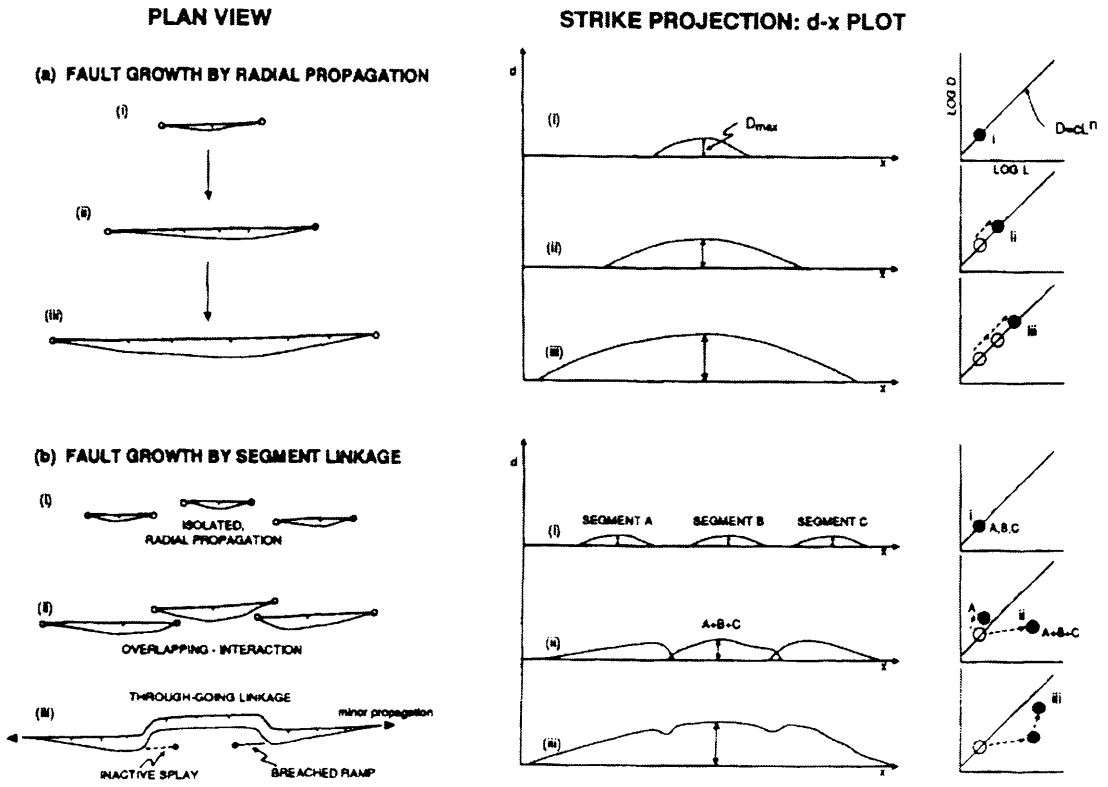

Fig. 1.7: Comparison of two different model of fault growth (Cartwright et al., 1995). Three stages of growth evolution are compared for both models in plan view, on a displacement-distance plot and on a log-log maximum displacement (D) versus maximum length (L). The radially propagating fault follows a linear growth path whereas the segmented fault follows a step-like path.

All these observations suggest that, as fault segments overlap, the scaling relationship between displacement (Watterson 1986, Walsh & Watterson 1988, Cowie & Scholz 1992c) is no longer applicable.

1.3.2.3.2 Fault growth by dip linkage

Anomalies in displacement distribution due to linkage have been described as elongated sub-vertical zones, with the long axis sub-parallel to the slip direction (e.g. Walsh & Watterson 1991, Childs et al. 1993, Childs et al. 1995). Several studies have also suggested the linkage of individual segments in the dip direction (e.g. Muraoka & Kamata 1983, Ellis & Dunlap 1988, Peacock & Zhang 1994).

Precursor fault segments grow by propagation, overlap and link in the dip direction. This is characterised by displacement anomalies with the long axis

orthogonal to the slip direction (Mansfield & Cartwright 1996). This dip-linkage results in relay structures which are sub-parallel to the strike of the fault (Fig. 1.8). It has been observed that the number of offsets per length of fault trace decreases as the fault displacement increases (Childs et al. 1996a). This suggests a progressive destruction of the points of linkage during the growth of the fault. Any original topological irregularities are unlikely to be well preserved during the fault slip and imaged on seismic profiles. However, they might leave a strong signature in the displacement field (Mansfield 1996). Provided a sufficient lateral and vertical seismic resolution associated to high sampling density, the zones of dip linkage between two originally independent segments can be recognised as local and sub-horizontal anomalies of displacement minima.

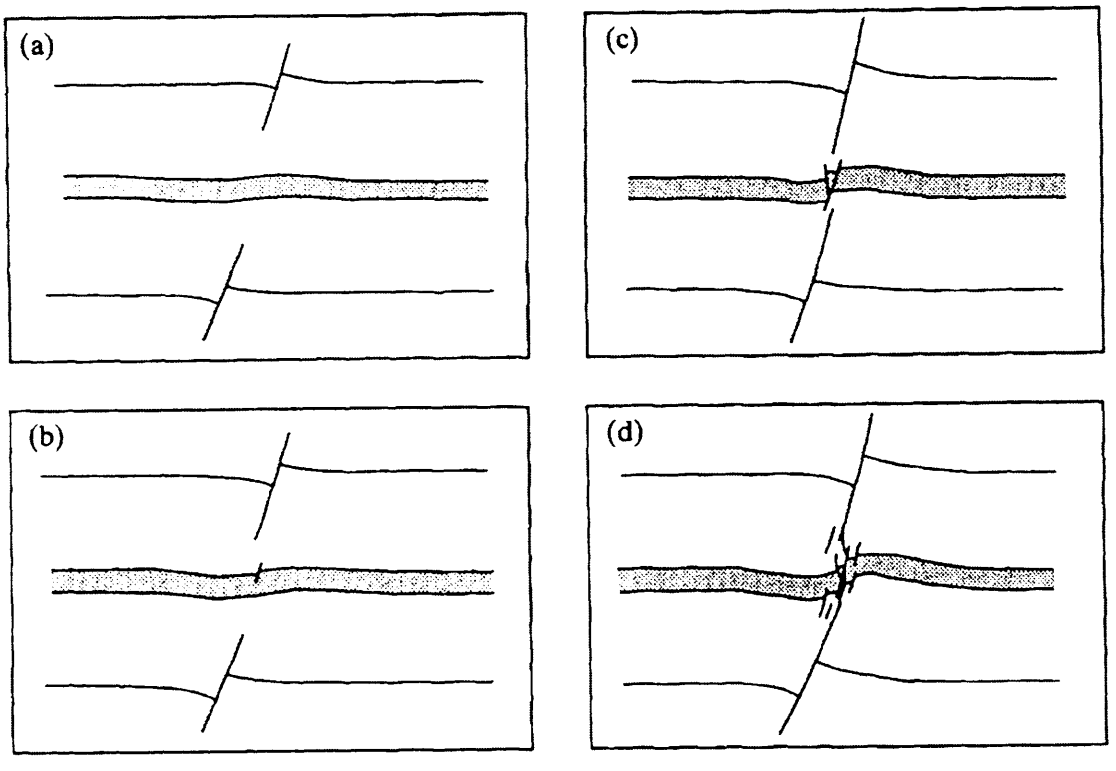

Fig. 1.8: Model describing the progressive evolution of linkage in the dip direction between two originally isolated fault segments (Mansfield and Cartwright, 1996). As the neighbouring tips approach one another, a mix of brittle and ductile deformation occurs in the region between them until the segments link to form a single, coherent structure.

1.3.2.4 The coherent fault model

Segmented fault arrays have been described by several authors as the overlap, interaction and linkage of previous unrelated and independent faults in both the strike and dip direction (Peacock & Sanderson 1991, Trudgill & Cartwright 1994, Cartwright et al. 1995, Dawers & Anders 1995, Cartwright et al. 1996). However a coherent fault model has also been proposed in which the segments of a fault array are thought to be kinematically interrelated from their initiation (Childs et al. 1995, 1996b, Walsh et al. 2003). In this case, each fault segment initiates, propagates and grows as a component of a spatially and mechanically related fault array (Fig. 1.9). Mechanically related segments are created by fault surface bifurcation. The sum of displacement distribution profiles of faults segments that were initially kinematically linked is then expected to be very similar to a typical displacement profile for a single isolated fault (Walsh et al. 2003).

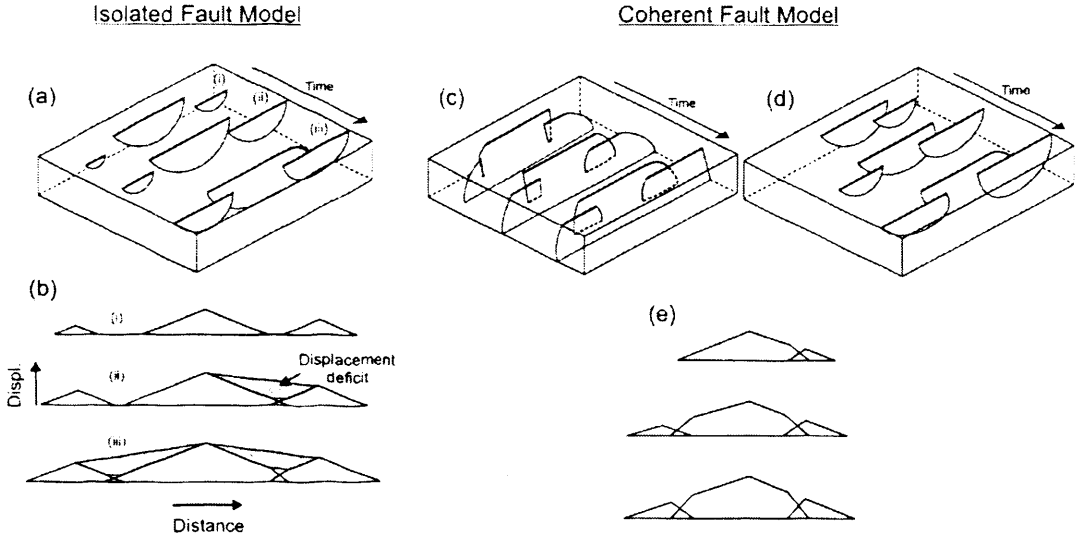

Fig. 1.9: Schematic block diagrams (a, b and c) and displacement-distance plots (d and e) of the two end-member models for the formation of segmented arrays (Walsh et al, 2003). The coherent fault model is illustrated for segmented arrays that are (c) hard-linked and formed by bifurcation of the fault plane and (d) soft-linked and formed by 3D segmentation.

This model contrasts with the "isolated fault" model and suggests that segmented fault arrays form by the incidental overlap of originally isolated and kinematically unrelated faults (Fig. 1.9). It had been agreed however, that both models can occurs in different settings and depends on the fault array evolution and system considered (Walsh et al. 2003).

1.3.2.5 Growth by accumulation of displacement for a near-constant length

Most of previous studies suggest that the initial length of a fault is significantly shorter than the final length (Walsh & Watterson 1988, Dawers et al. 1993, Schlische et al. 1996). It has been suggested that constant regional strain rate estimated in certain geological settings could be explained either by fault lengths established early in the growth evolution of a fault system or by a decreasing number of active faults (Nicol et al. 1997).

This led to the suggestion of a new model for the growth of faults that contrasts with the conventional models by which fault grow by a systematic increase in both dimension and maximum displacement (Walsh et al. 2002a). Faults resulting from the up-dip propagation of pre-existing underlying structures have been observed to follow growth paths that differ from the scaling laws previously suggested (Walsh et al. 2002b). Displacement can be added on these faults for a near constant length as lateral tips interact between neighbouring faults (Fig. 1.10). This model is in accordance with the idea that constant regional strain rate would be preferably accommodated with a rapid growth of fault length at an early stage of development of the fault in extension settings (Nicol et al. 1997).

Other studies in the Aegean region witness mature normal fault systems showing little evidence of propagation for added displacement on individual faults. This behaviour is either explained by lateral tips of the fault that are fixed at depth (Morewood & Roberts 1999) or by mechanical interaction with transverse faults or stress feedback mechanism (Poulimenos 2000).

Syn-sedimentary normal faults from the Timor Sea have been described to grow with similar rapid extension of the fault length attributed to reactivated underlying structures (Meyer et al. 2002). This departure from a fault growth by self-similarity has been observed at large scale in the same active continental regions (Armijo et al. 1996) and in the Turkana rift, North Kenya (Vetel et al. 2005). Displacement analysis in compressional settings also witnessed a rapid propagation of fault-propagation folds to near their final length (Krueger & Grant 2006).

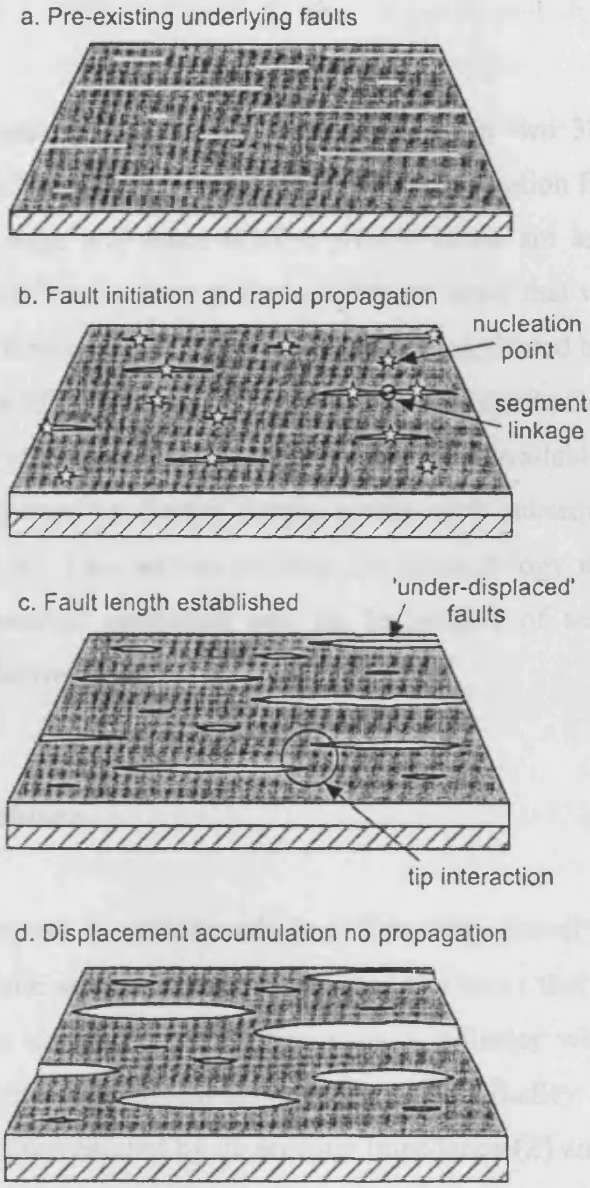

Fig. 1.10: Alternative model for the growth of faults (Walsh et al., 2002). (a) Pre-existing faults in the rocks beneath the faulted horizon. (b) Fault length increases rapidly with the nucleation point nearby the centre of the fault for relatively little displacements. (c) Faults accumulate displacement while the propagation stops as tips start to interact. (d) Near constant fault length and increase of displacement.

These studies collectively represent a subset of fault propagation wherein accumulation of displacement by reactivation of pre-existing fault surface is mechanically limited horizontally by interactions with other structures. As a consequence of this, departure from a systematic increase in size and maximum displacement only concerns the along strike dimension of the faults.

1.4 Methodology

This PhD research project was mainly based on two 3D seismic datasets. Blind faults, growth faults that have recently made the transition from a blind stage to a syn-sedimentary stage and more mature growth faults are analysed from a 3D seismic dataset located in the Levant Basin, offshore Israel that was provided by the project sponsor BG Group. Extensional growth faults reactivated by blind propagation are examined from a 3D seismic dataset situated in the Espirito-Santo Basin, offshore Brazil. The seismic resolution (quality, grid spacing, and available well data) of each dataset will be expressed in further details within each subsequent results chapter (Chapters 2, 3 and 4). This section outlines the methodology used for the general characteristics of seismic resolution and the techniques of seismic interpretation applicable to both datasets.

1.4.1 Seismic resolution

Both datasets are in milliseconds (ms) Two-Way-Travel Time (TWT). Each reflection on a seismic section illustrates the part of a wave that is reflected back to the surface when a seismic wavelet encounters a reflector which is an interface separating two layers with different acoustic properties (Badley 1985). The acoustic property of a rock is represented by its acoustic impedance (Z) and defined according to the equation:

$$Z = \rho.v$$

where ρ is the density of the formation and v the seismic velocity.

The vertical resolution indicates the thickness of a bed required to be displayed on a seismic section. It is obtained by the wavelength of the seismic signal (λ) which generally increases with depth according to the equation:

$$\lambda = v / F$$

where v, the seismic velocity, generally increases with depth and F, the frequency, tend to decrease with depth as higher frequencies are attenuated more quickly.

The horizontal resolution indicates how close two individual reflecting points can be situated. It can be obtained from the radial width of the Fresnel Zone for unmigrated data. In the case of 3D migrated data, as used in this thesis, it is difficult to estimate the horizontal resolution but it has been suggested to correspond to the bin spacing, which for these data, is equivalent to a few tens of meters (Ebrom et al. 1995).

Both 3D seismic datasets used in the project were processed to near zero phase data with SEG normal polarity. This means that an increase in impedance is represented by a positive amplitude seismic reflection (red colour in the seismic sections). Moreover, the datasets were migrated with a single-pass 3D post stack time migration.

1.4.2 3D seismic interpretation

The 3D seismic data were interpreted using Schlumberger GeoFrame 3.7 software on a UNIX workstation. A number of key horizons were mapped in each of the case study areas to the extent of the limits of both surveys. These seismic reflections were chosen for their regional continuity and were generally characterised by high amplitudes. The extensive database resulting from this has allowed the semi-regional setting to be investigated and related to the regional geological context found in the literature. Analysis of the general stratigraphic and structural context is systematically associated to the examination of specific faults. Numerous additional horizons were locally mapped to provide the most accurate fault network geometry in plan view. This also enabled the correlation of different stratigraphical units across the fault plane with little or no errors. Time structure maps and dip maps (attribute of the time structure map) resulting from this extensive interpretation. In addition to this, a coherency volume was created for both 3D seismic datasets. Horizontal slices cut from this coherency cubes at small increments (c. 4 ms TWT) particularly image the discontinuities such as faults and sedimentary features such as channels. Isochron maps between two chosen horizons were created to identify syn-kinematic intervals with respect to particular structures such as folds underlying the interpreted faults. Finally, the fault planes were mapped in 3 dimensions and imported in the Geoviz software allowing a visualisation in 3D of the objects.

1.4.3 Throw measurements

A detailed analysis of the throw distribution has been carried out on several tens of faults in each of the 3 study case areas. The throw (T) and the heave (h) are respectively the vertical and horizontal components of displacement (D) on a fault (Fig. 1.11).

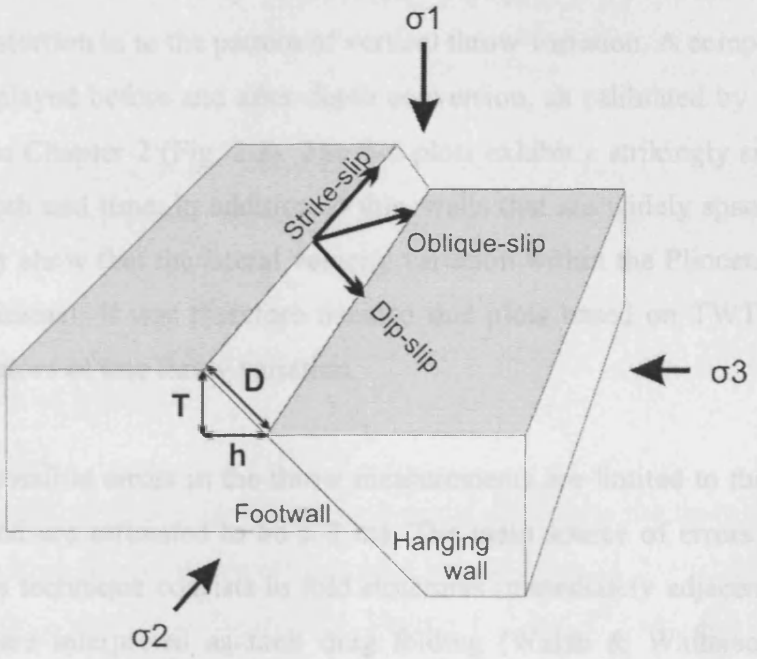

Fig. 1.11: 3D block diagram showing the displacement (D), the throw (T) and the heave (h) components of a schematic normal fault. σ1, 2 and 3 indicate the directions of the maximum, intermediate and least compressive stress respectively.

Throw measurements were displayed as individual transects representing the throw (ms TWT) on the horizontal axis against the time (ms TWT) on the vertical axis. These vertical throw distribution plots (T-z plots) were constructed from the upper tip line to the lower tip line on closely spaced seismic sections taken orthogonal to the strike of the fault plane. The high frequency content and intrinsically reflective nature of the seismic data meant that vertical throw measurements could be made at closely spaced intervals of c. 20-30 m, allowing subtle changes in gradient to be observed.

Throw contour plots were derived from regularly spaced transects of vertical throw distribution and transposed on a vertical projection of the fault plane. The projection followed standard techniques outlined by Barnett (1987) and illustrates the throw distribution on the entire fault plane as a vertical strike projection.

To simplify the analysis and because it was not possible to depth convert both datasets entirely, the T-z plots were displayed in values of TWT. Faults closest to the control wells located in the Levant survey were depth converted using the check-shot velocity data in order to verify whether the display in TWT would introduce any significant distortion in to the pattern of vertical throw variation. A comparison of two T-z plots displayed before and after depth conversion, as calibrated by Gaza-Marine 1, is shown in Chapter 2 (Fig. 2.3). The T-z plots exhibit a strikingly similar overall pattern in depth and time. In addition to this, wells that are widely spaced across the Levant survey show that the lateral velocity variation within the Pliocene-Quaternary interval is minimal. It was therefore decided that plots based on TWT values were reliable indicators of true throw variation.

Any possible errors in the throw measurements are limited to the sample rate of the data and are estimated to be ± 2 ms. The main source of errors in the throw measurements technique consists in fold structures immediately adjacent to the fault plane that were interpreted as fault drag folding (Walsh & Watterson 1987, e.g. Mansfield & Cartwright 1996). A consistent method of measuring was adopted all along this PhD research project in order to avoid major disparities between different settings (Fig. 1.12). Fault drag folding identified on reflections adjacent to the faults of both datasets have been separated into two main categories. Those of large wavelength (> c. 100 m) are considered part of the continuous deformation field around the faults and were thus included in the throw measurements for all faults. Drag folds with smaller wavelengths were considered to be within the spatial imaging error range, and throw measurements were made at the inflection points closest to the apparent hanging wall and footwall cut-offs (Mansfield & Cartwright 1996).

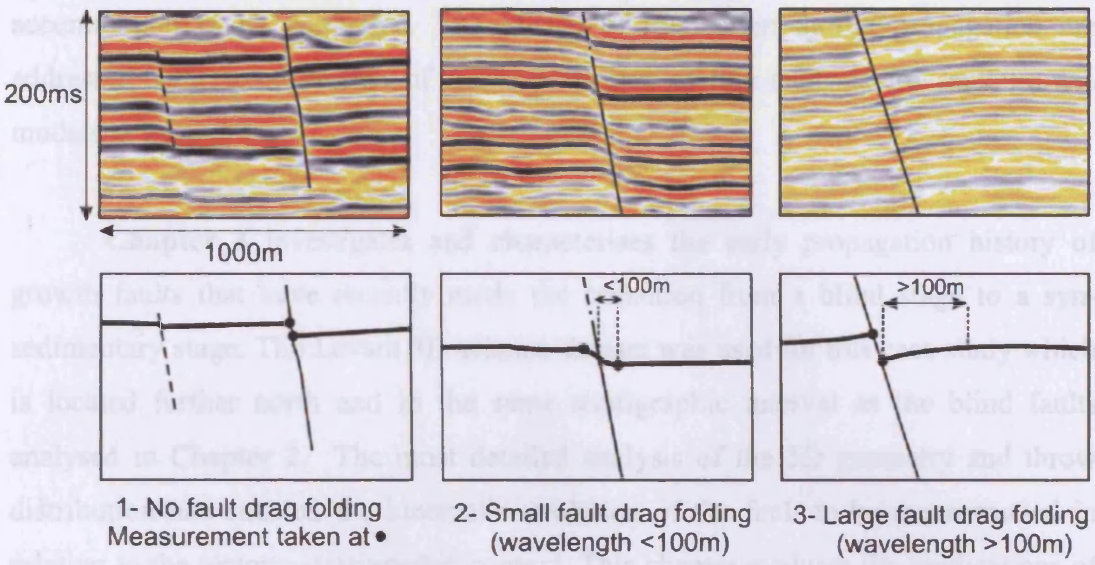

Fig. 1.12: Measurement method used in the thesis. In the presence of fault drag folding, the geometry and the wavelength were used to discriminate whether or not the drag fold is included in the measurements.

1.5 Structure of the thesis

The structure chosen for this thesis is mainly based on the three different case studies undertaking the main research points addressed during this project. Each case study constitutes a chapter in the thesis (Chapters 2, 3 and 4) and has been submitted as scientific publication in Journal of Structural Geology. All these chapters investigate different aspects of the propagation of extensional faults in different context. Each individual chapter discuss and conclude the main findings of individual case study area whereas the last two chapters (Chapters 5 and 6) constitute general discussions and conclusions compiled through the scientific research led during this PhD project.

Chapter 2 provides several case studies of small normal blind faults using the 3D seismic dataset located in the Levant Basin, in the eastern Mediterranean. This chapter first devise criteria to enable the recognition of blind faults and analyse the throw distribution of the fault planes. The purest blind faults are compare to those showing varying degrees of interaction with neighbouring faults, and varying relationships with the mechanical stratigraphy, thus allowing their affects on throw

accumulation to be calibrated. The effects of interaction during propagation are addressed with consideration of the implications of this analysis for fault growth models in general.

Chapter 3 investigates and characterises the early propagation history of growth faults that have recently made the transition from a blind stage to a syn-sedimentary stage. The Levant 3D seismic dataset was used for this case study which is located further north and in the same stratigraphic interval as the blind faults analysed in Chapter 2. The most detailed analysis of the 3D geometry and throw distribution has enabled the kinematic evolution of the fault to be reconstructed in relation to the tectono-stratigraphic context. This chapter evaluate the implications of the fault growth path interpreted from this case study on existing growth models and scaling relationship.

Chapter 4 describes growth faults organised in an extensional crestal collapse graben that were reactivated by normal blind propagation. The high quality 3D seismic data used in this case study is located in the Espirito-Santo Basin, offshore Brazil. A detailed displacement analysis conducted on these faults allows the effects of reactivation on the throw distribution over the fault planes to be constrained. An alternative model of reactivation by dip linkage is proposed and the factors influencing selective reactivation are investigated. This provides new insights into the understanding of reactivation and fault propagation in complex systems with particular attention on dating accurately fault kinematics in such contexts.

Chapter 5 forms the final discussion of the thesis and aims to summarise and collate the main findings of each of the result chapters and investigate and discuss further the characteristics of the strain field surrounding these faults in order to gain a better understanding of their 3D evolution.

Chapter 6 shortly summarizes the main findings and conclusions of the thesis. Eventual future work is finally proposed to conclude the chapter.

Chapter II

Blind faults

This chapter has been submitted for publication in Journal of Structural Geology as:

Baudon, C. & Cartwright, J. A. in review. 3D seismic characterisation of an array of blind normal faults in the Levant Basin, Eastern Mediterranean. Journal of Structural Geology.

Joe Cartwright provided discussion of the topics presented in this chapter and support during its writing.

2 BLIND NORMAL FAULTS IN THE LEVANT BASIN, EASTERN MEDITERRANEAN

2.1 Abstract

The geometry, throw distribution and kinematics of an exceptional array of blind normal faults were investigated using a high resolution 3D seismic dataset located in the Levant Basin, offshore Israel. We suggest three main criteria to assess whether or not a fault grew by blind propagation: (1) plunging upper tip line geometry, (2) presence of upper tip propagation folding, and (3) absence of clear stratigraphic or geomorphological evidences that the fault interacted with the free surface. A detailed analysis of the throw distribution on the fault planes show that the displacement profiles do not exhibit striking C-shape or triangular profiles as predicted for an ideal blind fault but mostly M-shape or hybrid type. Comparing the simplest individual blind fault to those that interacted with a mechanical boundary or another structure suggests that the dimension of the faults were established early in the development of the array and the displacement was added as a result of interactions. The results also show that the interaction of blind faults with a mechanical boundary or another structure affects the throw distribution on a major part of the fault plane and is not only localised to the tip regions. Reverse drag folding surrounding the fault plane is associated with the parts of the faults that accumulated additional displacement due to interaction. The blind faults exhibit upper tip folds that can span up to a third of the dimension of the fault plane. Finally, a systematic approach for measurements is recommended as including or not the tip folded zones for some faults can account for a significant scatter in displacement-length relationship.

2.2 Introduction

A conceptual framework for analysing the growth of faults introduced in the late 1980's (Watterson 1986, Barnett et al. 1987, Walsh & Watterson 1987, 1988) has had a

major impact on the structural interpretation of subsurface data, especially reflection seismic data. In particular, the analysis of the distribution of displacement on fault surfaces has transformed fault interpretation from being largely geometrical in emphasis, to include the kinematic aspects of fault nucleation and propagation (e.g. Childs et al. 1993, Dawers & Anders 1995).

The early work on fault analysis was based on the characteristics of a simple blind normal fault defined as a fault which does not intersect a free surface (Watterson 1986). On an idealised blind fault, the displacement is considered to decrease from a maximum at the centre of the fault plane to a tip line of zero displacement. In the absence of mechanical heterogeneity, this tip line would be elliptical and would grow by radial propagation with no migration of the point of maximum displacement. This growth model was qualified by the condition that it would only apply to growth in which each slip event, or stable sliding, occurred over the entire fault plane (Watterson 1986). Barnett et al. (1987) described ideal displacement distributions in the form of concentric ellipses of equal displacement centred on the point of maximum displacement, which could be taken to indicate the point of nucleation of the fault, ideally at the centre of the fault plane. They also described the near-field displacements surrounding an ideal, single normal fault. Reverse drag folding in both hanging wall and footwall is seen in this model fault as an expression of the strains required to maintain compatibility between rocks on either side of the fault, and its variation is complementary to the systematic changes in displacements over the fault surface.

The model of the simple blind normal fault has been modified in the last decade as improved imaging and analytical techniques have revealed more details of the complexities of strain fields associated with real examples. These modifications have, for example, focused on the role of segment linkage during propagation (Peacock & Sanderson 1991, Cartwright et al. 1995, Dawers & Anders 1995, Wojtal 1996), on the influence of mechanical heterogeneity in fault growth processes (Peacock & Zhang 1994, Mansfield & Cartwright 1996, Gross et al. 1997, Wilkins & Gross 2002) and on the role of mechanical interaction with other structures on fault propagation (Nicol et al. 1996, Maerten et al. 1999). In spite of these modifications, the simple model advanced by Watterson (1986) has more than fulfilled its original remit "to stimulate observations

and methods of data treatment rather than to provide an interpretive blueprint" (Barnett et al. 1987).

Given the importance of the conceptualised view of the simple blind normal fault to our current understanding of fault growth, there have been surprisingly few published descriptions of these structures from seismic data in the past two decades (Table 1).

Source	Data	Measurements	Dimension	Dmax
Barnett et al, 1987	Offshore UK North Sea (2D seismic)	52 vertical displacement measurements on 4 mapped reflectors	L ~ 1220m	45ms
Walsh and Watterson, 1991	Offshore oilfield (2D seismic)	62 displacement measurements on 4 mapped reflectors 100m spacing between seismic lines	L = 1800m	60m
Nicol et al, 1996	Gulf Coast (3D seismic)	106 throw readings on 5 horizons Estimation of tip lines positions by extrapolation of throw gradients	L = 1500m H =~1500m	42ms = 53m

Table 1: Blind faults with entire fault plane in the literature from seismic data

Over the same period, numerous extensive datasets of different types of faults, in varying contexts, have been published and used primarily to define a relationship between the maximum displacement and the dimension of faults (e.g. Muraoka & Kamata 1983, Watterson 1986, Dawers et al. 1993, Schlische et al. 1996). These empirical approaches to define displacement-length (D/L) scaling can provide insight into the mechanics of the initiation and the growth of faults and have been used to promote several fault growth models (e.g. Walsh & Watterson 1988, Cowie & Scholz 1992b, Cartwright et al. 1995). However, most of these published data are of faults that intersect the free surface or are exposed at surface so that they cannot be regarded as blind in the sense defined by Watterson (1986). This disparity between an idealised growth model, based on a blind fault concept, and real world data, based largely on faults that are not blind, might be inconsequential. This would suggest that there are no fundamental differences between the process of fault growth during the blind stage, and during a subsequent stage when a fault intersects a free surface. However, in order to evaluate this possibility, it is first necessary to identify blind faults with confidence, and then to analyse faults that have made the transition from the 'blind stage' to the 'post-blind stage' to see what changes have occurred, if any, across this transition.

One possible explanation for the relative paucity of published examples of blind faults is the difficulty in making a positive identification based on the standard definition of the fault not intersecting a free surface during its life span as an active fault. Where a fault is exposed at surface, it is usually impossible to reconstruct the upper tip sufficiently accurately to demonstrate that it did not intersect a free surface at any time during growth. On subsurface data such as reflection seismic or coal mine plans, the same problem applies if the fault has been subject to erosion after it ceased to be active. Even where reflection seismic data provides high resolution imaging of the entire fault plane, the displacement patterns of some synsedimentary faults can bear remarkable similarity to those of ideal blind faults, adding to the complexity of interpretation (Petersen et al. 1992).

The aims of this chapter are two fold: firstly, to present several case studies of some small normal faults interpreted using high resolution 3D seismic data to illustrate some of the difficulties encountered to demonstrate that a fault is truly blind. Secondly, our aim is to analyse the distribution of throw on these faults to examine the propagation of blind faults in multi-layered clastic sedimentary successions and to expand the sparse existing published database on blind faults. The examples presented in this chapter are from an array of small normal faults developed at the margins of the Levant Basin, in the eastern Mediterranean. They can all be shown to have propagated by blind propagation using specific criteria, and show varying degrees of interaction with neighbouring faults, and varying relationships with the mechanical stratigraphy, thus allowing their affects on throw accumulation to be calibrated. A longer-term goal of this research is to gain a better understanding of blind propagation as a prelude to investigate the early propagation history of synsedimentary faults that have recently made the transition to a post-blind stage of growth, to compare the two styles of growth history.

2.3 Regional setting

The study area is located in the Eastern Mediterranean Levant basin and its continental margin, offshore Israel (Fig. 2.1).

Fig. 2.1: Location map of the 3D seismic survey (rectangle) offshore Israel. The dashed line represents the margin of the Messinian evaporites.

The basin formed by rifting during the Early Permian to the middle Jurassic and was associated with the evolution of the Neo-Tethys Ocean (Garfunkel 1998). It is located at the zone of interaction between the Anatolian, African and Arabian plates. As a result, the evolution of the Levant margin has been influenced by the proximal plate boundaries, the Dead Sea Transform to the east, the Gulf of Suez to the SW, the Cyprian Arc to the NW, Taurus mountains and Bitlis suture to the North (Tibor & Ben-Avraham 2005). The late Cretaceous saw a compressive stress-regime related to a change of motion between the African plate and the Eurasian plate induced a change in the depositional systems (Tibor & Ben-Avraham 1992) replacing the carbonate platforms with pelagic sediments (Druckman et al. 1995). Tectonic uplift of the shelf associated with a subsidence of the slope and basin occurred during the Miocene (Frey Martinez et al. 2005). In the Late Miocene, a major desiccation of the Mediterranean region occurred, known as the Messinian Salinity Crisis, which led to the deposition of thick evaporites in the basin floor regions (Tibor & Ben-Avraham 1992), pinching out laterally against the basin margins along trends that were influenced both by structure and relict topography (Bertoni & Cartwright 2006).

The Pliocene-Quaternary succession above the Messinian unconformity forms the main interval of interest of this study. During the Pliocene, a major transgression led

to the deposition of an important accumulation of clay-rich marls, sandstones and claystones mainly derived from the Nile Delta (Tibor & Ben-Avraham 1992, Frey Martinez et al. 2005). The shelf-slope system continued to prograde and aggrade through the Pleistocene and Holocene, fed by a continuous supply of sediments sourced from the Nile and supplemented by local riverine input along the basin margin. Commencing in the mid-late Pliocene, abrupt tilting of the margin resulted in two scales of gravity-driven deformation, thin-skinned sliding and slumping of slope units (Frey Martinez et al. 2005) and more substantial gravity sliding and spreading rooted in the thick Messinian evaporites (Garfunkel & Almagor 1987, Netzeband et al. 2006). This latter deformation has resulted in an updip extensional domain located at the pinch-out of the Messinian evaporites, and a downdip contractional domain located in the basin floor region and extending outward as far as the Eratosthenes Seamount and the Cyprus Arc (Gradmann et al. 2005). The extensional domain is characterised by a series of downslope and upslope dipping extensional faults, whose updip limit coincides along the entire length of the fault system with the pinch-out of the evaporites (Bertoni & Cartwright 2006) (Fig. 2.1). The number and size of faults in the extensional domain varies along the margin, and relates in part to the original salt thickness (detachment layer thickness) and to the post-Messinian tilt history.

The study area is located in the southern part of this extensional domain, where the depositional edge of the Messinian evaporite basin defines a 'salt salient' that resulted from the interplay between the Messinian base levels and the relict topography of a series of pre-Messinian submarine canyons (Bertoni & Cartwright 2006). The study area is located above one of these canyons (called the El Arish) and the extensional domain follows the outline of the Messinian evaporite pinch-out controlled along this canyon salient (Bertoni & Cartwright 2006).

2.4 Database, Methods and Limitations

The main database for this study is a high-resolution 3D seismic survey located in the southern part of the Levant Basin (Fig. 2.1), supplemented by a regional 2D reflection survey covering the entire continental margin, offshore Israel. The 3D coverage amounts to 2200 km^2 with excellent stratigraphic resolution throughout. The frequency ranges between 35 Hz and 80 Hz with a dominant frequency of 50 Hz at the

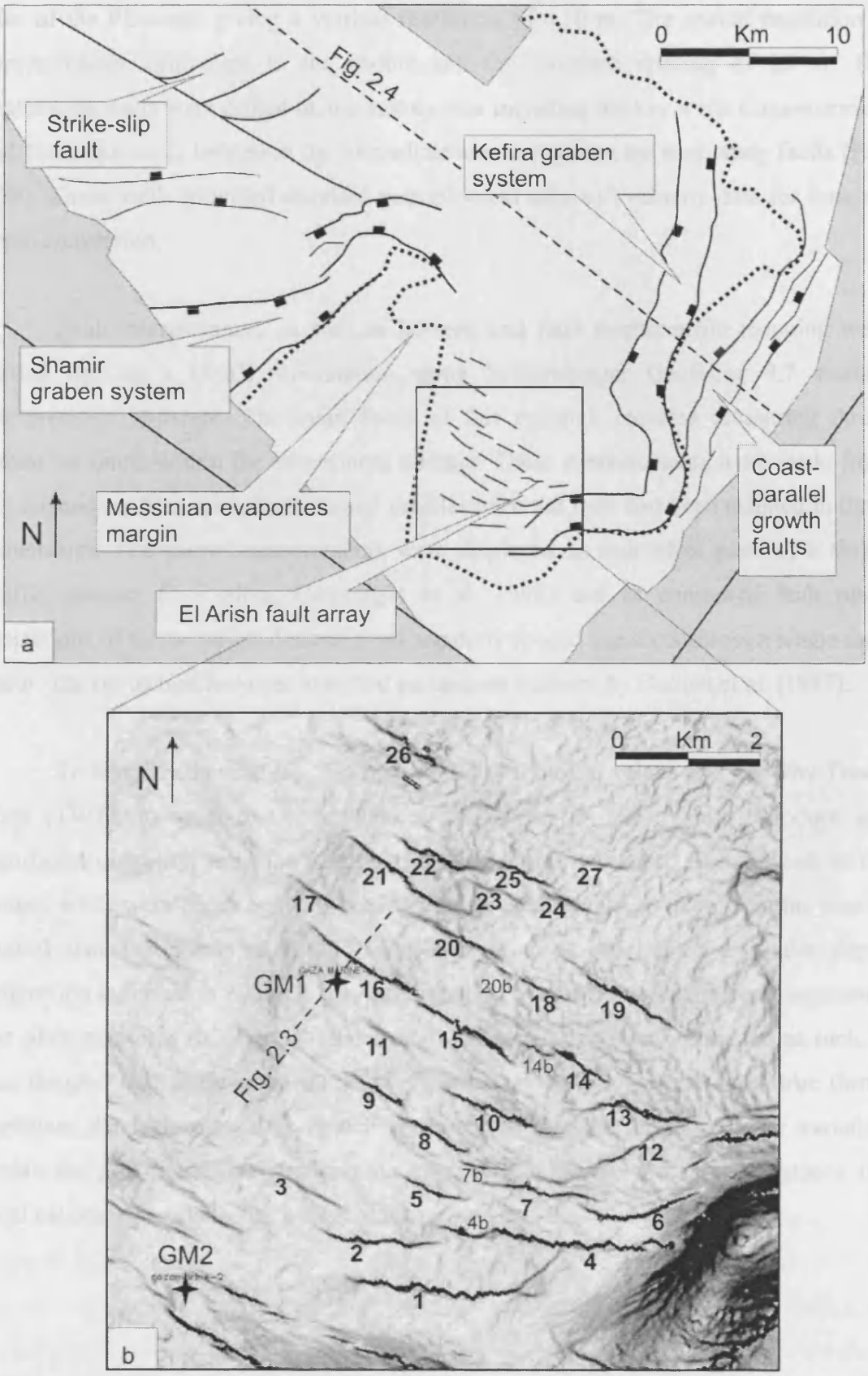

Fig. 2.2: (a) Structural map of the Levant survey based on a Pleistocene horizon. (b) Dip map showing the El Arish fault array and location of wells Gaza-marine 1 and 2 (GM1 and GM2).

base of the Pliocene, giving a vertical resolution of c.10 m. The spatial resolution is approximately equivalent to the in-line and the crossline spacing of 25 m. Ten exploration wells were drilled on the survey area including the key wells Gaza-marine 1 and Gaza-marine 2, located in the immediate area containing the case study faults (Fig. 2.2b). These wells provided standard petrophysical data and velocity data for time-to-depth conversion.

Fault interpretation, as well as horizon and fault displacement mapping were carried out on a UNIX workstation using Schlumberger Geoframe 3.7 seismic interpretation software. The main focus of this research required measuring throw values on faults within the extensional domain. These measurements were made from the seismic profiles using fault normal profiles once the fault had been mapped in three dimensions. The throw measurements were displayed as individual plots of a single profile transect (T-Z plots, Cartwright et al. 1998) and as contoured fault plane projections of throw values derived from regularly spaced transects across a single fault plane. The projection followed standard techniques outlined by Barnett et al. (1987).

To simplify the analysis, T-z plots were displayed in values of Two-Way-Travel Time (TWT). In order to verify whether the display in TWT would introduce any significant distortion in to the pattern of vertical throw variation, faults closest to the control wells were depth converted using the check-shot velocity data from the nearby control wells. A comparison of two T-z plots displayed before and after depth conversion is shown in Figure 2.3, as calibrated by Gaza-Marine 1. The depth converted T-z plots exhibit a strikingly similar overall pattern in depth and time, and as such, it was decided that plots based on TWT values were reliable indicators of true throw variation. Analysis of widely spaced wells shows that the lateral velocity variation within the post-Messinian stratigraphic interval is minimal, and this strengthens the local calibration provided by wells Gaza-Marine 1 and 2.

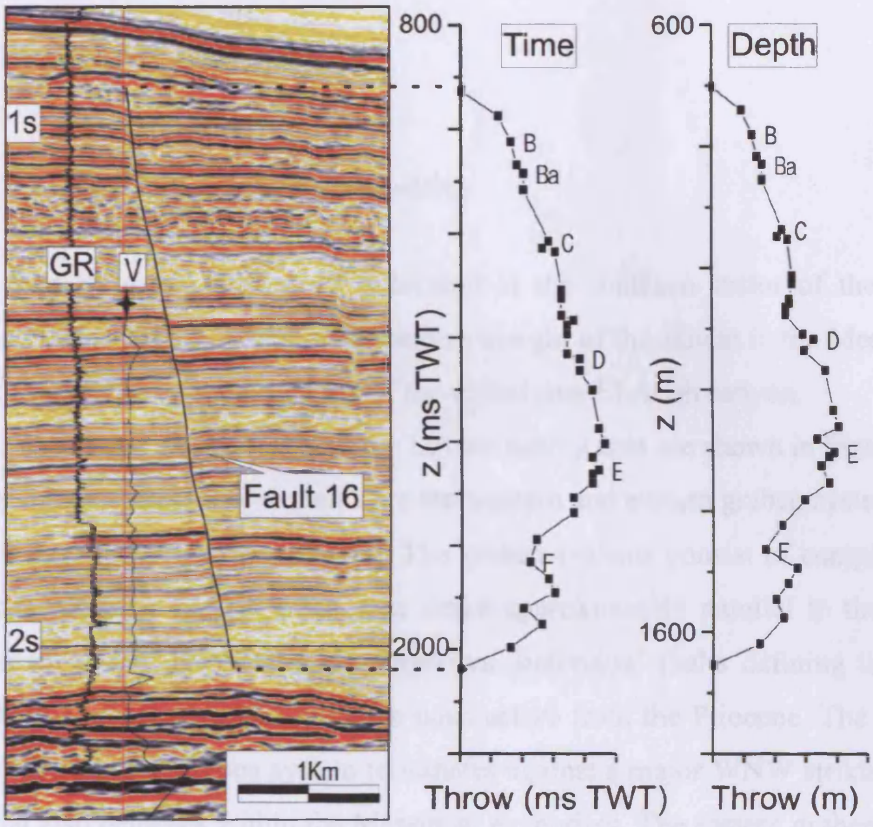

Fig. 2.3: Seismic section showing Gamma Ray (GR) and Velocity (V) profiles from well Gaza-Marine 1 in the proximity of Fault 16. Star symbol marks the uphole limit of velocity data. The T-z plots for Fault 16 in time and in depth exhibit very few differences.

Any errors in the throw measurement are estimated to be ± 2 ms. Errors due to differential compaction between hanging wall and footwall sequence are negligible in this study and would only be significant in the case of a sufficiently large throw (Mansfield 1996, Cartwright et al. 1998). Finally, fault drag can also introduce errors in the displacement measurements as previously discussed by several authors (e.g. Walsh & Watterson 1987, Mansfield & Cartwright 1996). For the purpose of the study drag folds associated with the faults of this dataset have been separated into two categories. Those of large wavelength (>100 m) are considered part of the continuous deformation field around the faults and were thus included in the throw measurements for all faults. Drag folds with smaller wavelengths were considered to be within the spatial imaging error range, and throw measurements were made at the inflection points closest to the apparent hanging wall and footwall cut-offs (Mansfield & Cartwright 1996).

2.5 The El Arish fault array

2.5.1 Structural and stratigraphic setting

The El Arish fault array is located in the southern sector of the Levant 3D seismic survey (Fig. 2.2), along the western margin of the salient in the Messinian basin that exploited the relict topography of the underlying El Arish canyon.

The main structures within the Levant survey area are shown in Figure 2.2a. The most prominent structural elements are the western and eastern graben systems, adjacent to the Messinian evaporite pinchout. The graben systems consist of complex arrays of oppositely dipping normal faults that strike approximately parallel to the underlying detachment within the Messinian evaporites. Individual faults defining these grabens have throws of up to 400 m and have been active from the Pliocene. The northeastern limit of the western graben system terminates against a major WNW striking strike-slip fault that also detaches within the Messinian evaporites. The eastern graben system dies out in a northeasterly direction along the trace of the evaporite pinchout, but to the southwest its strike swings around to WNW direction at the head of the salient. At this position, the well defined graben bounding faults die out, and are replaced by the El Arish fault array, consisting of a set of WNW striking small extensional faults. These faults strike perpendicular to the local slope direction defined at the regional detachment level and thus appear to represent a lower strain continuation of the extensional domain along the western margin of the salient. The overall trend of the array is northerly (parallel to the edge of the salient), but the individual strikes of the faults are oblique to this because they are aligned with respect to the slope of the underlying detachment as is the norm for this type of gravity driven deformation (Jackson 1995).

The structural and stratigraphic context of the El Arish fault array is further illustrated with a representative seismic profile through the margin (Fig. 2.4). The faults offset clay-rich marls, sandstones and claystones slope sediments of Plio- Pleistocene age, directly above the pinchout of the Messinian. The faults generally tip out

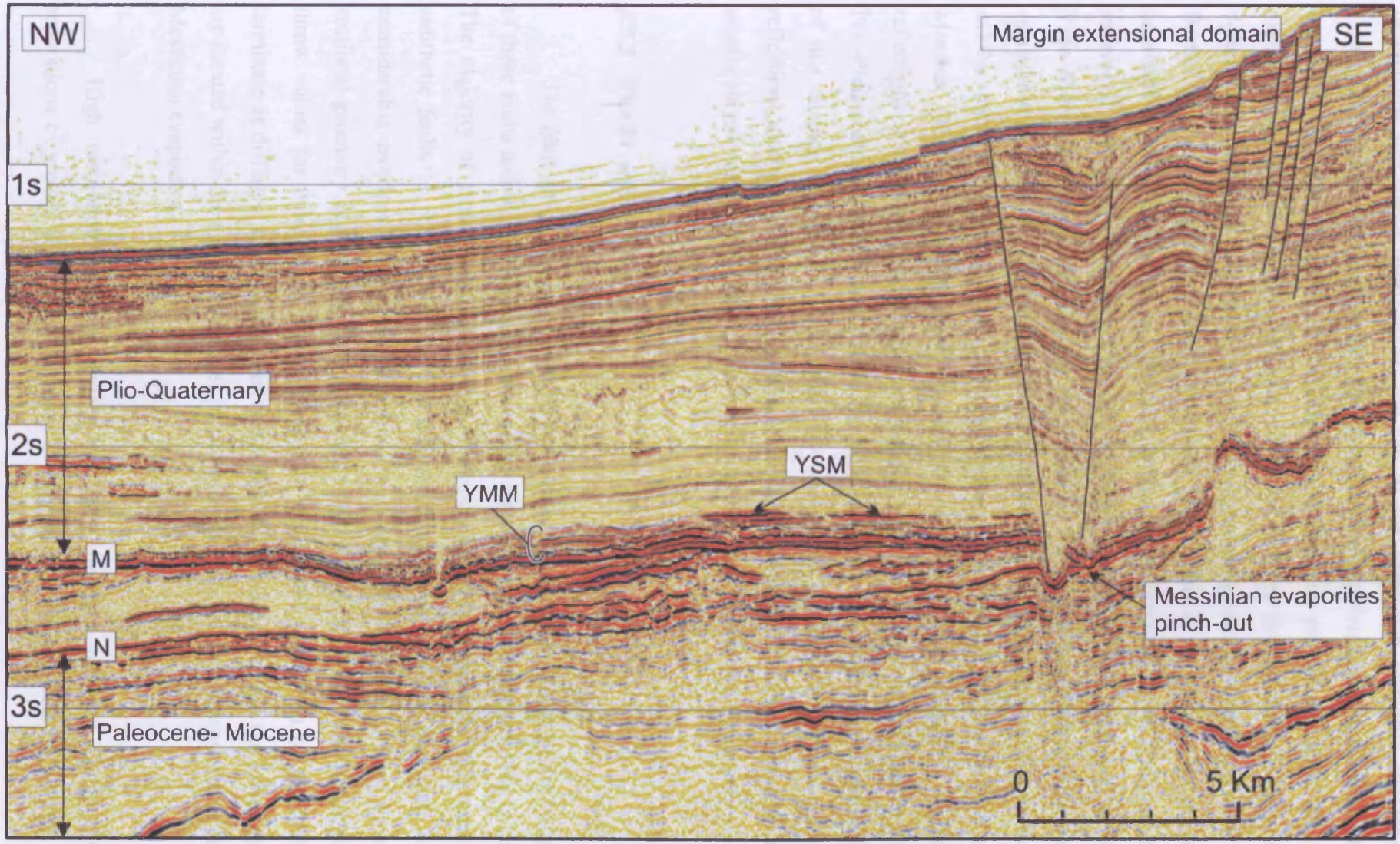

Fig. 2.4: Regional seismic section across the Levant Basin continental margin showing the main stratigraphic units including Yafo Marls Member (YMM) and Yafo Sand Member (YSM). Horizons M and N respectively indicate top and base of the Messinian evaporites. The marginal extensional faults located on the shelf break are controlled by the pinch-out of the Messinian evaporites.

downwards just above Horizon M, the top of the Messinian evaporite succession (Mavqiim Formation).The upper tips are located within the Pleistocene interval, several hundreds of metres beneath the seabed. The Messinian evaporites appear as an alternation of low and high amplitude reflections that are locally chaotic. They are delimited by two high amplitude continuous seismic reflections (Horizons M and N, Bertoni & Cartwright 2006), and consist mainly of halite in the basinal facies, and interbeds of anhydrite, halite and thin claystones in the marginal facies updip of the seismically resolvable pinchout. The post-Messinian sediments are composed of the Yafo Marl Member at the base of the Pliocene. The marls interbedded with thin sandstones and siltstones are characterised by high amplitude seismic reflections which exhibit restricted discontinuities. Locally, these are succeeded by the Yafo Sand Member (YSM). This formation appears as continuous high amplitude seismic reflections consisting of sandstones interbedded with thin claystones and marls. The Plio-Pleistocene sediments that overlie the YSM comprise the main interval of interest of this chapter. These are characterised by continuous moderate amplitude seismic reflections alternating with high amplitude seismic reflections. These sediments are mostly claystones interbedded with trace of limestones, sandstones and siltstones.

2.5.2 The El Arish fault array

The fault array consists of over 50 small extensional faults. Thirty of the largest of these faults located at the southern end of the array were studied in detail (Fig. 2.2b). The majority of these faults dip in a downslope direction towards the NE, except antithetic faults 11, 12, 20 and 26. The mapped fault traces are linear and there are considerable overlaps of varying magnitude between adjacent faults. Their cross-sectional geometry is planar, with average dips ranging from 50 to 60°. The maximum throw values for these faults ranges from 7 to 40 m. The upper tips of the faults terminate at different stratigraphic intervals within the Pleistocene, and the lower tips are located within the early Pliocene, or less commonly within the uppermost part of the Messinian evaporites.

High resolution mapping shows that hard linkages between faults with separations of greater than 100 m are rare. Strong curvature of a lateral tip towards a

neighbouring fault is only seen for Fault 1 (Fig. 2.2b). Faults 17 and 26 are the most isolated faults of the El Arish array. These two faults show no interaction with other structures and have basal tips located above the Messinian evaporites. Faults 17 and 26 thus provide a good reference to compare with the other less isolated faults that exhibit different levels of interaction with faults or with layers of major lithological contrast.

2.6 Throw analysis

A detailed analysis of the throw distribution has been carried out on four faults chosen as being representative of the different types of faults within the array with regards to the degree of isolation and interaction with other faults or with the mechanical stratigraphy. Throw distribution plots (T-z plots) were constructed from the upper tip to the lower tip on closely spaced seismic sections (50 to 250 m) taken orthogonal to strike. The high frequency content of the seismic data meant that vertical throw measurements could be made at closely spaced intervals of c. 20-30 m, allowing subtle changes in gradient to be observed.

2.6.1 Fault 17

Fault 17 is located at the western edge of the array (Figs. 2.2b and 2.5). The fault strikes at 124° and has a planar geometry with an average dip of 58° down-slope towards the NE. Its maximum length mapped at Pliocene Horizon E is 1080 m and its maximum height is c. 700 m. The upper tip line is between 200 and 300 m beneath the present day seabed in the centre of the fault, and plunges 200-500 m towards the lateral tips, cutting stratigraphically downsection as it does so. The lower tip terminates a few tens of metres above the YSM (Fig. 2.5c).

Critically, there is no evidence of stratigraphic expansion in the hanging wall (Fig. 2.5). Seismic attribute analysis of horizons bracketing the upper tip line shows no geomorphological evidence that Fault 17 interacted with the free surface at any point during its growth history, and it is therefore interpreted as a blind fault. There are no antithetic or synthetic faults interacting with any part of the fault plane and the closest neighbouring fault is approximately 390 m away from Fault 17. Fault drag folding

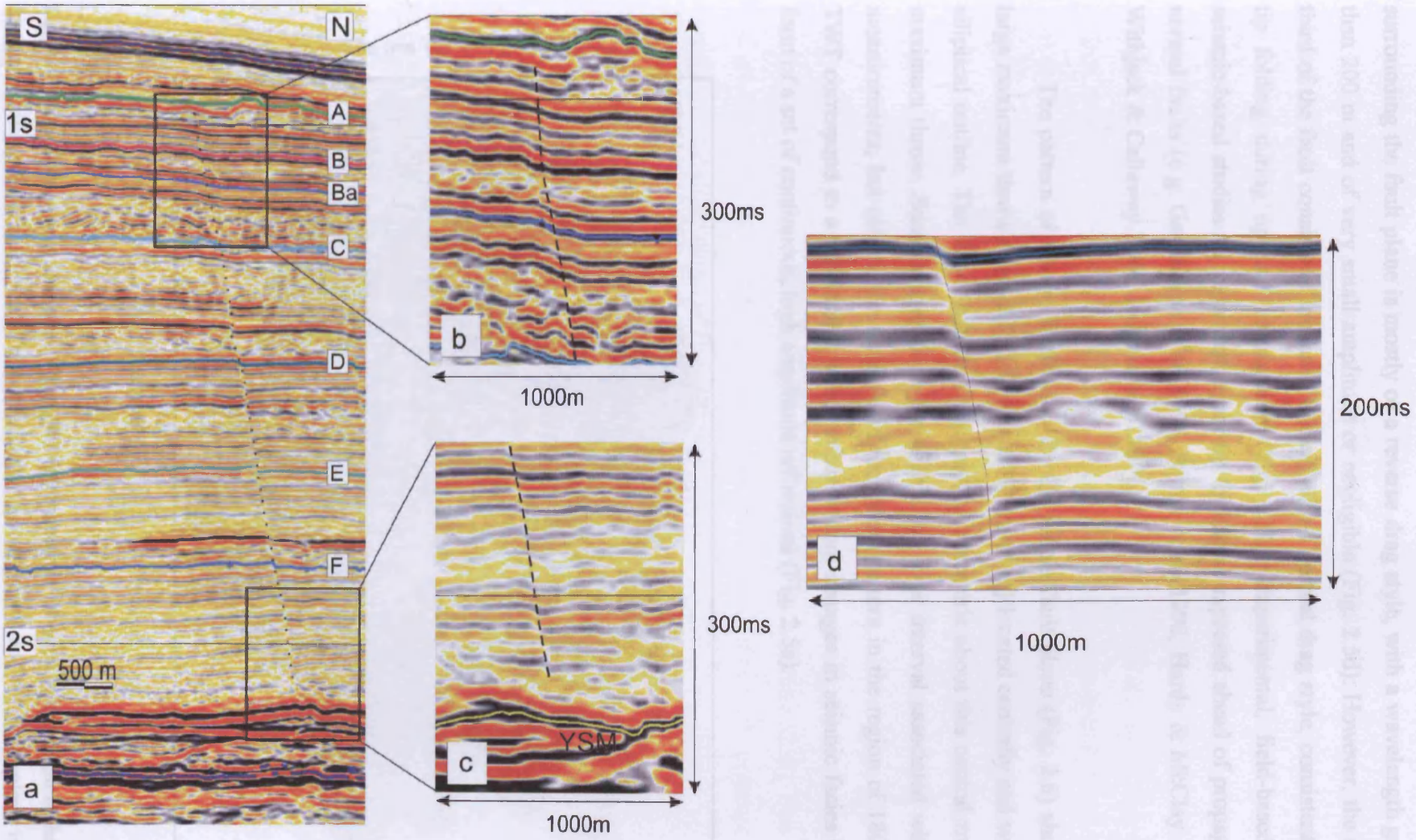

Fig. 2.5: (a) Seismic section across Fault 17 shows the position of upper and lower tips and small magnitude of displacement over the fault height. Key horizons are labelled A- F. (b) Close-up showing the significant upper tip folding. (c) Close-up showing the faulted lower tip dying out just above the YSM. (d) Very small amplitude or negligible reverse drag folding.

surrounding the fault plane is mostly of a reverse drag style, with a wavelength greater than 200 m and of very small amplitude or negligible (Fig. 2.5d). However, the upper third of the fault consists of localised folding with a normal drag style, consistent with tip folding during upward propagation (Fig. 2.5b). Experimental, field-based and seismic-based studies all show that upper tip folding is expected ahead of propagating normal faults (e.g. Gawthorpe et al. 1997, Patton et al. 1998, Hardy & McClay 1999, Withjack & Callaway 2000, Jackson et al. 2006).

The pattern of throw distribution for the whole fault plane (Fig. 2.6) shows a large maximum throw zone of 12 to13 ms TWT (c. 11 m) located centrally and with an elliptical outline. The throw contours are crudely concentric about this central zone of maximum throw. Some irregularities are within the error interval associated with the measurements, but others, for example in the throw pattern in the region of 1800 ms TWT correspond to a lithological effect inferred from changes in seismic facies in the form of a set of continuous, high amplitude reflections (Fig. 2.5a).

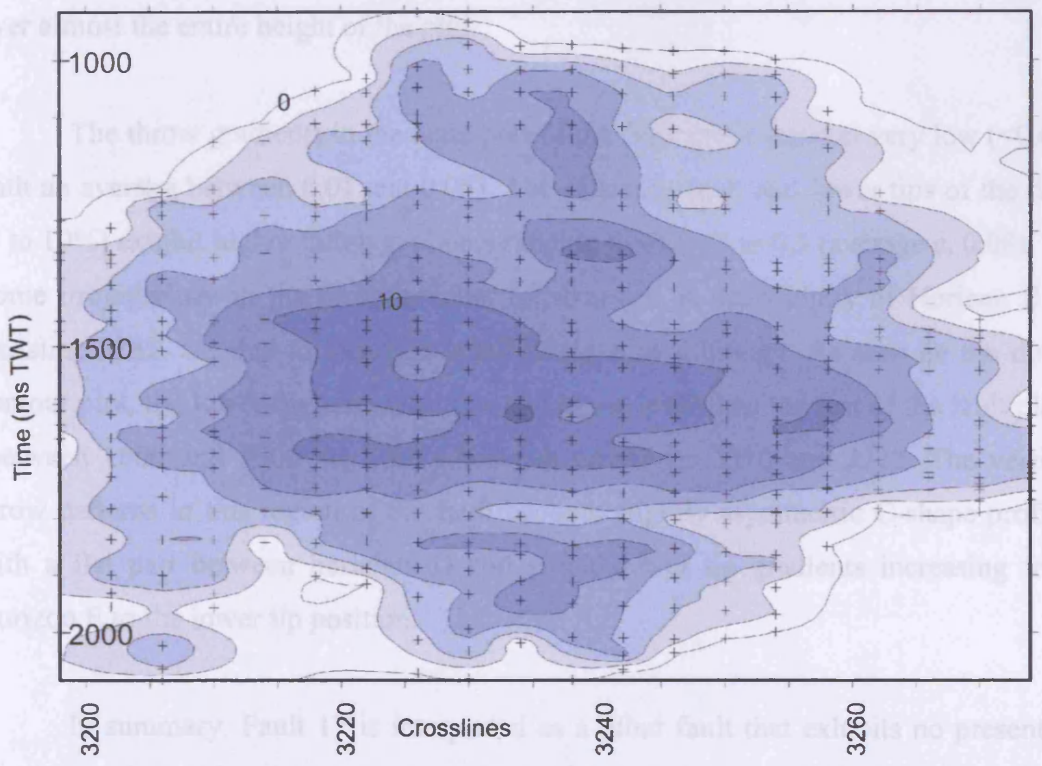

Fig. 2.6: Throw contour plot for Fault 17 using 410 measurements taken along the length of the fault. Interval between crosslines is c. 50 m. Throw contours are spaced every 2 ms TWT. Dark colours indicate high throw values (T max = 12 ms TWT).

The vertical throw distribution plots for Fault 17 exhibit mostly mesa-shaped patterns (M-type of Muraoka & Kamata 1983) with some degrees of variation (Fig. 2.7). The average throw is c. 8 m which for an average fault height of 700 m gives a low throw to height ratio of 0.0125. The small magnitude of throw values means that reverse drag is so small as to be almost imperceptible. The central section of most of the plots (40 to 95% of the fault height) exhibits no significant change of throw. This central region between 1400 and 1750 ms TWT is also the region of maximum throw values. The throw gradient in the upper half of the fault plane in this zone has an average value of 0.018. The lower part of the fault plane below the central region exhibits even lower throw gradients and is separated from the central part by a thin continuous high amplitude package of reflections located at 1800 ms TWT. Some of the T-z plots (crossline 3214) might be described as exhibiting asymmetric conical-shape profiles (C-type of Muraoka & Kamata 1983) with extremely low gradients. Some other profiles can be described as a hybrid type between C and M-type (crossline 3258). The lateral tips are interesting in that they exhibit throws profiles with a virtually constant throw over almost the entire height of the plot.

The throw gradients in the main part of the fault are in general very low (<0.023 with an average between 0.01 and 0.05). The extreme upper and lower tips of the fault (5 to 10%) exhibit higher throw gradients ranging from 0.03 to 0.3 (average c. 0.08). Some irregularities in the throw profile, for example in the vicinity of Horizon E on crossline 3242, are due to localised small changes in lithology. As seen on the throw contour plot, the lower tip terminates at a shallower level than the rest of the fault plane (between 1800 and 1900 ms TWT) between crosslines 3210 and 3222. The vertical throw patterns in this region of the fault become slightly asymmetric C-shape profiles with a flat part between horizons D and E and lower tip gradients increasing from Horizon E to the lower tip position.

In summary, Fault 17 is interpreted as a blind fault that exhibits no present or past interaction with a free surface, another structure or important lithological boundary such as the YMM or the Messinian evaporites. The T-z plots are characterised mainly by M-type or hybrid profiles over the entire fault plane with very low throw gradients except in close proximity to the upper and lower tips. The tip line is elliptical, and throw

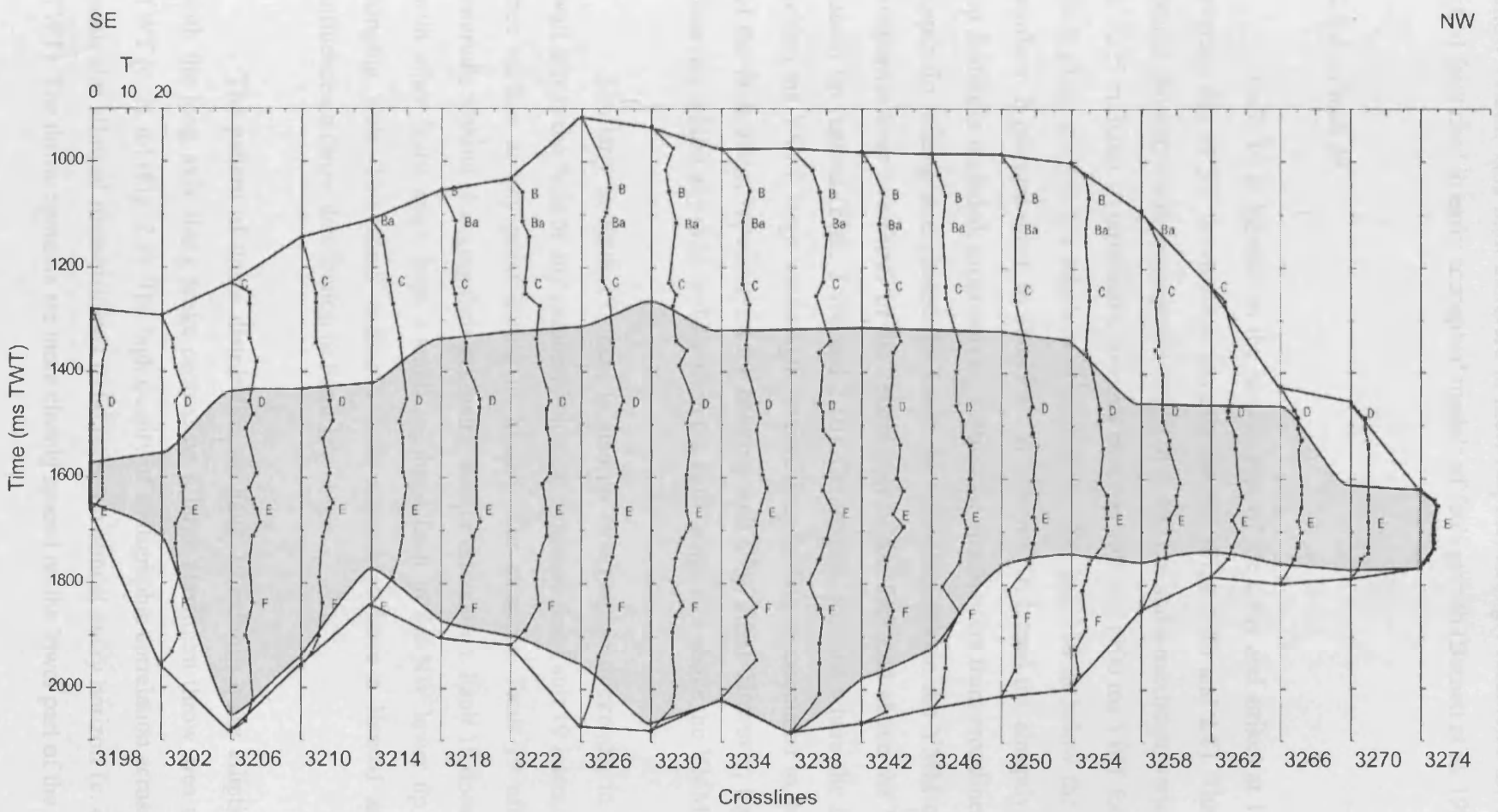

Fig. 2.7: Vertical throw distribution graph for Fault 17 showing T-z plots every 4 crosslines (c. 50 m). Each T-z plot represents the throw value (T) up to 20 ms TWT plotted against z in ms TWT.The blank area represents the tip folding surrounding the part of the fault plane that exhibits clear stratigraphic offset (shaded area). Key horizons are labelled B-F.

contours are concentric with respect to the tip line and to the central region of peak throw values. This fault therefore in most respects strongly resembles the ideal normal blind fault used in early conceptual models of fault growth (Barnett et al. 1987).

2.6.2 Fault 19

Fault 19 is located on the eastern part of the array and strikes at 123° with an average dip of 55° down-slope towards the NE (Figs. 2.2b and 2.8). The fault has a planar geometry with a maximum length of c. 1925 m and a maximum vertical height of c. 1225 m. Fault 19 terminates upwards between 950 and 1100 ms TWT for most of the fault plane (Fig. 2.10) which is equivalent to 200 and 300 m below the present day seafloor. It plunges down to 1800 ms TWT on the SE lateral tip, abruptly if the upper tip folding is included, progressively cutting the stratigraphy from crosslines 2860 if the upper tip folding is excluded. Its lower tip terminates within the YMM or Messinian evaporites over two thirds of the central part of the fault and above the YMM at the lateral tip regions (Figs. 2.8bc and 2.10). On seismic sections where the fault tips out within the YMM, large wavelength reverse drag folding is associated to the lower half of the fault plane, especially in the hanging wall (Fig. 2.8a). However, the fault plane does not exhibit any drag folding when the fault terminates above the YMM (Fig. 2.8d).

Similarly to Fault 17, there is also no stratigraphic thickening in the hanging wall across the fault or any geomorphological evidence that Fault 19 interacted with the free surface at any point during its history. For example, Fault 19 offsets slumps intervals without changing their geometry, size or orientation. Fault 19 does not interact with other faults apart from a small antithetic fault in the NW lower tip of Fault 19 hanging wall. This small antithetic fault appears to have a limited and localised influence on throw distribution of Fault 19.

The pattern of throw distribution on Fault 19 exhibits quasi elliptical contours with the long axis along strike centred on a large maximum throw area up to 24 ms TWT (c. 21 m) (Fig. 2.9). The high quality of stratigraphic correlation across Fault 19 in particular allowed measurements to be taken on almost every horizon (c. every 20 ms TWT). The throw contours are more closely spaced on the lower part of the fault plane

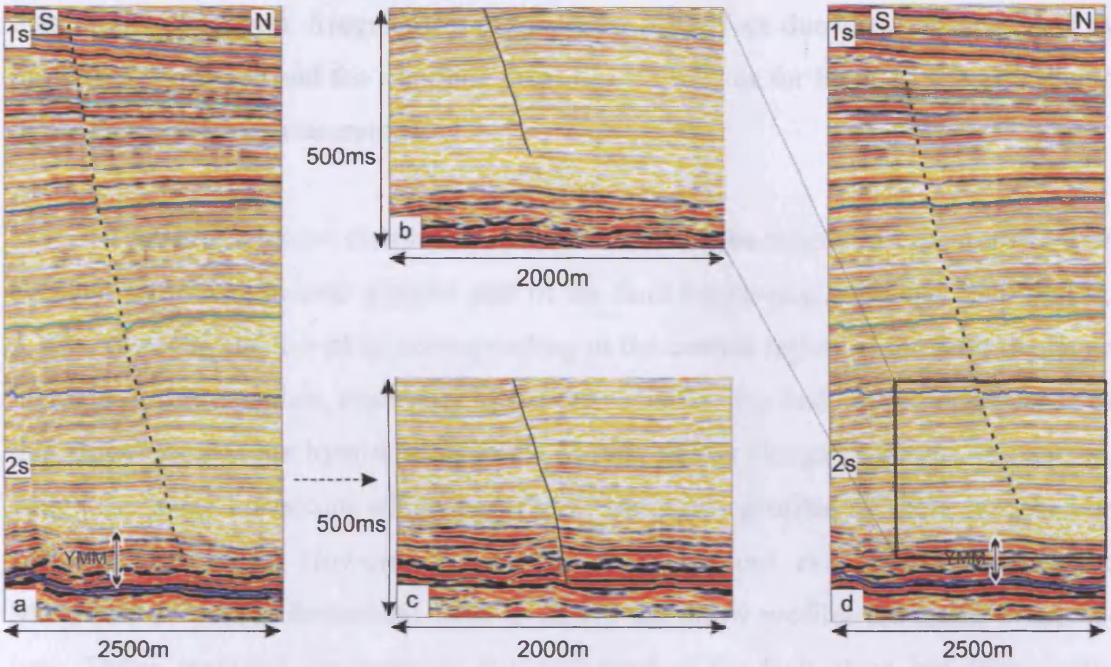

Fig. 2.8: (a) Seismic section across Fault 19 at crossline 2856 illustrating no drag folding in the upper half of the fault and large wavelength reverse drag folding in the lower half (b) Lower tip at crossline 2836 dies out above the YMM and the Messinian evaporites (c) Lower tip at crossline 2892 dies out within the YMM (d) Seismic section across Fault 19 at crossline 2836 showing no drag folding.

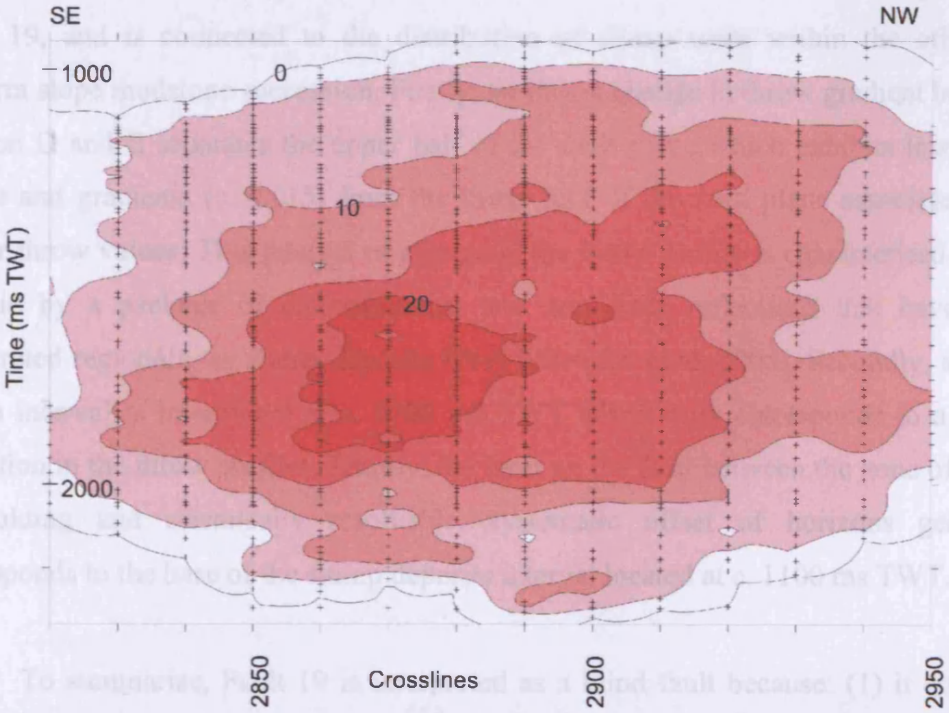

Fig. 2.9: Throw contour plot for Fault 19 showing lines of equal throw value every 5 ms TWT. 809 throw values were measured on 14 seismic sections equally spaced at 125 m. Higher throw values (>20 ms TWT) are expressed as dark colours.

than on the upper part. Irregularities in the throw pattern are due to the spacing used by the kriging software and the sampling error (2ms TWT) as for Fault 17 but also due to the large number of measurements.

The vertical throw distribution for Fault 19 exhibits mainly M-type profiles with constant throw values over a major part of the fault height (e.g. crossline 2940 on Fig. 2.10). However, the T-z plots corresponding to the central region of the fault depict an increase of throw values, especially in the lower half of the fault. As a consequence of this, throw profiles are hybrid between the M-type and an elongated C-type. In contrast, where the basal tip occurs within the YMM, the throw profiles are best described as asymmetric C-types. However, where the fault tips out even deeper, within the Messinian evaporites (crosslines 2890 to 2910), the throw profiles are closer to the M-type. Throw gradients are generally low over most of the fault plane, but dramatically increase (by c. 50%) close to the upper and lower tip regions. Increases in the throw values and gradients in the lower half of the fault plane are associated with large wavelength reverse drag folding.

The influence of lithology on throw distribution can be seen at several places on Fault 19, and is connected to the distribution of slump units within the otherwise uniform slope mudstone succession. Firstly, an abrupt change in throw gradient between horizon D and E separates the upper half of the fault plane which exhibits low throw values and gradients (c. 0.015) from the lower half of the fault plane associated with higher throw values. This interval of change in the throw profile is characterised on the seismic by a package of discontinuous, low amplitude reflections that have been interpreted regionally as slump deposits (Frey Martinez et al. 2005). Secondly, another slump interval is interpreted at c. 1700 ms TWT which only corresponds to a minor inflection in the throw profiles. Thirdly, the limit on the fault between the zone of upper tip folding and seismically resolvable, systematic offset of horizons generally corresponds to the base of the slump deposits interval located at c. 1100 ms TWT.

To summarise, Fault 19 is interpreted as a blind fault because: (1) it does not exhibit any stratigraphic or geomorphological evidence of synsedimentary motion; (2) the throw contour plot shows approximately elliptical lines centred onto a large zone of maximum throw values; (3) the upper tip plunges down towards the lateral tips cutting

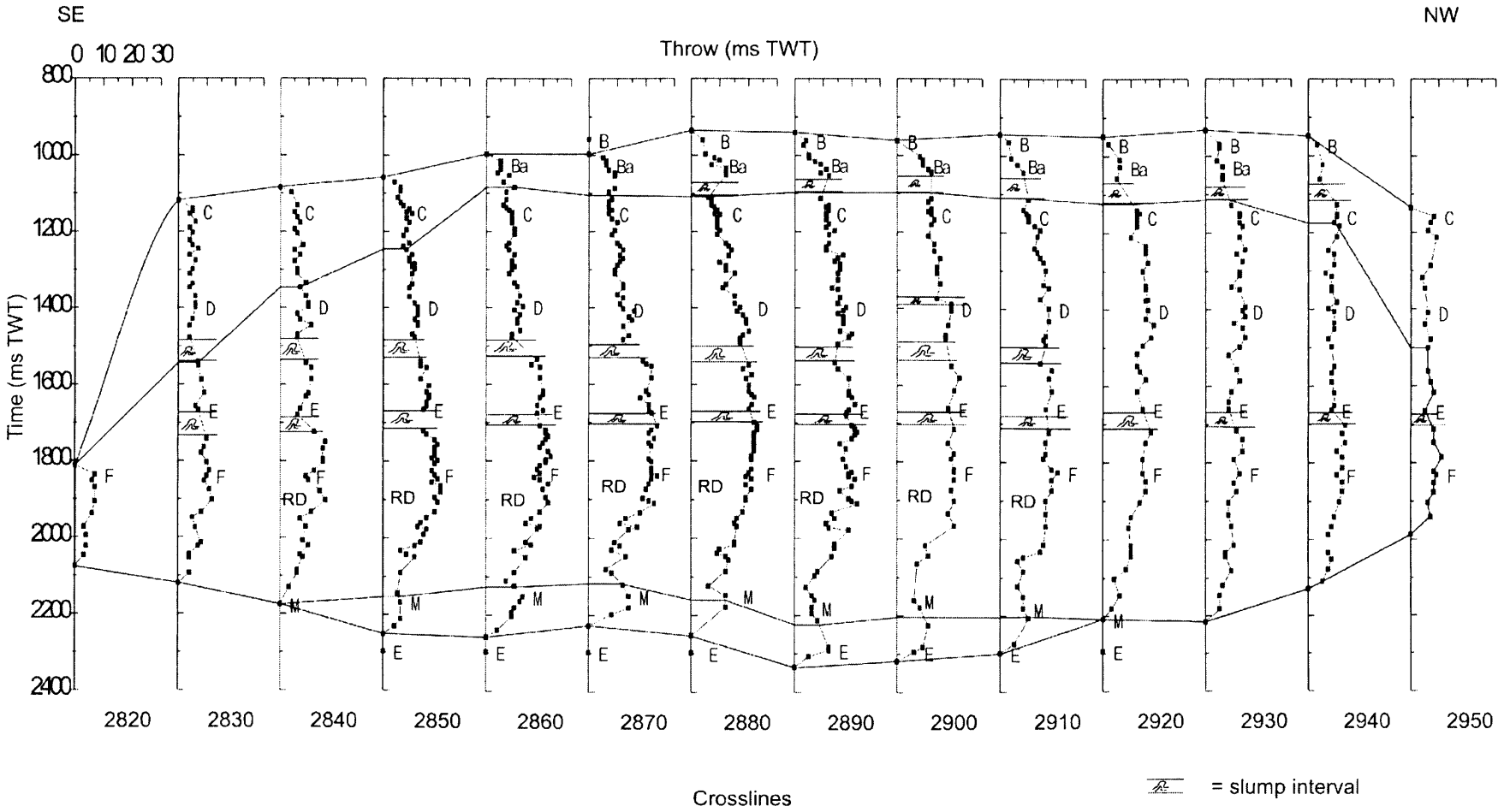

Fig. 2.10: T-z plots for Fault 19 illustrating the vertical throw distribution every 10 crosslines (c. 125 m). Blank area represents the tip folding surrounding the fault. Reverse drag folding (RD) is observed in the part of the fault that accumulated the most displacement. B, Ba, C, D, E and F are mapped Plio-Pleistocene horizons. M and E are respectively the top of the Yafo Marls Member and the top of the Messinian evaporites.

the stratigraphy as it does so. The vertical throw distribution is mainly of the M type, although departures from this are associated with the stratigraphic unit in which the basal tip is located, indicating a first-order control by the mechano-stratigraphy.

2.6.3 Faults 15 and 16

Faults 15 and 16 are two similar sized fault segments that are linked across a small relay zone (Fig. 2.2b). Figure 2.11 shows a typical cross section through Fault 16 that is also representative for the geometry of Fault 15. Planar fault segments strike at 123° dipping between 55 and 58° towards the NE. Faults 15 and 16 have maximum heights of respectively c. 1015 m and 970 m for a maximum length of c. 1735 m and 1970 m and a maximum throw of 24 ms TWT. The faults do not show any evidence of synsedimentary interval at any point of their evolution. Fault 20 is antithetic to faults 15 and 16 and interacts with their lower tip lines between crosslines 3010 and 3150.

The upper tip, propagation fold included, terminates c. 100 to 200 m beneath the present day seafloor and progressively cuts the stratigraphy plunging c. 100 to 300 m down towards the lateral tips (Fig. 2.13). The region of the fault dominated by upper tip folding extends for about 100 m below the resolvable upper tip (10% of maximum fault height). This region extends further down the fault plane in two areas, (1) towards the lateral tips and (2) in and around the relay zone between Faults 15 and 16. The upper tip folding terminates at the same level over Faults 15 and 16 as well as for the relay zone in between both faults (Fig. 2.13). If upper tip folding is excluded however, the upper tip marks the linkage zone between the two faults by minima throw values. This suggests that the present day upper tip folding is due to the propagation of Faults 15 and 16 during their kinematically linked evolution i.e. post-hard linkage. The lower tip of both faults can be interpreted as being just above the YSM at the centre of both segments. The lower tip position shallows towards the lateral tips and towards the relay zone where the lower tip is located 100 ms TWT above the YSM (Fig. 2.11).

The throw contour plot for Faults 15 and 16 is presented in Figure 2.12. The elliptical throw contours are parallel to each other from the outer line of zero throw to the 6 ms TWT contour. For values above the 6 ms TWT contour, the contours are

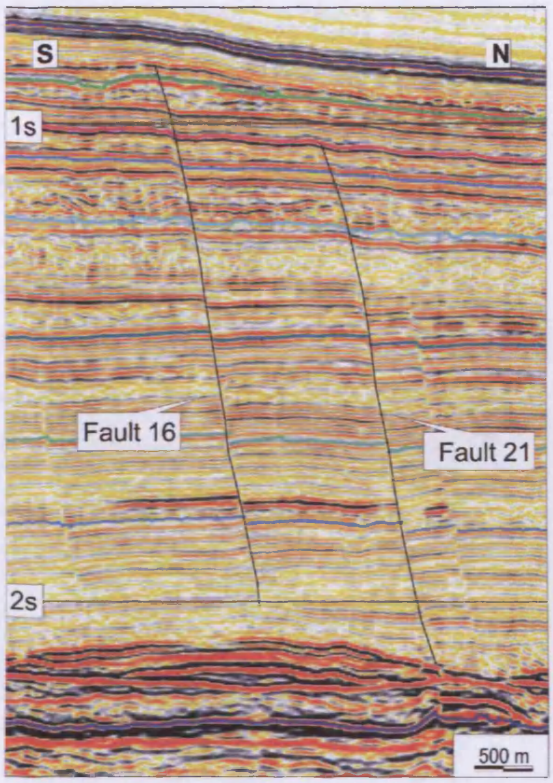

Fig. 2.11: Seismic cross section showing locations and geometries of Faults 16 and 21.

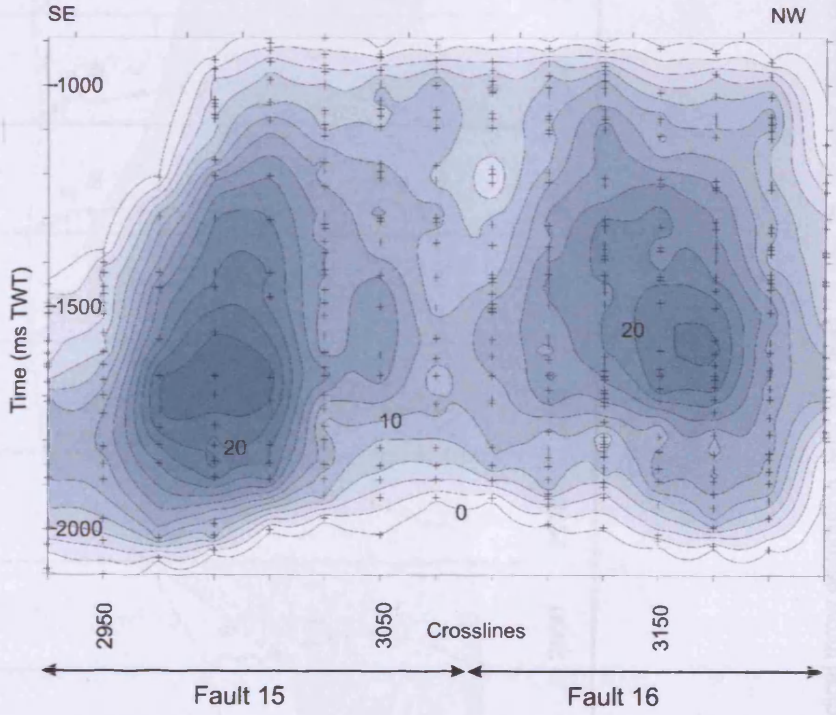

Fig. 2.12: Throw contour plot for Faults 15 and 16. Throw contours are spaced every 2 ms TWT. Crosses indicate the 446 measurements presented every 20 crosslines (c. 250 m).

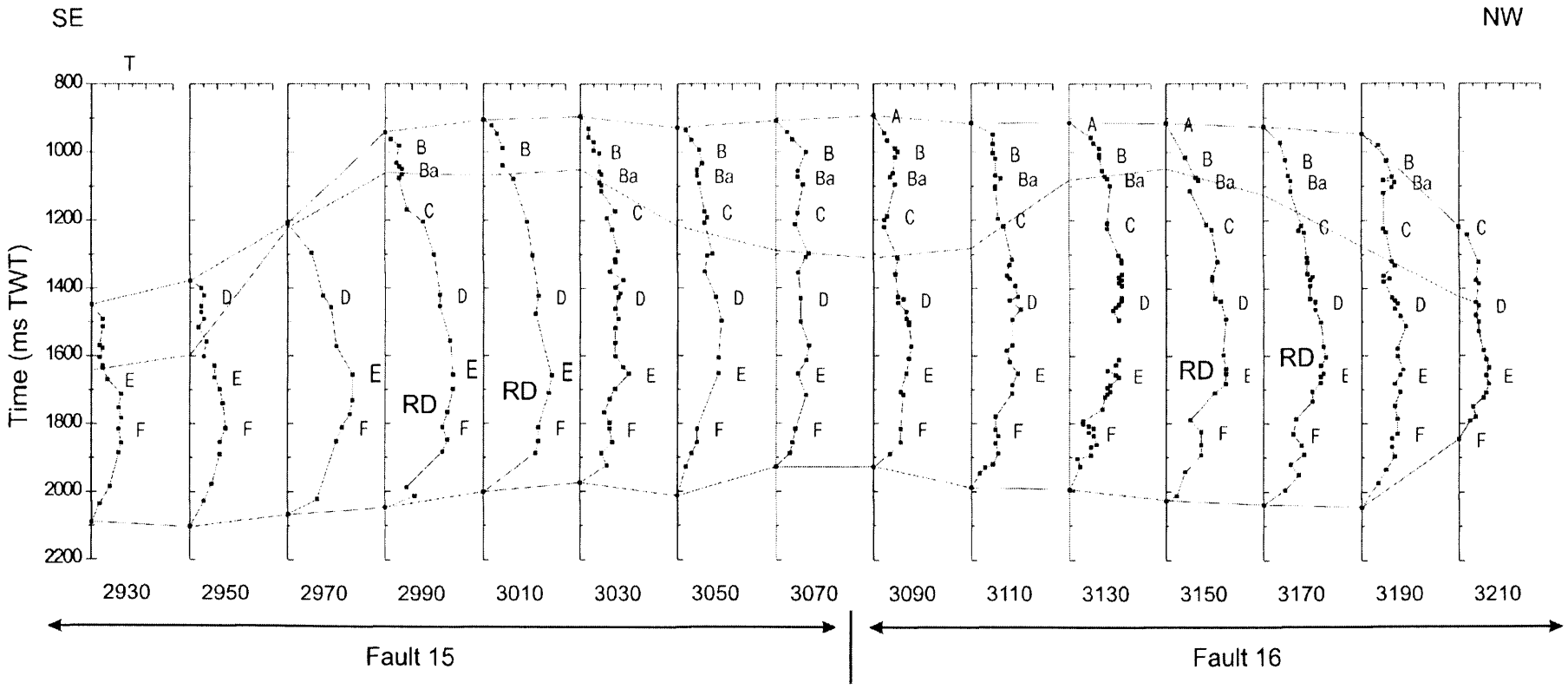

Fig. 2.13: Vertical throw distribution plots for Faults 15 and 16. Shaded area is faulted and blank area is upper tip folding. T-z plots represent the throw values (T) up to 30 ms TWT plotted against time (z) every 20 crosslines (c. 250 m). RD indicates reverse drag folding associated to this part of the fault.

concentric and centred on the two distinct zones of maximum throw located at the middle of the two segments. The highest throw gradients occur in the lower part of the fault plane. A sub-vertical zone of minimal throw values separates the two segments as is expected in the case of soft linkage (e.g. Peacock & Sanderson 1991, Walsh & Watterson 1991).

The vertical throw distribution for Faults 15 and 16 is mainly characterised by patterns that are a hybrid of C and M types (Fig. 2.13). T-z plots from the relay zone are closer to M-type than C-type whereas T-z plots from the central part of Faults 15 and 16 are best described as asymmetric C-shaped throw profiles. Crossline 3130 is a good example of a typical hybrid C-shape throw profile with a flat portion extending over more than 300 ms TWT in the central part of the plot. However throw profiles are closer to asymmetric C-type for the fault centres where more displacement accumulated and these regions are also associated with large wavelength reverse drag folding (labelled RD on Fig. 2.13). A small decrease in throw values is observable on most of the T-z plots just above Horizon F. This corresponds to a thin package of continuous high amplitude reflections indicative of an abrupt contrast in lithology.

In summary, Faults 15 and 16 are interpreted as blind faults on the basis that (1) they show no evidence of having interacted with the free surface, (2) the geometry of the upper tip line is strongly plunging towards the SE lateral tip.

2.6.4 Fault 21

Fault 21 is located at the northwestern edge of the El Arish array (Figs. 2.2b and 2.11). The fault has a planar geometry dipping 56° towards the NE and strikes at 130°. Its maximum length is 2050 m for a maximum height of 985 m and the maximum throw is c. 21 m. There is no evidence of any interaction of Fault 21 with the free surface, in that none of the mapped horizons intersecting the upper half of the fault plane show any geomorphological expression of the presence of a fault scarp. The region of the fault plane characterised by upper tip folding spans almost a third of the height of the Fault 21. The upper tip line is sub-horizontal in the centre and plunges over 200m towards the southeastern tip. This steeply plunging region of the upper tip is within the zone of

interaction with antithetic Fault 20 upper tip (Fig. 2.15). It is possible that the upward propagation of Fault 21 was inhibited by interaction with Fault 20 (c.f. Segall & Pollard 1980). The lower tip terminates at the top of the YSM on crosslines 3160 to 3220 and becomes progressively shallower towards the lateral tips. A small antithetic fault interacts with the lower tip of Fault 21 but this interaction does not affect the throw distribution pattern to any significant extent.

Two distinct zones of throw maxima can be seen from the throw contour pattern shown in Figure 2.14. The larger of these has a maximum value of 24 ms TWT and is centred on crossline 3180. This is separated by a sub-vertical zone of minimal throw values from the second and smaller maximum, centred on crossline 3140. These two regions of throw maxima are surrounded by quasi-elliptical throw contours. This pattern is interpreted as having resulted from the hard linkage of two fault segments (Walsh & Watterson 1991, Nicol et al. 1996).

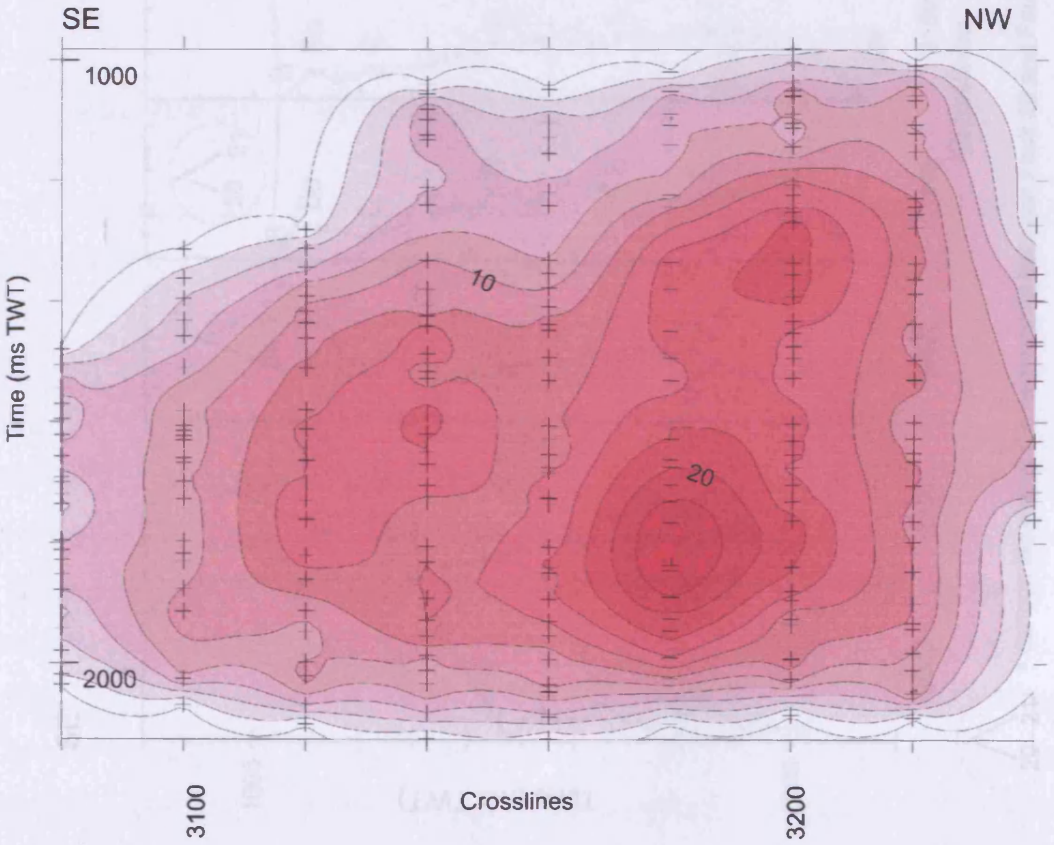

Fig. 2.14: Throw contour plot for Fault 21 based on 234 measurements and presented every 20 crosslines (c. 250 m). Throw contours spaced every 2 ms TWT.

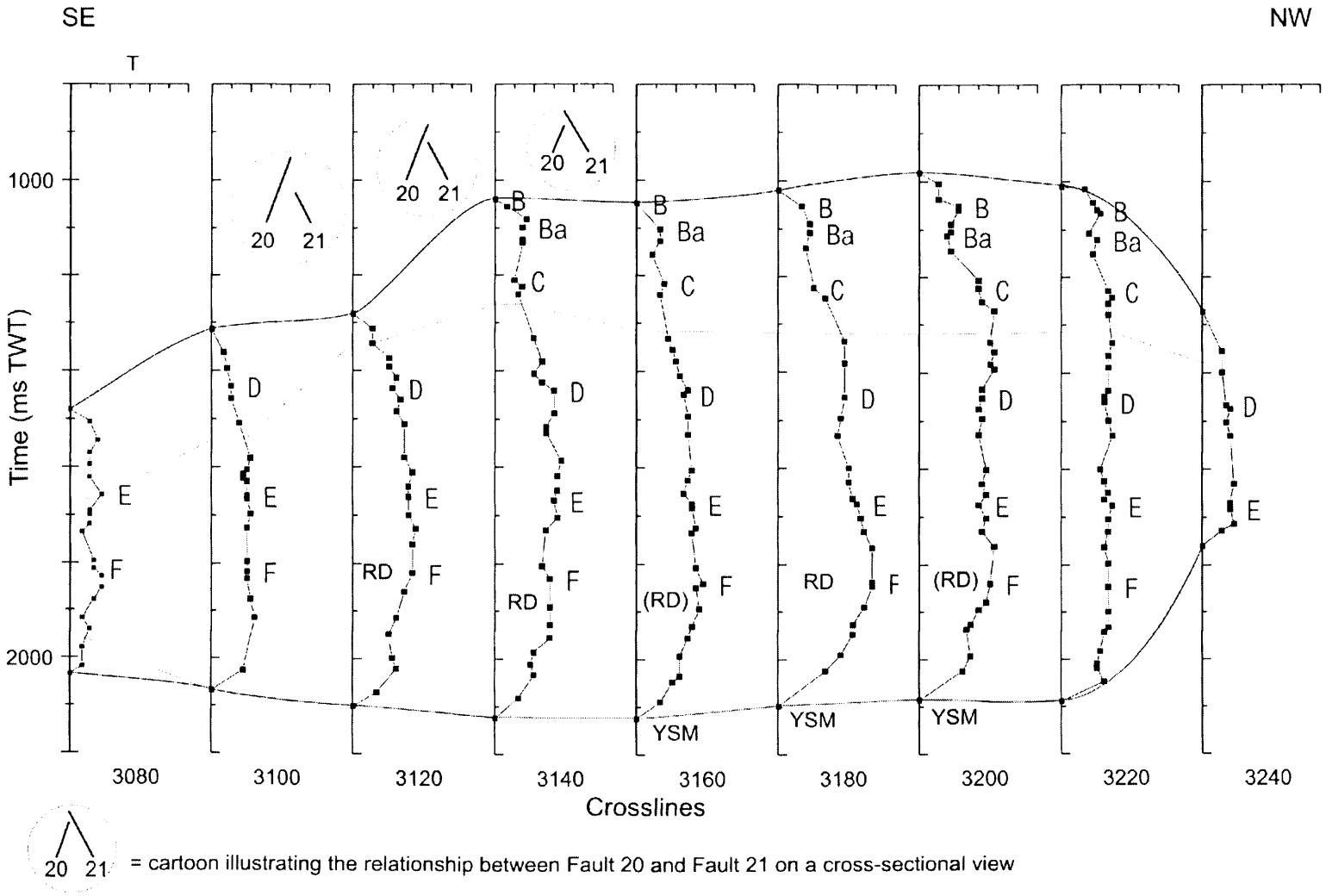

Fig. 2.15: T-z plots for Fault 21. T is the throw values in ms TWT and up to 30. B, Ba, C, D, E, F and Yafo Sand Member (YSM) are mapped horizons. RD is reverse drag folding, the brackets indicating small amplitude.

The vertical throw distribution of Fault 21 varies considerably along the fault trace. M-type patterns with throw gradients increasing just abruptly at the upper and lower tips for the lateral tip regions are seen for T-z profiles at crosslines 3080, 3220 and 3240 (Fig. 2.15). Hybrid profiles are seen on crosslines 3100, 3120, 3140 and 3200, and these can best be described as elongated C-shape throw profiles with generally low throw gradients in the tip regions and a large central portion with very small variation in the throw values. Asymmetric C-shape throw profiles are only observed in the central part of the fault (crosslines 3160 and 3180) with the maximum throw value located in the lower part of the fault plane. This part of the fault that accumulated the most displacement also corresponds to where the fault tips out at the top of the YSM. The seismic data reveals large wavelength reverse drag folding associated with the lower half of the fault plane coincident with the highest throw values.

In summary, Fault 21 is a single fault formed by the hard linkage of two originally blind segments with no evidence of having intersected the free surface.

2.6.5 Maximum throw versus maximum length

The dimensions of the 30 selected faults from the El Arish array are plotted in a maximum throw versus maximum fault length graph (Fig. 2.16). These faults are all considered to be blind faults using the criteria outlined above for the individual case studies. A linear regression line passing through the origin and the data points gives a slope of 0.0113 with $R^2 = 0.3478$ and an exponential regression line is expressed as $y = 8.9974e^{0.0004x}$ with $R^2 = 0.5525$. However, the dataset exhibits however significant scatter. Faults of similar maximum throw can have a range of trace lengths that vary by a factor of 2. In the same way, faults with similar length can be characterised by markedly different maximum throw values as previously suggested (e.g. Cowie & Scholz 1992a, Cartwright et al. 1995). What is particularly interesting with this dataset is that the scatter is present in an exclusively blind population, whereas previous studies of scatter in D versus L have been largely based on faults that intersect a free surface.

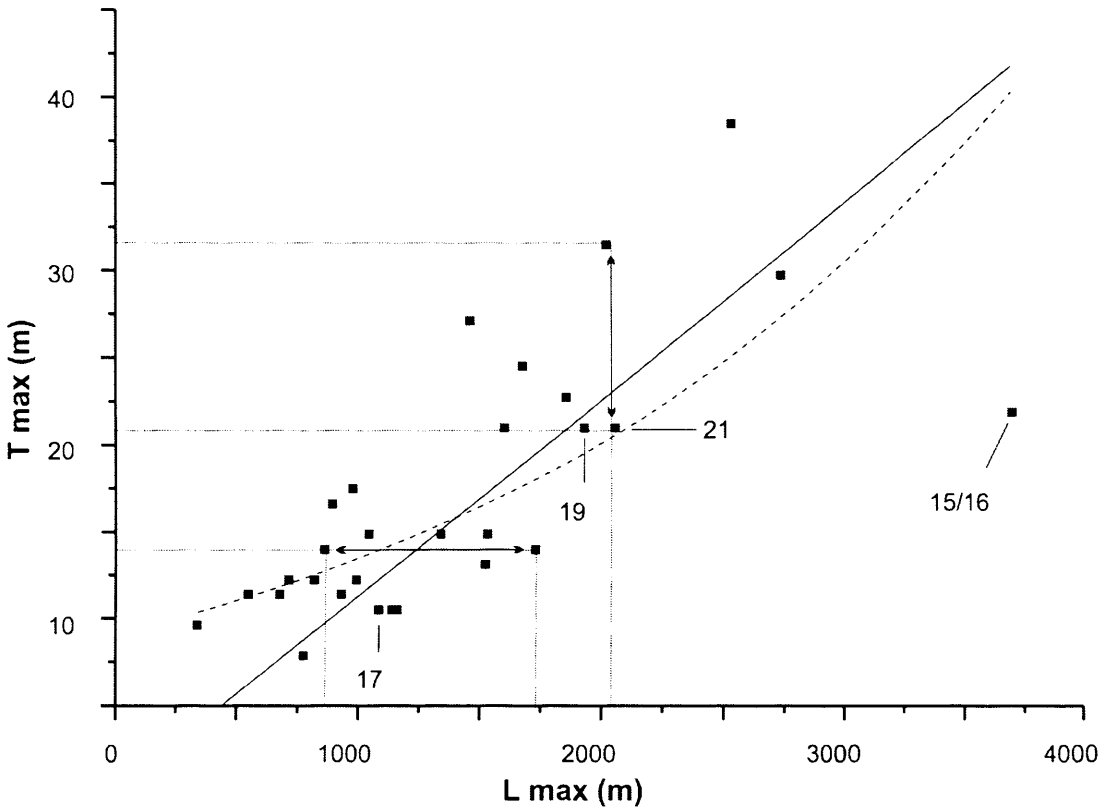

Fig. 2.16: Maximum throw (T max) versus maximum length (L max) plot for the 30 faults selected from the El Arish array. Detailed throw analyses are presented in this chapter for Faults 17, 15/16, 19 and 21. Linear regression line ($y = 0.0113x$) and exponential regression line ($y = 8.9974e^{0.0004x}$) are respectively shown in solid and dashed lines. Arrows underline the scatter that characterises the data.

2.7 Discussion

The case studies presented above focused on the throw distribution for a population of blind normal faults. Based on these examples, we now proceed to summarise and discuss the criteria that could be regarded as most diagnostic when assessing whether or not faults interpreted on seismic data are blind structures. The discussion also addresses the effects of interaction during propagation between neighbouring structures or with a major lithological barrier. The discussion closes with some consideration of the implications of this analysis for fault growth models in general.

2.7.1 Criteria for recognition of blind faults

Based on the original definition of blind faults (Watterson 1986), we suggest three main criteria for use when assessing whether or not a fault is blind: (1) plunging upper tip line geometry, (2) presence of upper tip propagation folds, and (3) absence of clear sedimentary or geomorphological indicators of the fault plane intersecting a paleo-seafloor.

2.7.1.1 Tip line plunging

It has been suggested that sub-horizontal throw contours indicate synsedimentary fault movement (Childs et al. 2003). Throw contours exhibit an abrupt change from sub-vertical, characterising a post-sedimentary behaviour of the fault, to sub-horizontal, indicating a synsedimentary movement of the fault. However, recognising synsedimentary movement based on throw contour geometry alone is not systematic. Tip line plunge is perhaps the least ambiguous diagnostic indicator, because it is generally highly unlikely that a similar geometry could be achieved by any fault that was intersecting the free surface. Fault 17 is an excellent example to present this argument in more detail. The upper tip plunges down several hundreds of metres from the central part towards the lateral tip region (Fig. 2.7). The stratigraphic level at which the fault tips out upwards in the central part is c. 350 m above the stratigraphic level of the tipline towards the lateral margins of the fault. This stratigraphic interval of 350 m is equivalent to over a million years of sediment deposition. Were the fault to have been a synsedimentary fault intersecting the sediment interface rather than a blind fault, then to achieve this current geometry would require that the fault propagated to a maximum length, and then continued activity to become more and more centralised with time, with a steady decrease in active strike length through time. This seems intrinsically unlikely and counter to the general model of fault growth that suggests an extension of strike length as displacement accrues.

The same observation can be drawn from the throw analysis for Fault 19 (Fig. 2.10). If the propagation fold is excluded, the upper tip line plunges c. 600 m vertically over a distance of 500 m towards the SE lateral tip. The fault tips out at progressively

shallower stratigraphic levels arguing strongly that this fault is indeed a blind fault. Faults 15 and 16 exhibit the same tipline geometry (Fig. 2.13), reinforcing the view that this is a recognisable indicator of blind faulting.

2.7.1.2 Upper tip propagation fold

Upper tip folding in a monoclinal style is frequently recognised to be associated with upward propagation of blind normal faults (e.g. Gawthorpe et al. 1997, Patton et al. 1998, Hardy & McClay 1999, Withjack & Callaway 2000, Jackson et al. 2006). Provided that the seismic resolution (spatial and vertical) is sufficient to enable this type of folding to be distinguished from imaging artefacts, the presence of a region beneath the upper tipline with systematic tip folds is regarded as a good criterion to recognise blind faults.

In the examples presented in this chapter, the proportion of the fault surface that is apparently (to seismic resolution) expressed as a region of upper tip folding is a variable, but significant percentage of the total surface area of the fault. For Faults 17 and 21, for example, this proportion is over 30% (Figs. 2.7 and 2.15), whereas for Fault 19 it is only 10% (Fig. 2.10). Throw gradients, or more specifically the gradient of decay, in the tip fold amplitude are generally low, but comparable with upper tip gradients where the gradient is measured from vertical variation in true fault offset of stratal reflections. The significance of the low gradients applies to the wider application of this criterion. In our case studies, the recognition of upper tip folds was possible because of the very good spatial and vertical resolution relative to the scale of the offsets or fold amplitudes. This allowed us to differentiate systematic offset of unfolded strata (fault offsets) from short wavelength monoclines (tip fold). However, we note that on poorer quality (lower frequency) seismic data, it may not be possible to separate these two end members (Walsh & Watterson 1987). Hence the use of this criterion is dependent on scale and data quality.

A final point to note is that the examples presented here show that upper tip folding can span up to a third of the surface area of a fault. This might lead us to ask whether 'displacement' in the form of tip folding should be included in conventional

measurements of throw profiles. The need for a systematic approach here to measuring fault parameters is clear: failure to include tip folded zones in our studies for some faults would have added to the already scattered D-L data presented in Figure 2.16.

2.7.1.3 Absence of sedimentogical and geomorphological evidence of synsedimentary fauting.

True synsedimentary faulting is, in many cases, patently expressed in the form of growth packages, with significant thickening in the hanging wall (e.g. Wadsworth 1953, Hardin & Hardin 1961, Thorsen 1963). However, many small synsedimentary faults with low expansion factors are much harder to recognise as such. For individual faults it may be impossible to argue whether they are small synsedimentary faults or blind faults. If, however, an array of faults is under scrutiny, the problem is in some ways easier. If all the faults in an array tip out upwards at a single horizon, it is very unlikely that the faults were blind. As we have shown, plunging tip lines often reveal true blind character, and by analogy, clustering of tip lines at a single horizon for a fault array is more likely for synsedimentary faults. More potently, of course, faults that intersect the present day sediment surface by definition cannot be blind faults, so this approach applies specifically to buried upper tip lines.

The faults of the El Arish array do not cut up to the present seabed and the upper tips of different faults terminate at different stratigraphic levels. Given the distribution and close spacing of faults in the array, it is very unlikely that they died and were buried at different times and therefore at such a range of stratigraphic levels if these faults were synsedimentary. It is much more probable that they are all blind faults, and have propagated upwards to differing levels. Their current upper tipline positions thus reflect the stage of blind propagation and this has no temporal significance.

It was noted above that for the case study faults there is no obvious stratigraphic thickening in the hanging wall of any fault. The absence of geomorphologic evidence of fault interaction with the seabed, such as a change in the shape, size or direction of slope channels or mass transport complexes also supports the interpretation that these faults are blind. However, the extent to which synsedimentary faults can potentially impact

the surface morphology and sediment transport patterns is governed by slip rate versus sedimentation rate (Edwards 1995, Cartwright et al. 1998) so the absence of these indicators can sometimes be due to resolution and scale problems rather than to the lack of surface interaction. For this reason, caution should be applied when using this criterion and it should only really be used in conjunction with the other two.

2.7.2 Fault drag folding

Fault drag folding is an important element to consider when assessing blind fault growth because when combined with fault offset it completes the full description of deformational field in the volume surrounding the fault (Barnett et al. 1987, Schlische 1995, Rykkelid & Fossen 2002, Grasemann et al. 2005).

Seismically resolvable drag folding surrounding Fault 17 is almost non-existent. Fault 19 exhibit large wavelength drag folding along with the part of the fault plane that accumulated the most displacement (Figs. 2.8 and 2.13) in the lower part of the central zone that terminates within the YMM or the Messinian evaporites. However, the upper half of the fault and the lateral tips that exhibit M-shape profiles do not seem to be associated with any drag folding. Like Fault 19, Faults 15, 16 and 21 are only associated with reverse drag folding in the parts of the faults that exhibits asymmetric C-shape profiles or hybrids (Figs. 2.12 and 2.15). These parts accumulated additional displacement because their lower tips terminate at the top of the YSM. This poses the question of whether the drag folding is actually due to rock wall straining associated with the initiation and propagation of the blind fault or if it is due to the additional slip accumulated in the lower part of the fault when the lower tips interacted with the YMM and Messinian evaporites.

2.7.3 Barriers to fault growth and lithological controls

2.7.3.1 Lower tip terminates within YSM, YMM or Messinian evaporites

The importance of mechanical stratigraphy has been emphasised in some recent studies, specifically those suggesting that lithological boundaries might act as barriers to fault propagation (Rippon 1985, Gross 1995, Childs et al. 1996, Nicol et al. 1996, Wilkins & Gross 2002). The general concept advanced in these studies that when a fault abuts against a mechanical barrier, its propagation is then restricted, displacement gradients increase at the fault tip as a result of additional slip in the lower part of the fault.

In this study, a number of examples of mechano-stratigraphic influences on propagation were recognised. Fault 17 terminates just a few tens of metres above the YSM which directly overlies the YMM and the Messinian evaporites (Fig. 2.5). However, it does not exhibit steeper throw gradients at its lower tip and its throw profiles remain fairly M-shaped (Fig. 2.7).

The question is whether or not Fault 17 is restricted by this different lithological interval because such layers could act as a mechanical barrier to the fault propagation (e.g. Nicol et al. 1996). Restricted faults are generally characterised by higher displacement gradients on a part of the tip line or on half of the fault plane close to the structure or lithological barrier (Nicol et al. 1996, Wilkins & Gross 2002). This anomalous displacement increase provides the additional strain necessary for the fault to propagate through a mechanical barrier (Nicol et al. 1996, Gupta & Scholz 2000, Wilkins & Gross 2002). Faults directly in contact with a mechanical boundary have been observed in some cases to preserve low throw gradients along fault tips, even in faults that propagated from shale to sandstones (Wilkins & Gross 2002). However, these faults were not considered as fully restricted by the mechanical barrier. Fault 17 does not exhibit steeper gradients in the vicinity of the YSM than it does at the upper tip. Fault 17 is therefore considered as unrestricted.

Faults 15, 16, 19 and 21 exhibit asymmetric C-shape throw profiles with added displacement in the lower part of the fault planes in the zones where the faults terminate just at the top of, or within, the YSM (Figs. 2.10, 2.13 and 2.15). It is suggested that the propagation of these faults was inhibited by the mechanical boundary and throw was added in the lower part of the faults above the contact with the YSM.

2.7.3.2 Interval of slump deposits

The faults of the El Arish array offset the slump deposits recognised on the Levant basin 3D survey (Frey Martinez et al. 2005) without changing their geometry and orientation. However, the slump intervals influenced the propagation of the blind faults and the throw distribution on the fault planes.

The slump deposits do not have significant effect on Fault 17 propagation and the throw distribution over the fault plane. However, each slump interval, acting as a mechanical barrier, seems to have restricted a part of the upward propagation of Fault 19 especially in the central part of the fault plane (crossline 2850 in Fig. 2.10). The lateral tips of the fault revealing M-type throw profiles still exhibit a rapid and small upward decrease in the throw values when the fault propagated through a slump deposit (example 2940 in Fig. 2.10).

The boundary between folding and faulting at the upper tip corresponds to the base of a slump deposit. This suggests that the dimension of the upper tip folding is controlled by the location of a different mechanical stratigraphy.

2.7.3.3 Continuous, high amplitude package of 3 or 4 reflections

The negative throw anomaly located generally just above Horizon F at c. 1800 ms TWT on Faults 17, 15 and 16 corresponds to a continuous high amplitude package observable on the seismic data (Figs. 2.5, 2.7, 2.11 and 2.13). A part of the lower tip in the SE of Fault 17 does not propagate downward through this interval. It is also very likely that this package is responsible for the anomalous lower tip folding between crosslines 3242 and 3258. The central part in Fault 17 probably accumulated more displacement in order to be able to subsequently propagate through this package.

The information provided by the well Gaza-Marine 1 indicates that a thin trace of limestone overlies an interval of sandstones at the depth corresponding to that interval. The seismic characteristics of these high amplitude reflections suggest that these are thin layers of sands filled with gas interbedded in the clay-stones. This could

explain the decrease in throw values at that level on several faults due to a small and abrupt decrease in the velocity, but also could have acted as a mechanical barrier to faults propagation.

2.7.4 Interacting faults

2.7.4.1 Synthetic faults

As two faults propagate towards each other, tip stress fields are altered (Segall & Pollard 1980) and fault propagation is inhibited. Fault tips gradients have been shown to steepen as a result of interaction with others faults (Walsh & Watterson 1989, Peacock & Sanderson 1991, Cartwright et al. 1995, Nicol et al. 1996, Gupta & Scholz 2000, Wilkins & Gross 2002). Cowie & Scholz (1992b) suggested a post-yield fracture mechanics model in which lateral displacement would become bell-shaped when the peak stress equals the shear strength of the surrounding rock. A physical model was later proposed in which the fault propagates in small patches relative to the dimensions of the fault (Cowie & Shipton 1998). Some faults from the El Arish array interact in different ways with synthetic faults. Faults 15 and 16 intersected and linked by their lateral tips trough a relay zone (Fig. 2.12) and Fault 21 shows the scar of a linkage between two segments (Fig. 2.14). This raises a question concerning how far from the intersection can the extra displacement be added. It also questions the origin of certain C-shape throw profiles that could be due to linkage rather than the way the faults grew.

2.7.4.2 Antithetic faults

Antithetic faults interact or intersect with the upper and lower tips of Faults 15, 16 and 19 with more or less perturbation on the throw distribution. A small antithetic fault intersects with the NW lower tip of Fault 19 in its hanging wall. This small antithetic fault appears to have a limited and localised influence on Fault 19 throw distribution (Fig. 2.9).

The lower tip of Faults 15 and 16 interact between crosslines 3010 and 3150 with the lower tip of antithetic Fault 20. The T-z plots on crosslines 3010 and 3030 are very different although the geometry and position of interaction between Fault 15 and Fault 20 is very similar (Fig. 2.12). However, T-z plots on crosslines 2990 and 3010 are extremely similar although Fault 20 is not present on crossline 2990. Therefore, in this particular case, the antithetic fault is very likely to have very limited effects on the throw distribution pattern. This is likely to be due to the position of the fault planes lower tips that form almost a perfect "V" shape that is not completely closed just at the top of the YSM. These are examples of antithetic faults that do not have a significant effect on the throw distribution of the synthetic fault.

It is however, different for antithetic Fault 20 upper tip terminating just above Fault 21 upper tip (Fig. 2.15). The stress field surrounding Fault 20 acted as a barrier to Fault 21 propagation. Fault 21 propagates upwards rapidly when Fault 20 upper tip retreats slightly. Its upper tip terminates by upper tip folding on 300 ms TWT at the same stratigraphic level except on two cross-sections 3120 and 3100. This can be explained by the fact that antithetic Fault 20 tips out upwards just above Fault 21 upper tip (see cartoons on Fig. 2.15). If Fault 20 propagated before Fault 21, the stress field surrounding its upper tip could have acted as a barrier to Fault 21 propagation. On crossline 3140, Fault 20 upper tip retreats slightly, which is enough to allow Fault 20 upper tip to propagate upwards. This could explain the increase in the positive throw gradients and the additional throw values on T-z plot 3120 as well as the anomaly in the upper tip geometry.

2.7.5 Throw distribution patterns on the fault planes and growth model for the El Arish faults

2.7.5.1 Throw distribution patterns

Most previous examples of throw contour plots of normal faults are characterised by crudely elliptical contours centred on the region of maximum accumulated displacement. This type of pattern has been widely interpreted as being due to fault growth by radial propagation (Barnett et al. 1987). However, an analysis

including detailed vertical throw distribution plots correlated to the stratigraphy is a powerful addition to the graphical methods used to reconstruct fault growth.

Fault 17 is interpreted as an individual, unrestricted blind fault. Simple blind normal faults, in the absence of barriers and strong interaction with others faults are expected to exhibit C-shape or triangular displacement profiles (Peacock & Sanderson 1991, Nicol et al. 1996, Manighetti et al. 2001). However, most T-z plots measured from Fault 17 exhibit M-shape or hybrid profiles with very low throw values (< 12 ms TWT) and particularly low throw gradients (0.005-0.02) except at the extreme upper and lower tips (Fig. 2.7). The only clearly asymmetrical C-shape profiles are due to the high amplitude reflection interval at c.1800 ms TWT that acted as a mechanical barrier.

Asymmetric or hybrid C-shape throw profiles are more commonly observed on the other faults. This can be attributed to the growth of the faults and their interactions with other structures or contact with the YSM, YMM and Messinian evaporites.

Fault 19 exhibits elongated C-type throw profiles for the part of the fault that tips out within the YMM whereas when the fault terminates within the Messinian evaporites, throw profiles exhibit more M-type patterns, with crossline 2890 being a hybrid between both patterns (Fig. 2.10). The Gaza-Marine 1 well information indicates that the YMM is mainly composed of marls with traces of siltstones and sandstones and the Messinian evaporites mostly composed of anhydrite with traces of clay-stones. The marls seem to act as a mechanical barrier restricting the fault from propagating further. The fault decelerates its downward propagation and throw gradients increase on the lower part of the fault. C-shape throw profiles develop as a consequence of the additional throw in the lower part of the fault. When the lower tip of a fault accumulates more strain energy than the mechanical layer that it abut against, the fault can propagate through (Gupta & Scholz 2000, Wilkins & Gross 2002). Between crosslines 2890 and 2910, the fault had to transect the YMM before tipping out within the Messinian evaporites. The question is to know why this part of the fault still exhibits an M-shape profile if it went through the same lithological barrier. As 100 ms TWT extra height is observed in this area, an explanation could be that a small segment within the evaporites linked with the lower tip of the fault before this part reached the YMM.

Faults 15 and 16 exhibit mostly hybrids or asymmetric C-shape throw profiles with the sections that accumulated the most slip in the central parts of the segments (Fig. 2.13). The lateral tips and the relay zone exhibit mostly M-shape throw profiles. An explanation could be that these zones are the parts of the two segments that accumulated the most slip because they were in a region initiated before the rest of the fault (e.g. Walsh & Watterson 1987). However, since these throw profiles tend to be asymmetric on the sector of the fault at which the lower tip is particularly close to the YSM; it is fair to assume that the YSM acted as a lithological barrier. The fault propagation was restricted by the lithological barrier, throw gradients increased at the lower tip and displacement was accumulated in the lower part of the fault creating the asymmetry on the C-shape throw profiles.

Fault 21 only exhibits asymmetric C-shape throw profiles on the part of the fault that accumulated the most displacement that also corresponds to the area where the fault tips out at the top of the YSM (Fig. 2.15).

2.7.5.2 Growth model for the El Arish array faults

A classical interpretation of the throw contour plots for all faults of the El Arish array would argue that each fault nucleated within the higher throw value zone. From this area, the fault would have propagated in a radial manner towards the present day tip line.

Fault 17 is an interesting example because it is the simplest individual fault of the El Arish array. If Fault 17 is compared to the other faults of similar dimension, the main observation is that the T-z plots exhibit hydrid to M-type profiles with very low throw gradients. The asymmetrical C-shaped throw profiles from the other selected faults can be attributed to strong interaction with other faults or the different mechanical boundary. Most of the displacement on these faults is therefore very likely to be added in a latter stage of evolution.

It has been suggested that the along strike length of normal faults can be established at an early stage of evolution of the fault and increasing in cumulative

displacement is added for near constant length (Morewood & Roberts 1999, Poulimenos 2000, Meyer et al. 2002, Walsh et al. 2002, Childs et al. 2003, Nicol et al. 2005, Vetel et al. 2005). These studies interpreted the approximately constant fault length as being inherited from the reactivation of earlier underlying structures and therefore only concern the along strike dimension of the faults. Our study differs from these in that we are examining primary propagation, rather than the secondary propagation arising when originally formed fault surfaces are reactivated during some much later phase of activity. Our analysis of throw profiles suggests that in our examples, the height of the faults is established rapidly in the history of the El Arish array. If displacement is added on a fault whose length remains almost constant, displacement gradients increase and fault growth paths on D-L ratios do not follow perfectly linear but more step-like pathways.

A fundamental observation is that no striking sharp peak C-type or triangular profile can be observed. Most of the T-z plots exhibit hybrids patterns with a broad central region and very gentle gradients. The significance of M-shape throw profiles has been attributed to a constant wall rock strain on footwall and hanging wall in intervals of stiff materials (Muraoka & Kamata 1983). However, the M-shape and C-shape profiles are representative of faults offsetting the same stratigraphic intervals. This suggests that the shape of the throw profiles might not only be due to mechanical stratigraphy effects but also and perhaps primarily by the way the fault grew and what structures it interacted with. This observation has wide implication for fault growth models.

As a consequence of the M-shape profiles, it is difficult to isolate a clear point of maximum throw value. The maximum throw or displacement position of a fault is often taken to indicate the point of nucleation of the fault according to conceptual models (Watterson 1986, Barnett et al. 1987). However, it has been widely observed that the point of maximum displacement is generally not located at the centre of a fault segment (e.g. Peacock & Sanderson 1991, Willemse et al. 1996). The point of maximum displacement can probably migrate away from the point of fault initiation (Peacock 1991) due to interactions with other faults or variations in elastic properties (Burgmann et al. 1994, Cowie 1998, Cowie & Shipton 1998, Maerten et al. 1999, Schultz 2000) or mechanical barriers (Wilkins & Gross 2002). This study suggests that not only does the

point of maximum displacement migrate from its original position but also that the early propagation of some faults is so fast that it may be more realistic to think of the early stage fault dimension rather than a single point nucleus.

2.8 Conclusions

- This study regards a blind fault as a post-sedimentary fault that shows no evidence that it interacted with the free surface at any time during its evolution. Three main criteria are suggested to help the recognition of blind faults from 3D seismic data: (1) plunging upper tip line geometry, (2) presence of upper tip propagation folds, and (3) absence of stratigraphic or geomorphological evidences of the fault intersecting the free surface and being synsedimentary.

- A detailed analysis of the throw distribution show more variations than previously suggested. Throw contour plots seem to confirm a growth of the El Arish array faults by radial propagation. However, these faults do not exhibit striking triangular or C type vertical throw profile as expected for blind faults but mostly M-type or hybrid throw profiles.

- Throw profiles are greatly influenced by fault interaction with lithological boundaries acting as mechanical barriers or other faults. The consequence of these interactions is an increase in throw gradients and values in the large proximity of the zone of interaction and is not localised to the tip region.

- Comparing the simplest individual unrestricted blind fault with the other blind faults that interacted with a mechanical boundary or another structure suggests that the propagation and establishment of the dimensions of the faults preceded the accumulation of displacement on the El Arish faults.

- Seismically resolvable drag folding surrounding the fault planes is associated with the parts of the faults that accumulated additional displacement due to interaction with a mechanical boundary or another fault. It is, however, not

systematically associated with the early stage of development of blind faults to the extent described in the blind fault model (Barnett et al. 1987).

- The upper tip folding can span up to a third of the surface area of a fault. A systematic approach for measurements is recommended as including or not the tip folded zones for some faults can add a significant scatter in displacement-length relationship.

Chapter III

Growth faults

This chapter has been submitted for publication in Journal of Structural Geology as:

Baudon, C. & Cartwright, J. A. in review. Early stage of evolution of growth faults: 3D seismic insights from the Levant Basin, offshore Israel. Journal of Structural Geology.

Joe Cartwright provided discussion of the topics presented in this chapter and support during its writing.

3 EARLY STAGE OF EVOLUTION OF GROWTH FAULTS LOCATED IN THE LEVANT BASIN, OFFSHORE ISRAEL

3.1 Abstract

Detailed analysis of the 3D geometry and throw distribution of small growth faults is presented from a high resolution 3D seismic dataset located at the margins of the Levant Basin, in the eastern Mediterranean. The kinematic evolution of one particular fault was reconstructed to evaluate changes in dimension and displacement distribution that occurred during the transition from purely blind propagation to propagation at the free surface. Plots of vertical throw distribution exhibit M-type profiles at the lateral tip regions of this fault and skewed or asymmetric M-type profiles over the central portions. This variation of throw profile along strike is interpreted as being the consequence of fault interaction with the free surface. The fault is considered to have grown by blind radial propagation of three main segments that hard-linked prior to surface interaction. On reaching the seabed, the fault continued to accrue displacement as a syn-sedimentary fault. Most of the fault surface area formed during the blind propagation phase, but most of the displacement was added during the syn-sedimentary phase of the growth history with little increase in surface area. The interaction of the fault with the free surface led to a change in the position of the point of maximum displacement as well as shifting the entire vertical throw distribution. The amount of displacement added after this transition from blind fault to growth fault decreases systematically towards the lower tip, preserving a constant low negative gradient as a relict of the blind stage. Finally, a significant overlap is observed between the throw gradients measured from syn-sedimentary faults and blind faults in the area, suggesting that throw gradients are not a good discriminator between these two types of faults. This result has important implications for dating small syn-sedimentary faults.

3.2 Introduction

Syn-sedimentary normal faults (often referred to as 'growth faults') have been the subject of extensive research, mainly with an aim of defining their tectono-stratigraphical evolution in the context of a local petroleum systems analysis (e.g. Ocamb 1961, Bruce 1973, Crans et al. 1980). Normal faulting active at the surface during sedimentation results in primary stratigraphic thickness changes across the fault and correlations of hanging wall and footwall successions enable the throw that accumulates during deposition to be calculated (e.g. Thorsen 1963, Edwards 1995).

However, small syn-sedimentary faults can be extremely difficult to distinguish from blind faults i.e. those that grew by blind propagation (Petersen et al. 1992). This difficulty arises because the overall distribution of displacement on blind faults and small syn-sedimentary faults can in theory be identical. Whereas for a syn-sedimentary fault, the upwards decrease in throw might reasonably equate to a minor stratigraphic expansion across the fault (Thorsen 1963), for a blind fault the upwards decrease relates to a propagation gradient (Walsh and Watterson 1987).

Syn-sedimentary faults are likely to consist in part of a blind fault component, since propagation of the upper tip to the free surface necessarily proceeds whilst continued tip line propagation occurs in a blind mode elsewhere on the fault tip line (Meyer et al. 2002, Childs et al. 2003). Little is known of the precise effects on fault propagation of free surface interaction along the upper tip, for example, in the changes that might occur to displacement and dimension systematics. There is therefore a need to further understand the characteristics of blind versus syn-sedimentary propagation and the transition between the two contrasting stages of faulting.

The relationship between blind and syn-sedimentary modes of fault propagation is also important to understand in the context of fault scaling. The relationship between displacement maxima and the dimension of faults has been extensively discussed for many types of normal faults, in numerous datasets from contrasting geological settings (Muraoka & Kamata 1983, Watterson 1986, Dawers et al. 1993, Schlische et al. 1996). These different studies defining displacement-length (D/L) scaling provided insight into the mechanics of fault growth and have given rise to several growth models (e.g. Walsh & Watterson 1988, Cowie & Scholz 1992b, Cartwright et al. 1995). Numerous models predict a systematic increase in both the dimensions and displacement of faults through

time defined by a specific scaling law between displacement and fault dimension (Walsh & Watterson 1988, Cowie & Scholz 1992a, Gillespie et al. 1992, Dawers et al. 1993, Schlische et al. 1996). Departures from this type of scaling relationship have been attributed to a number of complicating factors including (1) segment linkage during propagation (Peacock & Sanderson 1991, Cartwright et al. 1995, Dawers & Anders 1995, Wojtal 1996), (2) mechanical heterogeneity (Peacock & Zhang 1994, Mansfield & Cartwright 1996, Gross et al. 1997, Wilkins & Gross 2002) and (3) mechanical interaction with other structures (Nicol et al. 1996a, Maerten et al. 1999). It has recently been suggested that the along strike length of normal faults can be established at an early stage of evolution of the fault and that increase in cumulative displacement is added for near constant length (e.g. Morewood & Roberts 1999, Poulimenos 2000, Meyer et al. 2002, Walsh et al. 2002, Nicol et al. 2005, Vetel et al. 2005). However, these studies interpreted the approximately constant fault length as being inherited from the reactivation of earlier underlying structures.

The aims of this study were firstly to investigate and characterise the early propagation history of growth faults that have recently made the transition from a blind stage to a syn-sedimentary stage and secondly to evaluate the implications for existing fault growth models and scaling relationship. The main focus of this study is an array of simple gravity-driven extensional faults mapped on a high quality 3D seismic survey located at the margin of the Levant Basin, in the eastern Mediterranean. The bulk of the descriptive section of this chapter is on a single, segmented fault in this array, selected particularly for detailed analysis of its 3D geometry and throw distribution by virtue of its relatively simple geometry and a kinematic history that straddles the transition from blind to syn-sedimentary propagation. This chapter concludes with a discussion of the wider importance of this kinematic progression.

3.3 Geological setting and dataset

3.3.1 Regional setting

The study area is located in the Levant Basin, in a passive continental margin setting in the eastern Mediterranean (Fig. 3.1). The basin formed through several phases of rifting from the Early Permian to the middle Jurassic and is associated with the evolution of the Neo-Tethys Ocean (Garfunkel 1998). The Levant Basin has been influenced by its location at the zone of interaction between the Anatolian, African and Arabian plates and is bounded by the Dead Sea Transform to the East, the Gulf of Suez to the SW, the Cyprian Arc to the NW, Taurus mountains and Bitlis suture to the North (Tibor & Ben-Avraham 2005). The margin was characterised by carbonate platforms that were replaced by pelagic sedimentation in the Late Cretaceous (Druckman et al. 1995) due to a change of motion and subsequent collision between the African and Eurasian plates (Tibor & Ben-Avraham 1992). Tectonic uplift of the shelf associated with a subsidence of the slope and basin during the Miocene (Frey Martinez et al. 2005) led to an increase in siliciclastic sediment supply (Druckman et al. 1995). At the end of the Miocene, the Levant Basin underwent a major desiccation through the Messinian Salinity Crisis (MSC) (Hsü et al. 1978). This led to extensive erosion and deposition of thick evaporites in the basin floor regions (Tibor & Ben-Avraham 1992) pinching out laterally against the basin margins (Bertoni & Cartwright 2006).

The Pliocene-Quaternary succession forms the main interval of interest of this chapter. A major transgression and re-establishment of normal marine conditions at the beginning of the Pliocene led to the deposition of an interval of turbidite sandstones fan named the Yafo Sand Member (Frey Martinez et al. 2005). The Plio-Pleistocene succession comprises an important accumulation of clay-rich marls and claystones sediments mainly derived from the Nile Delta continuously prograding over the YSM (Tibor & Ben-Avraham 1992). Tilting of the margin resulted in two scales of gravity-driven deformation during the Pliocene: thin-skinned sliding and landslides (Frey Martinez et al. 2005) and more regionally gravity spreading of the Plio-Pleistocene succession detaching in the Messinian evaporites (Garfunkel & Almagor 1987, Netzeband et al. 2006). The extensional domain was characterised by a series of downslope and upslope dipping extensional faults localised at the pinch-out of the Messinian evaporites (Gradmann et al. 2005, Bertoni & Cartwright 2006). The high sedimentation rates and the tectonic subsidence in the shelf area and coastal plain decreased during the quaternary (Tibor & Ben-Avraham 1992). The Pliocene-Quaternary succession of the outer shelf and slope is deformed by several coast-parallel

growth faults that resulted mainly from gravitational sliding of the sediments towards the basin (Garfunkel & Almagor 1985).

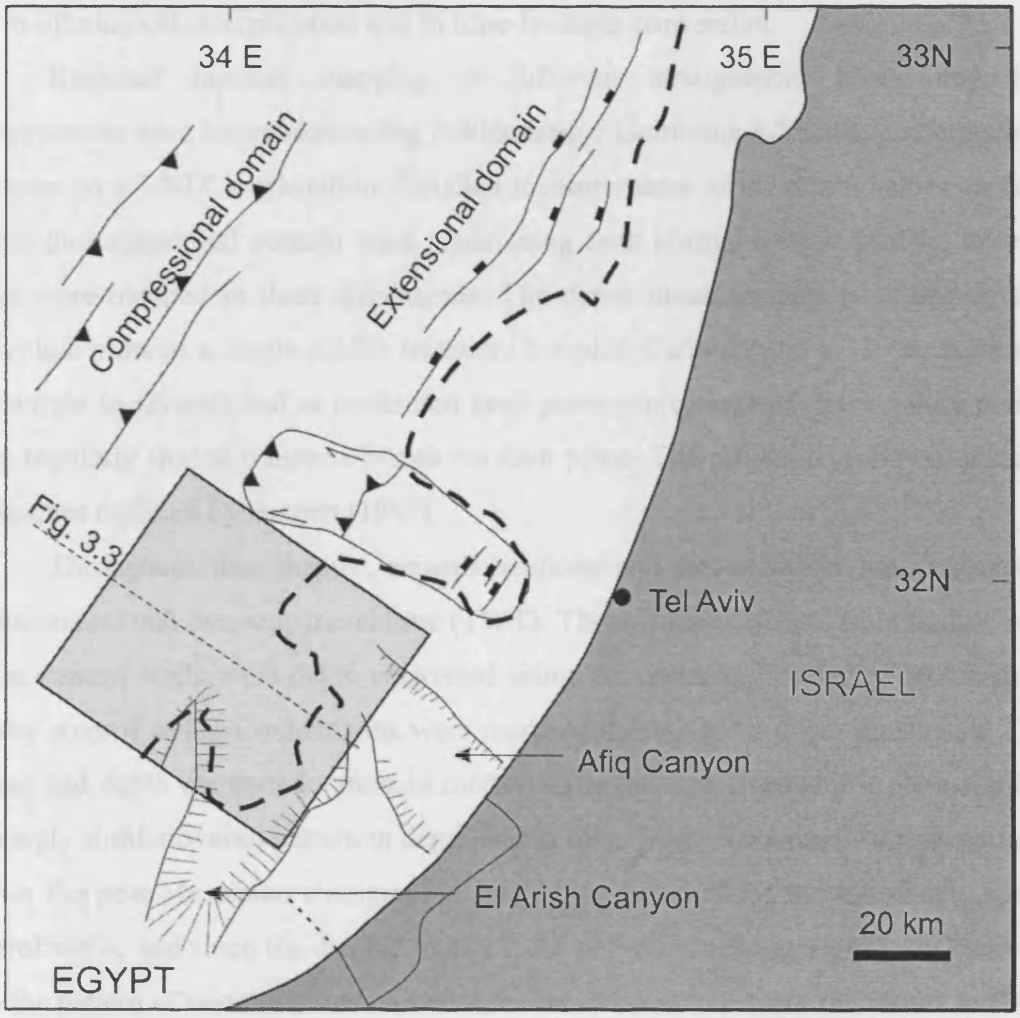

Fig. 3.1: Location map of the 3D seismic survey (shaded square) situated offshore Israel. Dashed line represents the margin of the Messinian evaporites.

3.3.2 Dataset and methodology

This study is based on a high-resolution 3D seismic survey located in the southern part of the Levant Basin (Fig. 3.1), supplemented by a regional 2D reflection survey covering the passive continental margin of offshore Israel. The 3D coverage amounts to 2200 km^2 with excellent stratigraphic resolution throughout. The frequency ranges between 35 Hz and 80 Hz with a dominant frequency of 50 Hz at the base of the

Pliocene, giving a vertical resolution of c.10 m. The spatial resolution is approximately equivalent to the in-line and the crossline spacing of 25 m. Ten exploration wells were drilled within the survey area and provide standard petrophysical and velocity data for use in lithological interpretation and in time-to-depth conversion.

Regional horizon mapping at different stratigraphic levels and fault interpretation were undertaken using Schlumberger Geoframe 3.7 seismic interpretation software on a UNIX workstation. Detailed measurements of the throw values on faults within the extensional domain were made using fault normal seismic profiles once the faults were mapped in three dimensions. The throw measurements were displayed as individual plots of a single profile transect (T-z plot, Cartwright et al. 1998, Baudon & Cartwright in review) and as contoured fault plane projections of throw values derived from regularly spaced transects across the fault plane. The projection followed standard techniques outlined by Barnett (1987).

Throughout this chapter, seismic sections and throw values are displayed in milliseconds (ms) two-way travel time (TWT). Throw measurements from faults closest to the control wells were depth converted using the check-shot velocity data from the nearby control wells. Comparisons were made of throw versus depth plots using TWT values and depth converted values in metres. The depth converted T-z plots exhibit a strikingly similar overall pattern in depth and in time. Since the lateral velocity variation within the post-Messinian stratigraphic interval is minimal for the ten widely spaced control wells, and since the display in TWT did not introduce any significant distortion into the pattern of vertical throw variation, it was decided to present the results in TWT.

Any errors in the throw measurement are estimated to be ± 2 ms. It has been suggested that T-z plot measurements can be greatly influenced by lithological effects and the development of fault scarps (Cartwright et al. 1998, Castelltort et al. 2004, Back et al. 2006). In conditions where the hanging wall accommodation space created by movement of the fault is filled by sediment soon after the slip occurs, no surface scarp is produced and filled accommodation space can be taken as a proxy for displacement (Cartwright et al. 1998). In this situation, zero slope gradients of throw versus depth indicate periods of fault inactivity. Where there is no rapid filling of accommodation space created by faulting, a scarp can result at the free surface, and hemi-pelagic sediments can deposit with the same thickness each side of the fault plane. In this situation, zero throw gradients can be attributed to changes in depositional conditions rather than to any inactivity of the fault (Castelltort et al. 2004). The main interval of

interest of this chapter, the Plio-Pleistocene succession, is mainly composed of clastic sediments deposited in a high sedimentation rate context (Garfunkel & Almagor 1985, Tibor & Ben-Avraham 1992), so it is reasonable to assume that sediment thicknesses represent a good proxy for throw. This chapter focuses primarily on the general pattern and change of slope of the throw profiles rather than subtle throw variations. Furthermore, time slices were analysed from a coherency volume to investigate the paleoenvironment history and geomorphological evolution of the fault. Differential compaction between hanging wall and footwall sequence can also introduce errors in the throw measurements (e.g. Mansfield 1996, Cartwright et al. 1998). However, these would only be significant in the case of a sufficiently large throw values and therefore considered as negligible in this study. Finally, additional errors in the throw measurements can be introduced by fault drag folds of the horizons in contact with the fault plane (Walsh & Watterson 1987, e.g. Mansfield & Cartwright 1996). For the purpose of the study, drag folds of large wavelength (>100 m) are considered part of the continuous deformation field around the faults and were thus included in the throw measurements. Drag folds with smaller wavelengths were considered to be within the spatial imaging error range, and throw measurements were in that case made at the inflection points closest to the fault plane (Mansfield & Cartwright 1996).

3.3.3 Semi-regional structural and stratigraphic framework

The study area is located in the southeastern region of the Levant 3D seismic survey. This area is dominated by a series of extensional structures that are related to the gravity-driven tectonics of the innermost part of the Levant Basin (Fig. 3.2).

The most prominent structures include the Shamir Graben system, generally striking NE-SW and the Kefira Graben striking mainly in a N-S direction. Activity on both grabens commenced in the Pliocene. They consist of complex arrays of oppositely dipping normal faults characterised by throws of up to 350 m with expansion indices of up to 2.15 calculated with the method used by Thorsen (1963). Both graben systems strike approximately parallel to the underlying detachment within the Messinian evaporites and their position in the basin is coincident with the updip pinch-out of the evaporites (Gradmann et al. 2005, Bertoni & Cartwright 2006).

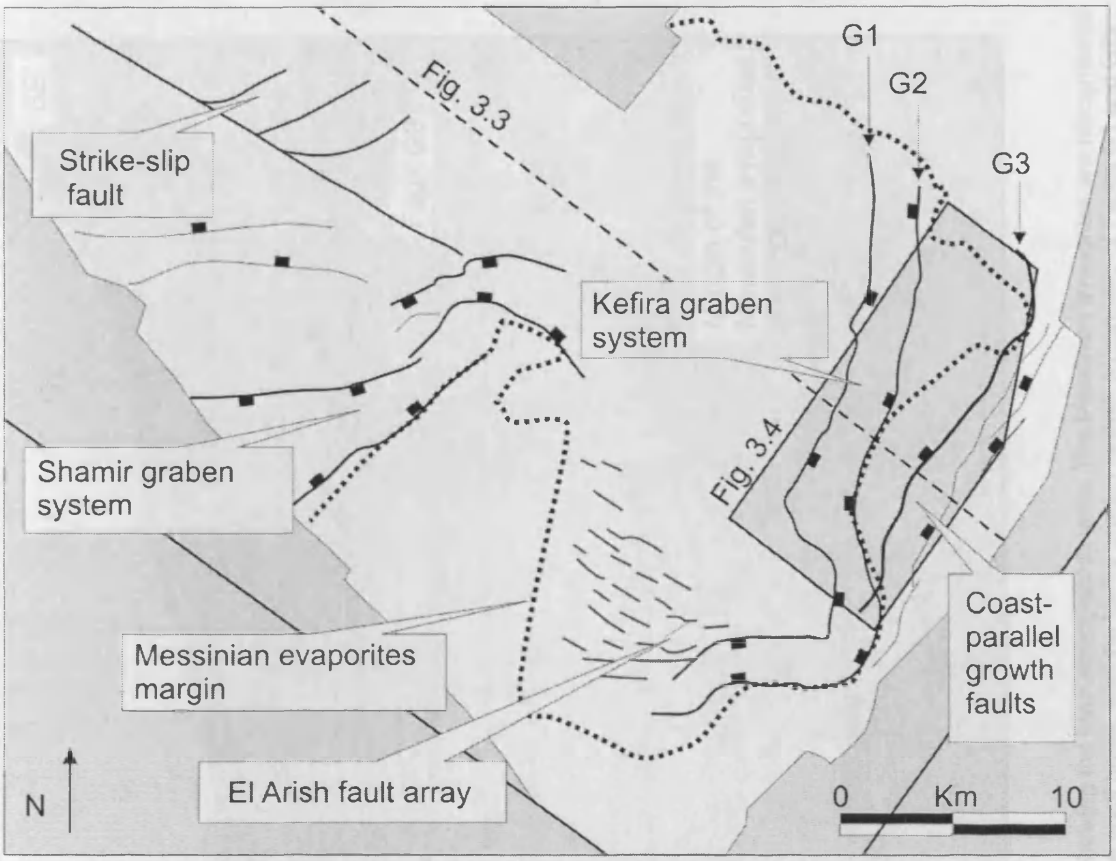

Fig. 3.2: Structural map of the Levant survey based on a Pleistocene Horizon.

An array of blind faults (the El Arish fault array in Baudon & Cartwright in review) is located between the NE lateral tip of the Shamir graben and the SW lateral tip of the Kefira graben. The El Arish fault array consists of a set of small extensional faults striking NW-SE, perpendicular to the local slope direction and is interpreted as being the result of a lower strain continuation of the extensional domain along the margin of a prominent salient in the original location of the Messinian pinch-out.
Finally, the syn-sedimentary faults forming the main focus of this study are located close to the present-day shelf-slope break and strike parallel to the coastline in a NE-SW direction. They are sub-parallel to each other and are bounded to the west by the Kefira Graben.

The general stratigraphy of the study area is illustrated on a representative seismic section from the 3D volume taken in a direction normal to the faults in the extensional domain of the margin (Fig. 3.3). The Pliocene-Quaternary succession discordantly overlies the Miocene-Oligocene sediments. These two megasequences are bounded by an extensive erosional surface, the Messinian Unconformity. This correlates

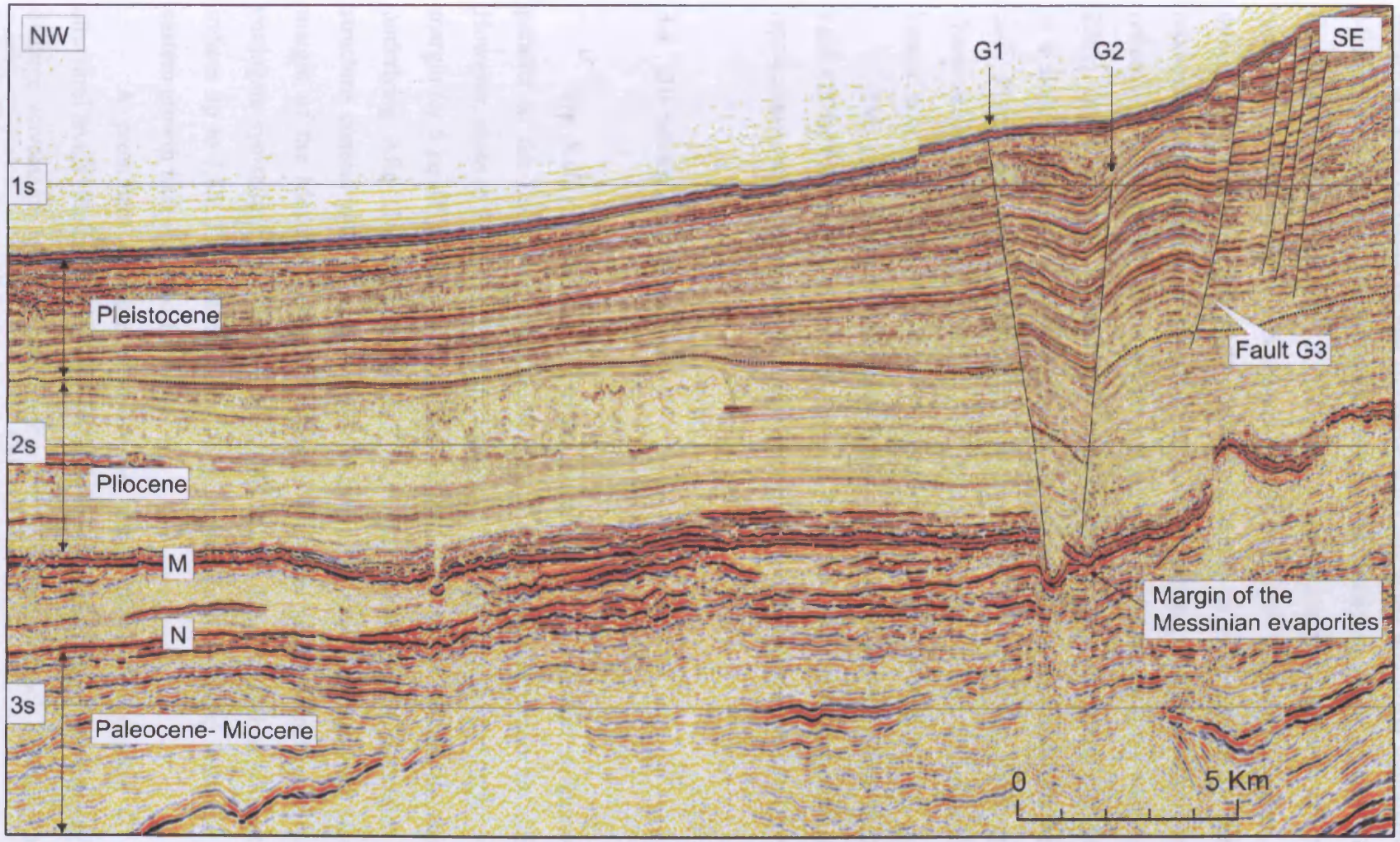

Fig. 3.3: Seismic regional section across the Levant Basin continental margin showing the main stratigraphic units. The Messinian evaporites are recognisable by the strong basal (N) and top (M) reflections. The growth faults, located on the shelf break, and the Kefira graben system (composed of Faults G1 and G2) are controlled by the pinch-out of the Messinian evaporites.

basinward with Horizons M and N, representing the upper and lower boundaries of the Messinian evaporite sequence deposited during the Messinian Salinity Crisis (Bertoni & Cartwright 2006, Gradmann et al. 2005). The Plio-Quaternary sediments comprise the main interval of interest of this chapter as they are offset by the main graben and the minor faults updip of this graben. This succession is characterised by continuous moderate to high amplitude seismic reflections alternating with chaotic low amplitude reflection packages that have been interpreted as slump deposits (Frey Martinez et al. 2005). These sediments are mostly clay-rich marls, sandstones and claystones deposited in a slope position. The coast-parallel faults generally tip out downwards within the early Pleistocene sediments and some segments detach in weaker layers generally characterised by low amplitude seismic reflection intervals. The upper tip lines are located at or within a few tens of metres beneath the present day seabed.

This chapter focuses on the propagation history of one particular fault named Fault G3 for the purpose of the study (Figs. 3.2 and 3.3). This fault has been chosen as a representative example of the coast-parallel growth faults located on the shelf break.

3.4 3D Seismic interpretation

The Kefira Graben strikes in an overall N-S direction and is approximately parallel to the underlying detachment within the Messinian evaporites (Fig. 3.2). However, close to Fault G3, the graben strikes NNE-SSW and does not follow the salt margin for 5 km (Fig. 3.4) where the head of the salient curves towards the east due to underlying Afiq Canyon (Bertoni & Cartwright 2006). This is illustrated on the structure contour map by a divergence between the fault trace and the underlying margin of the Messinian evaporites (Fig. 3.4a). This graben consists of two main conjugate syn-sedimentary faults that exhibit throws of up to 250 m with expansion indices up to 1.85. The western, SE dipping growth fault is named Fault G1 and the eastern growth fault is named Fault G2.

A prominent syncline is developed within the Kefira Graben at shallow structural levels (Pleistocene) (Fig. 3.3). Seismic reflections exhibit normal drag folding of large wavelength and high amplitude in the downthrown block between Faults G1 and G2. This syncline is illustrated on the structural map by contours centred onto zones of low values (represented in red in Fig. 3.4a) and by a change of relief on the Geoviz

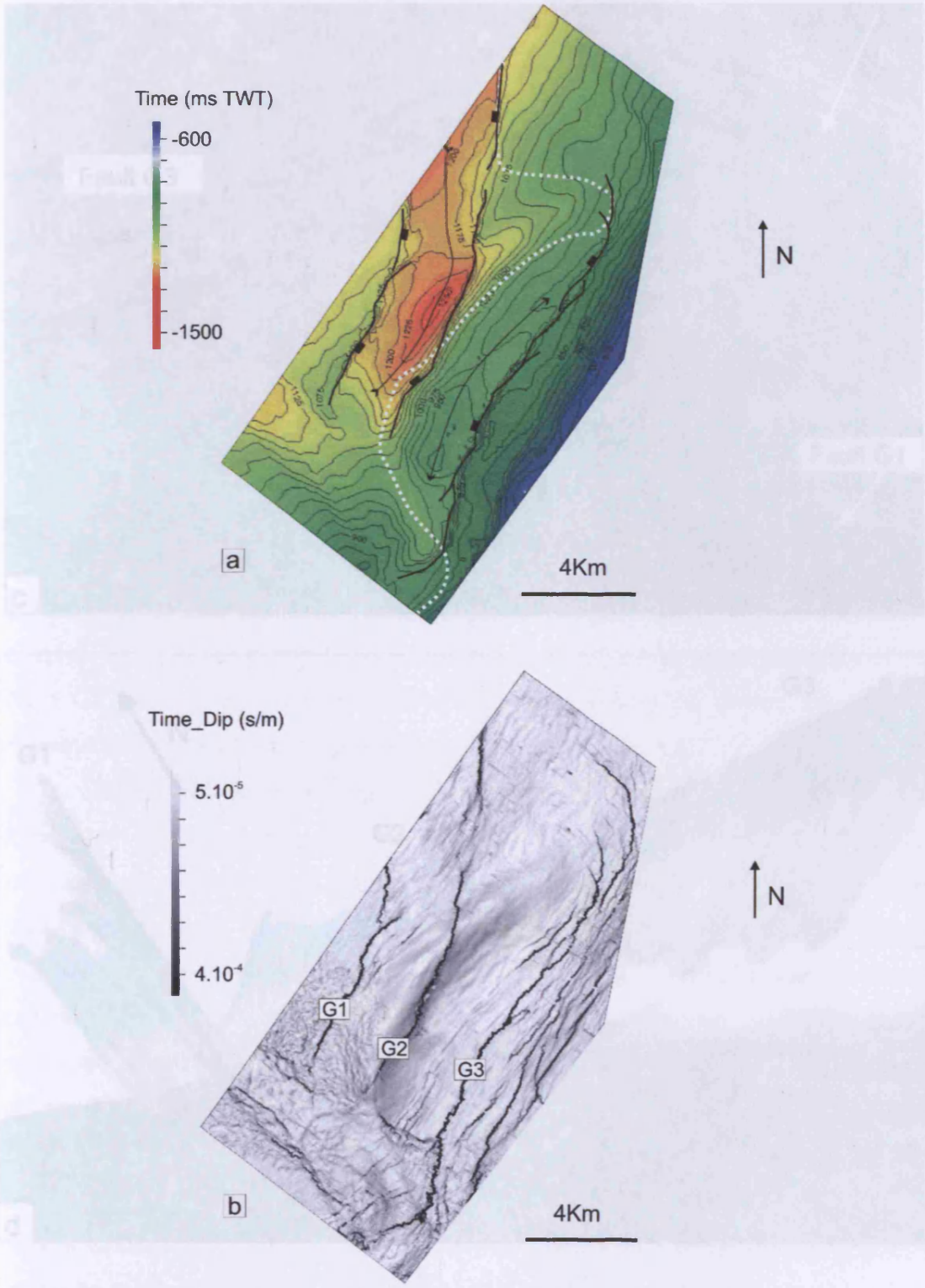

Fig. 3.4: Structural map of the area and Geoviz visualisation of the Kefira graben and the coast parallel faults based on Pleistocene Horizon Ba. (a) Two-way-time map showing contours spaced at 25 ms TWT with low values in red and high values in blue colour. Dashed line represents the edge of the Messinian evaporites. Arrows indicate syncline and anticline. (b) Dip map showing the traces of the main Faults G1, G2 and G3.

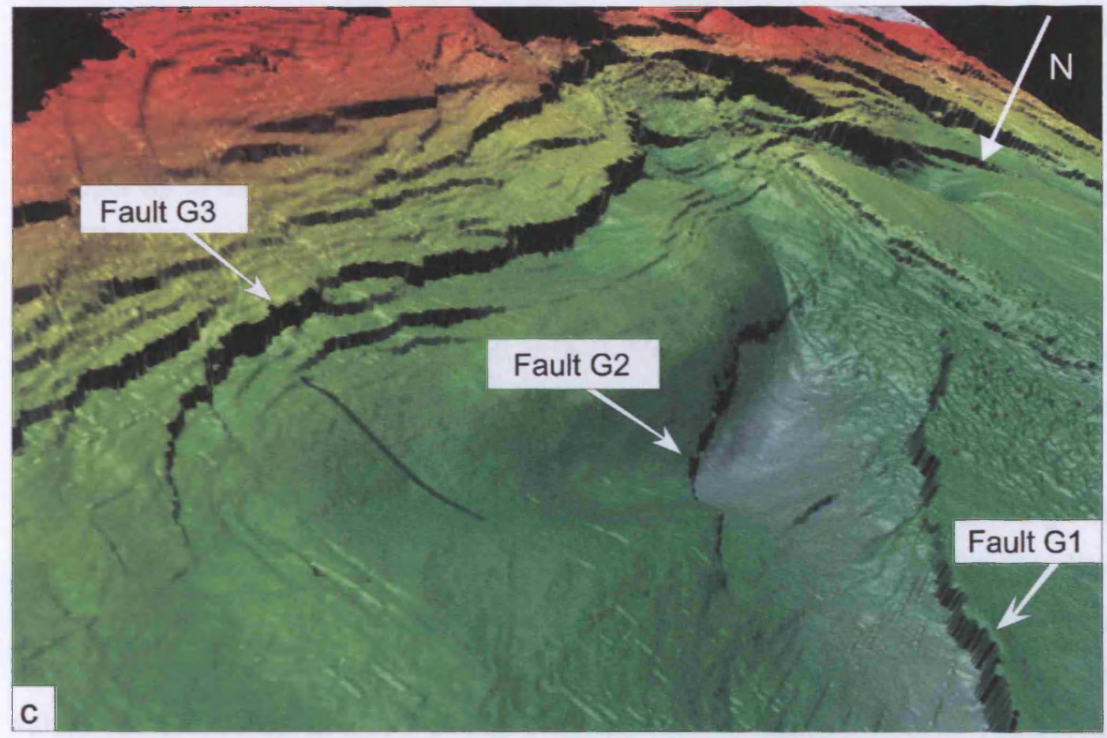

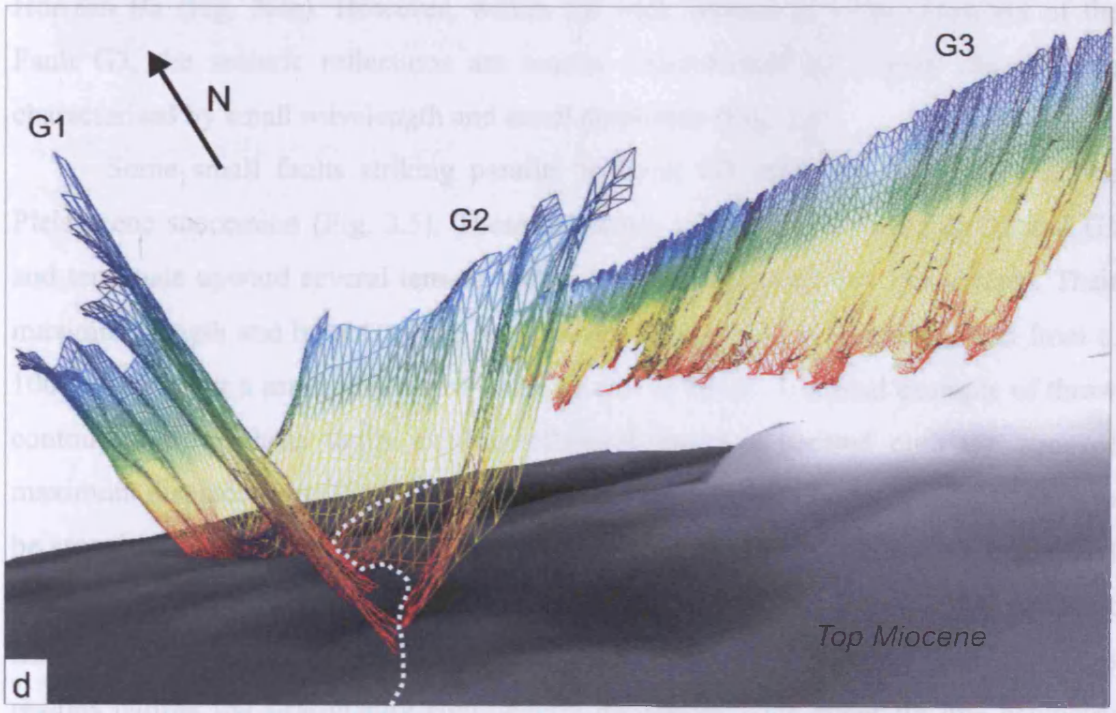

Fig. 3.4: (c) Geoviz image of Pleistocene Horizon Ba (d) Geoviz visualisation of the 3D geometry of Faults G1, 2 and 3 related to the top Miocene.

visualisation of a Pleistocene horizon (Fig. 3.4c). The syncline is asymmetrical and the depocentre is closer to Fault G2 than to Fault G1. Both faults exhibit a fairly consistent stratigraphic thickening in the hanging wall that increases with increasing depth from the upper tip to the level of the late Pliocene, with high throw gradients up to 0.85 (Fig. 3.4). This increase of throw by stratigraphic expansion dates the onset of faulting from the late Pliocene-early Pleistocene for the Kefira Graben. Fault G1 is characterised by a small scarp at the surface (<10 m) and is therefore interpreted as an active fault at the present day. Fault G2 terminates upwards at stratigraphic levels situated between 0 and 200 m beneath the present day seabed (Fig. 3.3).

Seismic reflections between Faults G2 and G3 define an antiform trending NE-SW (Fig. 3.3). This folding is interpreted as a roll over anticline in the hanging wall of Fault G3 as expected in the downthrown block of detaching growth faults (Hamblin 1965). The anticline is visible on the structural map by contours centred onto smaller values (underlined by an arrow in Fig. 3.4a) and on the Geoviz image of Pleistocene Horizon Ba (Fig. 3.4c). However, within the rock volume in close proximity of the Fault G3, the seismic reflections are mostly characterised by normal drag folding characterised by small wavelength and small amplitude (Fig. 3.5).

Some small faults striking parallel to Fault G3 offset the upper part of the Pleistocene succession (Fig. 3.5). These faults are situated between Fault G2 and G3 and terminate upward several tens of metres below the present day free surface. Their maximum length and heights range respectively from c. 400 m to 2300 m and from c. 100 to 450 m for a maximum throw value of c. 9 to 18 m. A typical example of throw contour plot for these faults exhibits elliptical contours centred onto the zone of maximum displacement (Fig. 3.6). This type of throw distribution has been described to be associated with blind fault propagation (Barnett et al. 1987, Childs et al. 2003), and based on this similarity, these faults are therefore interpreted as blind faults. For fault B2 as for most of the blind faults, the upper tip line plunges towards the lateral tip regions cutting the stratigraphy significantly by 100 m. This upper tip line geometry would be most unlikely to be developed if the faults were syn-sedimentary, since it would require a highly diachronous growth history with individual faults younging to the centre of the fault trace. Furthermore, there is no stratigraphic or geomorphological evidence of interaction with a paleo-seabed, such as a change in the shape, size or direction of slope channels or mass transport complexes. This also supports the interpretation that these faults are blind. No seismically resolvable drag folding is

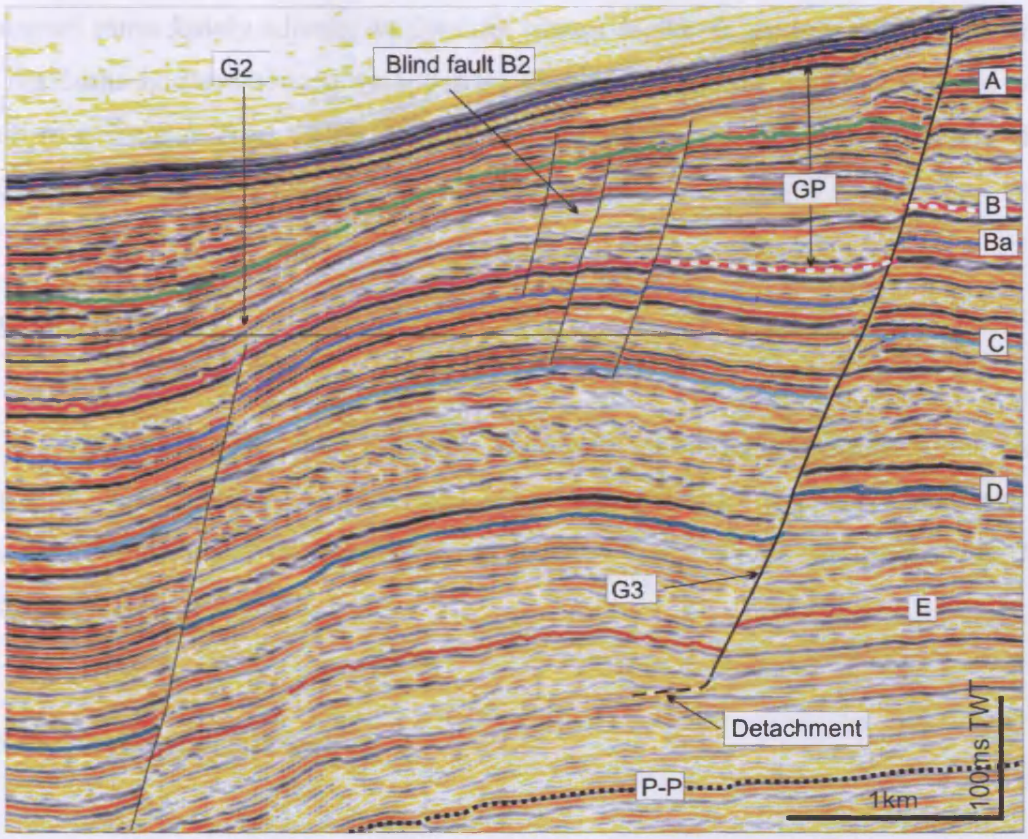

Fig. 3.5: Seismic section through Faults G2 and G3 showing the stratigraphy and key Pleistocene horizons (A, B, Ba, C, D and E). P-P marks the Pliocene-Pleistocene boundary. Stratigraphic thickening is expressed under the form of growth packages (GP) in the hanging wall of Fault G3 between Horizon B and the seabed. White doted line marks the base of syn-kinematic sequence.

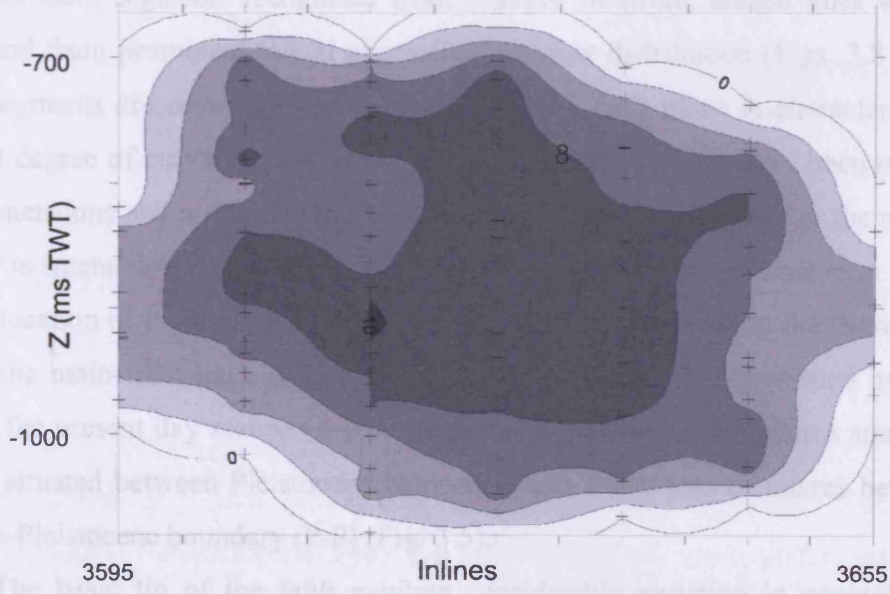

Fig. 3.6: Throw contour plot for one of the blind faults (B2) located between Faults G2 and G3. Lines of equal throw values spaced at 2 ms TWT show elliptical contours ranging from 0 to 11.

observed immediately adjacent to the fault planes. However, up to a third of the height of the faults is characterised by upper tip folding as expected ahead of a propagating fault (e.g. Jackson et al. 2006) All these arguments support the interpretation of these faults as having grown entirely by blind propagation.

3.5 Fault G3

Fault G3 is the fault selected for detailed analysis of geometry and throw variation. The geometry is described, and aspects of the segmented structure are discussed, and this is followed by a description of the throw variation on the fault surface.

3.5.1 3D geometry of Fault G3

Fault G3 is one of the coast-parallel faults located on the shelf-break (Fig. 3.2). The fault strikes an average of 040° and dips at c. 55° toward the NW although a variation of 5° in dip is observed along strike of the fault plane. The maximum length (sub-horizontal dimension) of the fault trace is c. 14 km and its maximum height is c. 1300 m for a maximum throw of c. 115 m. The fault is segmented (see next section) into three main segments recognised from changes in strike, branch lines with splay faults, and from prominent lateral anomalies in throw distribution (Figs. 3.8 and 3.9). These segments are referred to as A, B and C. The fault plane is characterised by a minimal degree of curvature with depth. Five major branch lines have been mapped in three-dimensions and are interpreted as being due to splays and relays in the main fault plane or to interaction with another fault. These branch lines are referred to as v-v' to z-z'. The location of these branch lines is represented by thick lines on the throw contour plot of the main fault trace (Fig. 3.8c). Fault G3 is generally represented by a small scarp at the present day seabed (< 10 m) and tips out downwards within a stratigraphic interval situated between Pleistocene Horizon E and a few tens of metres beneath the Pliocene-Pleistocene boundary (P-P) (Fig. 3.5).

The basal tip of the fault exhibits considerable variation in geometry along strike. The fault dies out downward without detachment at the lateral tip regions. In

contrast, along the central portions of the fault plane, the basal part of the fault plane flattens in dip abruptly a few tens of metres above the deepest offset stratal reflections. The basal reflections in the hanging wall exhibit anomalous large rotation close to the fault cut-off, suggesting a detachment geometry for the basal tip region. The detachment of the basal tip is only apparent in Segment A. Segments B and C seems to tip out downwards without any appreciable signs of detachment. The detachment interval is mainly characterised by a unit of low amplitude seismic reflections within the lower Pleistocene.

3.5.2 Evidence for syn-sedimentary faulting

Fault G3 exhibits a stratigraphic thickening in the hanging wall in the upper part of the fault plane (Fig. 3.5). Divergent seismic reflections thickening systematically towards the fault plane define a syn-kinematic sequence in the Pleistocene sediments. The base of this syn-kinematic interval (labelled X in Fig. 3.7a) is generally located between Horizon B and a few tens of metres beneath Horizon A. This interval is characterised by growth packages in the downthrown block immediately adjacent to the fault plane (Fig. 3.7b). These packages are all defined on the basis that reflection-bound units thicken systematically to the cut-off, with divergent configurations and occasionally discrete onlaps, similar to that seen on growth faults elsewhere (e.g. Gibbs 1983, Xiao & Suppe 1992, Bischke 1994, Edwards 1995).

Time slices from a coherency volume were created from the 3D dataset. These coherence slices were then examined at small time increments (4 ms TWT) with an aim to correlate any stratigraphic pattern or sedimentary features across the fault plane. Figure 3.7d shows a channel being cross-cut by Fault G3 within the syn-kinematic interval. The direction of the channel switches abruptly towards the NW of c. 45° and the width of the channel decrease slightly between the hanging wall and the footwall of Fault G3. This is interpreted as being the result of syn-sedimentary movement of the fault whilst the channel was deposited. On the contrary, no stratigraphic thickening is detectable across the fault plane beneath Horizon X (Fig. 3.7a). There is no geomorphological indication that Fault G3 interacted with a paleo-seabed beneath this stratigraphic level. An example of a small channel being cross-cut by Fault G3 within the interpreted pre-kinematic sequence confirms this interpretation as no change of size,

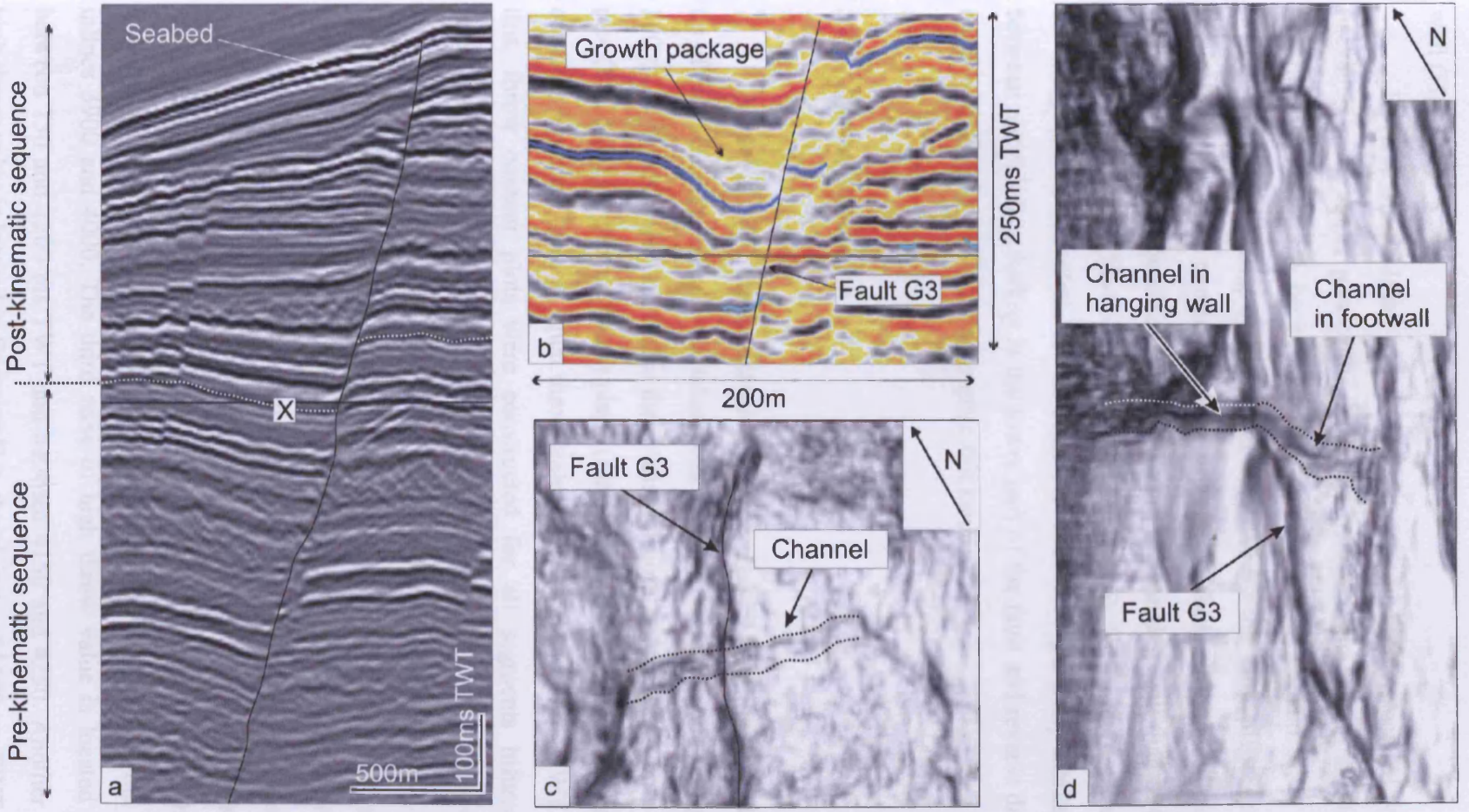

Fig. 3.7: (a) Seismic cross-section showing the stratigraphic thickening in the hanging wall within the syn-kinematic sequence. X indicates the onset of growth packages. (b) Seismic section showing a growth package in the hanging wall of Fault G3 in the syn-kinematic sequence. (c) Coherency slice at 1416 ms TWT showing a channel cross-cut by Fault G3 within the pre-kinematic sequence. The size, direction and geometry of the channel are unchanged. (d) Coherency slice at 528 ms TWT showing the change of direction of a channel being cross-cut by Fault G3.

geometry or orientation of the sedimentary feature between the footwall and hanging wall (Fig. 3.7c).

Reverse drag folding surrounding the fault plane is associated with the growth packages in the upper part of the fault plane whereas the central and lower parts are generally characterised by normal drag folding (Figs. 3.5 and 3.7a). A systematic mapping of drag folding of the horizons offset by the fault plane verifies that this vertical distribution is consistent along strike. Drag folds surrounding the fault plane is more developed and persistent along strike in the hanging wall than in the footwall as previously suggested (Hamblin 1965, Mansfield 1996). The onset of growth packages in the hanging wall (labelled "X" in Figs. 3.5 and 3.7a) generally marks the transition between normal drag folding in the lower part of the fault and reverse drag folds in the upper part associated with stratigraphic thickening.

3.5.3 Throw distribution

A total of 1753 throw measurements were taken from the upper tip to the lower tip of Fault G3 on cross sections taken orthogonal to the fault plane and spaced at 250 to 500 m. A strike projection of the throw distribution is represented on a throw contour plot (Fig. 3.8c) for the main fault plane (represented by the thick line in Fig. 3.8b). The contours represent lines of equal throw values spaced every 10 ms TWT. In addition to this, throw contour plots were constructed for all segments bifurcating from or interacting with the main fault plane. These are Segments T, A2, RH and C2 (Fig. 3.9).

The throw contour plot for the main fault trace shows several zones of high throw value (represented by the dark colours in Fig. 3.8c) separated by areas of vertical lower throw values (lighter colours). Three main zones of high throw values were identified.The main area of throw maxima (up to c. 125 ms TWT) is located in Segment A between 750 and 1200 ms TWT and between inlines 3500 and 3800. This zone of high throw value is composed of two smaller and interconnected ones. The second zone of high throw values is situated in Segment B between 750 and 850 ms TWT between inlines 3900 and 4000. The third zone of high throw value is located in Segment C between 750 and 1200 ms TWT and between 4150 and 4250. Another small zone of high throw value is located in Segment C in the vicinity of 1600 ms TWT. The throw

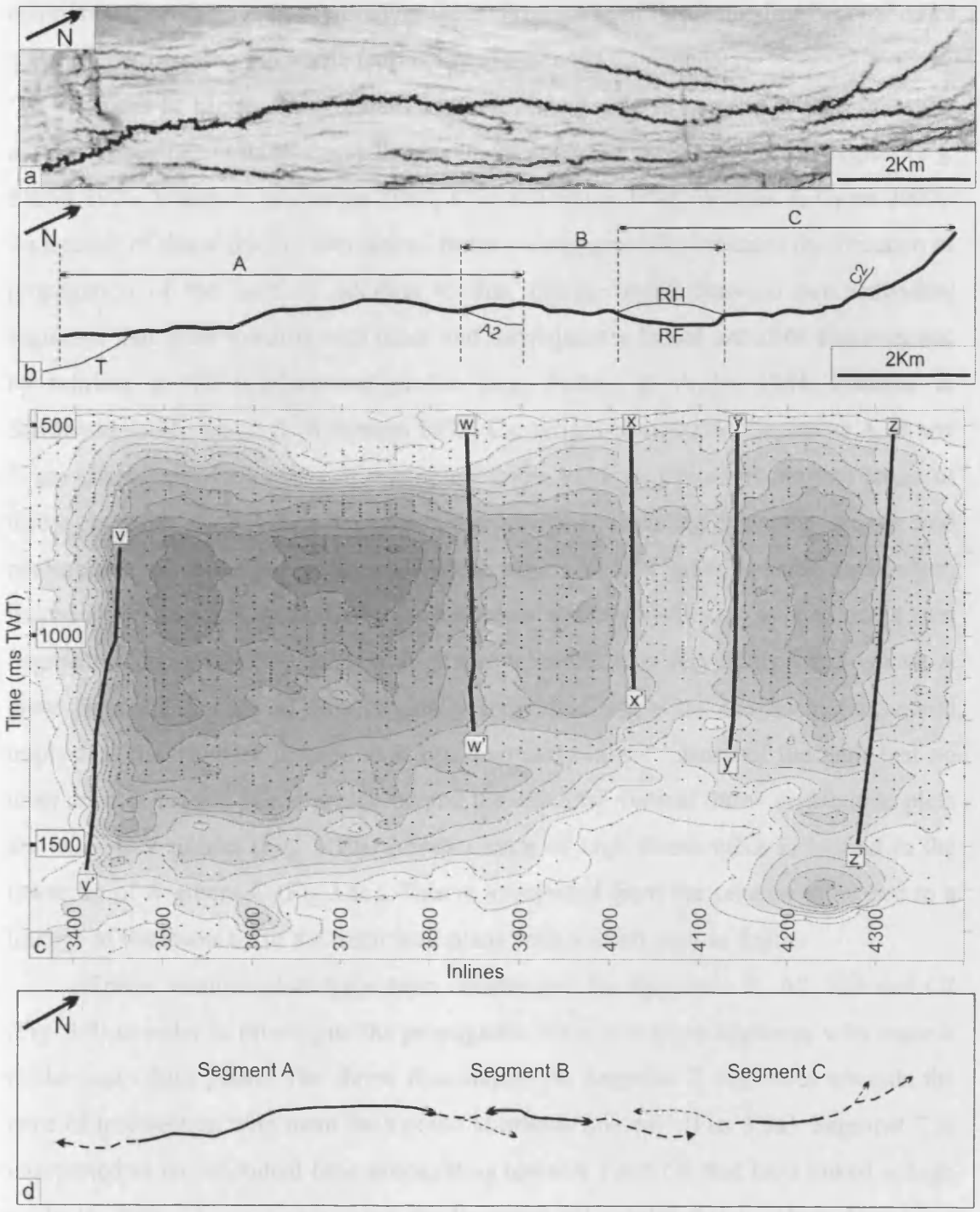

Fig. 3.8: (a) Dip map of Pleistocene Horizon D showing the trace of Fault G3. (b) Schematic representation of the fault trace and names of different segments. (c) Throw contour plot for Fault G3 showing lines of equal throw values spaced every 10 ms TWT. V-v' to z-z' indicate the branch lines. A total of 1753 throw measurements were taken along the main fault trace (represented by a thick line on figure 3.6b). (d) Cartoon showing lateral segment linkage that formed Fault G3.

contours are concentric and centred on these three zones of throw maxima become more elliptical surrounding the whole fault plane towards the tip regions.

Zones of higher throw values are often interpreted as regions of fault initiation as they have accumulated more displacement than the recent lateral tip region (e.g. Elliott 1976, Walsh & Watterson 1987, Ellis & Dunlap 1988, Wilkins & Gross 2002). As a result of this a smooth decrease of throw values generally indicates the direction of propagation of the fault. In addition to this, linkage zones between two individual segments that grew towards each other and subsequently linked are often characterised by minima in the displacement profile (e.g. Pollard & Aydin 1984, Peacock & Sanderson 1991, Walsh & Watterson 1991, Cartwright et al. 1995). Segments A, B and C are characterised by zones of maximum throw value separated by vertical zones of throw minima. Fault G3 is therefore interpreted as resulting from the growth and coalescence of three previously individual segments that grew towards each other, linked and subsequently underwent a common growth history. It is also noted that Segment A comprises two zones of high throw values. It is very likely that Segment A grew from the linkage of two originally individual segments. However, this would imply that the segment linkage took place so early in the history of the fault that no relay zone or branch line is preserved and the resulting vertical throw distribution plots are extremely similar (Fig. 3.10). Another zone of high throw value is located in the lower tip of Segment C (Fig.3.8c). This is interpreted from the seismic to be due to a linkage of the lower tip of the main fault plane with a small fault in depth.

Throw contour plots have been constructed for Segments T, A2, RH and C2 (Fig. 3.9) in order to investigate the propagation history of these segments with regards to the main fault plane. The throw distribution on Segment T decreases towards the zone of intersection with main fault plane at branch line v-v' (Fig. 3.9a). Segment T is interpreted as an individual fault propagating towards Fault G3 that hard linked at high angle (c. 20°). Throw contour plot for Segment A2 exhibit throw values decreasing away from the branch line w-w' on the main fault plane towards the NE lateral tip of Segment A2 (Fig. 3.9b). Segment A2 is interpreted as being the NE lateral tip of Segment A as no clear cut off in the throw distribution is observable between Segments A and A2 through the branch line. However, Segment A2 extends for only the upper 70% of the total height of Segment A (Fig. 3.8a). This places the timing of interaction of Segment B with Segment A prior to most of the propagation of Segment A in a NE direction to form Segment A2. Segments B and C interact with each other through a

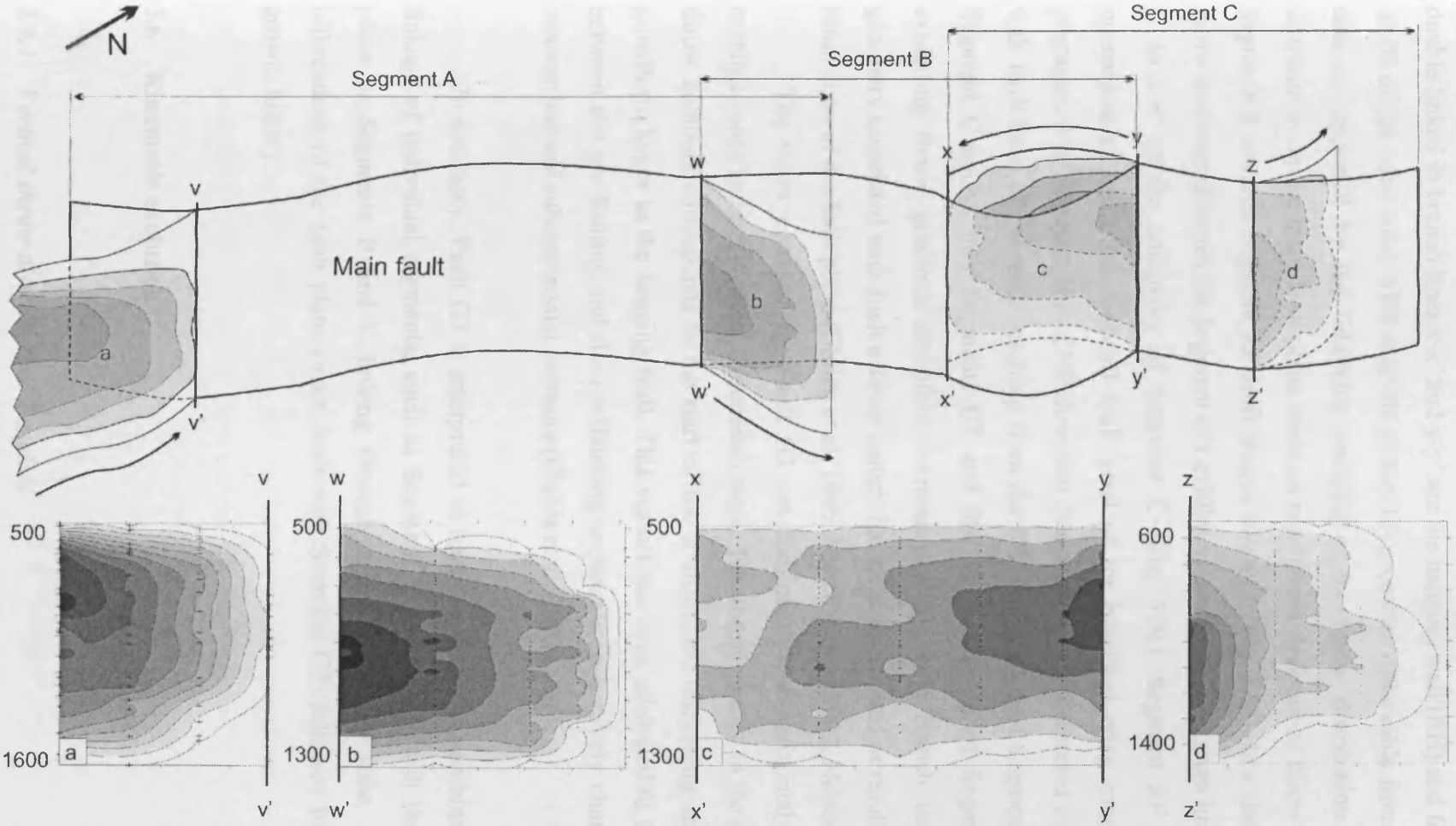

Fig. 3.9: (Top) 3D geometry of Fault G3 with respect to its segmentation (A, B and C), interaction with other fault segments or bifurcation of the fault plane. Arrows showing decreasing throw values indicate the direction of propagation of the fault segments. (Bottom) Throw contour plots showing lines of equal throw values (a) The throw values for Segment T range from 0 to 110 ms TWT (represented by dark colour) and are represented spaced every 10 ms TWT. (b) Throw contour plot for Segment A2 exhibit throw values ranging from 0 to 16 ms TWT decreasing away from the branch line. The spacing of the contours is 2 ms TWT. (c) Throw distribution on the hanging wall branch of the relay zone shows throw values ranging from 0 to 30 ms TWT and spaced at 5 ms TWT. (d) Throw contours plot for Segment C2 showing throw values ranging from 0 to 45 ms TWT and spaced at 5 ms TWT decreasing away from the branch line.

breached relay zone (Trudgill & Cartwright 1994). Breached overlapping faults that are double linked in branch lines x-x' and y-y' are the hanging wall (RH) and footwall (RF) faults of the relay zone. This analysis of the 3D geometry observable from the seismic data is supported by the following analysis of the throw distribution. The throw distribution on the main fault plane shows a continuous decrease of throw values from Segment B towards Segment RF until branch line y-y' (Fig. 3.8a). In a similar manner, throw contours obtained for Segment RH exhibit values decreasing from branch lines y-y' to x-x' in the continuity of Segment C (Fig. 3.9c). Segment RF is therefore interpreted as being the footwall fault bend of the breached relay zone due to the propagation of Segment B in a NE direction. Segment RH is interpreted as the hanging wall fault bend of the relay resulting from the SW propagation of Segment C. Finally, Segment C splays into Segments C2 and the NE lateral tip of Segment C, both exhibiting throw gradients smoothly decreasing away from branch line z-z'. The geometry associated with such a throw pattern has been interpreted as resulting from the bifurcation of the fault plane (Childs et al. 1996, Marchal et al. 2003, Nelson 2007).

The throw contours for Fault G3 are dominantly sub-horizontal above these maxima zones and sub-vertical underneath them. The abrupt change in the plunge of the throw contours corresponds to the start of the stratigraphic thickening and associated growth packages in the hanging wall. This cut-off has been attributed to the transition between the pre-faulting and the syn-faulting sequences respectively characterised by sub-vertical and sub-horizontal contours (Childs et al. 2003).

In summary, Fault G3 is interpreted as resulting from the combination of hard linkage of individual segments, such as Segment T intersecting with the main fault plane or Segments B and C linking through a breached relay zone, and vertical bifurcations of the fault plane (main fault with Segment C2) followed by a common growth history.

3.6 Kinematic evolution

3.6.1 Vertical throw distribution: T-z plots

Vertical throw distribution plots have been measured along Fault G3 on sections normal to the fault plane, every 250 or 500 m from a lateral tip to another (Fig. 3.10). The T-z plots add complementary information to the throw contour plots. Vertical throw measurements could be made at closely spaced intervals of c. 20-30 m due to the high frequency content of the seismic data. This allowed a detailed analysis of throw distribution and variation of throw gradients to be conducted on the entire fault plane. Fifteen of these T-z plots are shown as representative throw profiles along the strike of Fault G3 (Fig. 3.10).

The vertical throw distribution plots can be grouped in two main categories according to the shapes. The plots located in the lateral tip regions are characterised by vertical throw profiles that are mesa shaped (M-type of Muraoka & Kamata 1983). These T-z plots an almost uniform throw distribution with the exception of the regions immediately adjacent to the upper and lower tips. The upper tip line of the fault terminates a few tens of metres beneath the present day seabed in these lateral termination zones. The second category of T-z plots is representative of the main part of the fault plane, away from the lateral tip regions. These vertical throw distribution plots exhibit strongly skewed M-type throw profiles which consist of the 3 following separated parts. The upper tip of Fault G3 is characterised by a very high positive gradient ranging from 0.8 to 1.30 between the seabed horizon and the point of the maximum throw value generally located between Horizons A and B. The large central portion of the fault exhibits an extremely constant negative slope with low throw gradients (c. 0.06) from the point of maximum displacement to an inflection point located in the lower half of the fault plane. Linear regression analysis of the central portions of these plots yields regression lines with r^2 greater than 0.9. This confirms that throw gradients are virtually constant in the central part of T-z plots obtained for fault G3. The third and lower part of vertical throw profiles for fault G3 is characterised by an increase of throw gradient values up to 0.39 from the inflection point to the lower tip. Basal tip gradients were calculated from each T-z plots obtained for Fault G3, between the point of inflexion within the post-sedimentary part of the fault plane and the lower tip point. All 49 values of lower tip gradients were then grouped in intervals of 0.05 and presented in a frequency histogram and curve (Fig. 3.11). The values range from 0 to 0.39 and are characterised by a well defined peak corresponding to throw gradients between 0.15 and 0.2, the median value for ungrouped data points being 0.18.

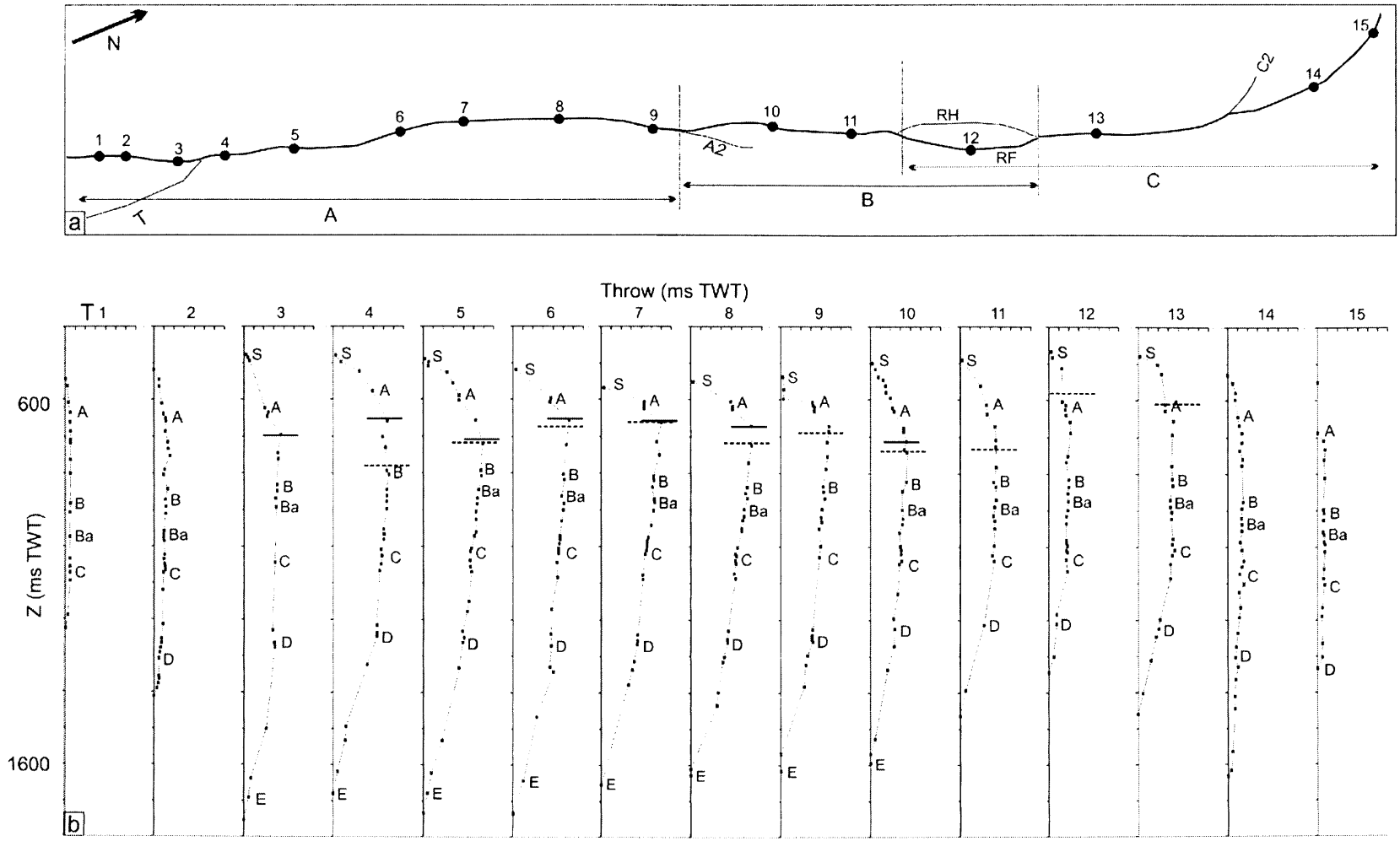

Fig. 3.10: (a) Schematic fault trace of Fault G3 based on the Pleistocene Horizon D with location of the 15 T-z plots. (b) Vertical throw distribution plots for 15 representative sections of Fault G3. Each T-z plot shows the throw values (T) horizontally, up to 140 ms TWT, plotted against the time (Z) in ms TWT. Horizontal lines represent the base of growth packages across the fault plane and the dashed lines represent the stratigraphic interval in which G2 became inactive.

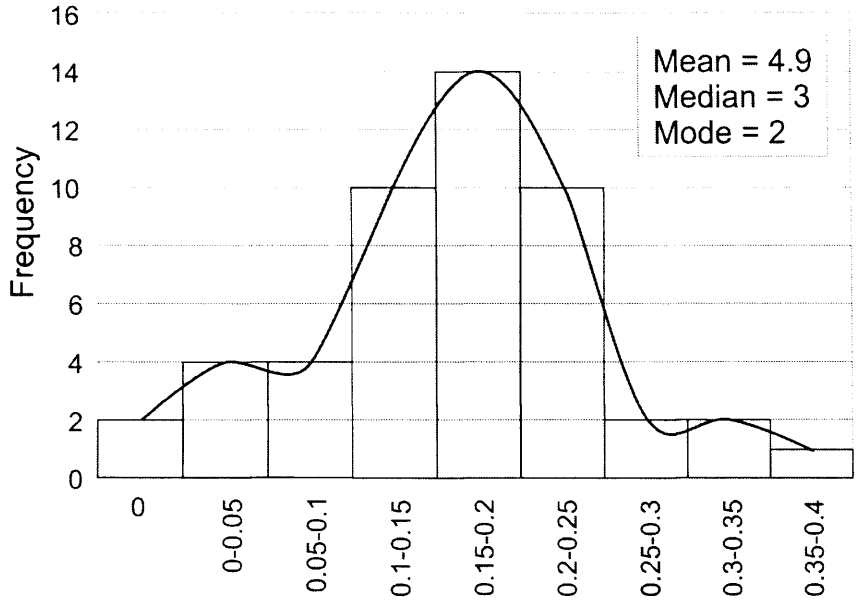

Fig. 3.11: Frequency histogram and curve of the basal tip gradients along Fault G3. The plot represents throw gradients between 0 and 0.4 that have been grouped in intervals of 0.05. The data are characterised by a well defined peak corresponding to throw gradient values between 0.15 and 0.2. Mean value, median and mode are indicated in the top right corner of the plot. For ungrouped data points, mean is 0.17, median is 0.18 and mode is 0.13.

The base of the syn-kinematic interval (labelled X in Fig. 3.7) corresponds to the maximum throw value zone on most of the fault plane (represented by the horizontal lines in Fig. 3.10). An analysis of the throw pattern in the upper tip region of the fault plane shows high throw gradients with changes of slope and steps. Sloping portions are separated with zero slope portions that are characterised by no change in throw values for a period of time, such as in the proximity of Horizon A in the central part of Fault G3. These steps in displacement could be interpreted as non-activity of the fault (Cartwright et al. 1998) or lithological effects due to a change in the type of deposition from a clastic to hemipelagic sedimentation (Castelltort et al. 2004). In either case, these steps confirm that the upper part of the fault plane is characteristic of syn-sedimentary movement of the fault.

However, the fault plane beneath the point of maximum throw values exhibits a negative slope characterised by very small and constant throw gradients with extremely continuous and regular decrease in throw values. This supports the interpretation that this part of the fault plane results from blind propagation.

3.6.2 Timing of Fault G3 in relation to the Kefira Graben

The kinematic relationship between the Kefira Graben and the growth faults located updip of the graben close to the shelf-break is investigated with particular attention drawn to Faults G2 and G3. Fault G2 ceased activity in the late Pleistocene and tips out upward in the interval between Horizon B and a few tens of metres below the present day seabed. The throw distribution on the fault plane is characteristic of growth faults (Fig. 3.12a). The upper part is characterised by near horizontal contours of increasing throw values with depth. Contours are centred onto zone of throw maxima (represented in dark colour) separated by throw minima indicating linkage zone.

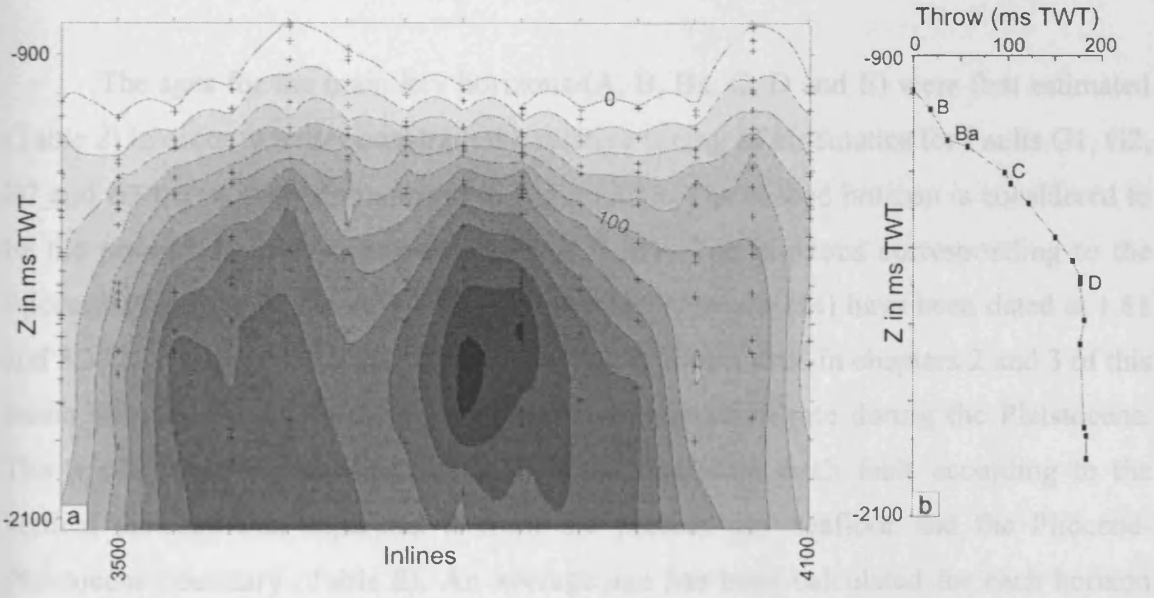

Fig. 3.12: (a) Throw contour plot for Fault G2 showing lines of equal throw values spaced at 20 ms TWT. (b) Example of a typical vertical throw distribution plot for Fault G2 showing throw values increasing systematically from the upper tip to Horizon D.

Figure 3.12b provides a typical example of vertical throw distribution for Fault G2. The throw increases with depth from the upper tip to a stratigraphic level situated in the vicinity of early Pleistocene Horizon D. The throw gradient tends towards zero beneath Horizon D until a few tens of metres beneath the P-P boundary. Then throw gradients decrease slowly towards the lower tip which is located at the Top Messinian. The horizon immediately above the upper tip of Fault G2 is interpreted as marking the end

of its activity. Continuous high throw gradients related to stratigraphic expansion and syn-sedimentary activity persist up to the upper tip (Fig. 3.5). The corresponding horizon on Fault G3 is reported as horizontal dashed lines on the T-z plots (Fig. 3.10) and is located c. 0 to 50 m beneath the base of the syn-kinematic sequence (plain line in Fig. 3.10). The stratigraphic level marking the onset of syn-sedimentary faulting and the horizon corresponding to the termination of activity of Fault G2 vary along the strike of the fault. However, the horizon marking the termination of activity of Fault G2 always very closely precedes the onset of growth packages on Fault G3. This suggests that Fault G2 became inactive immediately prior to the time when Fault G3 reached the free surface suggesting that there might be some kinematic coherence between these two faults. A similar interdependence of timing on adjacent faults in a gravity driven growth fault array was described by Cartwright (1998) from the Gulf of Mexico.

The ages for the main key horizons (A, B, Ba, C, D and E) were first estimated (Table 2) in order to better constrain the relative timing of kinematics for Faults G1, G2, B2 and G3 that is then summarised in Figure 3.13. The seabed horizon is considered to be the present day sedimentation dated at 0 My. The horizons corresponding to the Pliocene-Pleistocene boundary (P-P) and the Top Miocene (M) have been dated at 1.81 and 5.33 My respectively. The ages for the key horizons used in chapters 2 and 3 of this thesis were estimated assuming a constant sedimentation rate during the Pleistocene. The age of each horizon was calculated separately for each fault according to the vertical distance that separates it from the present day seafloor and the Pliocene-Pleistocene boundary (Table 2). An average age has been calculated for each horizon from the different ages obtained from the four faults and differences in age obtained for the same horizon from different faults have been used for errors estimations. The location of the Pliocene-Pleistocene boundary was interpreted from previous work from Garfunkel (1979) and from information in the completion logs for wells located within the survey area, and is estimated to have a positioning error of 50 m.

Horizons	Ages on Fault G1	Ages on Fault G2	Ages on Fault B2	Ages on Fault G3	Average ages (± errors)
Seabed	0	0	0	0	0
A	0.247	0.258	0.182	0.196	0.221 (± 0.039)
B	0.437	0.468	0.511	0.497	0.478 (± 0.041)
Ba	0.551	0.58	0.584	0.557	0.568 (± 0.017)
C	0.779	0.758	0.803	0.768	0.777 (± 0.026)
D	1.217	1.242	1.204	1.084	1.187 (± 0.103)
E	1.559	1.564	1.532	1.354	1.502 (± 0.148)
P-P	1.806	1.806	1.806	1.806	1.806
M	5.332	5.332	5.332	5.332	5.332

Table 2: Summary table of the estimated ages of Pleistocene stratigraphic horizons calculated from Faults G1, G2, B2 and G3. A maximum error of 150Ka has been calculated according to the differences in ages found for the same horizon from different faults.

The observations and interpretation made through the previous sections led to the reconstruction of the movement of relative faulting displayed in Figure 3.13.

Fault G1 is active at the present day whereas Fault G2 ceased activity and has been buried at a time that corresponds to the deposition of Horizon B (c. 490 Ky) in the southern region and a few thousands of years ago in the northern regions. Both growth faults that composed the Kefira Graben (G1 and G2) are characterised by an increase of throw with depth from the Seabed to the vicinity of Horizon D. This interval is characterised by sub-horizontal throw contours (Fig. 3.12). These faults are therefore interpreted as being syn-sedimentary in the parts that offset the stratigraphy between Horizon D and the seabed (represented by the dark grey large column on Fig. 3.13). The earliest growth package on Fault G2 just predated the initial growth package on Fault G1 located in the vicinity of Horizon D (dated as c. 1.19 My). The throw gradients tend towards zero between Horizon D and the P-P boundary and the throw contour switch to the sub-vertical in this interval (Fig. 3.12). These characteristics suggest that the growth faults have initiated within this interval of maximum throw values (represented by the thin light grey column on Fig. 3.13). Both faults are characterised by throw values decreasing downwards to the top Miocene which suggests that they have propagated by blind propagation (represented by the thick black lines on Fig. 3.13).

Fault B2 is taken as a typical example of the blind faults located between the Kefira Graben and the coast-parallel faults situated on the shelf-break. Fault B2 offsets sediments deposited between a horizon located between Horizons C and D (c. 1My) and Horizon A (c. 180 Ky). Fault B2 has been interpreted as a blind fault that grew entirely

by blind propagation. Therefore, the fault could only have initiated after the deposition of Horizon A. This places the time of initiation of Fault B2 between c.180 Ky and the present day.

Fault G3 is active at the present day seabed and is characterised by an increase of throw with depth associated with stratigraphic growth packages between the seabed and an interval located between Horizons A and B (between c. 490 and 180 Ky). This upper part of Fault G3 has been interpreted as syn-sedimentary (Fig. 3.13). The displacement analysis presented in Section 3.6.1 suggests that Fault G3 initiated as a blind fault at its early stage of development. The base of interval of maximum throw values is located in the vicinity of Horizon B. The interval situated below Horizon B has been interpreted as resulting from blind propagation. This suggests that the fault initiated after deposition of Horizon B. Therefore, the possible zone of initiation of the zone is located between the top of the blind fault part (Horizon B at c. 490 Ky) and the beginning of the growth packages. Fault G3 propagated downwards to reach the P-P boundary by blind propagation.

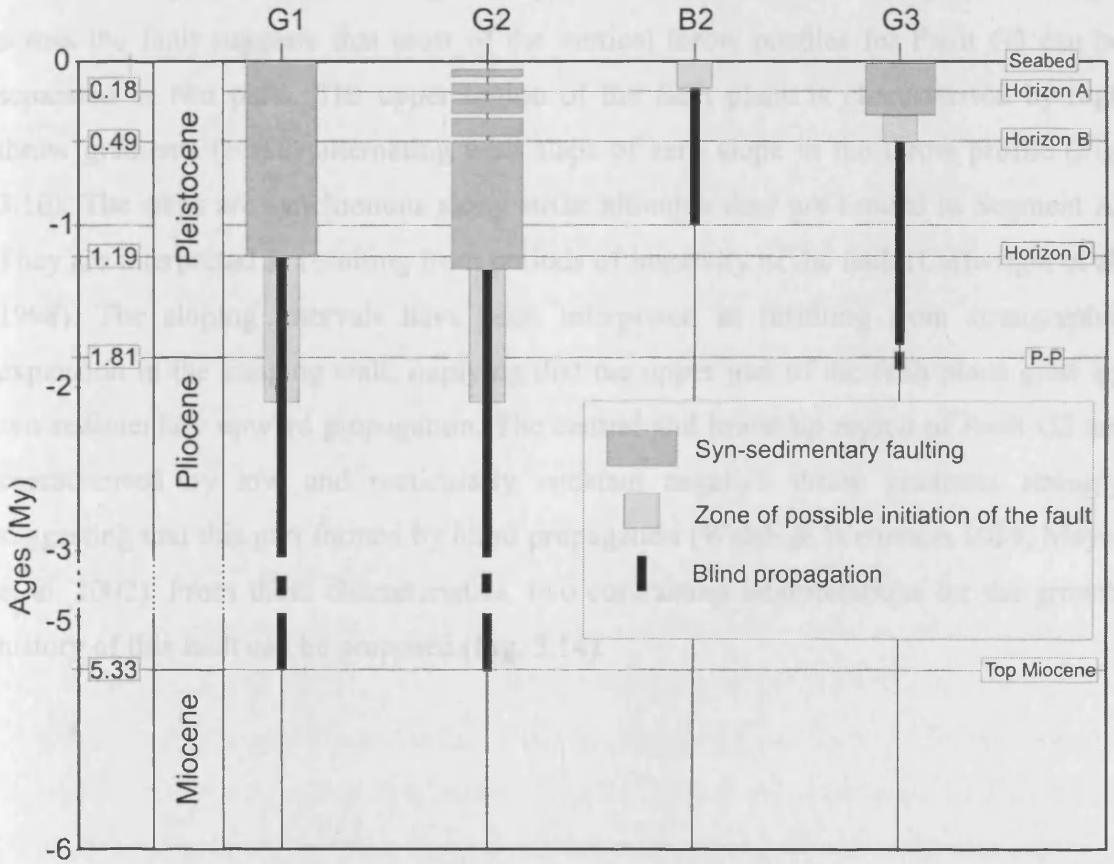

Fig. 3.13: Graphic synthesising the timing of kinematics for Faults G1, G2, B2 and G3.

3.7 Discussion

The preceding sections described the 3D geometry and the throw distribution of Fault G3. This segmented fault evidently grew in response to gravity-driven deformation of the updip region of the Levant Basin, and the specific timing and growth of Fault G3 was closely coupled to the structural evolution of nearby graben structures. The mode of initiation and early propagation of Fault G3 is now discussed in more detail, based largely on observations from the throw distribution plots. The suggested evolution for this fault is then compared to existing fault growth models.

3.7.1 Fault initiation

3.7.1.1 Model for fault initiation

A detailed analysis of the geometry, throw distribution and stratigraphic changes across the fault suggests that most of the vertical throw profiles for Fault G3 can be separated in two parts. The upper region of the fault plane is characterised by high throw gradients (> 0.8) alternating with steps of zero slope in the throw profile (Fig. 3.10). The steps are synchronous along strike although they are limited to Segment A. They are interpreted as resulting from periods of inactivity of the fault (Cartwright et al. 1998). The sloping intervals have been interpreted as resulting from stratigraphic expansion in the hanging wall, implying that the upper part of the fault plane grew by syn-sedimentary upward propagation. The central and lower tip region of Fault G3 are characterised by low and particularly constant negative throw gradients strongly suggesting that this part formed by blind propagation (Walsh & Watterson 1989, Meyer et al. 2002). From these characteristics, two contrasting interpretations for the growth history of this fault can be proposed (Fig. 3.14).

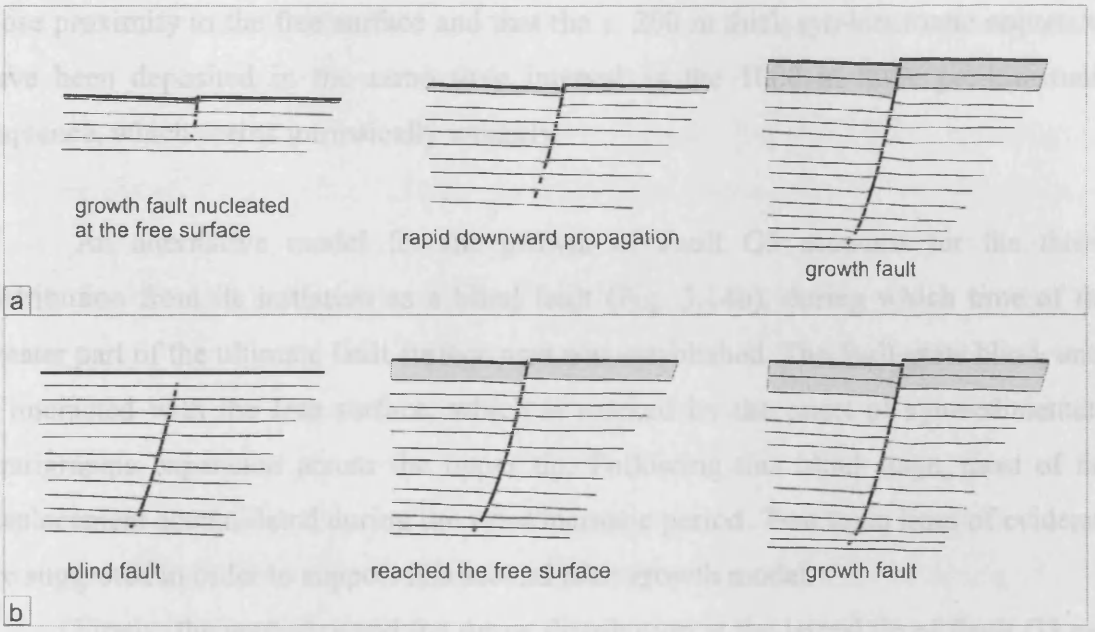

Fig. 3.14: Two different models of growth for Fault G3. (a) Nucleation of the fault at the free surface and accumulation of the synsedimentary interval (shaded area) whilst rapid downward propagation of the lower tip. (b) Nucleation as a blind fault which reached the surface and become a growth fault in a later stage of evolution.

The first interpretation is based on classical models for fault growth and conceptual framework for fault propagation. The ideal blind fault model predicts that the point of nucleation is indicated by the maximum throw value (Watterson 1986, Barnett et al. 1987). In a more general context, maximum throw values are often interpreted as indicators of fault initiation as older portions of the fault have accumulated more displacement than the recent lateral tip region (e.g. Elliott 1976, Walsh & Watterson 1987, Ellis & Dunlap 1988, Wilkins & Gross 2002). For syn-sedimentary faults in particular, it has been suggested that a significant change in the gradient of the throw profile indicates the onset of faulting and that the faults initiated within areas of maximum throw values (Childs et al. 1993, Meyer et al. 2002).

This maximum throw value corresponds to the base of the growth packages in the hanging wall of Fault G3. This would therefore place the point of nucleation at the free surface approximately at the time of deposition of Pleistocene sediments located between Horizons A and B (represented by the horizontal solid lines on Fig. 3.10). From this, it follows that the fault would have accumulated syn-kinematic (growth) sequences above the nucleation point whilst propagating laterally and downwards towards the present day lower tip line (Fig. 3.14a). This implies that the fault initiated in

close proximity to the free surface and that the c. 200 m thick syn-kinematic sequences have been deposited in the same time interval as the 1000 m thick pre-kinematic sequence, which seems intrinsically unlikely.

An alternative model for the growth of Fault G3 accounts for the throw distribution from its initiation as a blind fault (Fig. 3.14b), during which time of the greater part of the ultimate fault surface area was established. The fault grew blind, until it interacted with the free surface, which is marked by the onset of syn-sedimentary stratigraphic expansion across the upper tip. Following this blind stage, most of the displacement accumulated during the syn-kinematic period. Two main lines of evidence are suggested in order to support this second fault growth model.

Firstly, the geometry and the throw distribution at the lateral tip of Fault G3 can provide insights onto the way the fault grew (e.g. Cowie & Scholz 1992b, Cartwright & Mansfield 1998). As the fault grows and extends its dimension, the lateral tip lines propagate further away from the zone of initiation. We assume here that when a fault grows, its lateral tip regions are representative of the early evolution of the more central portions. We note that the lateral tip region undergo an anti-plane shear Mode III propagation whereas the central part of the fault grow mainly with a in-plane Mode II propagation (e.g. Atkinson 1987). However, as a result of radial propagation, the central portions of each segment were very likely to be at the edge of the fault segment at the early stage of evolution. The central parts of Segments A and C underwent propagation under Mode III conditions, before slip was confined to Mode II conditions as expected for the central portions. Vertical throw distributions at the SW and NE lateral tip regions of Fault G3 are taken as being representative of the early evolution of the main part of Segments A and C, respectively. This assumption seems reasonable given the known lateral propagation involved in the growth of Fault G3. Central portions of the fault at present were originally close to lateral tips themselves. The lateral tip regions of Fault G3 are characterised by typical M-type vertical throw distribution plots with low and constant throw gradients. These profiles exhibit striking similarity with a typical vertical throw profile obtained for the blind faults mapped in neighbouring parts of the study area within the same stratigraphic interval (Fig. 3.15). This suggests that Fault G3 initiated as a blind fault entirely within the sub-surface domain before becoming the syn-sedimentary fault in more recent times.

Secondly, the characteristic shape of the central parts of the T-z plots can be linked to the early evolution of Fault G3 (Fig. 3.10). The central portions of these profiles have been shown to exhibit extremely constant throw gradients characterised with regression lines with r^2 greater than 0.9. An explanation for this could be to consider these uniform gradient portions as being somehow a relict of the initial blind fault stage. This explanation is supported by comparing the vertical throw profiles for the centre of Fault G3 to those of the lateral tip regions (Fig. 3.15a). The vertical extent of the region marked by near-constant gradients corresponds remarkably to the vertical extent of the lateral tips. Understanding the preservation of the near-constant gradients is essential to a better understanding of the kinematics of Fault G3. From this, we can infer that Fault G3 initiated as a blind fault with very low and constant throw gradients. This fault then reached the free surface and became a syn-sedimentary fault, accumulating stratigraphic expansion at the upper tip. Displacement was then added over the entire height of the fault of a value decreasing away from the free surface with almost a constant gradient. The amount of displacement added on the fault plane after interaction with the free surface is represented by the shaded area in Figure 3.15. As a result of this systematic addition of decreasing throw values with depth on the fault plane, the central part exhibits a straight gradient, preserved as a relict of the initial blind fault stage.

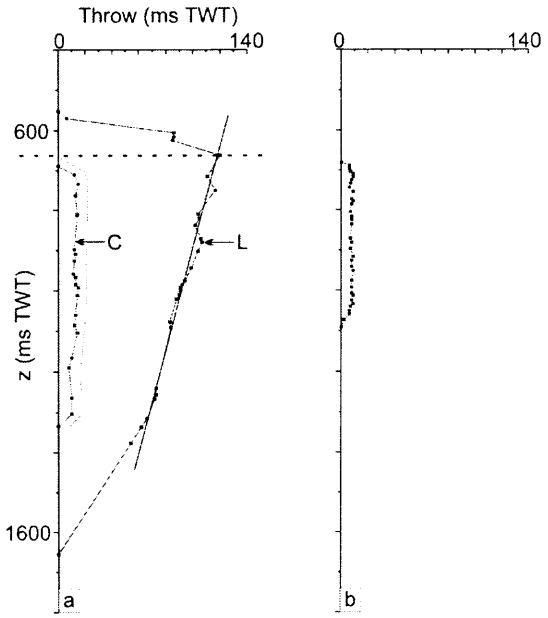

Fig. 3.15: (a) Vertical throw profile on the central region (C) and lateral tip region (L) of Fault G. The shaded area represents the displacement accumulated by Fault G3 after it reached the surface. The dash line marks the limit between pre-faulting and syn-faulting sequences (b) Vertical throw profile for a blind fault offsetting the same stratigraphic interval nearby.

3.7.1.2 Significance of the point of maximum throw value

Numerous studies have interpreted the point of maximum displacement as an indicator of the point of nucleation of the fault, in particular for isolated blind faults (Watterson 1986, Barnett et al. 1987) but also for syn-sedimentary faults (Childs et al. 1993, Meyer et al. 2002). However, it has already been suggested that the point of maximum displacement can migrate away from the point of nucleation of the fault (Peacock 1991). This has been attributed to interactions with other faults or variations in elastic properties (Burgmann et al. 1994, Cowie 1998, Cowie & Shipton 1998, Maerten et al. 1999, Schultz 2000) or mechanical barriers (e.g. Wilkins & Gross 2002).

In the study case presented in this chapter, Fault G3 is interpreted to have formed initially by the radial propagation and subsequent linkages of three main blind segments characterised by low throw/height ratios (Fig. 3.8d). In a later stage of evolution fault and as a consequence of interaction of the fault plane with the free surface, Fault G3 accumulated displacement with a near-constant gradient (Fig. 3.15). This suggests that interaction of the fault plane with the free surface changes the position of the maximum displacement but also the complete vertical throw distribution on the fault plane. This has important implications on interpretation of fault kinematics inferred from throw distribution as well as for general models of fault growth.

3.7.2 Gradients

The displacement patterns of some syn-sedimentary faults can bear remarkable similarity to those of ideal blind faults (Petersen et al. 1992). Parts of the same fault can be active at different times and the syn-sedimentary part can also comprise a post-sedimentary component (Meyer et al. 2002, Childs et al. 2003). There is therefore a need to establish criteria to differentiate blind from syn-sedimentary propagation effects in order to better reconstruct the kinematics of faults. It has been suggested that isolated

blind faults are characterised by throw gradients of a maximum value of 0.1. This implies that a gradient value greater than 0.1 would be characteristic of syn-sedimentary faults (Walsh & Watterson 1989, Meyer et al. 2002, Childs et al. 2003). Furthermore, displacement gradients in the blind propagation portion of a syn-sedimentary fault are expected to be similar to those of blind faults as they share the same controls (Childs et al. 2003). A gradient value of 0.22 has been cited as a maximum throw gradient for blind faults (assuming that this concern post-sedimentary faults) measured from seismic data (Nicol et al. 1996b).

The gradients analysis for Fault G3 in this study shows that the ranges of throw gradients for blind propagation and syn-sedimentary faults can considerably overlap (Fig. 3.11). The throw gradients measured on the lower tip of Fault G3 range from 0 to 3.9. These throw gradients are representative of the pre-faulting sequence on Fault G3. This has significant implications for dating the fault activity accurately and the amount of displacement associated with each of these two different mechanisms. Firstly, overlapping values for blind and syn-sedimentary gradients suggests that this 0.1 value is not a cut-off for blind propagation and can not be used as a single criterion to distinguish blind faults from syn-sedimentary faults. Secondly, considering 0.1 as a maximum gradient for blind propagation can lead to serious misinterpretation.

3.7.3 Fault scaling and fault growth models

Numerous extensive datasets of different types of faults from various settings have been used to define a relationship between the maximum displacement and the dimension of faults (e.g. Muraoka & Kamata 1983, Watterson 1986, Dawers et al. 1993, Schlische et al. 1996). From this, a systematic increase in both maximum displacement (D) and length (L) has been expressed as $D = cL^n$, where c is a constant related to the material properties. These different approaches to define displacement-length (D/L) scaling provide insight into the mechanics of fault growth and have been used to advance several fault growth models (e.g. Walsh & Watterson 1988, Cowie & Scholz 1992b, Cartwright et al. 1995). Diverse factors affect the D/L relationship including material property, measurement techniques, earthquake rupture or slip/propagation history and segment linkage (e.g. Cartwright et al. 1995, Kim & Sanderson 2005).

It has been suggested that a rapid growth of fault length at an early stage of development of the fault in extension settings would accommodate constant regional strain (Nicol et al. 1997). A model for faults resulting from the up-dip propagation of pre-existing underlying structures suggested that displacement can be added for a near constant length as lateral tips interact between neighbouring faults (Walsh et al. 2002). Syn-sedimentary normal faults from the Timor Sea have been described to grow with rapid extension of the fault length which can be attributed to reactivated underlying structures (Meyer et al. 2002). Other studies in the Aegean region give examples of mature normal fault systems showing little evidence of propagation for added displacement on individual faults. This behaviour is either explained by lateral tips of the fault that are fixed at depth (Morewood & Roberts 1999) or by stress feedback mechanism or mechanical interaction with transverse faults (Poulimenos 2000). This departure from a fault growth by self-similarity has been observed at large scale in the same active continental regions (Armijo et al. 1996) and in the Turkana rift, North Kenya (Vetel et al. 2005). Displacement analysis in compressional settings also witnessed a rapid propagation of fault-propagation folds to near their final length (Krueger & Grant 2006). However, these studies concern faults that propagated by reactivation and upward propagation of underlying structures or faults that are confined horizontally by interactions with other structures.

Our study focused on gravity-driven extensional faults that show no evidence of reactivation of underlying structures and no tip line restriction. Fault G3 has been shown to be the result of blind segments that linked and interacted with the free surface to become a syn-sedimentary fault at a later stage. As a consequence of this, most of the dimension of the fault was accumulated in the first blind propagation stage and most of the displacement was then added afterwards during the syn-sedimentary stage. At both stages, the fault conforms to a gross scaling law for the D/L relationship (Fig. 3.16). However, the growth path of this fault, within the interval considered by the scaling law, can be argued to be step-like. The dimension was established at an early stage of development of the fault according to a low D/L ratio (c. 0.015). This was followed by a stage of accumulation of displacement for a near-constant height of the fault along a sub-vertical growth path increasing the D/L ratio by a factor of 7 (c. 0. 073).

Ideal blind faults have been described to propagate in a manner that requires strain to develop to accommodate displacement gradients (Barnett et al. 1987). As a

consequence of this propagation model, ideal blind faults are expected to be characterised by triangular or C-type throw profiles. On the contrary, ideal M-type throw profiles are characterised by a zero throw gradient for a significant area of the fault plane (Muraoka & Kamata 1983). This can be explained by an absence of near-fault wallrock straining during the formation of this part of the fault. The lateral tips of Fault G3 exhibit M-shape vertical throw profiles with near zero gradients. The central portion of the fault plane preserved a relict of this constant gradient.

In summary, intersecting the free surface for Fault G3 changed the way displacement accumulated and the final throw distribution on the fault plane. This resulted in dramatic steps in the growth pathway and implies that the dimension of the fault, and the vertical in particular, established at an early stage of evolution whereas the displacement was accumulated associated with very small increase in dimension in a later stage.

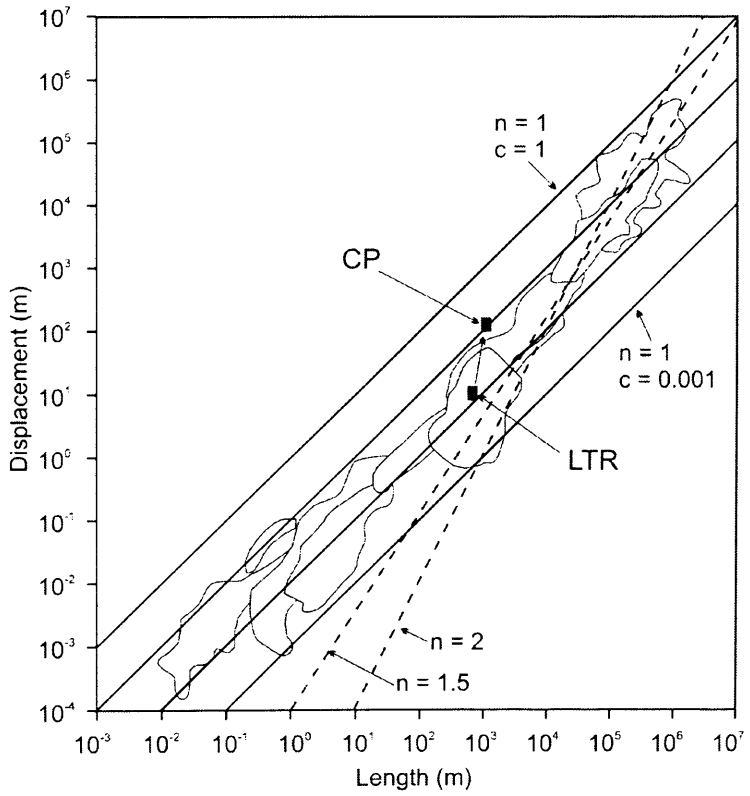

Fig. 3.16: Log-log plot of displacement vs. length for various fault populations (shaded areas) compiled by Schlische et al., 1996. The central portion (CP) and lateral tip regions (LTR) measurements for Fault G3 plotted on this graph show the interpreted growth path for this fault from early evolution until present day.

3.8 Conclusions

Coast parallel growth faults located on the shelf break of the Levant passive continental margin have been investigated in relation to the tectono-stratigraphic environment. A detailed analysis of the 3D geometry and throw distribution on one particular fault (Fault G3) provided essential information on the kinematics of this fault. The conclusions that can be drawn from this study are as following.

- Fault G3 is interpreted as resulting from the combination of radial propagation of the fault plane, hard linkage of individual blind segments and vertical bifurcations of the fault plane followed by a common growth history.

- T-z plots for this fault exhibit M-type profiles at the lateral tip regions and skewed M-type on the central portions. The skewed M-type consists of an upper part characterised by high positive throw gradients. This zone is associated with growth packages and reverse drag folding in the hanging wall of the fault plane. Constant low negative throw gradients are observed beneath the point of maximum throw value. This corresponds to a pre-kinematic sequence mostly associated with normal drag folding.

- Fault G3 is interpreted as initiated as a blind fault that subsequently reached the surface and became a syn-sedimentary fault. This is based on 3 main indications: (i) similarity between the throw profiles in the lateral tip region of Fault G3 with those of blind faults, assuming that lateral segments can reflect the same process of propagation as central segments during the early stage of development of the fault, (ii) interpretation of the central portion of the T-z plots as a relict of the blind fault stage and (iii) analogy with parallel blind faults located between the Kefira Graben and Fault G3.

- The interaction of the fault plane with the free surface changes the position of the point of maximum displacement as well as the complete vertical distribution of throw values. The amount of displacement added on the fault plane after

interaction with the free surface decrease away from the maximum displacement and downwards with almost a constant gradient.

- As a consequence of this, most of the dimension of the fault was accumulated by post-sedimentary process and most of the displacement has been added afterwards by syn-sedimentary faulting. Although being within the interval predicted by scaling laws, this behaviour suggests an extremely step like growth trajectory.

- A significant overlap is observed between the throw gradients measured from syn-sedimentary faults and post-sedimentary parts that grew by blind propagation. The previously published maximum blind gradients might therefore be misleading in assessing accurately the kinematics of faults in general.

Chapter IV

Reactivated faults

This chapter has been submitted for publication in Journal of Structural Geology as:

Baudon, C. & Cartwright, J. A. in review. The kinematics of reactivation of normal faults using high resolution displacement mapping. Journal of Structural Geology.

Joe Cartwright provided discussion of the topics presented in this chapter and support during its writing.

4 THE KINEMATICS OF REACTIVATION OF NORMAL FAULTS; EXAMPLE FROM THE ESPIRITO SANTO BASIN

4.1 Abstract

Normal reactivation of extensional faults offsetting Cenozoic clastic sediments is investigated using a high quality 3D seismic data from offshore Brazil. These faults form complex crestal collapse grabens and result from elliptical doming of the underlying Cretaceous sequence due to Early Cenozoic uplift. The exceptional quality of this dataset allows an extremely detailed analysis of the throw distribution to be conducted on the faults. This, in addition to a reconstruction of the 3D geometry of the fault network, gives insights into the mechanisms and kinematics of reactivation.

Two distinct modes of reactivation are recognised from this dataset. The main mode is a classical reactivation by upward propagation of pre-existing structures. A second mode of reactivation results from the propagation of an individual fault segment initiated above the pre-existing faults that hard link in the dip direction. This is termed reactivation by dip linkage. For both mechanisms, reactivation processes are selective and only occur on some portions of faults. Factors controlling the preferential reactivation of some segments above others include: (1) orientation of the pre-existing fault plane relative to the principal stresses responsible for the reactivation, (2) segmentation of the pre-existing network (3) maximum dimensions and throw values of pre-existing faults and (4) basal tip line geometry associated with a detachment. Reactivation is an important process that may account for part of the scatter in scaling relationship and should be included in fault growth models.

4.2 Introduction

Fault propagation has been investigated in numerous studies based on seismic data, outcrop data, and analogue and numerical modelling. These studies have led to a

number of fault growth models (e.g. Walsh & Watterson 1988, Cowie & Scholz 1992b, Cartwright et al. 1995). A systematic increase in both the maximum displacement and the dimension of faults has been used to derive fault scaling relationships (e.g. Walsh & Watterson 1988, Cowie & Scholz 1992a, Dawers et al. 1993, Schlische et al. 1996). However, departure from scaling behaviour between dimensions and displacement has been attributed to mechanical interactions with neighbouring structures (e.g. Nicol et al. 1996, Maerten et al. 1999), the mechanical heterogeneity due to major stratigraphic boundaries (e.g. Peacock & Zhang 1994, Wilkins & Gross 2002) or to segment linkage during propagation (e.g. Peacock & Sanderson 1991, Cartwright et al. 1995, Dawers & Anders 1995, Wojtal 1996).

Reactivation processes have only recently been considered as an important controlling parameter in fault propagation (Walsh et al. 2002, Bellahsen & Daniel 2005). Small normal faults have been recognised as exhibiting discrete episodes of activity (e.g. Blair & Bilodeau 1988, Cartwright et al. 1998, Lisle & Srivastava 2004). Episodic motion can affect growth trajectories for faults as defined by the scaling relationships (Cartwright et al. 1998). Reactivated faults have been shown to follow different growth behaviour than previously suggested by conventional models (e.g. Meyer et al. 2002, Walsh et al. 2002, Nicol et al. 2005). A better understanding of reactivation is therefore fundamentally important. In addition to this, reactivated structures can act as pathways for fluid migration and can greatly affect fault seal quality (Holdsworth et al. 1997). Another major issue arises from the difficulty to establish whether a fault is extinct or not (Muir Wood & Mallard 1992) and a better appreciation of the underlying controls of reactivation would greatly improve the assessment of seismic hazards (Lisle & Srivastava 2004).

Numerous examples of extensional reactivation of thrusts (e.g. Brewer & Smythe 1984, Enfield & Coward 1987), reverse reactivation of normal faults (e.g. Jackson 1980, Kelly et al. 1999), normal and reverse faults reactivated in strike-slip mode and lateral reactivation of strike-slip faults (e.g. Kim et al. 2001) have been presented from diverse basin types. Reactivation has been defined as discrete displacement events separated by a period of quiescence (Holdsworth et al. 1997). However, the term reactivation is perhaps most commonly used to define tectonic inversion, and in this context, the vast majority of studies provide examples of

reactivated faults that experienced their later history of motion during an inversion episode, in which inheritance of basement structures often features as one of the major controls. There have in contrast, been far fewer studies of extensional reactivation of pre-existing normal faults, and those few that have been undertaken are largely based on basement-linked structures. There is therefore a need for additional case studies of normal reactivation of extensional faults that are not controlled by basement structures. There is a reasonable understanding of the processes leading to the rheological weakening necessary for reactivation. Creating new faults requires higher stress levels than reactivating pre-existing ones (Krantz 1991) as pre-existing structures are weaker zones than the surrounding rock volume (White et al. 1986, White & Green 1986). However, it is still not really understood why some faults reactivate and others do not (e.g. Butler et al. 1997, Kelly et al. 1999).

This chapter aims to examine the factors influencing selection of faults or fault segments for reactivation using a high quality 3D seismic data from offshore Brazil (Fig. 4.1). Small crestal extensional faults offsetting Cenozoic clastic sediments are reactivated in an extensional manner. A detailed displacement analysis conducted on these faults allows the characterisation of reactivation and the effect of reactivation on the throw distribution over the fault planes. A model of evolution for the reactivated fault system is proposed in which the normal faults undergo normal reactivation by both upward propagation and a process of dip linkage with the above normal faults. The reasons for selective reactivation are then investigated and discussed. This chapter provides new insights in the understanding of reactivation and fault propagation in complex systems with particular attention on accurately dating fault kinematics in such contexts.

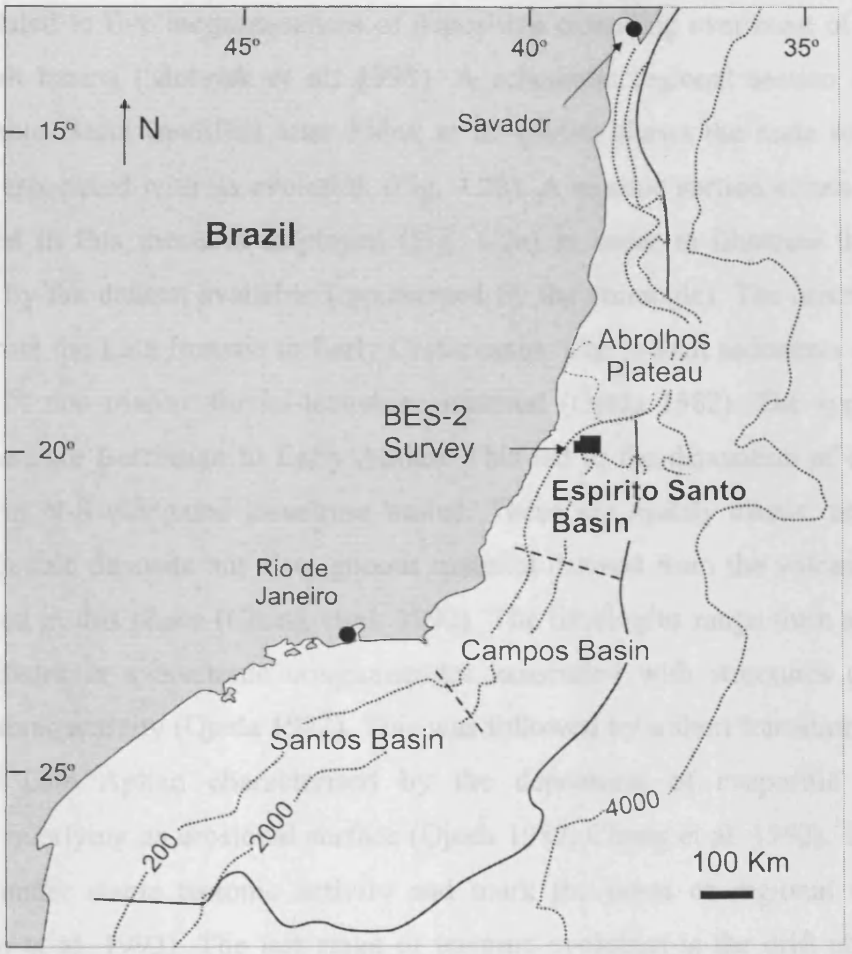

Fig. 4.1: Location of the BES-2 Survey in the Espirito Santo Basin, offshore Brazil (after Chang et al., 92). Dotted lines indicate the bathymetry (m), dashed lines symbolise the limits between different basins and solid line indicates the margin of the evaporites.

4.3 Geological setting

4.3.1 General geological setting

The Espirito Santo Basin is located on the passive margin of Brazil and was part of the east Brazil rift system (Chang et al. 1992). The rift system that led to the opening of the Atlantic started Late Triassic-Early Jurassic in southern Africa and expanded along the Brazil margin in the Early Cretaceous (Austin & Uchupi 1982, Meisling et al. 2001). The Espirito Santo Basin, along with most South Atlantic passive continental margins, underwent four evolutionary stages (Fiduk et al. 2004). These periods have

been correlated to five megasequences of deposition extending over most of the South Atlantic salt basins (Mohriak et al. 1998). A schematic regional section across the Espirito Santo Basin modified after Fiduk et al. (2004) shows the main sedimentary sequences associated with its evolution (Fig. 4.2b). A seismic section across the BES2 dataset used in this thesis is displayed (Fig. 4.2a) in order to illustrate the interval comprised by the dataset available (represented by the rectangle). The onset of rifting occurred from the Late Jurassic to Early Cretaceaous. The pre-rift sediments are mainly composed of non marine fluvial-lacustrine material (Ojeda 1982). The syn-rift stage spanned the Late Berriasian to Early Aptian. This led to the deposition of continental sediments in N-S elongated lacustrine basins. These are mainly clastic, non marine, fluvial or deltaic deposits but also igneous material derived from the volcanic activity that occurred in this phase (Chang et al. 1992). The lithologies range from sandstones, silts and shales to syntectonic conglomerates associated with structures due to the intense tectonic activity (Ojeda 1982). This was followed by a short transitional stage in Middle to Late Aptian characterised by the deposition of evaporitic sediments sometimes overlying an erosional surface (Ojeda 1982, Chang et al. 1992). These were deposited under stable tectonic activity and mark the onset of regional subsidence (Demercian et al. 1993). The last stage of tectonic evolution is the drift phase and it corresponds to two main megasequences of deposition (Mohriak et al. 1998). An Albian marine-transgressive megasequence is characterised by shallow carbonate platforms of a high-energy semi-restricted environment and deeper water pelitic sediments in the axial parts of the basins (Chang et al. 1992, Demercian et al. 1993). Further deepening of the basin at the end of the Albian associated with marine transgressions results in the deposition of low-energy sediments such as marls and shales. The Cenozoic marine-regressive megasequence constitutes the main interval of interest of this work. The bathyal conditions allow deposition of prograding siliciclastic sediments derived from the erosion of coastal mountains whereas carbonate platforms dominate over the shales in the northern areas (Chang et al. 1992). Major unconformities separate the megasequences between Paleozoic and Mesozoic, at the Early Cretaceous, at the pre-Aptian corresponding to the breakup and at the Early Cenozoic (Fiduk et al. 2004). The Early Cenozoic boundary is interpreted as the Cretaceous/Cenozoic boundary (Top K) in this chapter.

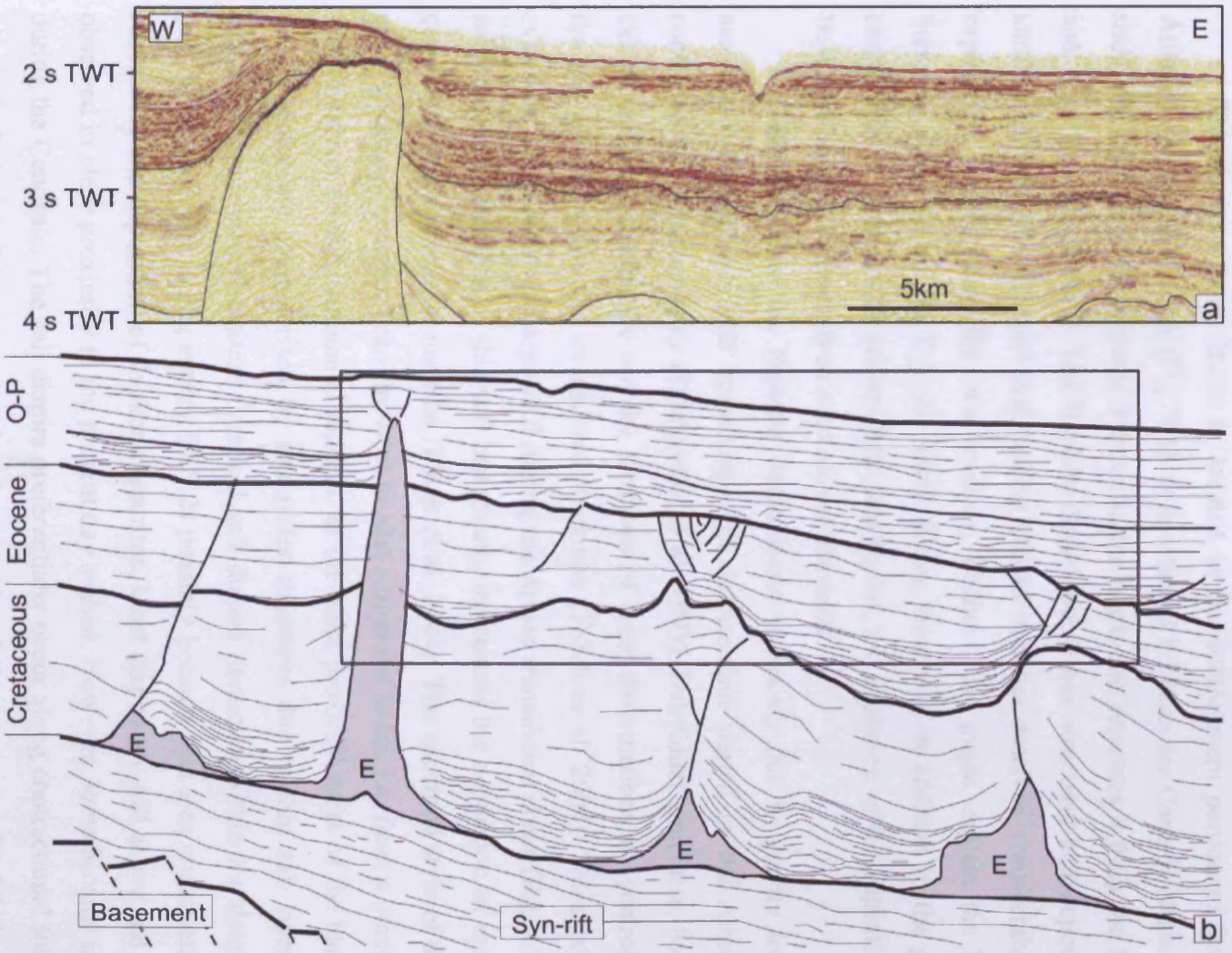

Fig. 4.2: (a) Seismic section across the 3D data in the BES-2 survey. Location of the line on Fig. 4.4. (b) Schematic regional section across the Espirito Santo Basin (after Fiduk et al., 2004). Deformation of the evaporites (E) in major salt diapirs has been active since the Albian. N-S folding of the Cretaceous sequence and strata above result from early Cenozoic compression. O-P is Oligocene to Present day.

4.3.2 Regional and semi-regional geological setting

The Espirito Santo Basin is located in the southeastern portion of Brazilian Atlantic continental margin (Fig. 4.1). It is situated between the Campos Basin to the south and the Abrolhos volcanic Plateau to the north that separates it from the Mucuri and Cumuruxatiba Basins. The Espirito Santo Basin has structural and depositional similarities with the Campos and Santos Basins and has received considerably less exploration interest than the two southern Basins. This might explain the limited literature available on the Espirito Santo Basin. However, in addition to the general characteristics common to eastern Brazilian basins, the evolution of the Espirito Santo Basin has been influenced by several unique elements.

Deformation in the Espirito Santo Basin is mainly due to gravity tectonics associated with gliding and spreading. Salt deformation started in the Albian and continued to the present day (Demercian et al. 1993). Individual structures, however, exhibit different kinematics and the locations of these deformations are controlled by the salt geometry and the overburden thickness (Fiduk et al. 2004). Thick layers of evaporitic sediments were deposited during the Aptian transitional phase (Fig. 4.2). The subsequent deformation of this salt has greatly influenced the deposition of overlying carbonates and siliciclastic material (Fiduk et al. 2004). The structural style of the salt-cored structures changes from the west to east across the basin, i.e. from a proximal to distal position on the continental margin. In the most proximal areas of the basin, the salt tectonics are characterised by salt roller structures due to thin salt layers in a dominantly extensional context. Vertical salt diapirs dominate within the deep water part of the basin (including survey BES 2) possibly because this area underwent more subsidence and deposition of thicker evaporites. Most diapirs are still active and can be observed in close proximity to the present day seabed. However, some became inactive during the Cenozoic. The salt diapirs preferentially occur along contractional folds and accommodate part of the extensional and contractional strains as a result of their weaker rheology than the surrounding rocks (e.g. Vendeville & Jackson 1992b, Rowan et al. 2004). In more distal locations, overhangs or allochthonous tongues developed from the vertical diapirs. These can evolve into salt canopies due to the coalescence of several tongues. The movement of salt underlying the Cretaceous strata and the salt diapirs

piercing through the Cenozoic sequence strongly influenced the location and geometry of the structures studied in this chapter.

Several phases of volcanic activity strongly affected the evolution of the Espirito Santo Basin including in the Early to Middle Eocene with the emplacement of the Abrolhos Plateau created by the Trinidade hot spot (Meisling et al. 2001). It has been suggested that the Trinidade hot spot was a significant factor in the coastal uplift, the increase of sediment supply, the offshore volcanism and the reactivation of structures on the passive margin (Meisling et al. 2001). Igneous intrusions with a characteristic saucer-shape geometry (Hansen & Cartwright 2006) and extrusive flows have been interpreted over large areas of the Espirito Santo Basin (Fiduk et al. 2004). Furthermore, volcaniclastic materials derived from the erosion of the Abrolhos Plateau compose an important part of the post-Eocene sedimentary succession (Fiduk et al. 2004).

Finally, several ancient and modern canyons systems incise and infill thick sequences affecting the geometry of the basin and its depositional evolution (Fiduk et al. 2004).

4.4 3D seismic interpretation

4.4.1 Dataset

The BES-2 survey of 3D seismic data used in this study covers an area of c. 1600 km^2 within the Espirito Santo Basin in water depths ranging from c.100 to 1800 m. The data were collected using 6 x 5 700 m streamers and a 12.5 x 25 m bin grid. The survey has a time-migrated 12.5 x 12.5 m inline and crossline spacing after final processing. The data are zero-phase migrated and the dominant frequency within the Cenozoic interval ranges from 35 to 60 Hz decreasing with depth. No velocities information was available for this dataset. An average velocity value of 1800 m s^{-1} was estimated from typical seismic velocity values of clastic sediments in various slope and deep-water settings and from analogy with shallow seismic sections in other basins of the brazilian continental margin (Rodger et al. 2006). This places the vertical resolution within the interval of interest between c. 7 and 13 m, assuming an average velocity value of 1800 m s^{-1}. Seismic data beneath 4s TWT were not available for this study. As

a result of this, only a part of the Cretaceous and stratigraphy above were visible. However, the Cenozoic is the main interval of interest for this work (Fig. 4.2a).

Regional key horizons and fault planes were mapped at different stratigraphic levels using Schlumberger Geoframe 3.7 seismic interpretation software. Detailed measurements of the throw values on faults were made using fault normal seismic profiles and displayed as individual vertical throw distribution plots (T-z plot) for single profile transects (Cartwright et al. 1998, Baudon & Cartwright in review).

4.4.2 Seismic stratigraphic framework

The lower part of the seismic data available for this study is characterised by a several hundred metres thick interval of low amplitude and low continuity reflections. This low amplitude package is interpreted as being Cretaceous in age based on earlier work from Fiduk (2004). The top of the Cretaceous interval is marked by a thin interval of 2 or 3 continuous and high amplitude seismic reflections that is interpreted as the boundary between the upper Cretaceous and the Cenozoic (labelled Top K in Fig. 4.3). The seismic reflections corresponding to the Cretaceous sediments are folded and underlie major anticlines and synclines with differences in depth of up to 800 m.

The Cenozoic sediments constitute the main interval of interest of this study. These marine-regressive sediments are composed of prograding siliciclastic material, mainly shales, deposited in bathyal conditions passing into carbonates platforms in some areas. Three main units were defined based on differences in seismic characteristics that are fairly consistent over the whole survey area (Fig. 4.3).

Unit 1 overlies directly the top Cretaceous sediments in a discordant manner and is bounded at the top by an erosional surface observable over most of the area of interest. This unconformity is believed to be post middle Eocene to Oligocene (E-O) in age (Fiduk et al. 2004). Unit 1 is expressed as a package of moderate amplitude and continuous seismic reflections and is separated into 2 sub-units. Unit 1a comprises the stratigraphic interval between the Top Cretaceous and Horizon C60 and is characterised by onlap of reflections onto the Top Cretaceous (Fig. 4.3). This interval thickens within the synclines and becomes thinner above the anticlines. More chaotic packages of seismic reflections interpreted as mass transport complexes (MTC) can be seen at the

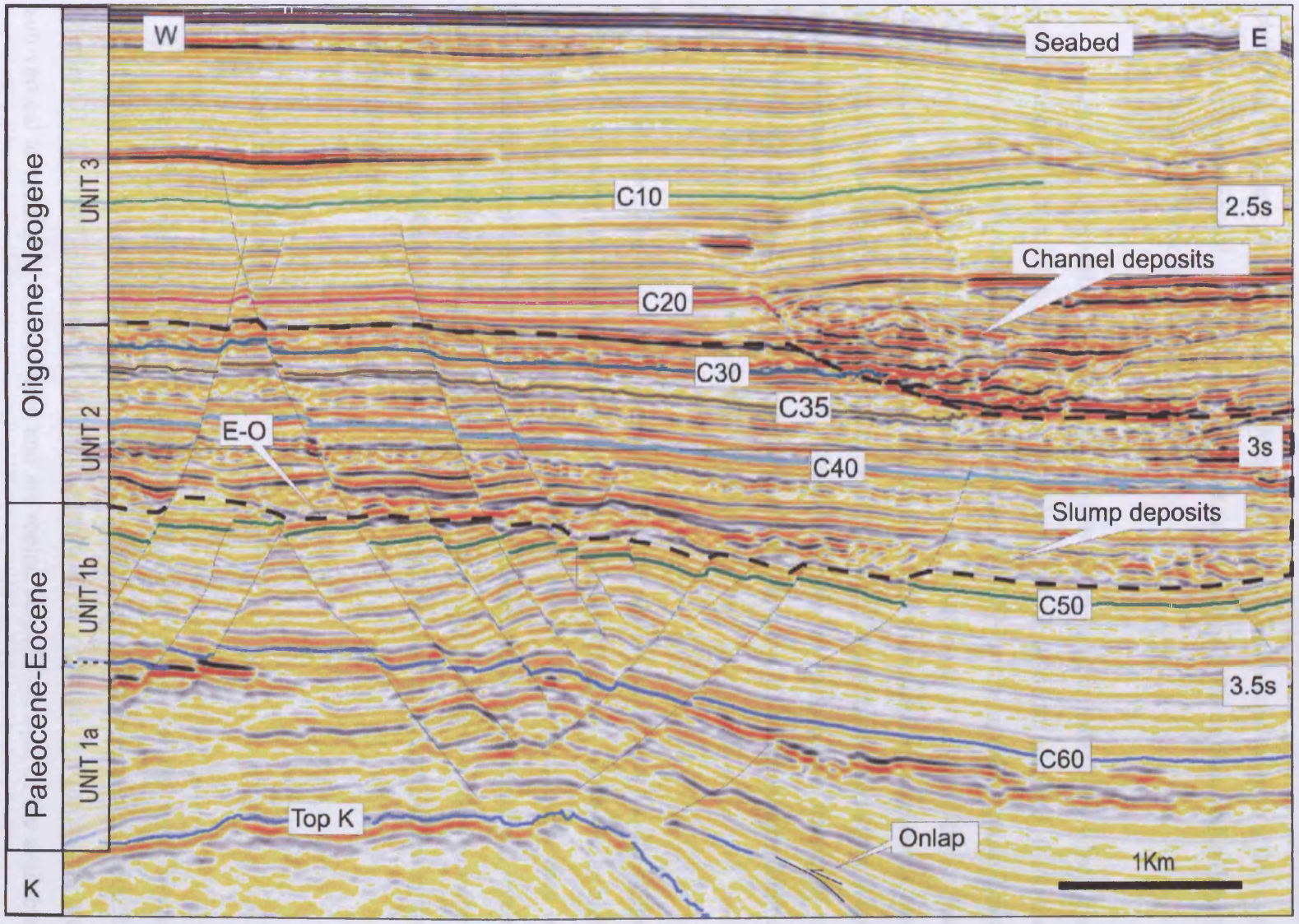

Fig. 4.3: 3D seismic section showing the main stratigraphic units above the Cretaceous (K) and key Cenozoic horizons. The erosional surface (E-O) situated at the base of Unit 2 is post middle Eocene to Oligocene in age.

top of Unit 1a and particularly on the flanks of the anticlines and within the synclines. Unit 1b is characterised by moderate amplitude and very continuous seismic reflections between Horizon C60 and the E-O boundary forming an interval with no significant change in thickness. Packages of high amplitude and discontinuous seismic reflections with an erosional basal surface are interpreted as channel complexes that eroded deeply Unit 1b and were subsequently infilled.

Unit 2 is characterised by a striking increase in seismic reflectivity which has been attributed to a high proportion of volcani-clastic material derived from the Abrolhos Plateau (Fiduk et al. 2004). The basal part of this unit is mostly expressed as a c. 100 m thick interval of chaotic seismic facies interpreted as slump deposits that directly overlie the erosional surface. The overlying strata consist of continuous and high amplitude seismic reflections characteristic of siliciclastic material of lower slope facies deposited in bathyal conditions. These sediments alternate with a few c. 50 m thick intervals of chaotic facies interpreted as slump deposits. Unit 2 does not exhibit a significant change in thickness over the whole survey.

Unit 3 overlies Unit 2 in a concordant manner and is bounded at the top by the Seabed. It consists in a package of high frequency continuous and moderate to high amplitude seismic reflections. This unit is characterised by the frequent occurrence of major channel complexes deposited in a slope position and associated to channel levees that alternate with the background stratigraphy. The overall thickness of this unit does not change significantly part from the areas being eroded and subsequently filled by the channel complexes.

4.4.3 Structural framework

The most prominent structures of the 3D seismic survey are the 9 major salt diapirs (Fig. 4.4). The diapirs are generally between 2 and 6 km in diameter although Diapirs D1, D2 and D3 coalesced to form a single larger structure. All the diapirs are sub-vertical to vertical in cross section and are rooted beneath the base of the available dataset (data are truncated at 4seconds TWT). Some diapirs have ceased movement during the Cretaceous and others have pierced through the whole Cretaceous-Cenozoic

sequence up to a few tens of metres below the present day seafloor (Fig. 4.4). The degree to which some diapirs continue their activity longer than others depends on the salt budget coming in the local source layer and the local contractional and extensional strain (Fiduk et al. 2004). Salt diapirs are weaker than the surrounding rocks and can therefore preferentially accommodate local strains (Vendeville & Jackson 1992b). Most diapirs are flanked by folded seismic reflections and are located along major anticlines of the Cretaceous intervals described below.

The folding of the Cretaceous sequence is illustrated by a time structure map of the Top Cretaceous Horizon (Fig. 4.4). Some parts the synclines are not represented as data below 4s TWT is not available for this study and mapping has not been pushed into areas where reliable interpretation of the Top Cretaceous was unviable. However, the map shows clear folding of the Top Cretaceous horizon with values comprised between 3 and 4 s TWT, respectively in blue and pink colours (Fig. 4.4). Elongated zones of shallow values surrounded by deeper values define anticlines separated by large deeper zones that are the synclines. For example, a 15 km long anticline oriented NW-SE is observable in the southwest corner of the map. This anticline is pierced by Diapir D9 in its approximate centre. Another major anticline striking NW-SE to NNW-SSE is located in the centre of the survey. This anticline is pierced by Diapir D5 at its NW lateral termination. A third major anticline trending NNE-SSW is located in the east of the structural map. This anticline trends between the grouped Diapirs D1, D2 and D3 at its NNE termination and another suspected diapir just outside of the 3D seismic survey at its SSW termination. In addition to this, circular domes surround each major diapir such as the ones visible in the close proximity of Diapirs D9, D8, D7, D5, D2 and D3. Apart from these three well defined anticlines, a number of other antiforms in the eastern or northern parts of the survey fold the Cretaceous sequence with no obvious relationship with other structures.

The fault network mapped on Horizon C50 has been superimposed on the map of the top Cretaceous horizon. This enabled the geometry and distribution of the faults in the upper part of Unit 1 to be related to the folding pattern of the Cretaceous strata and the salt diapirs.

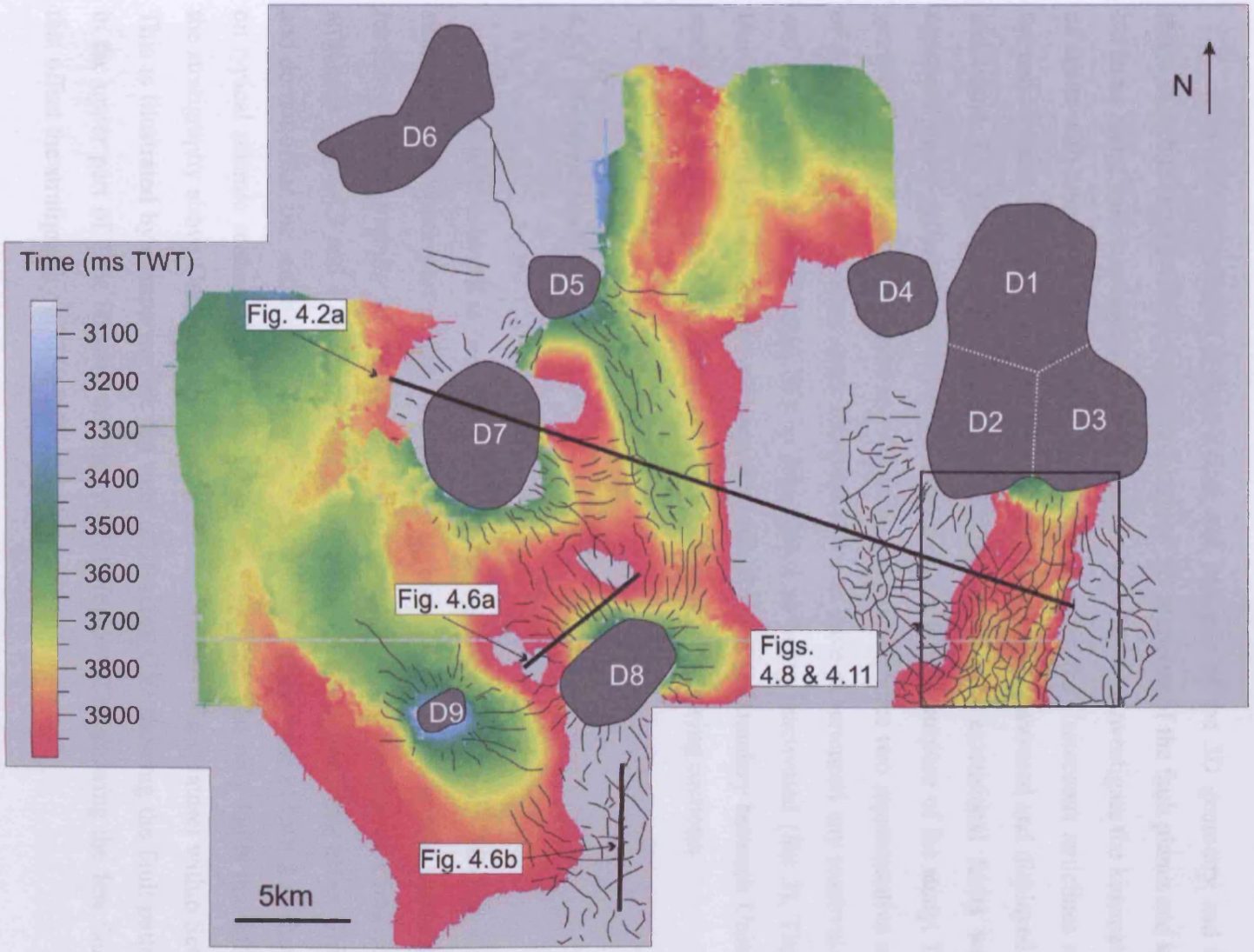

Fig. 4.4: Structural map of the Top Cretaceous Horizon in ms TWT from the 3D seismic survey. Dark grey rounded structures are the salt diapirs (D) piercing through the Cenozoic sequence. The fault network mapped on Horizon C50 is superimposed on the Top Cretaceous map.

4.5 Structural analysis

This section presents a description and analysis of the 3D geometry and the throw distribution of faults in the BES-2 survey. 3D mapping of the fault planes and key horizons along with displacement reconstruction were used to investigate the kinematics of faults with respect to the different stratigraphic units, the Cretaceous anticlines and the salt tectonic evolution. Vertical throw distributions were measured and displayed as individual T-z plots for 57 faults over the survey. These extensional faults were separated into 3 different sets based on their location for the purpose of the study. The general fault network is analysed in two parts; the first includes two representative sets of faults (Sets 1 and 2) from areas interpreted not to have experienced any reactivation and the second, a set of faults that is interpreted as being reactivated (Set 3). Those faults that can be seen to have propagated through the E-O boundary between Units 1 and 2 are interpreted as reactivated faults, as discussed in following sections.

4.5.1 General fault network

The fault network is best illustrated on the dip map of Horizon C50 (Fig. 4.5a) situated in the upper part of Unit 1b (Fig. 4.3). Most of the faults in this dataset are localised in the vicinity of the recent salt diapirs and/or on the top of Cretaceous anticlines (Figs. 4.3 and 4.4). Furthermore, most faults in this dataset only offset Unit 1 and do not offset the sediments above the E-O boundary at the base of Unit 2 as shown on typical seismic sections through Sets 1 and 2 (Fig. 4.6). The only faults that offset the stratigraphy above Unit 1b are located in the eastern part of the dataset within Set 3. This is illustrated by comparing the dip map of Horizon C50 showing the fault pattern in the upper part of Unit 1b with the dip map of Horizon C35 showing the few faults that offset the stratigraphy in Unit 2 (Fig. 4.5b).

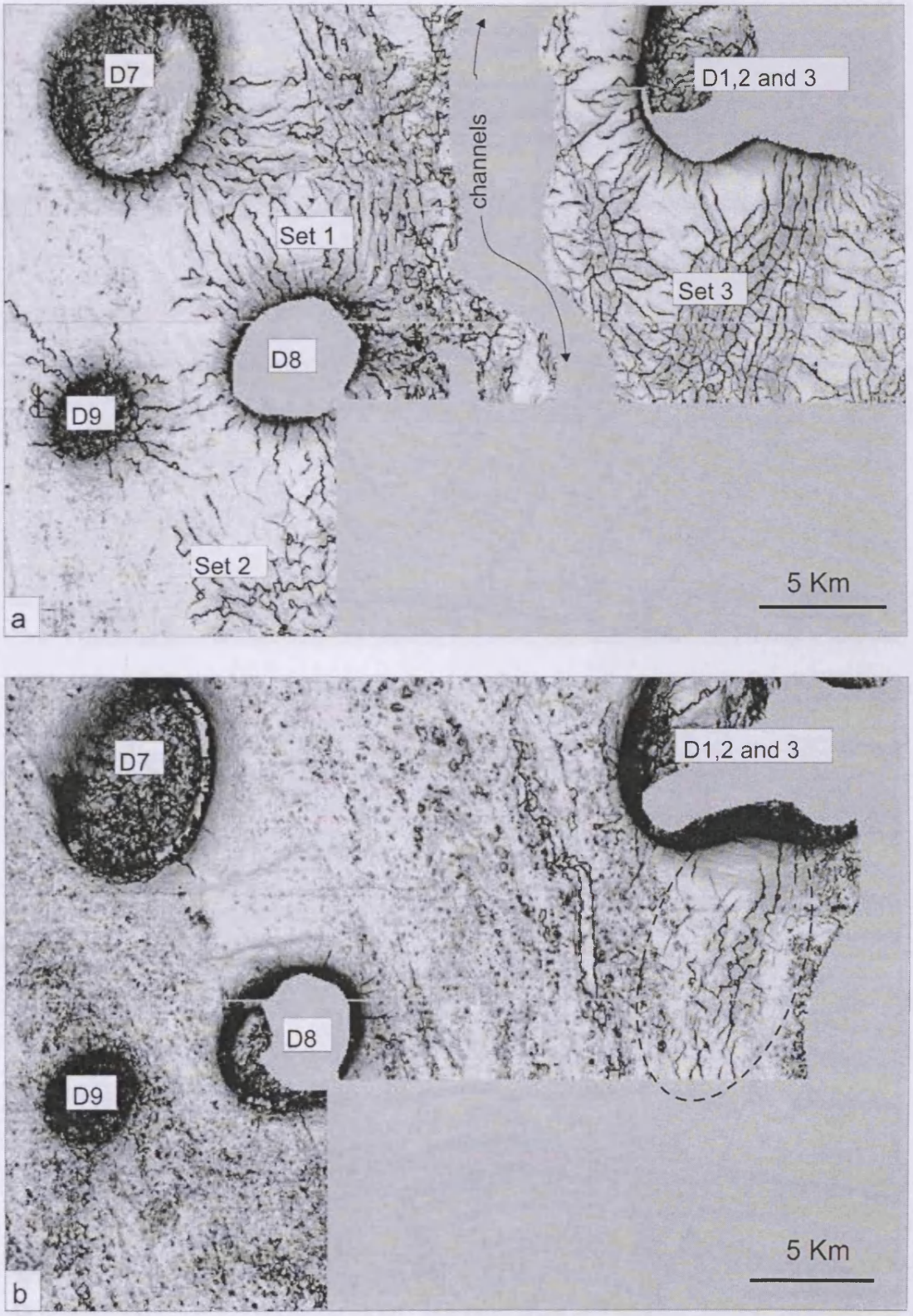

Fig. 4.5: (a) Dip map of Horizon C50 showing the fault pattern in the upper part of Unit 1b beneath the E-O boundary. The faults were grouped into 3 distinct sets for the purpose of the study. Radial faults are organised around salt diapirs (SD) and overlie the Mesozoic anticlines. (b) Dip map of Horizon C35 showing that only a few faults (highlighted by the dashed circle) offset Unit 2 above the E-O boundary.

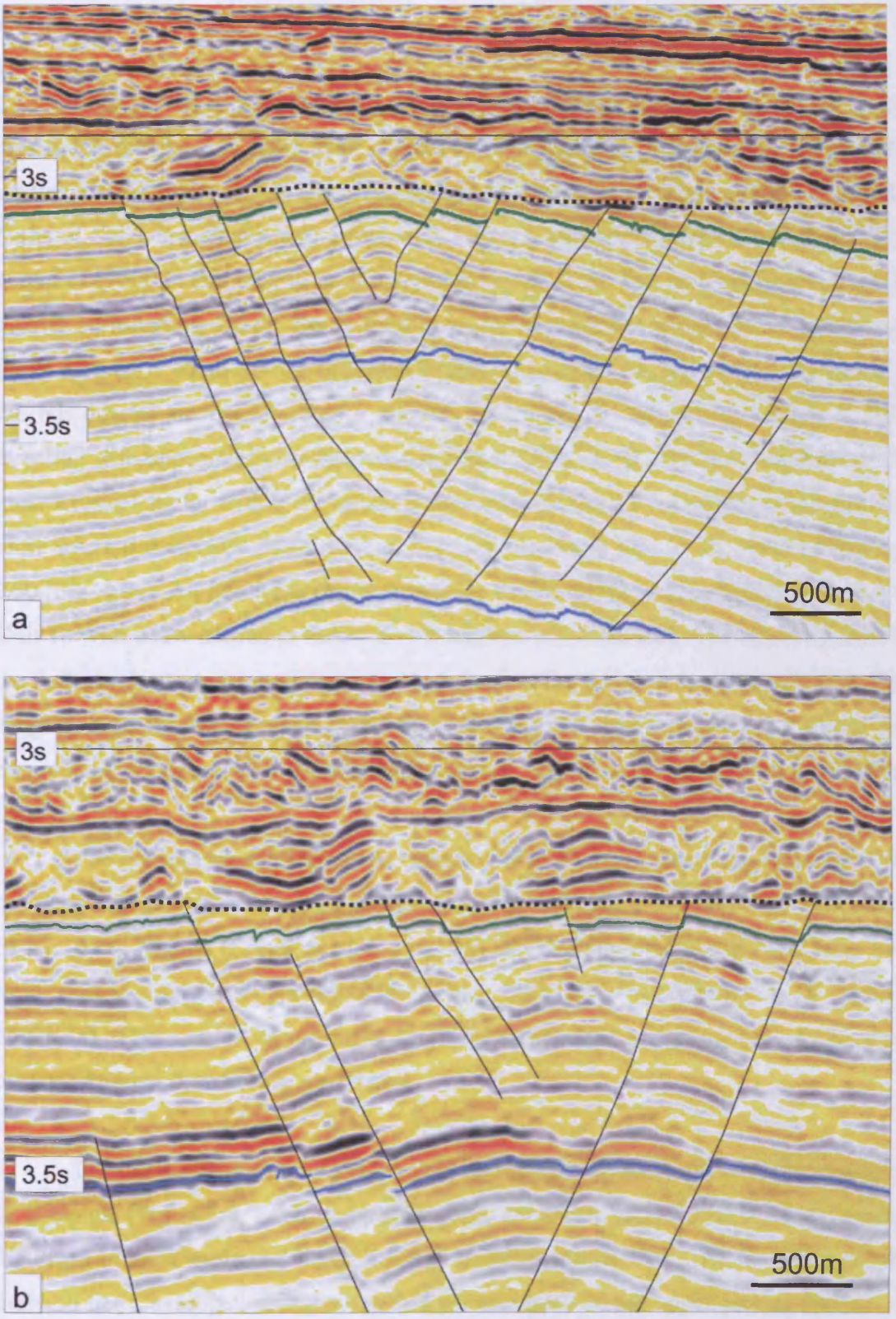

Fig. 4.6: Representative 3D seismic sections showing that the faults offset Unit 1 and tip out at the E-O erosional basal surface (dashed lines) of the slump deposit at the base of Unit 2. (a) Seismic section through faults of Set 1. (b) Seismic section through faults in Set 2.

4.5.1.1 Set 1

The faults that compose Set 1 are the northern faults organised around Diapir D8 in a radial manner and have been chosen as a representative example of radial faults located around major salt diapirs such as D5, D7, D8 and D9 (Figs. 4.4 and 4.5a). The faults of Set 1 are extensional faults with a length ranging between 1 and 3 km for a height of c. 500 m and maximum throw values up to 40 m. The fault network in the NW quarter surrounding Diapir D8 is a complex graben system composed of extensional faults dipping c. 52 to 58 ° in opposite directions towards the NE or the SW. Faults in the NE quarter are organised in a similar graben system striking in a NNE to ENE direction with opposing faults dipping towards the NW or SE. The lower tip lines of the most external faults within the grabens terminate at the Top Cretaceous horizon and more internal conjugate faults terminate c. 200 m above this, at the level of Horizon C60 (Fig. 4.6a). All faults are characterised by an abrupt upper termination at the top of Unit 1b with a few metres of throw on the highest offset horizon. The upper tip lines of the faults in Set 1 are located at the level of the E-O boundary at the base of Unit 2. This suggests that the stratigraphic interval containing the upper tips of the faults was removed by erosion and Unit 2 was subsequently deposited on the erosionally modified Unit 1b.

The grabens are interpreted as typical crestal collapse structures of the type that has been recognised in various geological settings such as in the Gulf of Mexico (e.g. Bruce 1973), Nigeria (Cohen & McClay 1996) and Angola (Duval et al. 1992) and have been studied from analogue modelling (e.g. McClay 1990, Vendeville & Jackson 1992b, a). These faults are thought to result from outer arc stretching of the strata overlying domal or anticlinal structures.

The throw distribution on these faults is illustrated with representative examples of T-z plots (Fig. 4.7a). Each graph represents the throw across a fault plotted against the depth of each measured offset horizon in milliseconds TWT. All T-z plots for the faults in Set 1 exhibit throw profiles that are truncated in the upper part as opposed to typical positive throw gradients decreasing smoothly to zero at the upper tip. The profiles illustrate that faults upper tips terminate c. 50 to 100 m above Horizon C50 with c. 5 to 20 ms TWT throw values. The lower parts of the T-z plots are characterised by throw values decreasing to zero at the lower tip point located in the close proximity of

the Top Cretaceous horizon (c. 100 m) with gradients between c. 0.16 and 0.28. The vertical throw profiles for different faults of Set 1 exhibit various shapes between a typical M-type (Muraoka & Kamata 1983) such as T-z plot 1 (Fig. 4.7a) and a skewed M-type (Baudon & Cartwright in review) such as T-z plot 4 with maximum throw values located between 3200 and 3700 ms TWT.

4.5.1.2 Set 2

Set 2 is characterised by a more multidirectional fault network than Set 1 (Fig. 4.5a). However, dominant faults with higher displacement values are organised in a symmetrical crestal collapse graben system in a similar way to that observed in Set 1. The graben is composed of conjugate extensional faults generally striking NNW to NE and dipping c. 50 to 60 ° towards the east or towards the west (Fig. 4.6b). The graben is located at the top of an anticline deforming the Cretaceous interval with a fold axis striking in a NW direction towards Diapir D9.

Vertical throw distribution plots constructed for the faults of Set 2 (Fig. 4.7b) exhibit striking similarity with those obtained for Set 1. The truncated upper part of all T-z plots illustrates that the upper tip lines of the faults, located at the boundary between Unit 1b and Unit 2, are characterised by throw values from c. 5 to 17 m. The lower tip geometry of the faults in Set 2 depends on whether the fault detaches on the flanks of the anticline or dies out without detachment. Faults that detach generally exhibit higher throw values than the faults that do not detach. Detaching faults are characterised by zones of maximum throw values that are located within Unit 1a, between the detaching lower tip and Horizon C60, such as T-z plots 13, 14, 15 and 16 (Fig. 4.7b). These T-z profiles can be described in two distinct parts: an upper part characterised by throw gradients tending to zero and a lower part exhibiting a C-type or M-type vertical throw distribution. The T-z plots obtained for faults that do not detach are characterised by single asymmetrical C-type or M-type profiles with maximum throw values generally located within Unit 1b between Horizon C60 and the erosional surface (T-z plots 10, 11 and 12 in Fig. 4.7b). The faults only offset Unit 1 and are truncated by the erosional surface at the base of the slump interval in the lower part of Unit 2.

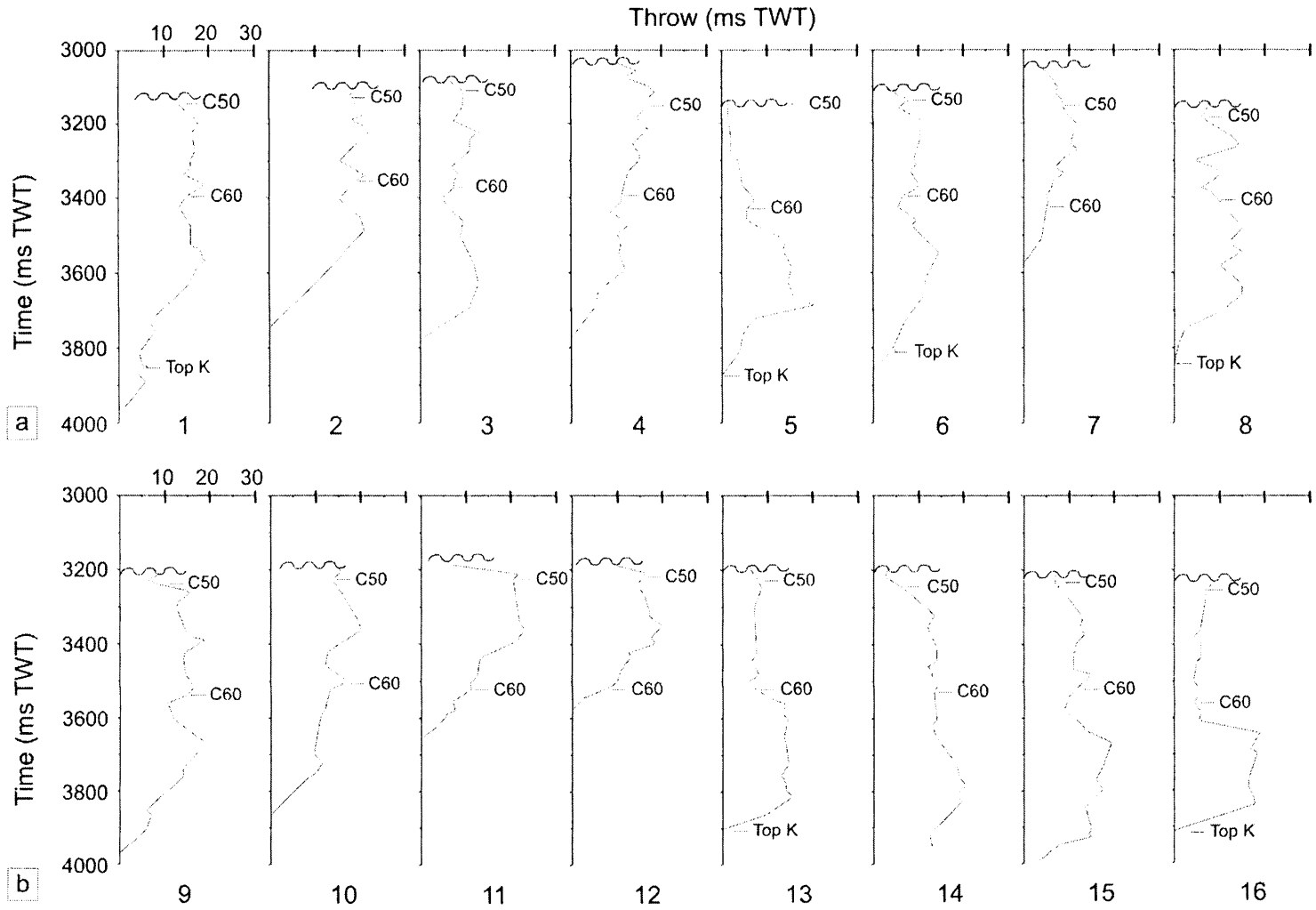

Fig. 4.7: (a) Vertical throw distribution plots for 8 representative faults in Set1. Each T-z plot exhibits the throw values up to 60 ms TWT plotted against the time. Undulating lines indicate the E-O boundary characterised by an erosional surface at the base of the slump deposit situated at the base of Unit 2. (b) T-z plots obtained for 8 faults located in Set 2.

4.5.2 Set 3: Case study of a semi-elliptical dome

The faults in Set 3 are presented in more detail than those in Sets 1 and 2 because they are partially reactivated and are therefore the main focus of this study. Set 3 faults are found in a c. 12 km^2 faulted area. The fault array is characterised by a highly segmented pattern (Fig. 4.8). Segment lengths vary from 100 to 1000 m with heights comprised between 200 and 1400 m for maximum throw values ranging from c. 10 m to 100 m. The faults are planar to slightly concave upward in cross section and the dip ranges from 48 to 59 ° assuming a velocity of 1800 m s^{-1}. The main characteristic of Set 3 is that 43 % of the faults terminate upwards at the top of Unit 1b, whilst 57 % tip out within Units 2 and 3 and are interpreted as reactivated.

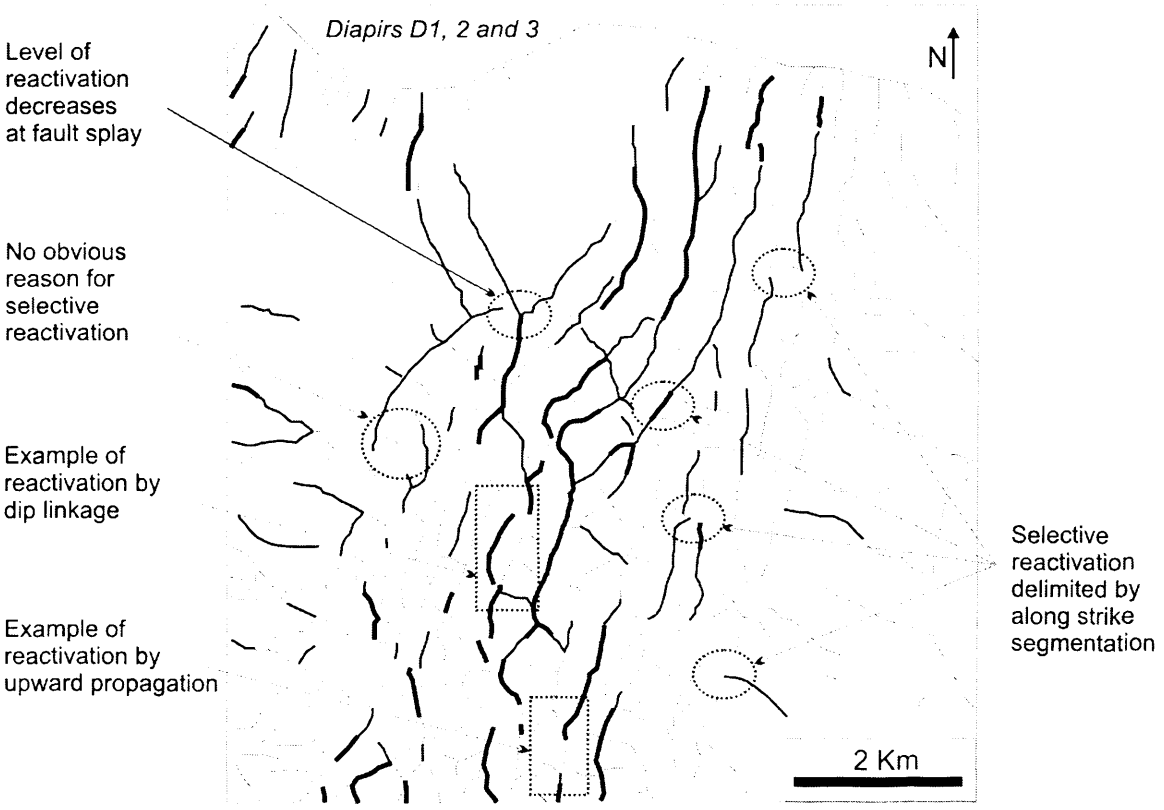

Fig. 4.8: Fault pattern in Set 3 based on the dip map of Horizon C50 situated in the upper part of Unit 1b. The figure shows non- reactivated faults (in thin lines) and reactivated fault segments terminating in Unit 2 (in medium lines) or Unit 3 (in thick lines). Doted rectangles indicate the location of the examples of reactivation by upward propagation developed in Figure 14 and reactivation by dip linkage analysed in Figure 15. Typical selective reactivation examples are highlighted with doted circles.

Rose diagrams were constructed for the faults located in Set 3 in order to illustrate and quantify the strike of the faults (Fig. 4.9). The fault network was divided into straight segments allowing the measurements to be taken with an estimated maximum error of 2 °. The rose plot displaying the strike of all faults is characterised by two different populations striking at c. 110 ° (Fig. 4.9a). The faults located on the crest of the anticline are characterised by strike directions comprised between N and N050 ° with a mean value at N015 °, which is very close to the direction of the axis of the anticline (N018 °). The reactivated fault segments mainly strike between N and N50 ° (Fig. 4.9b). Of the reactivated faults, 37 % have upper tip lines situated within Unit 2 (Fig. 4.9c) and 20 % within Unit 3 (Fig. 4.9d), offsetting most of the Cenozoic megasequence as they do so. Very few of the fault segments that terminate in Unit 2, and only one terminating in Unit 3, strike in a direction away from the main fault set (N to N050 °). The lower tip geometry seems to be linked to the orientation of the fault segments and therefore may control whether they are reactivated or not. Fault segments terminating within Unit 3 generally tip out at the top of the anticline and frequently detach on the limbs of the anticline.

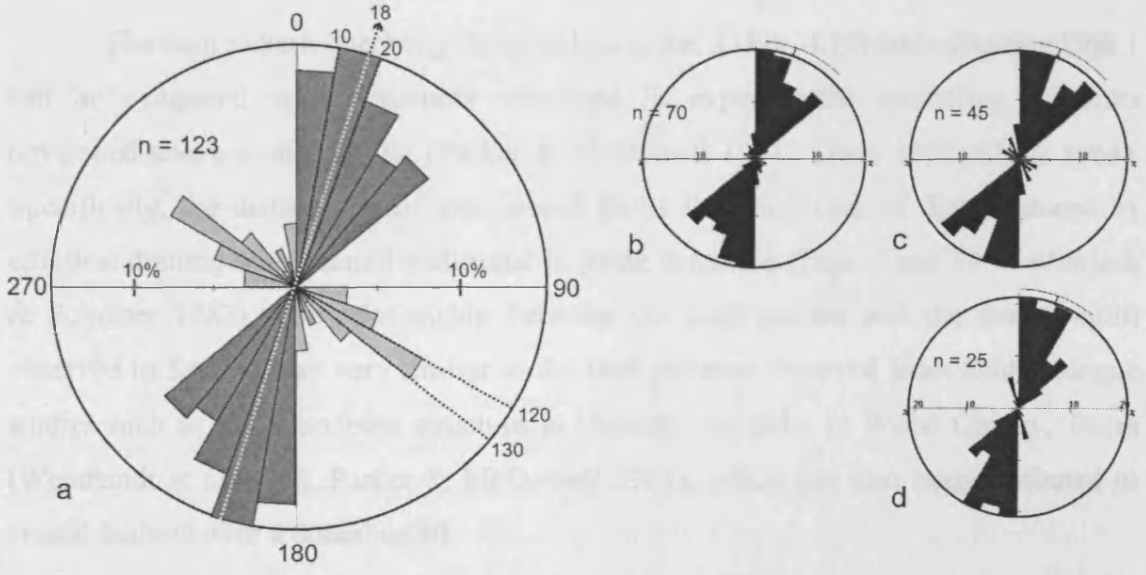

Fig. 4.9: Rose diagrams for faults of Set 3. The fault network was divided into small straight segments. Vertical and horizontal axes show percentage of fault segments (based on total fault length). n indicates the number of fault segments measured (a) Rose plot representing the strike of all faults in Set 3. White dashed line indicates the strike of the axial plane of the anticline. (b) Rose plot for reactivated faults terminating in Units 2 and 3. (c) Reactivated faults terminating in Unit 2 only. (d) Reactivated faults terminating in Unit 3 only.

4.5.2.1 Fault network in Unit 1

In seismic cross section, the faults within Unit 1 form a complex graben system that tips out downwards on the crest of the anticline (Fig. 4.10). This graben can be further described as a buried and superposed crestal collapse graben (McClay 1990, Crook et al. 2006). The symmetrical graben is bounded by large extensional faults that are slightly concave upward. The internal deformation is accommodated by arrays of domino faults. Dimensions and values of maximum displacement on the faults generally decrease towards the centre of the graben system. This suggests that the faults nucleated progressively towards the centre of the crestal graben as has been described elsewhere for this type of structure (McClay 1990). The major Cretaceous anticline beneath the buried graben is situated in the SE corner of the BES-2 survey (Fig. 4.4). The axial plane strikes in a NE-SW direction and plunges c. 2.3 ° towards the NE. The SW lateral termination of the anticline is situated outside the 3D seismic survey. It is interpreted as a semi-elliptical dome trending NE in the direction of Diapirs D1, D2 and D3.

The fault pattern overlying the anticline in Set 3 (Fig. 4.10) and offsetting Unit 1 can be compared with structures described in experimental modelling of faults developed above domal uplifts (Parker & McDowell 1951, Cloos 1955, Cloos 1968). Specifically, the distribution of extensional faults is reminiscent of that produced by elliptical doming with a small additional in plane extension.(Figs. 9 and 10 in Withjack & Scheiner 1982). The relationship between the fault pattern and the domal uplift observed in Set 3 is also very similar to the fault patterns observed from field analogue studies such as the Woodbine structure at Hawkins oil field, in Wood County, Texas (Wendlandt et al. 1946, Parker & McDowell 1951), which has also been attributed to crestal faulting over a domal uplift .

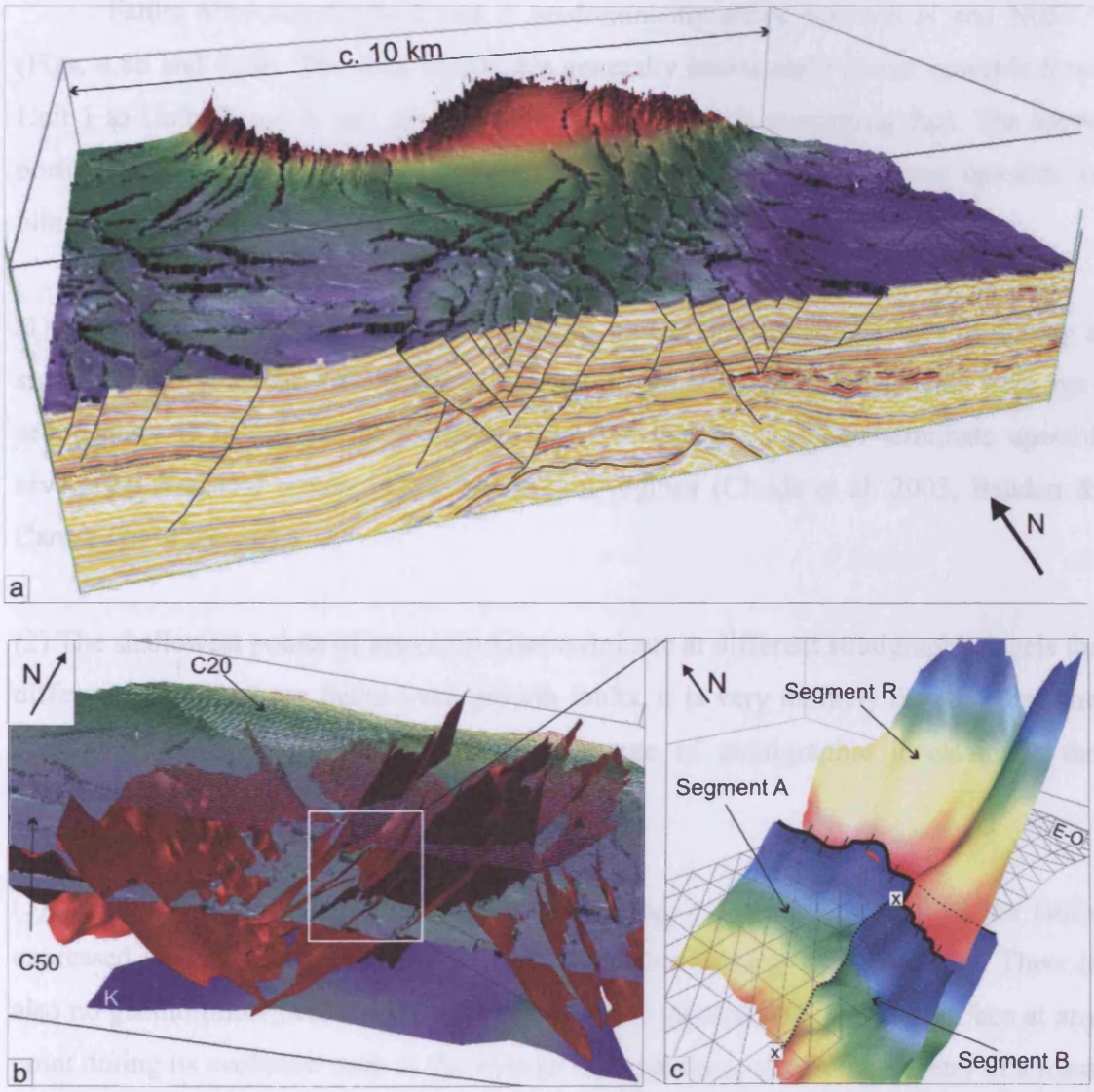

Fig. 4.10: Geoviz visualisations showing the faults located in Set 3 with key surfaces. (a) 3D block diagram showing the faults in seismic section with a map of Horizon C50. (b) 3D visualisation of the fault planes (in red colour) organised in a complex crestal collapse graben tipping out downwards at the Top Cretaceous Horizon (K). Key surfaces are Horizon C50 situated at the top of Unit 1b and Horizon C20 at the base of Unit 3. (c) Close-up on an example of reactivation by linkage. Segment B intersects Segment A through a vertical branch line (x-x'). Segment R initiated individually above the Eocene-Oligocene boundary (E-O) and propagated downward to hard link with Segment A towards the NE and switches to link with Segment B towards the SW.

4.5.2.2 Fault network in Units 2 and 3

Faults offsetting Units 2 and 3 predominantly strike between N and N050 ° (Figs. 4.8b and 4.9b). The fault planes are generally increasingly planar upwards from Unit 1 to Units 2 and 3, and are characterised by upwards steepening dips. The upper portions of the reactivated fault planes are interpreted to have propagated upwards as blind faults. This important interpretation is based on several critical observations:

(1) The upper tip lines of individual segments plunge towards the lateral tips cutting a significant portion of the stratigraphy as they do so. If these fault segments were syn-sedimentary it would be very unlikely that the lateral tip region terminate upward several hundreds of metres below the central regions (Childs et al. 2003, Baudon & Cartwright in review).

(2) The shallowest points of upper tip lines terminate at different stratigraphic levels for different faults. If these faults were growth faults, it is very unlikely that they became inactive at different times and at such a range of stratigraphic levels given the distribution and close spacing of faults in the array.

(3) There is no observable stratigraphic thickening in the hanging wall of the faults expressed as divergent package of seismic reflections towards the fault plane. There is also no geomorphological evidence that the fault interacted with the free surface at any point during its evolution such as the change in orientation, size and geometry of a mass transport complex or channel across the fault plane.

(4) The faults are characterised by upper tip folding in a monocline style as expected ahead of propagating blind faults (e.g. Gawthorpe et al. 1997, Hardy & McClay 1999, Withjack & Callaway 2000).

In addition to these observations, the characteristics of throw distribution on these upper portions of reactivated faults are typical for the range of blind fault upper tip gradients (see Section 4.7).

4.6 Timing of salt movement and Cretaceous anticlines

Salt deformation started in the Albian in the Espirito Santo Basin and is thought to be still active in recent time (Cobbold et al. 2001, Fiduk et al. 2004). It is very difficult to establish a more detailed reconstruction of the timing of salt deformation because of the lack of data beneath 4 s TWT in the dataset available for this study. However, it is possible to constrain the end of deformation for certain Cretaceous structures that are linked to the movement of the salt. The Cretaceous interval at the basal part of the dataset form anticlines that generally trend towards the major salt diapirs. Set 3 is taken as an example to reconstruct the timing of Cretaceous anticlines with respect to the stratigraphy.

An analysis of the relationship between Cretaceous anticlines beneath the different sets of faults and relative growth in the stratigraphic units above allows the deformation to be constrained to Early Cenozoic age. Firstly, Unit 1a overlies the top Cretaceous in a discordant manner. This is illustrated by stratigraphic onlaps observable in the seismic interval between the base of Unit 1 and Horizon C60 (Fig. 4.3). Secondly, the same interval in characterised by a significant convergent stratal thinning towards the anticline axis (Fig. 4.3) which is also evident on the isochron map (Fig. 4.11b). The isochron map of the stratigraphic interval comprised between Horizon C60 and the top of Unit 1b is, in contrast, characterised by no significant change in thickness (Fig. 4.11a). Moreover, no seismic interval above exhibits significant changes in stratigraphic thickness (Fig. 4.3). This suggests that most of the thickening due to the rising of that anticline occurred between the Early Paleogene and Horizon C60. The formation of the anticlines delimited upward by the Cretaceous/Cenozoic boundary is therefore mainly attributed to Early Cenozoic uplift. This uplift is interpreted to have resulted from salt movements at depth. It is very difficult to evaluate whether the extent of Early Cenozoic deformation is regional or merely specific to the survey area. However, it affects all visible anticlines of this dataset in a similar way.

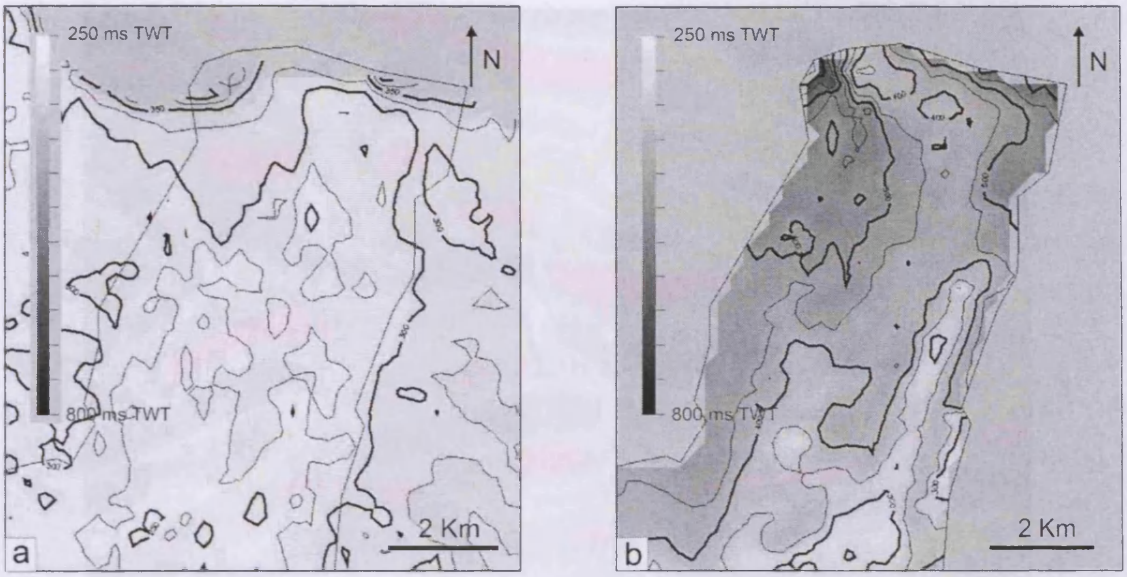

Fig. 4.11: (a) Isochron map between Horizons C50 and C60 showing very small thickening away from the Cretaceaous anticline axis (K axis). (b) Isochron map between Horizons C60 and top Cretaceous showing significant thickening away from the Cretaceous anticline axis. Thick contours spacing is 100ms TWT for both maps.

4.7 Timing of faulting

This section investigates the timing of faulting in Set 3 in further detail and the kinematic evidence for reactivation. The kinematics of fault segments within Unit 1, the characteristics of the basal surface of Unit 2 and the criteria to interpret faults offsetting Units 2 and 3 as reactivated are investigated. The kinematics of faulting are summarised and illustrated in a schematic model of evolution in 3 steps for the crestal graben in Set 3.

4.7.1 Seismic description and stratigraphic evidence for fault activity

Fault segments offsetting the upper part of Unit 1b clearly exhibit evidence of syn-sedimentary movement. Growth packages in hanging wall intervals are seen in close proximity of the fault planes in the upper part of the sequence (Fig. 4.12a). The faults are therefore interpreted as being active at the free surface during deposition of the sediments that compose the upper part of Unit 1b. However, it is particularly

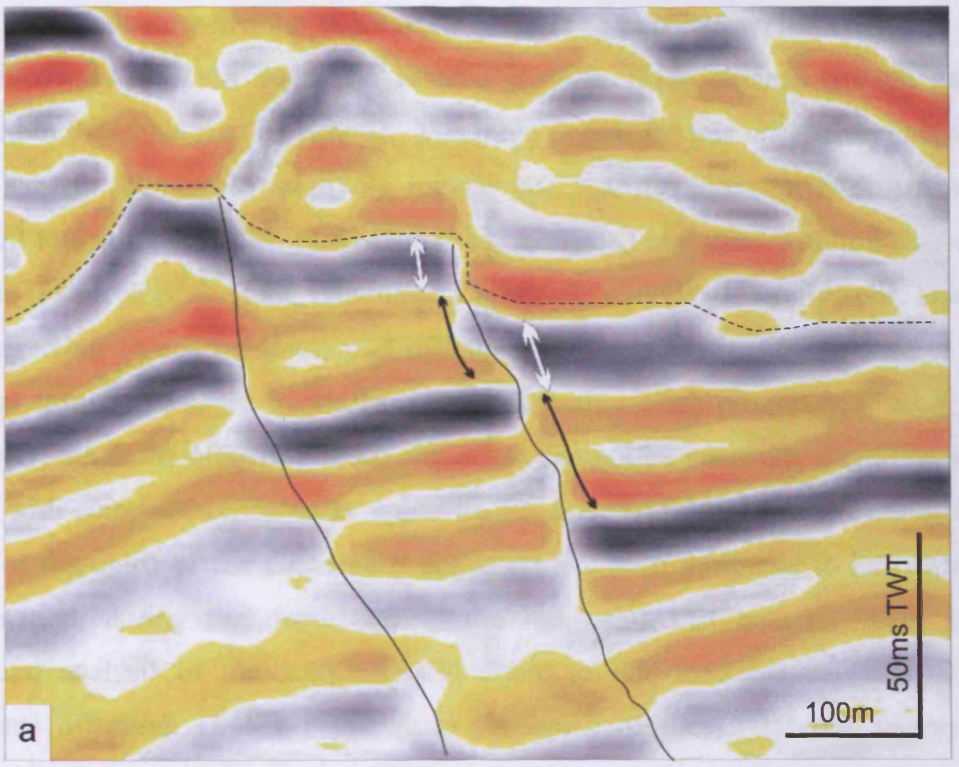

Fig. 4.12: (a) Seismic sections showing growth packages (shown by the arrows) situated at the top of Unit 1. (b) Seismic section showing erosional truncation surface (in dashed line) at the base of the slump interval.

difficult to evaluate when the exact onset of faulting occurred within Unit 1 as well as the kinematics of fault segments located beneath these obvious growth packages situated in the upper part of Unit 1b. The main reason for this uncertainty is that some small growth faults with relatively regular and low displacement rates can be very difficult to distinguish from blind faults that nucleated and grew within the subsurface domain (Petersen et al. 1992, Baudon & Cartwright in review). Stratigraphic layers that comprise Unit 1a and the lower part of Unit 1b are characterised by an absence of any obvious growth packages in the hanging wall within close proximity of fault planes. However, the faults offsetting these sequences can not be positively identified as blind faults with complete certitude as upper tip lines are truncated by the base of Unit 2. Most of the uplift of the Cretaceous sequence has been attributed to Early Cenozoic deformation, during the deposition of the sediments that comprise Unit 1a. The structural analysis of the semi-elliptical dome located in Set 3 suggests that fault segments offsetting Unit 1 result from the uplift of the Cretaceous interval. This constrains the onset of faulting within Unit 1 between Early Cenozoic (formation of major anticlines) and the Late Eocene (time of deposition of the upper part of Unit 1b).

In summary, faults located in Unit 1 were created during a phase of deformation that occurred between the Early Cenozoic and the Late Eocene. Regardless of the early kinematic evolution (growth faults or blind faults), these faults were active at the free surface in the Late Eocene. The period of deformation creating these faults is called phase 1of faulting for the purpose of the study (Fig. 4.13a).

The boundary between Units 1 and 2 is essential for the understanding of the evolution of this area. It consists, in most of the faulted areas of the survey, at the base of an interval of chaotic seismic facies that has been interpreted as slump deposits deposited at the basal part of Unit 2. The base of the slump interval is expressed as an erosional truncation surface characterised by stratigraphic toplap with respect to the seismic reflections beneath (Fig. 4.12c). The underlying strata are eroded over most of the survey and the upper tip lines of faults located in Unit 1 are truncated as a result of this erosion (Fig. 4.13b).

Portions of faults offsetting the stratigraphic Units 2 and 3 exhibit major differences to the ones observed in Unit 1. These are interpreted as being characteristic of blind propagation and expressed as such herein. All these criteria strongly suggest

that the faults grew by blind propagation through Units 2 and 3. As a result of this, sediments that comprise Unit 2 and most of Unit 3 were deposited before the second period of deformation called phase 2 of faulting (Fig. 4.13c).

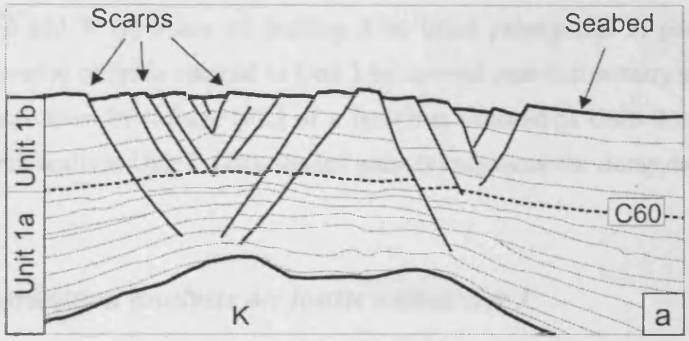

Faulting phase 1

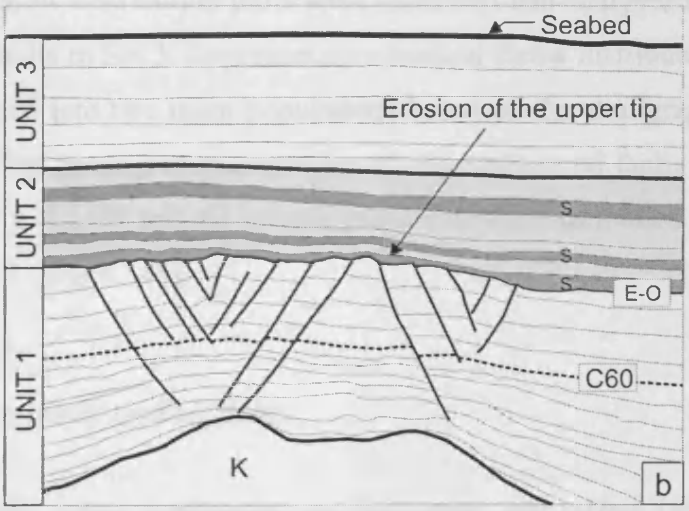

Period of quiescence

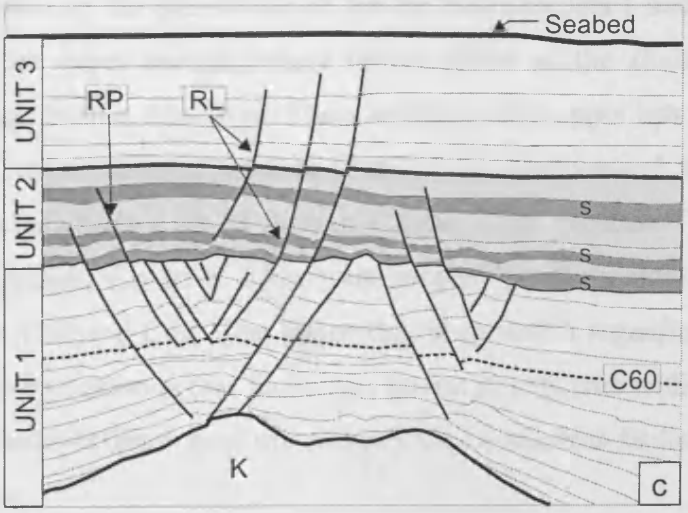

Faulting phase 2 (reactivation)

Fig. 4.13: A 3 steps evolutionary model for the crestal graben faults. (a) 1st phase of faulting occurred between the early Cenozoic (time of formation of major anticlines) and the late Eocene (time of deposition of the sediments in the upper part of Unit 1b). Most of the uplift of the Cretaceous sequence (K) was contemporaneous with the deposition of sediments that compose Unit 1a. The faults offsetting Unit 1 were active at the deposition of the upper part of Unit 1b. (b) Period of quiescence during deposition of Units 2 and 3. (c) Phase of faulting 2 by blind propagation of post-sedimentary faults resulting in the reactivation of faults situated in Unit 1 by upward post-sedimentary propagation (RP) into Units 2 and 3 or reactivation by linkage (RL) of a fault that initiated in Units 2 and 3 and propagated downwards to link with faults in Unit 1. Dark shaded areas (s) represent the slump deposit intervals.

4.7.2 Throw distribution analysis on faults within Set 3

Vertical throw distribution plots were measured and analysed in different places for 12 different faults in Set 3. Representative vertical throw distribution plots for these faults were grouped into two main populations based on the stratigraphic extent of the fault plane. The first group includes profiles of non-reactivated faults that tip out at the base of Unit 2 (Fig. 4.14a) and the second group contains reactivated faults terminating within Units 2 or 3 (Fig. 4.14b).

4.7.2.1 Non-reactivated eroded faults

The vertical throw distribution on faults that only offset Unit 1 exhibit very similar characteristics to the ones obtained for the faults in Sets 1 and 2. The T-z plots are truncated in the upper portion where throw values of the shallower measurable offset horizon range from c. 5 to 20 m. These correspond to upper tips of fault segments eroded by the slump on seismic sections (Fig. 4.12c). The vertical throw distribution plots are mostly characterised by M-type or C-type throw profiles. The intervals with maximum throw values (up to c. 25 m) are located predominantly within Unit 1b, between Horizons C50 and C60. One interesting observation regarding the location of the maximum throw position is that faults that tip out downwards without linking into a clear detachment exhibit throw maxima within Unit 1b whereas faults that detach have maxima in Unit 1a.

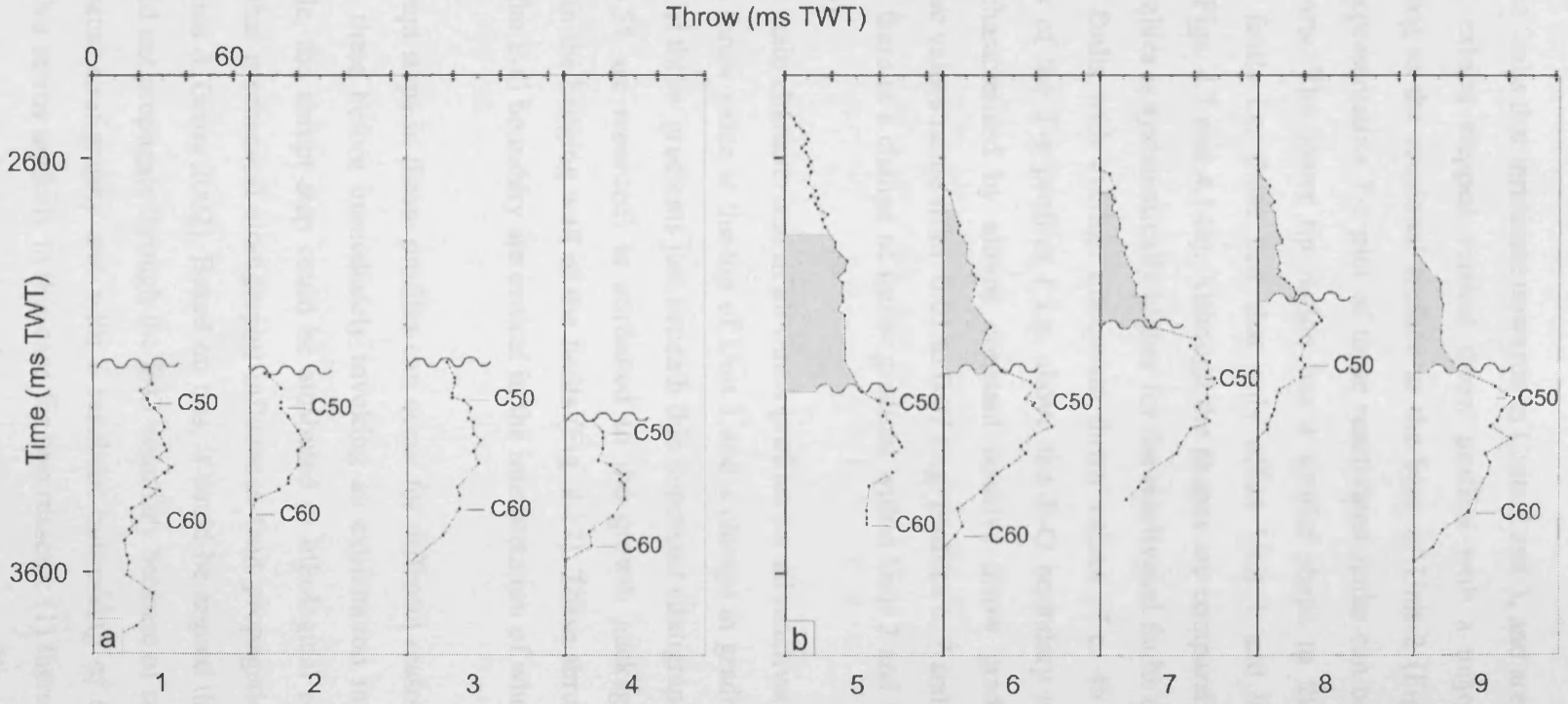

Fig. 4.14: Vertical throw distribution plots (T-z plots) obtained for the faults in Set 3. Each T-z plot represents the throw values plotted against the time in ms TWT. (a) Faults that are not reactivated and are eroded by the E-O surface are characterised by truncated throw profiles. (b) T-z plots for reactivated faults. C50 and C60 are key horizons, the wavy line indicates the location of E-O erosional surface and Unit 2 is represented by the shaded area.

4.7.2.2 Reactivated faults

Most faults that terminate upwards in Units 2 and 3, and are hence interpreted as reactivated, exhibit stepped vertical throw profiles with a major break in gradient corresponding to the erosional surface at the base of Unit 2 (Figs. 4.14b, 4.15c and 4.16c). A representative T-z plot of these reactivated faults can be typically separated into two parts. The lower tip region has a similar shape to the T-z plot for non-reactivated faults i.e. those that that only offset Unit 1 and have not propagated upsection (Figs. 4.7 and 4.14a). Although the shapes are comparable, the magnitude of the throw values is systematically higher for the reactivated faults compared to the non-reactivated faults with average maximum throw values of c. 45 m. The central and upper parts of the T-z profiles (i.e. above the E-O boundary to the upper tip) are generally characterised by almost constant positive throw gradients per individual faults, whose values range from 0.01 to 0.07 (e.g. profiles 6, 7 and 8 in Fig. 4.14). Less commonly, there is a change of throw gradient within Unit 2 and Unit 3 (e.g. profile 5 in Fig. 4.14).

The main characteristic of all throw profiles for all reactivated faults is an abrupt decrease in throw value at the top of Unit 1 and a change in gradient at this boundary. Steepening of throw gradients just beneath this important stratigraphic boundary (values up to c. 0.55 are recorded) is attributed to the growth packages and stratigraphic thickening in the hanging wall of the faults (Fig. 4.12). These abrupt steps in the throw profiles at the E-O boundary are critical in the interpretation of whether a fault has been reactivated.

Abrupt steps in throw profiles can occur for different reasons, so it is important to consider these before immediately invoking an explanation involving reactivation. For example, the abrupt step could be attributed to lithological effects as it has been suggested that mechanical stratigraphy influences fault propagation (e.g. Gross et al. 1997, Wilkins & Gross 2002). Based on this, it could be argued that most of the faults in Unit 1 did not propagate through the E-O boundary because of some major change in the mechanical stratigraphy and with a resultant buttressing of upward propagation. However, this seems unlikely in this case for two reasons: (1) there is no evidence from the acoustic character (acoustic impedance contrasts are small) of the sediments that there is a major change in the mechanical properties at this boundary, and (2) growth packages at the remnant upper tip regions of faults that die out at this boundary (Fig.

4.12c) indicate that the majority of these faults were active before erosion by the slump interval and deposition of Units 2 and 3. These faults cannot therefore be treated as exclusively blind faults as is required for a purely lithological explanation of the stepped profile.

To summarise, the reactivation process is particularly recognisable from vertical throw distribution profiles. These are characterised by an abrupt change in throw values and gradients in the part of the plot that corresponds to the zone of onset of reactivation (Figs. 4.14c and 4.16c).

4.7.2.3 Modes of reactivation

Two distinct modes of reactivation have been recognised from a combination of 3D fault plane mapping and throw analysis. These two modes are referred to here as (1) 'upward propagation', where reactivation is by dominantly upward propagation of selected segments of existing faults, and (2) reactivation by dip linkage, where a new fault nucleates in the cover sediments above a pre-existing fault (the parent fault) and then a combination of upward propagation of the parent fault and downward propagation of the new fault result in a dip linkage between the two to form a reactivated and enlarged structure.

The vast majority of the reactivated faults in the study area (Set 3) grew by upward propagation (Fig. 4.15a). For each of these faults, there is a seamless extension of the reactivated portion of the fault from the parent fault. There is no evidence of any linkage zones, or any significant geometrical features in the fault surface such as steps or jogs on these reactivated faults.

A representative example of the upward propagation mode is presented in Figures 4.8 and 4.15. Specific portions of the parent fault surface were selected for reactivation, and others not (Fig. 4.8). The central region of the parent fault in this case was not reactivated. This central portion is delimited by branch lines with interacting faults, and there is a close spatial association between the original segmentation of the parent fault and the subsequent selective reactivation (Fig. 4.15a).

The upward propagation mode of reactivation can also be discerned in the throw distribution on the reactivated fault (Fig. 4.15b). The upper tip line varies laterally in position from 2400 ms TWT at the lateral regions to 3000 ms TWT in the central portion of the fault. The basal tip line is located at c. 3800 ms TWT at the SSW and the central regions (lines 1 to 6) and terminates at progressively shallower levels up to 3550 ms TWT at the NNE lateral tip. The seismic data show the fault detaching on the limb of the underlying anticline between lines 1 and 6 whereas in contrast the lower tip line abuts against an antithetic fault between lines 7 and 11. Regions of maximum throw values are located between 3000 and 3800 ms TWT. More specifically, the contours are centred on two maxima situated between 3700 and 3800 ms TWT on those portions of the fault plane that detach at the base. Above the E-O boundary the contours are more widely spaced and sub-horizontal with no sign of perturbation or local maxima.

T-z plots obtained for the central portion of the fault plane (T-z plots 4, 5 and 6) are characterised by typical profiles of non reactivated faults (Figs. 4.7 and 4.14a). Throw maxima are located in the lower part of the profile between C60 and Top Cretaceous Horizons as expected for detaching faults. The t-z plots obtained for the portions of faults that are interpreted as reactivated (T-z plots 1, 2, 3, 7, 8, 9, 10 and 11) exhibit typical stepped profiles with a major break in throw gradients corresponding with the E-O boundary. Upper parts of the profiles overlying the E-O boundary are generally characterised by a constant positive throw gradient between c. 0.01 and 0.06 (such as T-z plots 7, 9 and 10). Alternatively, some profiles exhibit a near zero gradient between the E-O boundary and Horizon C30 (such as T-z plots 1, 2 and 11). However, there is no striking C type profile in the upper parts of these T-z plots or any significant irregularities in the throw gradients.

In summary, faults that are reactivated by upward propagation are characterised by typical stepped profiles with a major break in throw gradients corresponding the E-O boundary. The profiles exhibit a regular decrease in throw values and gradients up to the upper tip point.

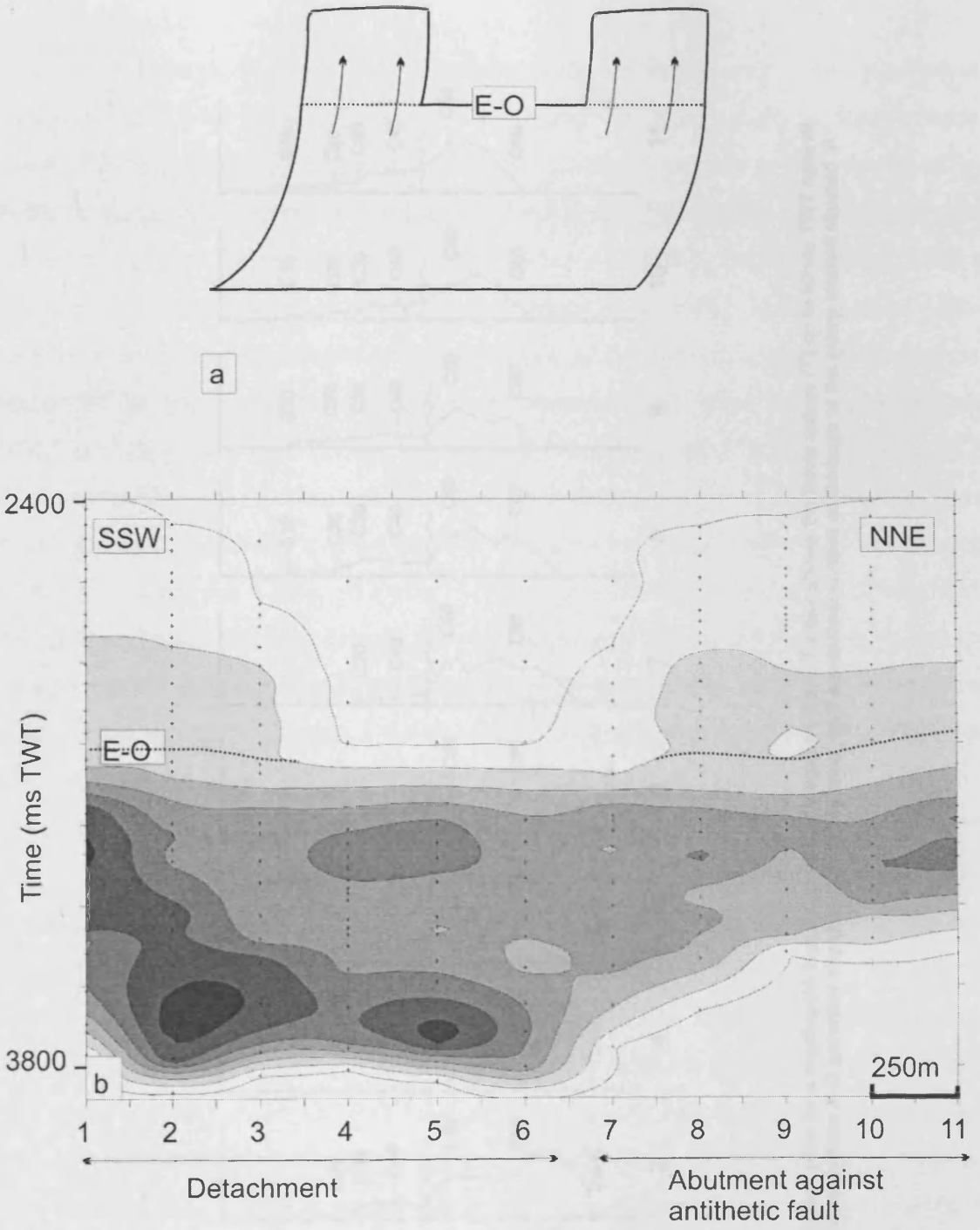

Fig. 4.15: (a) Schematic illustration of the 3D geometry of a typical example of a fault that reactivate by upward propagation (indicated by the arrows). The central portion that is not reactivated is delimited by vertical branch lines of interacting faults. (b) Throw contour plot showing lines of equal throw value spaced every 10 ms TWT and up to 70 ms TWT (dark colour). Doted lines indicate the areas of reactivation.

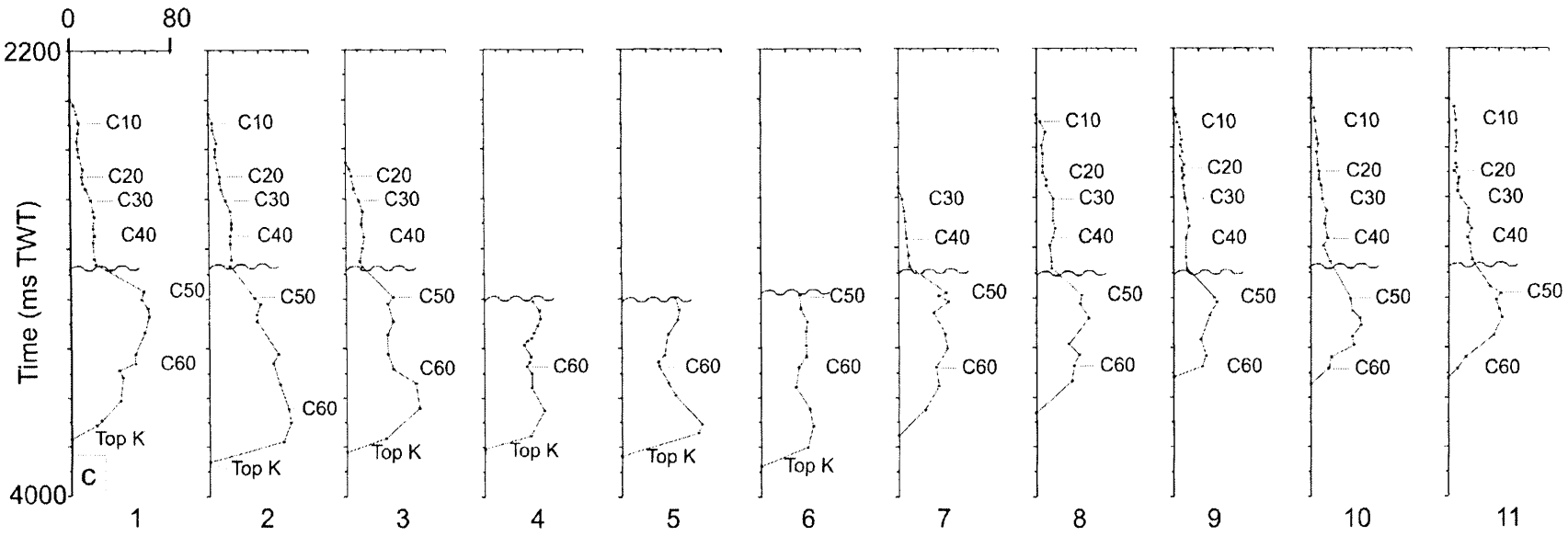

Fig. 4.15: (c) Vertical throw distribution plots for a reactivated fault by upward propagation. Each T-z plot shows the throw values (T) up to 80 ms TWT against the time in ms TWT. Wavy lines represent the E-O boundary characterised in this case by the erosional surface at the base of the slump interval situated at the base of Unit 2.

Dip linkage is much less frequent mode of reactivation, but nonetheless interesting and with potentially wider implications for reactivation in fault systems where strong mechanical layering anisotropy favours localisation of new faults in different mechanical 'tiers.' A representative example of reactivation by dip linkage is presented in Figure 4.10c. Segments A and B are pre-existing faults offsetting Unit 1 and result from the first phase of faulting. Segment B is smaller in length and is sub-parallel to Segment A. A schematic representation of the 3D geometry of the fault plane illustrates the spatial relationship and interaction between these faults (Fig. 4.16a). Segment R is a fault that initiated individually within Units 2 or 3 and strikes in a similar direction. The 3D visualisation shows that Segment R is hard linked to Segment A in a dip direction at the level of the E-O boundary towards the NNE and towards the SSW (Figs. 4.10c and 4.16a). However, Segment R switches towards the WNW at both branch lines to link with Segment B, leaving Segment A truncated at the E-O boundary. One of the conditions for reactivation by dip linkage in this case is the similarity between the dips and strikes of the segments nucleating in the upper units and the parental segments beneath.

The throw distribution of the reactivated fault provides additional evidence for the dip linkage interpretation presented above (Fig. 4.16b). Towards the NNE and the SSW the upper tip line of Fault A terminates between 2300 and 2400 ms TWT, but is deeper at c. 3000 ms TWT in the central portion where Segment A overlaps with Segment B. Two principal throw maxima are located between 3000 and 3400 ms TWT. The throw contours above the E-O boundary are irregular but crudely centred on small individual zones of maximum throw values such as between 2800 and 3000 ms TWT in the vicinity of line 3. This throw maximum is separated from the lower part of the fault plane by a horizontal zone of throw minima located in the vicinity of the E-O boundary at c. 3000 ms TWT.

Vertical throw distribution plots measured on individual transect normal to the strike of the fault plane show more subtle details of reactivation by dip linkage (Fig. 4.16c). The vertical throw distribution obtained on Fault A where it overlaps with Segment B (T-z plot 4) is characterised by a profile typical of non-reactivated faults (Fig. 4.14a). In contrast, T-z plots measured on portions of Fault A that are parallel to

Segment B exhibit profiles in 2 parts separated by a sharp change in throw values and gradients as it is expected for reactivated faults (Fig. 4.14c). However, the upper regions of these profiles above the E-O unconformity do not always have single positive gradients. T-z plots 1, 2, 3, 6 and 7 are characterised by near C-type throw profiles between the upper tip point and Horizon C20. Throw profiles 3 and 5 show a C-type vertical throw distribution plot between C30 and the E-O boundary. This is interpreted as being the consequence of reactivation by dip linkage of individual Segment R. The zone of linkage between two originally individual segments that hard linked is recognisable by a zone of throw minima and steepening of the throw gradients (e.g. Peacock & Sanderson 1994, Cartwright et al. 1995). This segment initiated within the upper part and propagated downward to link with the upper tip line of pre-existing Fault A.

Faults that are reactivated by the dip-linkage process are characterised by stepped profiles with a major break in throw gradients and possible zones of separated C-shape profiles above the E-O boundary. This type of reactivation is recognisable by throw maxima in the upper part of the fault plane separated from the pre-existing parts by throw minima.

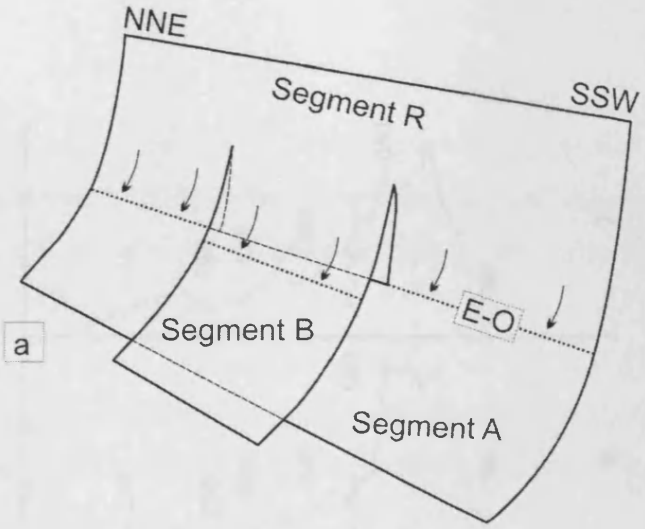

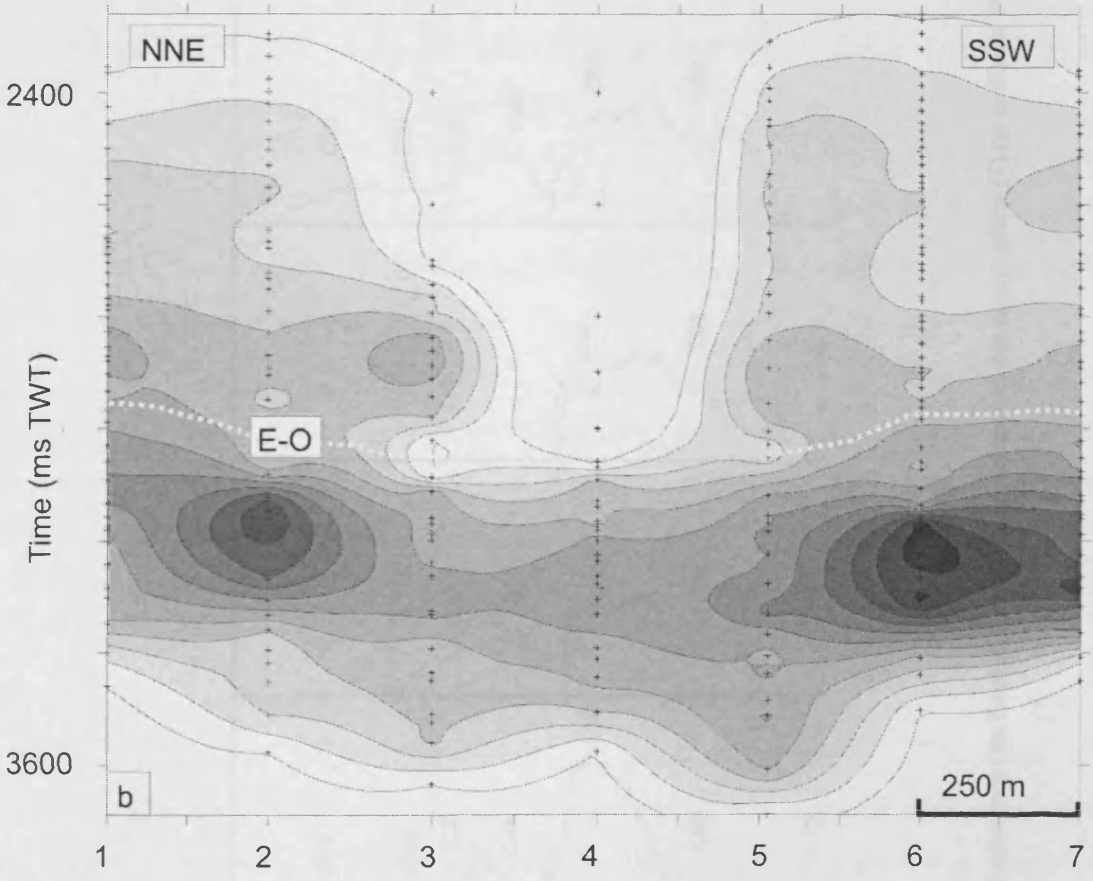

Fig. 4.16: (a) Schematic illustration of the 3D geometry and interaction between Segments A, B and R. Segment R hard linked with Segment A by downward propagation and reactivated it on most of the strike length except in the centre of the fault plane where Segment R reactivated Segment B. Dotted lines indicate the branch lines of dip linkage and arrows show the direction of propagation. (b) Throw contour plot showing lines of equal value up to 60 ms TWT (spacing is 10 ms TWT) on the main fault plane (Segment A) and the reactivated upper tip (Segment R). Branch lines of dip linkage between Segments A and R are indicated in dotted white lines.

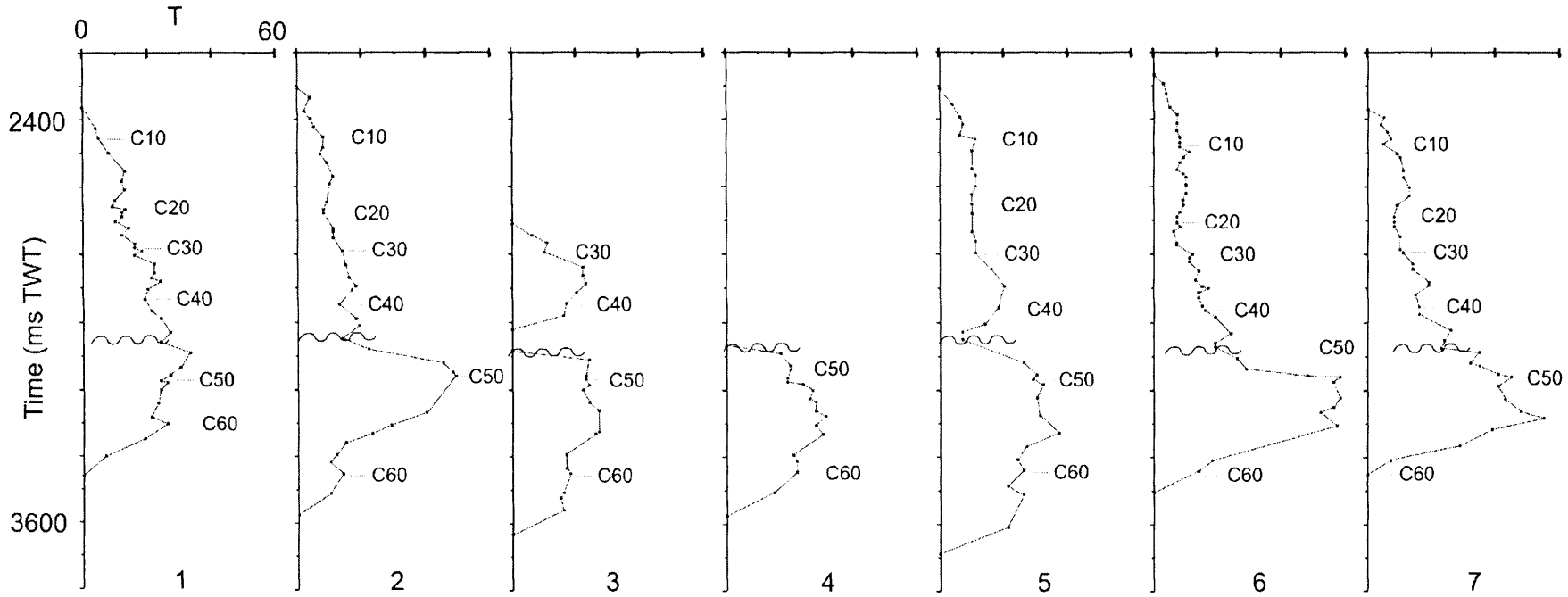

Fig. 4.16: (c) Vertical throw distribution plots for Fault A. Each T-z plot represents the throw values (T) up to 60 ms TWT plotted against the time.

4.8 Discussion

Geometrical and kinematic evidence has been presented to demonstrate the occurrence of reactivated faults in the study area. Several structural and stratigraphic criteria can be used in this study to demonstrate fault reactivation such as the following.

(1) All faults in Sets 1 and 2 terminate upwards at the top of Unit 1b being eroded by the E-O unconformity defining the base of Unit 2 in most areas of the survey (Figs. 4.5 and 6). In addition to this, a high percentage (43%) of the fault segments within Set 3 also tips out at the base of Unit 2 (Fig. 4.8).

(2) The faults were active at the free surface at the time of deposition of the sediments that form the upper part of Unit 1 (Fig. 4.12).

(3) Fault segments offsetting Units 2 and 3 grew entirely by blind propagation. The second phase of faulting is post-sedimentary and therefore necessity a period of quiescence while deposition of Units 2 and 3.

(4) Finally, an abrupt step in the vertical throw distribution (T-z plots) marks the important changes in the throw gradients and values at the zone of newly propagating portions of faults (Figs. 4.14c and 4.16c).

This discussion now addresses the underlying question of why some faults were reactivated and others not. Several factors have been suggested to control the degree to which new faults are initiated or pre-existing fractures are reactivated under a renewed period of extension. These include the difference in strike between the older structures and the orientation of new faults related to the principal stress axes and the differing strength between the unfaulted rock volume and the pre-existing structures (Morley 1999). Creating new faults requires higher stress levels than reactivate pre-existing ones (Krantz 1991). However, it is still poorly understood why some faults reactivate and some others do not (Butler et al. 1997, Kelly et al. 1999).

4.8.1 Modes of reactivation

Reactivated structures have previously been described as growing by further propagation of the pre-existing structure after a significant period of quiescence (e.g. Nicol et al. 2005). The classical model for reactivation is described as upward propagation from pre-existing structure as faults are generally generated at depth and grow upward (Richard & Krantz 1991). This study has identified two distinct modes of reactivation for the crestal extensional faults, upward propagation and dip linkage.
Both modes of reactivation recognised by typical stepped profiles with a major break in throw gradients corresponding to the E-O boundary. Subtle differences in the throw distribution provide insights into the recognition of either mode. Upward propagation is characterised by profiles exhibiting a regular decrease in throw values and gradients up to the upper tip point whereas reactivation by dip linkage can be identified by throw maxima in the upper part of the fault plane separated from the pre-existing parts by throw minima.

The 3D geometry of the fault network shows one fault in particular initiating in Unit 2 that linked at its basal tip with a fault in Unit 1 in one area and with a neighbouring fault in Unit 1 further south. The upper part of the fault switches from one fault to another along strike. The factors controlling preferential dip linkage reactivation include the location, the geometry and dip of the fault planes in Unit 1 and the correspondence between the strike of the upper segment and the lower ones.

4.8.2 Preferential reactivation

Numerous studies attributed selective reactivation to several factors such as the orientation of the fault planes relative to the principal stresses (White et al. 1986, Richard & Krantz 1991), the differences in friction coefficients and cohesion (Sibson 1985) and the fault connectivity and linkage with other structures (Kelly et al. 1999). The dimensions of the faults have been thought to play a role in preferential reactivation (Scott et al. 1994) as well as fluid circulation (Kelly et al. 1999).

4.8.2.1 Direction of reactivation-extension

It has been suggested that the probability of reactivation is directly related to the orientation of the fault planes relative to the principal stresses and their ability to accommodate the imposed strains (White et al. 1986, Richard & Krantz 1991); as well as difference in friction coefficients and cohesion (Sibson 1985).

It is difficult to evaluate the direction of extension that resulted in reactivation of pre-existing structure during the second phase of faulting. However, the faults interpreted as reactivated from the 3D seismic data mostly strike in a NNE-SSW direction, especially the faults that tip out in Unit 3 (Fig. 4.9). The dominant direction of reactivated faults suggests that the orientation of the pre-existing fault planes with respect to the direction of the principal stress axis characterising the second phase of deformation is an important factor influencing preferential reactivation.

In addition to this, comparison of the fault network in set 3 with analogue modelling and field studies suggests that this type of geometry is due to a WNW-ESE extension with respect to the direction of these faults. This direction also corresponds to the orientation of the second and smaller population of faults striking between N120 ° and N130 °. Such an extension is concordant with the orientation of the Cretaceous anticlinal axis (N018 °).

This suggests that the selection for reactivation is strongly influenced by the orientation of the faults with respect to the principal stress axes of the phase of deformation resulting in reactivation. However, no quantitative conclusion can be drawn from this in the absence of further information on the direction of the second extensional phase.

4.8.2.2 Selective reactivation influenced by segmentation

The crestal collapse faults from the Espirito Santo Basin are interpreted to be reactivated depending on their orientation. However, it is observed that faults do not always reactivate along the entirety of their length. Particular portions or segments of faults are preferentially reactivated although several non-reactivated segments strike in a similar direction as the reactivated segments (Fig. 4.8). If selective reactivation is influenced by the orientation of faults, it is surprising to observe that only some portions

or segments of a fault, striking in the same direction, are reactivated. It has been suggested that preferential reactivation of this type is related to fault connectivity (Kelly et al. 1999).

The study of the faults located in the Espirito-Santo Basin partly supports this suggestion. The portions of major faults that are reactivated are often delimited by intersections with other fault segments (Fig. 4.8). The horizontal limits of reactivation often correspond to overlapping zones with other interacting faults and zones of linkages through the branch lines on the fault planes (Figs. 4.8, 4.15 and 4.16). Moreover the magnitude of reactivation appears to be linked to the segmentation of the fault network. A fault terminating upward in Unit 3 can split into two segments of lower maximum displacement terminating in Unit 2.

However, caution must be applied to this concept as it has been observed that some portions of faults in Set 3 are reactivated whereas the neighbouring portion is not although no branch line or interaction with another structure is observable at seismic scale.

4.8.2.3 Influence of the dimensions of faults and basal tip geometry on selective reactivation

Preferential reactivation has been attributed to larger faults partly due to the low friction associated their smooth fault plane (Scott et al. 1994) and an abundance of fluid circulation in large fault networks (Kelly et al. 1999). It was suggested that in some cases smaller faults offsetting the cover do not reactivate as opposed to some larger basement faults.

In the Espirito Santo Basin, the fault segments that are reactivated generally correspond to those parts of the fault network that exhibit higher throw values. The question remains whether these portions were reactivated because of their higher throw values or if they gained higher throw values in consequence of the reactivation process. Comparing the reactivated portions to the non-reactivated portions on the examples chosen to illustrate reactivation by upward propagation (Fig. 4.15) and by dip linkage (Fig. 4.16) provide new insights into the issue. Reactivated faults that propagated upward exhibit larger throw values. In consequence of the reactivation process, it seems that displacement is added on the whole fault plane of the pre-existing fault. There is

therefore an increase in throw values due to the reactivation. However, with the dip linkage example, Segment R preferentially linked to Segment B although overlapping Segment A is characterised by higher throw values. The orientation might therefore be a dominant factor than the dimension or maximum throw values in the case of reactivation by dip linkage.

In addition to this, most of the reactivated faults that tip out upwards in Unit 3 are also the faults that detach downwards on the limbs of the Cretaceous anticlines. It is therefore proposed that the basal tip geometry and location in relationship to the crest and limbs of the anticlines influence the selection for reactivation.

4.8.3 Implications

As previously suggested in earlier papers on fault growth (e.g. Walsh et al. 2002, Vetel et al. 2005), a reactivated structure can exhibit an abnormal low displacement-to-length ratio. The length of faults is generally established during the phase of faulting that created the pre-existing faults. When the faults are reactivated, increase of the height and maximum displacement value shift the growth path of the fault vertically for a near-constant length. In the case of the Espirito Santo basin faults, the length was established during faulting phase 1. The reactivated faults resulting from faulting phase 2 accumulated twice the amount of displacement whist maintaining fault trace length. It is therefore necessary to consider reactivation as an important factor for scatter in displacement-length ratio as these scaling relationship have been used to promote several fault growth models (e.g. Walsh & Watterson 1988, Cowie & Scholz 1992a, Cartwright et al. 1995). Models of fault evolution of this type also provide insights into the timing of activity of faults that have a direct application to hydrocarbon migration and sealing of faults in petroleum reservoirs (McClay 1990). A further understanding of reactivation processes will greatly improve petroleum prediction of seal integrity, trap geometry and fluid circulation and migration.

4.9 Conclusions

This chapter investigated the kinematics of small crestal collapse faults offsetting Cenozoic clastic sediments that overlie Cretaceous anticlines using high quality 3D seismic data from offshore Brazil. Some faults localised in Set 3 show evidence of reactivation in an extensional manner.

- An analysis of the 3D geometry of the fault network with respect to the different stratigraphic units, the Cretaceous anticlines and the salt tectonic evolution associated to detailed measurements of the throw distribution allow the fault kinematics to be reconstructed.

- The reactivated faults are part of a network resulting from the uplift of a semi-elliptical dome of the Cretaceous sequence during Early Cenozoic deformation with very little simultaneous extension.

- Two different modes of reactivation have been recognised from this dataset. The main mode is a classical reactivation by upward propagation of pre-existing structures. The alternative mode of reactivation is termed reactivation by dip linkage. It involves the propagation of an individual fault initiated within the upper Units 2 and 3 during the second phase of faulting. Further propagation of this fault results in hard-linkage in the dip direction with the pre-existing faults.

- Reactivated faults are characterised by typical stepped profiles with a major break in throw gradients corresponding the E-O boundary. The throw profiles and contour plots exhibit a regular decrease in throw values and gradients up to the upper tip point for reactivated faults by upward propagation. Throw minima separate the upper parts from the pre-existing fault in the case of reactivation by dip-linkage.

- For both modes, reactivation processes are selective and only occurs on some portions of a number of faults. The factors that control or influence the preferential reactivation of some segments amongst others are (i) preferential orientation of the pre-existing faults at 90 to 110 ° relative to the estimated principal stresses resulting in faulting phase 1, (ii) segmentation of the pre-

existing network (iii) maximum dimensions and throw values of pre-existing faults and (iv) basal tip line geometry associated with a detachment.

These conclusions have wide implications for the understanding of fault reactivation in general. A further comprehension of these processes and the timing of activity of faults give insights into different fault growth models previously published. Improvement of our knowledge concerning fault reactivation can have direct applicability to petroleum systems.

Chapter V

Discussion

5 DISCUSSION

5.1 Introduction

High quality 3D seismic datasets from the Levant and the Espirito Santo Basins have been used in this thesis to provide new insight into the propagation of normal faults.

Many issues addressed in the thesis have been considered in Chapters 2, 3 and 4 and will therefore not be discussed further in this chapter. The aims of this discussion are two fold. Firstly this discussion aims to summarise and collate the main findings of each of the result chapters (Section 5.2) and secondly, to further investigate and discuss the characteristics of the strain field surrounding these faults in order to gain a better understanding of their 3D evolution (Section 5.3).

5.2 Summary

In order to gain an enhanced comprehension of fault propagation, it is necessary to examine different types of faults, of various dimensions, and from diverse contexts.

This research investigated normal fault propagation through a detailed analysis of three distinct case studies: (1) small individual blind faults, (2) gravity driven growth faults that initiated as blind faults and have only recently made the transition to the free surface and (3) complex crestal collapse faults that initiated as blind faults before reaching the surface and underwent a period of quiescence before being reactivated by blind propagation. The results of this thesis therefore follow a continuous progression from the simplest to more complex development of extensional faults.

Chapter 2 analysed the evolution of simple blind faults from a 3D seismic dataset located in the eastern Mediterranean. The main aim was to develop specific

criteria in order to confidently recognise blind faults using 3D seismic data. The chapter investigated the evolution of the dimensions (length, height) and throw distribution of the fault plane of extremely simple individual faults. These faults were then compared to those that subsequently interacted with another fault or a major lithological boundary, such as the Messinian evaporites and Yafo Sand Member in the Levant continental margin. This provided better constraint on the effects of various interactions on the throw distribution and the 3D geometry of the fault plane. The results suggested that the dimension of the faults were established early in the development of the array and that the displacement was added as a result of fault interactions. The results from this case study suggest that blind faults are mainly characterised by M-type throw profiles rather than C-type or triangular throw profiles as previously described (see Chapter 2). This could imply that no significant variation in rockwall straining occurs in the near-field volume surrounding the fault plane (Section 2.7.5.2). In addition to this, reverse drag folding characterises strata in contact with portions of the faults that accumulated additional displacement due to interaction, which has implications for near field displacement characteristics.

Chapter 2 provided a better understanding of blind propagation as a prelude to investigation of the early propagation history of syn-sedimentary faults that have recently made the transition from a blind stage to a growth stage, which aided in comparison of the two styles of growth history.

An example of such a fault is analysed in detail in Chapter 3. The 3D geometry and throw distribution was investigated in relation to the tectono-stratigraphic context of the Levant Basin and the kinematics of this fault thus proven to be linked to the long term kinematics of a larger graben system. The fault results from the hard-linkage of three main segments that grew by blind radial propagation before interacting with the free surface and accumulating displacement as a syn-sedimentary fault. The results show that most of the fault surface area formed during the blind propagation phase, but most of the displacement was added during the syn-sedimentary phase with near-constant dimensions. Reverse drag folding surrounding the fault plane is associated with the growth packages in the upper part of the fault plane whereas the central and lower parts, interpreted as having grown by blind propagation, are generally characterised by normal drag folding. The vertical throw

distribution is characterised by M-type profiles at the lateral tip regions of this fault and asymmetric skewed M-type profiles over the central portions. It was shown that the interaction of the fault with the free surface lead to a change in the position of the point of maximum displacement as well as shifting the entire vertical throw distribution. The amount of displacement added after this transition from blind fault to growth fault decreases systematically towards the lower tip, preserving a constant low negative gradient as a relict of the blind stage.

The examples investigated in Chapter 3 provided a good basis for the understanding of the kinematic evolution of more complex faults that were analysed in Chapter 4.

Chapter 4 describes and analyses crestal collapse extensional faults from the Espirito Santo Basin. The results suggest that the initial faults grew by blind propagation before reaching the free surface in a first phase of deformation. The upper tip lines of the faults were eroded prior the deposition of overlying sedimentary units during a period of non activity of the faults. The pre-existing faults were then reactivated by a second phase of extension. Analysis of the 3D geometry with detailed reconstruction of the throw distribution on the fault planes allowed reactivation by dip-linkage to be recognised as an alternative style of fault evolution, in addition to the main mode of reactivation by upward propagation. Main factors controlling the selective reactivation identified in this chapter are: (1) the orientation of the pre-existing faults relative to the principal stresses resulting from the second phase of deformation, (2) the segmentation of the pre-existing network (3) the maximum dimensions and throw values of initial fault segments and (4) the basal tip line geometry associated with a detachment.

5.3 Out-of-plane deformation

Consideration of the out-of-plane deformation of a fault provides new insight into the strain field surrounding the fault plane and thus important information on its 3D evolution. Heterogeneous stress and displacement fields develop in the rock volume surrounding a fault in response to slip (Pollard & Segall 1987). Folding of the

strata offset by a fault is an important element to consider when investigating the growth evolution of the fault because it completes the full description of near-field deformation (Barnett et al. 1987, Schlische 1995, Rykkelid & Fossen 2002, Grasemann et al. 2005). As such, the following section intends to investigate and discuss the characteristics and distribution of folding that develops in response to slip along some of the representative faults examined in the thesis.

5.3.1 Background on folding adjacent to fault planes

A proportion of the total displacement is accommodated by plastic or ductile processes on most faults (Walsh & Watterson 1990). Ductile deformation is often seen as folding of the beds adjacent to the fault plane. This folding illustrates the variation of displacement in the direction normal to the fault surface and is frequently called fault drag (e.g. Hamblin 1965, Twiss & Moore 1992). Normal and reverse drag folding (Fig. 5.1) have been described in association with extensional faults (e.g. Reches & Eidelman 1995, Schlische 1995).

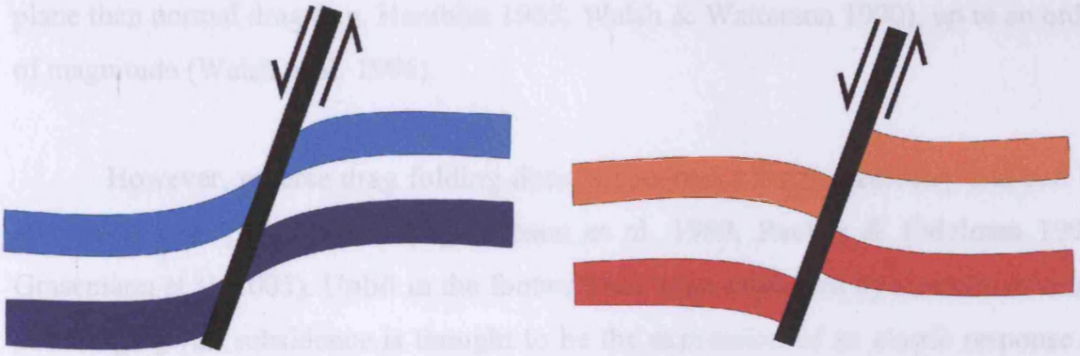

Fig. 5.1: Schematic illustration of normal (in blue) and reverse (in red) drag folding of strata immediately adjacent to a normal fault plane.

Normal drag folding has been recognised at various scales (e.g. Hamblin 1965, Wernicke & Burchfiel 1982) and is characterised by convex strata towards the direction of slip (Hamblin 1965, Peacock et al. 2000). This normal folding has been attributed to different mechanisms including the formation of a monocline ahead of a propagating fault (e.g. Hancock & Barka 1987, Walsh & Watterson 1987, Reches & Eidelman 1995), mechanical control of more ductile lithologies (Rykkelid & Fossen

2002) and frictional resistance of the rockwall strata to sliding on the fault surface (Ramsay & Huber 1987).

Reverse drag folding is also a common feature associated with normal faults (Hamblin 1965). These folds are characterised by layers that are concave towards the direction of slip and has also been named turnover (Hamblin 1965). It has often been described as uplift of the upthrown block and rollover of the downthrown block with respect to the fault plane (Barnett et al. 1987, Gibson et al. 1989, Walsh & Watterson 1990). Several possible mechanisms have been proposed to explain reverse drag folding such as multiple stages of deformation, elastic and isostatic rebound, diapirism, sagging, inversion of slip directions and differential compaction (Hamblin 1965, Reches & Eidelman 1995, Grasemann et al. 2005). Reverse drag folds have mostly been attributed to the geometry of listric faults and termed roll-over. Roll-over anticlines form in response to slip on concave upward faults that detach at depth. Instantaneous subsidence of the hanging wall strata fills the additional volume (or void) developed in the upper part of the fault (Hamblin 1965, Gibbs 1983). It has been suggested that reverse drag folding extends to much greater distances from the fault plane than normal drag (e.g. Hamblin 1965, Walsh & Watterson 1990), up to an order of magnitude (Walsh et al. 1996).

However, reverse drag folding does not require a listric geometry and can be associated with planar faults (e.g. Gibson et al. 1989, Reches & Eidelman 1995, Grasemann et al. 2005). Uplift in the footwall has been explained by isostatic rebound and hangingwall subsidence is thought to be the expression of an elastic response to coseismic slip (e.g. Jackson & McKenzie 1983).

Importantly, reverse drag folding is also seen as the geometric consequence of stratal folding in the ductile strain field around a fault and is the manifestation of the decrease in displacement with increasing distance from the fault surface (Barnett et al. 1987). It is regarded as the necessary ductile deformation to accommodate additional displacements within the volume closely surrounding the fault plane (Barnett et al. 1987). The cumulative near-field displacement is therefore equivalent to the displacement on the fault surface (Hamblin 1965, Barnett et al. 1987). This is important and does not require any of the mechanisms suggested above to create reverse drag.

5.3.2 Strain field surrounding blind faults

Numerous blind faults have been investigated in this thesis. These are the small extensional faults of the El Arish array (Fig. 2.2) located in the southern part of the Levant 3D seismic survey and the small normal faults, including Fault B2, located between the Kefira graben and Fault G3 in the eastern part of the same survey (Fig. 3.5). In addition to this, this section also considers the upper part of the crestal collapse faults (Fig. 4.3) analysed from the 3D seismic survey located in the Espirito Santo Basin, as the upper tips have been interpreted to have grown by blind propagation.

5.3.2.1 Unrestricted blind faults

A number of these blind faults are individual in the sense that they do not interact with any other structure or a major lithological boundary. The absence of interaction with such mechanical boundaries defines these faults as unrestricted. The stratal folding surrounding these unrestricted blind faults is investigated in further detail in this section.

Fault 17 (Section 2.5.1) provides a good example of unrestricted blind faults (Fig. 5.2). The fault does not reach the present day seabed and dies out a few tens of metres above the Yafo Sand Member (YSM) that overlie the Messinian evaporites (Fig. 5.2b). An analysis of the throw distribution over the entire fault plane reveals small amplitude displacements with very small throw gradients. The strata directly adjacent to the fault plane are characterised by an absence of folding except in the upper tip region where a monocline is evident, as expected ahead of propagating faults (e.g. Gawthorpe et al. 1997, Hardy & McClay 1999, Withjack & Callaway 2000). Individual blind faults have been described associated with reverse drag folding (Barnett et al. 1987). If reverse drag folding deforms the near field zone surrounding the fault plane, it is either smaller than the seismic resolution or the wavelength is so large and the amplitude is so small that the folding is negligible.

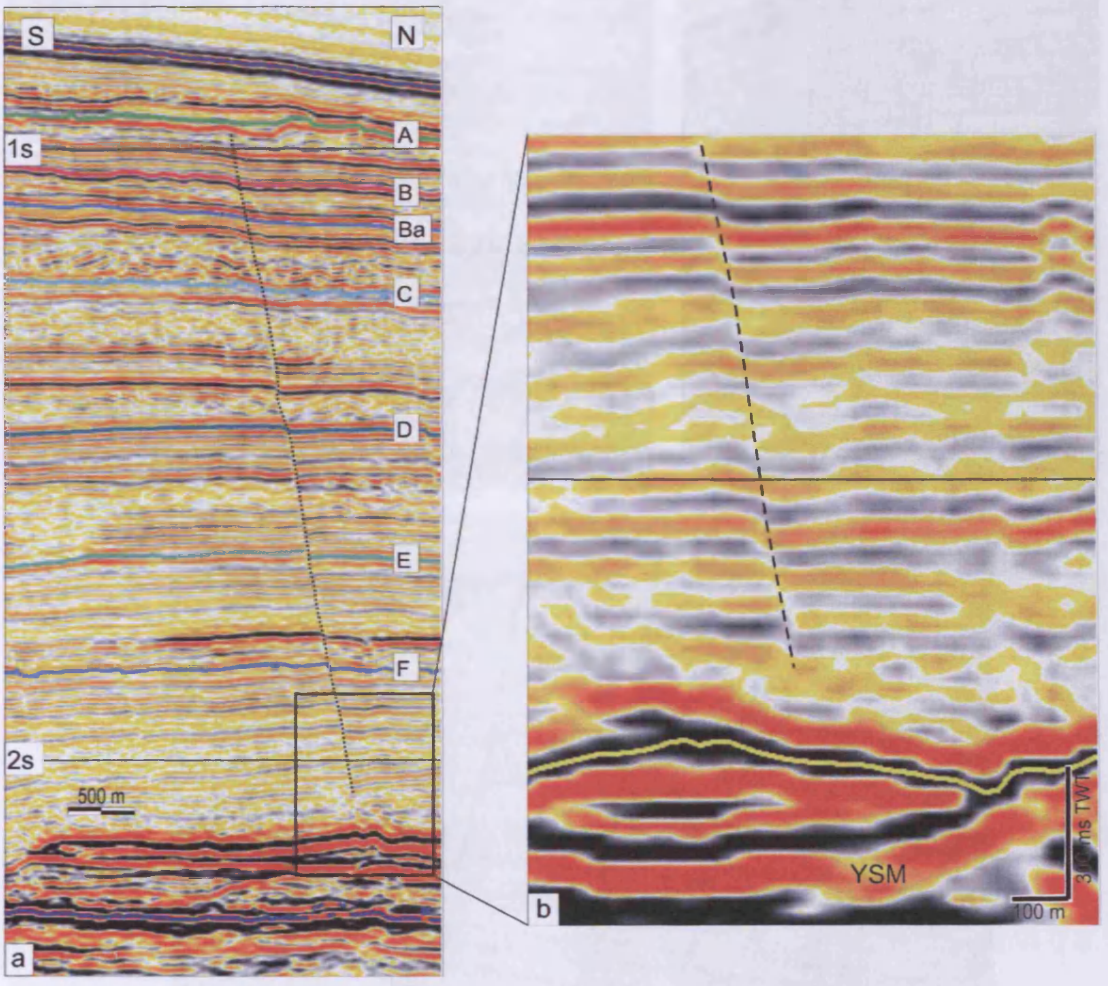

Fig. 5.2: (a) Seismic section across Fault 17 showing the position of upper and lower tips and small magnitude of displacement over the fault height. No significant reverse drag folding is observable. Key horizons are labelled A- F. (b) Close-up showing the lower tip of the fault terminating above the YSM.

Similar conclusions can be drawn from observations of other blind faults from the El Arish array (Fig. 5.3a), from the blind faults located between the Kefira Graben and Fault G3 (Fig. 5.3b) and from the upper tips of crestal collapse faults that grew by blind propagation (Fig. 5.3c). The blind portions of faults analysed from the BES-2 survey, offshore Brazil are not unrestricted as the lower tips form complex crestal collapse grabens. However, the upper portions located above the Eocene-Oligocene boundary propagated entirely by blind propagation and exhibit the same characteristics as other simple blind faults. All these faults are characterised by very small or no reverse drag folding observable from the 3D seismic data.

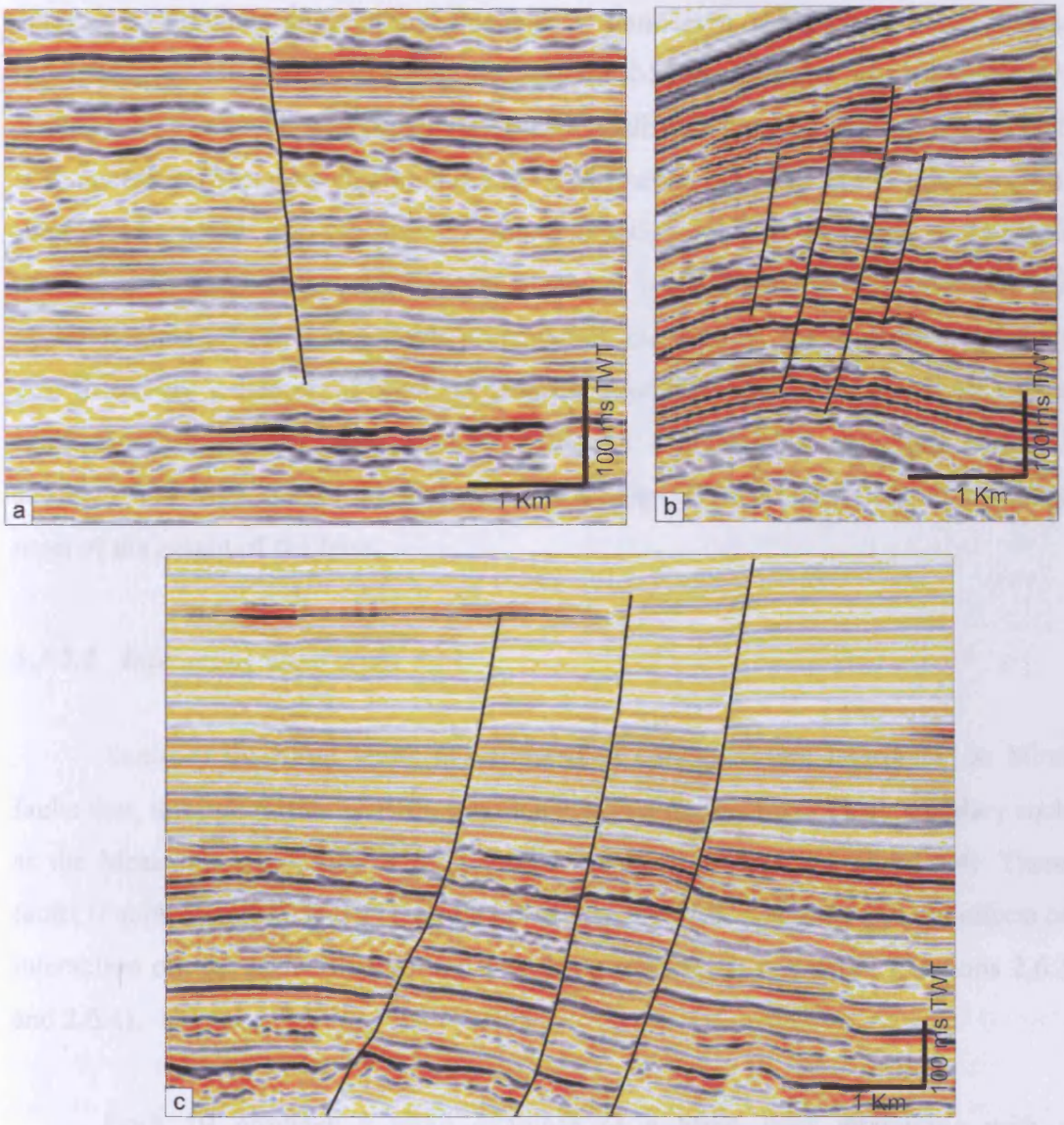

Fig. 5.3: Seismic section showing no significant folding of the stratal reflections in the close proximity of blind fault planes (a) Fault 9 in the El Arish fault array (Chapter 2) (b) blind faults located in between Faults G2 and G3 (Chapter 3) (c) the upper tip of reactivated faults in the BES-2 survey (Chapter 4).

One of the main observations drawn from the various unrestricted blind faults studied during this research is that the simplest blind faults are mostly characterised by M-type or hybrid vertical throw distribution plots with a broad central region and very gentle gradients. Throw distribution analysis conducted on Fault 17 (Section 2.5.1) and Fault B2 (Section 3.6.1.1) provide representative examples of M-type or hybrid vertical throw distribution (Figs. 2.7 and 3.15b), characteristic of the simplest blind faults. No striking, sharp peak C-type or triangular profiles were observed, as

opposed to previous suggestions (Peacock & Sanderson 1991, Nicol et al. 1996b, Manighetti et al. 2001). The significance of M-shape throw profiles has been attributed to a constant wall rock strain on footwalls and hanging walls in intervals of stiff materials (Muraoka & Kamata 1983). However, different faults offsetting the same stratigraphic interval can be characterised by either M-shape or C-shape profiles. This suggests that the shape of the throw profiles may not only be controlled by lithological effects during fault propagation, but also by the mechanism of fault growth and the existence of other mechanical boundaries that it interacted with. The significance of M-type throw profiles could be explained by very little rockwall straining from each side of the fault plane or a near-constant rockwall straining along most of the height of the fault.

5.3.2.2 Interacting blind faults

Some of the blind faults investigated in Chapter 2 are interpreted as blind faults that, through further growth, interacted with a major lithological boundary such as the Messinian evaporites or other faults (Sections 2.5.2, 2.5.3 and 2.5.4). These faults (Faults 19, 15-16 and 21) are therefore expressed as restricted and the effects of interaction on the throw distribution have been investigated in detail (Sections 2.6.3 and 2.6.4).

Fault 19 provides a good example of a blind fault interacting with a mechanical boundary. The throw distribution of the fault plane (Fig. 2.10) reflects the lower tip geometry and the interaction with the Yafo Sand Member (YSM) (Fig. 2.8). Lateral tip regions of the fault plane are characterised by free lower tips that die out above the YSM and exhibit M-type throw profiles. However, the fault is characterised by asymmetric C-type throw profiles on portions of the fault where the lower tip terminates within the YSM. Portions of the fault plane that accumulated more displacement are located in the central and lower part of the fault plane.

The strata that are offset by Fault 19 are characterised by reverse drag folding on portions of the fault plane that terminate within the YSM or the Messinian evaporites (Fig. 5.4a). However, no significant evidence of ductile strain is observable in the near field surrounding portions of the fault plane that dies out above the mechanical layer (Fig. 5.4b). When reverse folding occurs, large wavelength stratal

folding is greatest (up to c. 525 m) adjacent to the part of the fault that accumulated the most displacement, that is, in the lower part of the fault plane. Reverse folding is also more important in the hanging wall than in the footwall.

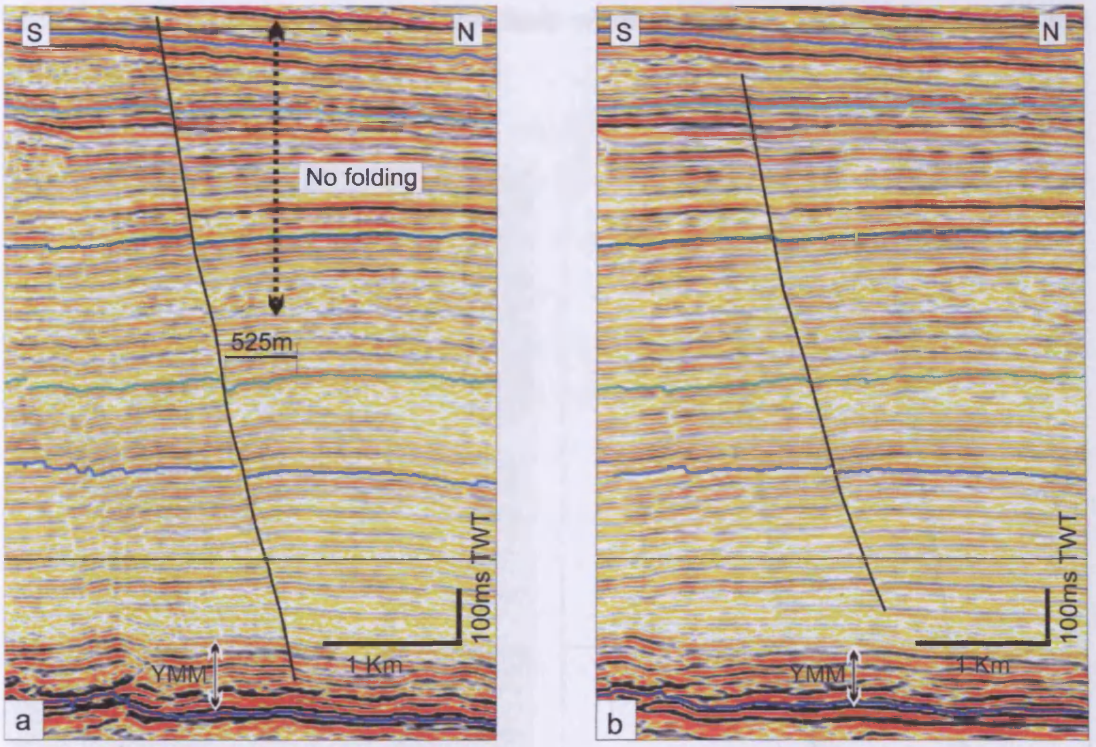

Fig. 5.4: (a) Seismic section across Fault 19 (Chapter 2) taken in the central portions where the fault terminate within the YSM and Messinian evaporites. Large wavelength (525m) reverse folding of the strata in the vicinity of the fault plane is localised to the lower part of the fault and greater in the hanging wall. (b) Seismic section across Fault 19 taken in the lateral tip region where the lower tip dies out above the mechanical boundary. The strata adjacent to the fault plane are characterised by no significant reverse folding.

In a similar way to Fault 19, Faults 15, 16 and 21 are only associated with reverse folding strata in the parts of the faults that exhibits asymmetric C-shape or hybrid profiles (Figs. 2.13 and 2.15). These parts are also interpreted as having accumulated additional displacement in response to the lower tips terminating at the top of or within the YSM. A striking example of the differences in folding between a fault that terminates within the YSM and a fault that terminates above it is illustrated by a seismic section across neighbouring Faults 16 and 20 (Fig. 5.5). Fault 16 dies out downwards within the YSM and exhibits reverse folding. The neighbouring fault (Fault 20) dies out downwards a few tens of metres above the YSM and does not

reflects any interaction with the mechanical boundary. No ductile deformation expressed as folding is observable on strata offset by the fault. This poses the question of whether the drag folding is actually due to rock wall straining associated with the initiation and propagation of the blind fault or if it is due to the additional slip accumulated in the lower part of the fault when the lower tips interacted with the YSM and Messinian evaporites.

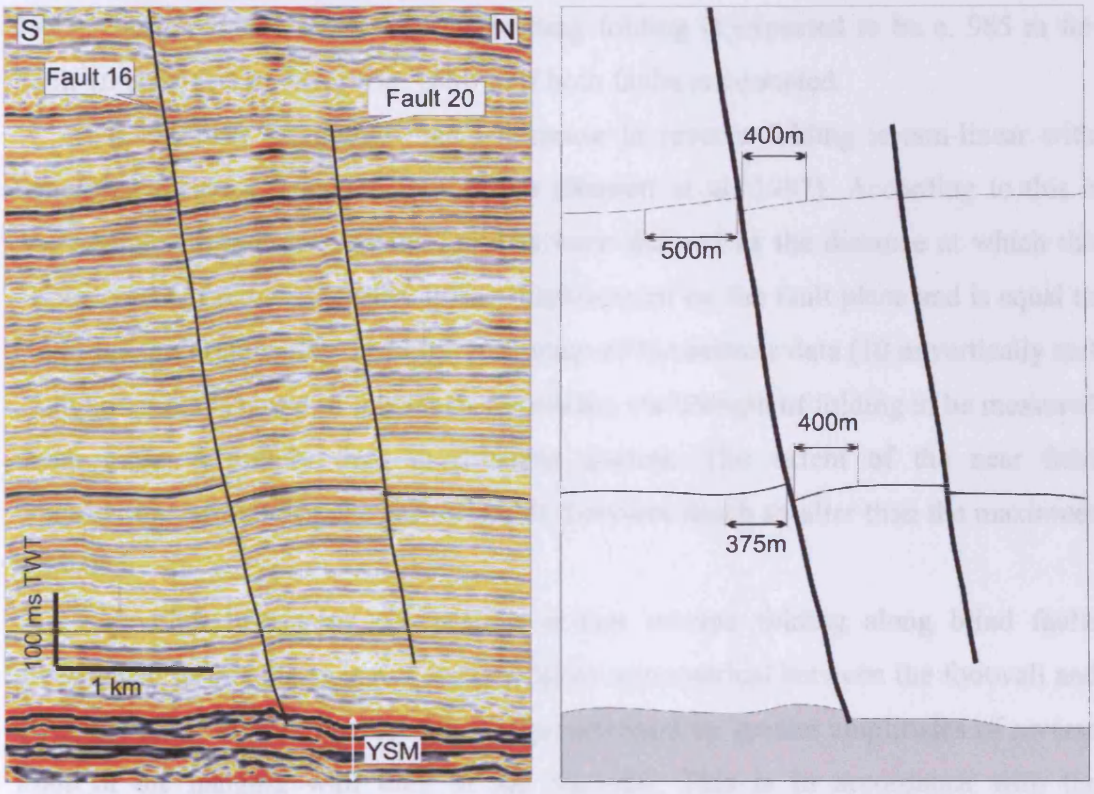

Fig. 5.5: (a) Seismic section across blind faults located in the El Arish array. Fault 16 terminates downwards within the Yafo Sand Member (YSM) above the Messinian evaporites whereas Fault 20 dies out above it. (b) Schematic representation of the folding of the strata in the volume surrounding the faults. Fault 16 is characterised by reverse drag folding, especially in the lower part of the fault. Arrows indicate the approximate extent of stratal folding associated to fault movement. No significant folding is observable in the vicinity of Fault 20.

5.3.2.3 Discussion and conclusions on the strain field surrounding blind faults

It has been suggested that the maximum extent of reverse drag folding in a direction normal to the fault plane is equal to the fault radius (R) for ideal blind faults (Barnett et al. 1987). The radius (R) is defined as half the maximum length (L max).

It follows that the maximum extent of reverse folding associated with Fault 19 (length 1925 m) is predicted to be 962 m. In fact, it was measured at 525 m. In a similar manner, reverse folds associated with Fault 16 are characterised by large wavelengths (up to c. 500 m) in both the hanging wall and footwall. The maximum length of Fault 16 is c. 1970 m. The fault is hard-linked to Fault 15 which has a maximum length of c. 1730 m. According to conventional studies (Barnett et al. 1987), the maximum extent of reverse drag folding is expected to be c. 985 m for Fault 16 considered alone, or c. 1850 m if both faults are counted.

It has been suggested that a decrease in reverse folding is non-linear with increasing distance from the fault plane (Barnett et al. 1987). According to this a "perceptible reverse drag radius (r)" has been defined as the distance at which the displacement is reduced to 20% of the displacement on the fault plane and is equal to 0.4 of the fault radius (R). The high resolution of the seismic data (10 m vertically and 25 m horizontally) used in this thesis allows the wavelength of folding to be measured much more accurately than in previous studies. The extent of the near field deformation surrounding the fault plane is therefore much smaller than the maximum predicted.

Another interesting observation is that reverse folding along blind faults investigated in this thesis is not systematically symmetrical between the footwall and hanging wall. Fault 19, for instance, is characterised by greater amplitudes of reverse folds in the hanging wall than in the footwall. This is in accordance with the observation that reverse drag folding, and therefore near-field ductile strain, is generally more developed in the hanging wall than in the footwall (Hamblin 1965, Gibson et al. 1989, Schlische 1995). For blind faults in particular, reverse drag folding is better developed in the lower part of the fault plane in the hanging wall and in the upper part of the footwall (Barnett et al. 1987). Reverse drag folding is believed to be only symmetrical when the fault nucleates and propagates perpendicularly to the bedding. In most cases, the amplitude (i.e. change in bed dip) of reverse folding is greater in the lower part of the hanging wall and in the upper part of the footwall and the asymmetry increases with decreasing angle between the fault and the strata (Barnett et al. 1987). Fault 16 exhibits surprisingly symmetrical reverse folded strata in both footwall and hanging wall. However, as expected, the amplitude of the folding is greater in the lower part of the fault plane than in the upper part.

Various factors have been suggested to control the displacement in the volume containing a single blind fault such as: (1) the ratio between the maximum displacement and the maximum dimension of the fault plane, (2) the displacement distribution on the fault plane from displacement maxima to tip line of the fault surface, (3) the ratio between the maximum displacement and the zero displacement in a direction normal to the fault plane and (4) the distribution of displacement between footwall and hanging wall (Barnett et al. 1987, Gibson et al. 1989).

The initial results from a 3D analysis of displacement surrounding blind faults suggest that variation in throw distribution on the fault plane due to interaction with mechanical boundaries is also a primary factor influencing the ductile deformation in the volume surrounding the faults. The wavelength of reverse folded strata is typically half the maximum distance predicted by conventional studies. It should be noted that these observations are mainly derived from a small number of faults and require further work before a wider applicability can be suggested.

5.3.3 Strain field surrounding growth faults

Several growth faults have been investigated in this thesis and in particular from the 3D seismic survey located in the Levant margin. The extensional faults that form the Shamir and Kefira grabens as well as the coast-parallel extensional faults located on the shelf-break have been interpreted as growth faults (Chapter 3).

5.3.3.1 Kefira graben

The Kefira graben, for example, consists of two main conjugate faults (Faults G1 and G2) that have been interpreted to be syn-sedimentary and exhibit throws of up to 250 m (Section 3.3). The graben strikes approximately parallel to the underlying detachment within the Messinian evaporites and its position in the basin is coincident with the updip pinch-out of the evaporites (e.g. Gradmann et al. 2005, Bertoni & Cartwright 2006). A prominent syncline is developed within the Pleistocene interval and is bounded by faults of the Kefira Graben. This syncline is generally marked by

large wavelength and high amplitude normal folding of the strata in the downthrown block between Faults G1 and G2 (Fig. 3.4). The syncline is asymmetrical and the depocentre is generally closer to Fault G2 than to Fault G1 although it switches to become closer to Fault G1 towards the north (Fig. 3.4a).

Figure 5.6 illustrates a representative seismic section taken normal to the fault strike across the Kefira graben. The strata offset by Fault G1 exhibit no seismically resolvable folding in the footwall block. The strata in the hanging wall are characterised by no clear folding but an abrupt change in dip which might be interpreted as sub-seismic fault arrays (represented by the dashed lines) situated parallel, and relatively close (<1 km), to Fault G1. This could explain the absence of high amplitude and large wavelength stratal folding expected in an extensional growth fault characterised by high expansion indices (Section 3.3). Fault G2 is characterised by typical large wavelength normal folding of the seismic strata offset by the fault plane in both the footwall and hanging wall for distances up to 5 km. Further north along strike of the Kefira graben, the syncline is characterised by an inverse asymmetry where the depocentre is situated closer to Fault G1 (Fig. 5.6b). The footwall of Fault G1 does not exhibit any significant folding whereas the hanging wall is characterised by normal drag folds systematically increasing with depth. On the contrary, the strata offset by Fault G2 exhibit large wavelength normal folds of small amplitude in the footwall whereas the seismic reflections in the hanging wall are characterised by an array of closely spaced (<1 km) extensional faults parallel to Fault G2 and no obvious folding.

In summary, the growth faults that form the Kefira graben are characterised by large wavelength normal folding in the footwall of Fault G2 and no significant folding in the footwall of Fault G1. This might imply that the Fault G1 footwall displays passive behaviour as opposed to Fault G2. The hanging wall block in between these two faults exhibits large wavelength normal folds except if sub-parallel faults offset the stratigraphy in the near-field volume surrounding the main fault.

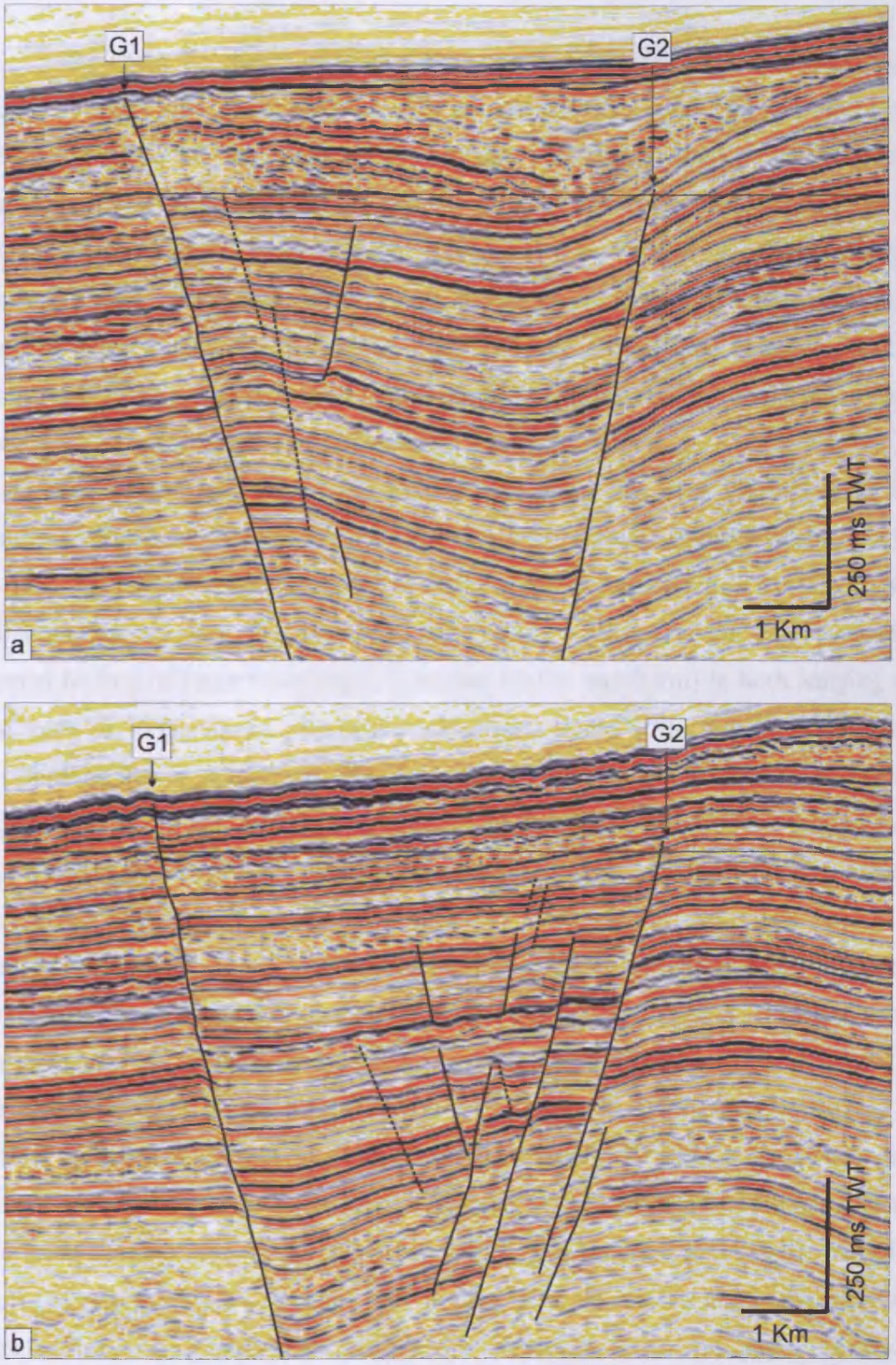

Fig. 5.6: Seismic section across the Kefira graben (a) inline 3801 and (b) further North inline 4101 showing the stratal folding surrounding Faults G1 and G2. Dashed lines represent suspected sub-seismic faults.

5.3.3.2 Fault G3

The upper tip region of Fault G3 has been interpreted to be syn-sedimentary, based on stratigraphic evidence such as growth packages and seismic stratal thickening as well as displacement analysis showing typical vertical throw distribution with high gradients (Section 3.4.2). The seismic reflections offset by this upper part of Fault G3 (Fig. 5.7) are characterised by no, or very small amplitude normal folding in the footwall. However, the strata adjacent to the fault plane in the hanging wall exhibit clear reverse drag folding. This folded interval could be interpreted to be a roll-over due to the sliding of sediments in the accommodation space created in the upper part of the fault (Hamblin 1965).

The central and lower part of the fault plane has been interpreted to have resulted from blind propagation although a certain amount of the displacement was accrued on this part when the fault was active at the surface (Section 3.6.1.1). Seismic reflections adjacent to this dominant part of the fault plane are characterised by normal folding of large wavelength (between 100 m and 2 km) in both hanging wall and footwall. In the central part between Horizons B and C, the normal stratal folding is approximately symmetrical. However, in the lower part of the fault, between Horizons D and F the folding is greater in the hanging wall. Normal folding in the close proximity of the fault plane is superimposed onto the limb of a N-S anticline (Fig. 5.7).

The distribution of stratal folding has been mapped along the entire length of Fault G3 on regularly spaced seismic sections (at least every 500 m). The occurrence of reverse and normal folds is overlain on the throw contour plot obtained for Fault G3 (Fig. 3.8c) represented as red and blue circles respectively in the hanging wall (Fig. 5.8) and in the footwall (Fig. 5.9). Both plots share common characteristics such as (1) normal drag folding is more frequent than reverse drag folding in both hanging wall and footwall distribution plots, (2) reverse folding is localised to the upper part of the plots (3) very few folds are observable in the lateral tip regions and in the relay zone situated between inlines 4050 and 4150. However, there are major observable differences that distinguish the footwall from the hanging wall. The frequency and the amplitude of folding are greater in the hanging wall than in the footwall. In addition to this, in the lower part of the fault plane, normal faulting is more important in the hanging wall than in the footwall.

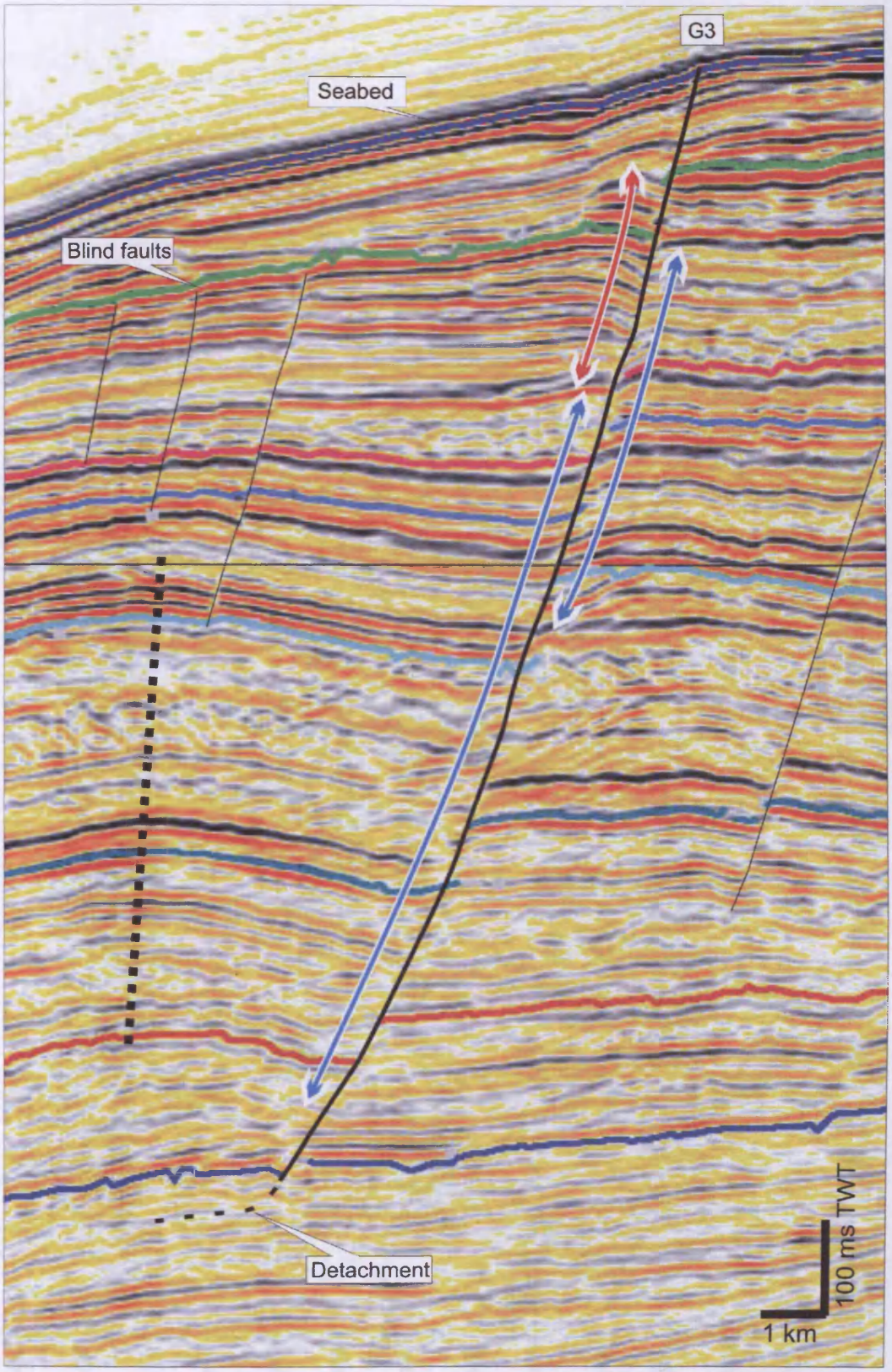

Fig. 5.7: Seismic section across Fault G3 showing the vertical distribution of stratal folding in the proximity of the fault plane. Red and blue arrows indicate reverse and normal folding respectively. The black dashed line represents the axial plane of the anticline due to detachment of the fault.

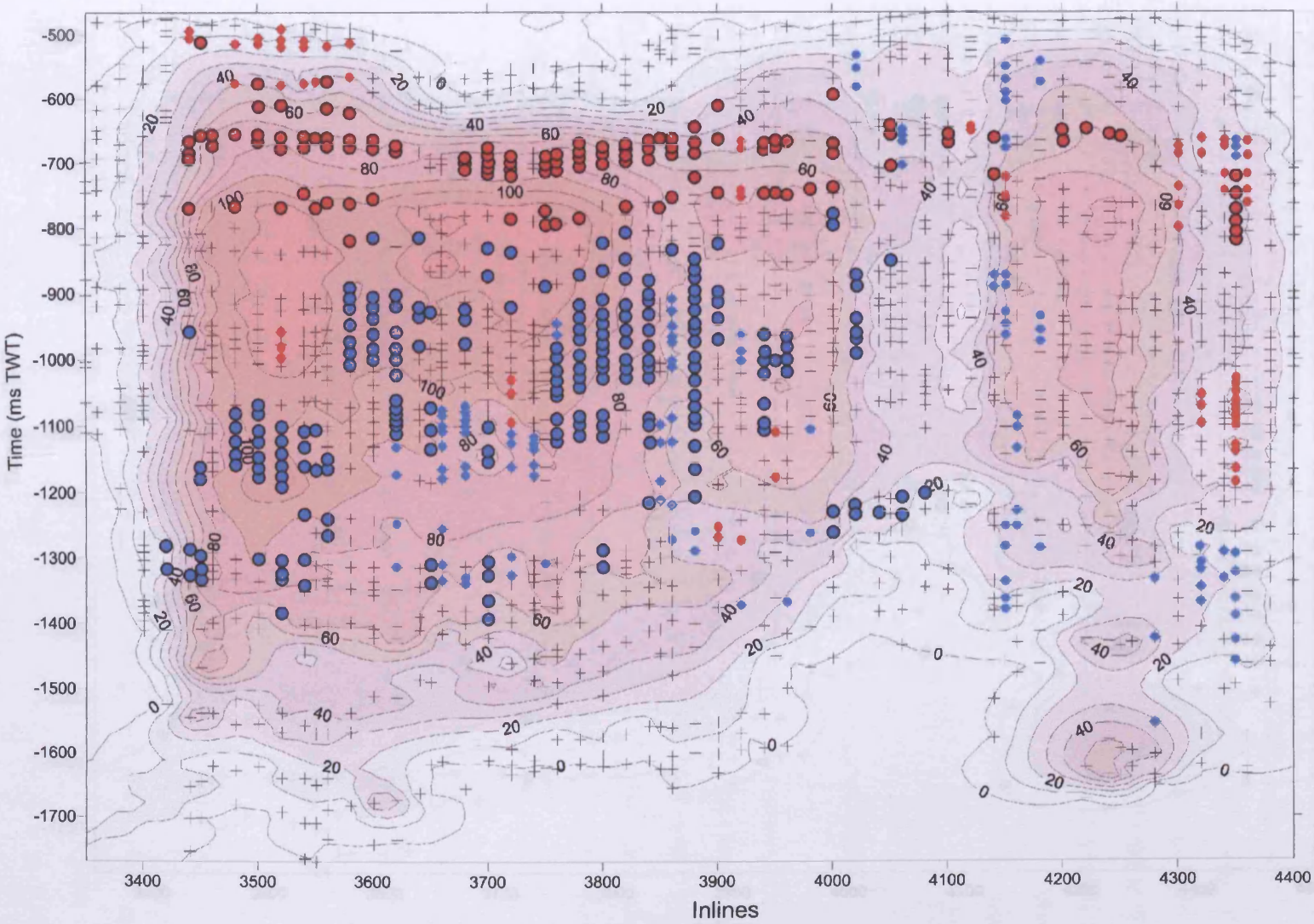

Fig. 5.8: Fault drag distribution in the hanging wall superimposed on the throw contour plot obtained for Fault G3 located in the Levant Basin (Fig. 3-8c). Reverse drag folding is indicated by the red circles, normal drags as blue circles. Diameter of circles indicates the amplitude of the folding.

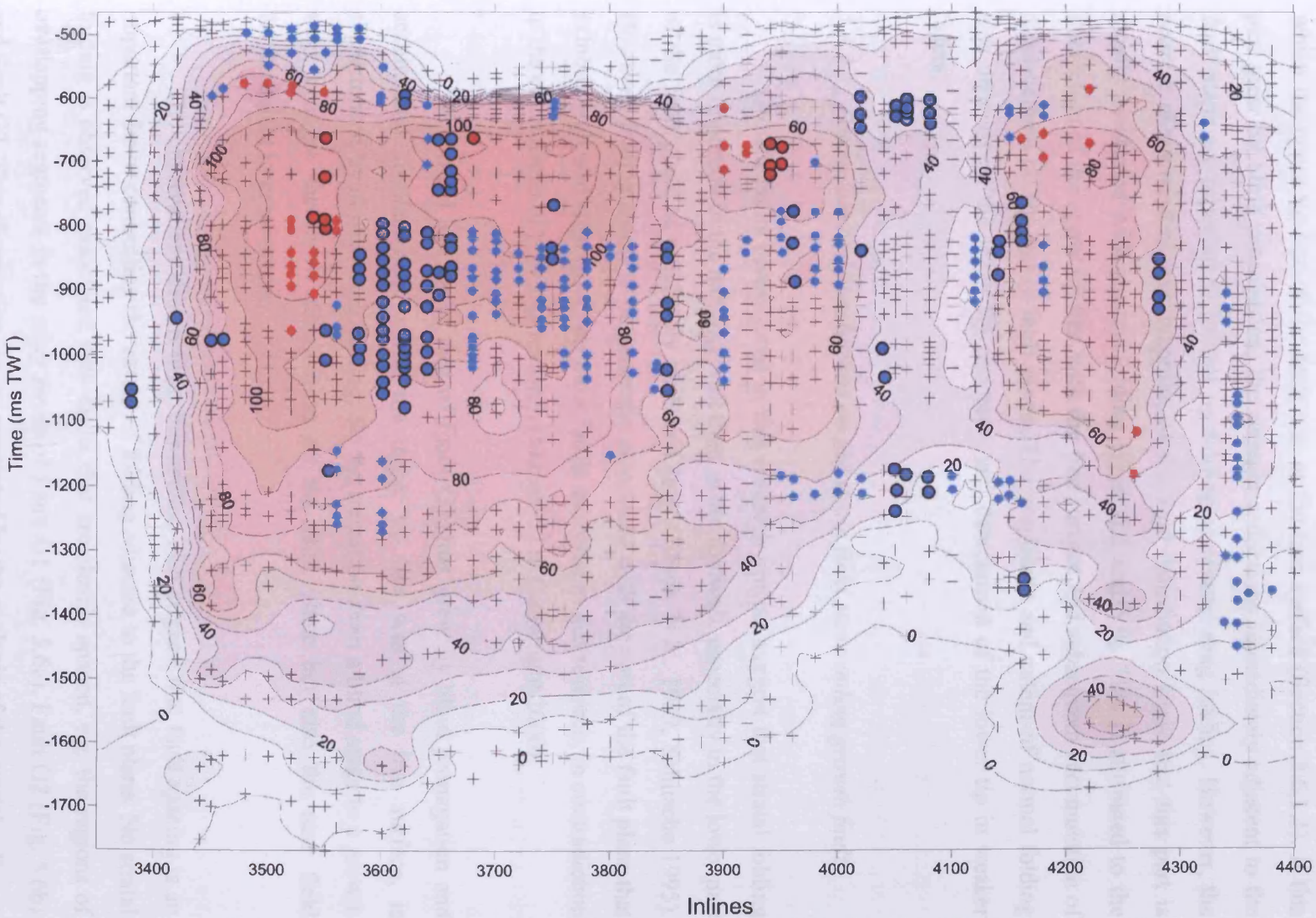

Fig. 5.9: Fault drag distribution in the footwall superimposed on the throw contour plot obtained for Fault G3 located in the Levant Basin (Fig. 3-8c). Reverse drag folding is indicated by the red circles, normal drags as blue circles. Diameter of circles indicates the amplitude of the folding.

The central and lower part of Fault G3 has been interpreted as a portion of the fault that grew entirely by blind propagation but accumulated most of its displacement whilst the upper tip line of the fault was at the free surface (Section 3.6.1.1). If this part grew by blind propagation, the seismic reflections immediately adjacent to the fault plane are expected to exhibit no folding or reverse drag folding. However, the seismic characteristics and mapping of the fold distribution show that this part is mostly associated with normal folding (Figs. 5.8 and 5.9). This is attributed to the interaction of the upper tip line with the free surface and subsequent accumulation of displacement on the entire fault plane. The amplitude and extent of normal folding also depends on the lower tip geometry and detachment of the lower tip in weaker layers.

5.3.3.3 Discussion and conclusions on the strain field surrounding growth faults

Growth faults investigated in this research project suggest that stratal folding is more important in the hanging wall than in the footwall, especially in the lower part of the fault plane as previously observed (e.g. Gibson et al. 1989, Schlische 1995). However, folding seems to be generally associated with the part of the fault plane that exhibits highest displacement on most faults analysed in this research, in contradiction to the conclusions of previous research (Mansfield & Cartwright 2000).

The central and lower part of Fault G3, that grew by blind propagation and accumulated displacement whilst the upper tip line was at the free surface, is characterised by normal drag folding. So the transition from a blind stage to a growth stage changes the throw distribution on the fault plane but also the near field displacement to great extent.

The observations drawn from this section also suggest that fault spacing is an important factor controlling the extent of folding adjacent to the fault plane. No stratal folding is observed associated with faults that are closely spaced, e.g. the regions of overlapping segments in the relay zones of Fault G1 (Fig. 5.6a), Fault G2 (Fig. 5.6b) and Fault G3. This observation is also supported by the analysis of the crestal collapse faults in the Espirito Santo Basin. The faults have been interpreted as blind faults that continued propagation until reaching the paleo-seabed, and were active at the free

surface at the moment of deposition of the upper part of Unit 1 (Section 4.6.1). The faults are characterised by an absence of folding in the seismic reflections immediately adjacent to the fault plane. All faults that form this complex graben system are closely spaced suggesting that the spacing of faulting might influence the development of folding. All these arguments suggest that stratal folding due to slip accumulation on extensional faults develops preferentially where no neighbouring fault offsets the strata in close proximity to the main fault.

5.3.4 Conclusions on the near field deformation

Blind faults studied in this thesis share a number of differences if compared with previous studies describing reverse folding. The simplest unrestricted blind faults are characterised by M-type throw profiles and an absence of seismically resolvable folding due to fault slip. Other blind faults are characterised by reverse folding of the strata offset by portions of faults that have accumulated higher displacement due to interaction with mechanical boundaries and exhibit C-type vertical throw profiles. The extent of the near field deformation surrounding those faults seems to be typically ¼ of the maximum length of the fault, that is half of the maximum distance predicted by previous studies (Barnett et al. 1987).

Other characteristics observed and discussed for blind faults analysed in this thesis are common with previous studies. Reverse folding is generally asymmetric and greater in the lower part of the hanging wall strata in close proximity to the fault plane. Factors influencing the displacement in the volume surrounding the fault include the displacement distribution on the fault plane and the interaction with mechanical boundaries.

Growth faults analysed during this research suggest that folding due to fault slip is generally greater in the hanging wall than in the footwall. However, the distribution of zones of higher displacement on the fault plane seems to control the wavelength, amplitude and frequency of stratal folding.

A change in kinematics, such as the transition from a blind fault to a syn-sedimentary fault, also influences greatly the ductile deformation in the close volume surrounding a fault.

Finally, the absence of drag folding on faults closely spaced to one other suggests that the spacing of the neighbouring fault controls the development of folding immediately adjacent to the main fault.

Chapter VI

Conclusions

6 CONCLUSIONS

Three separate case studies carried out in this research were analysed from 3D seismic datasets located in the Levant and Espirito Santo Basins in order to address the 3D evolution and kinematics of normal faults during propagation. The main findings from the three result chapters were combined and integrated to an analysis of the ductile deformation occurring in response to slip in the volume surrounding fault planes in the discussion chapter. This produced significant results that are synthesised in this conclusion chapter.

6.1 Blind faults

- This research regards a blind fault as a post-sedimentary fault that shows no evidence that it interacted with the free surface at any time during its evolution. This work documented several case studies of some small normal faults interpreted using high resolution 3D seismic data located in the Levant passive continental margin in order to illustrate some of the difficulties encountered in demonstrating that a fault is truly blind. This expanded considerably the small existing database of blind faults observed from 3D seismic data.

- Three main criteria are suggested to help the recognition of blind faults from 3D seismic data: (1) plunging upper tip line geometry, (2) presence of upper tip propagation folds, and (3) absence of stratigraphic or geomorphological evidence of the fault intersecting the free surface.

- A detailed analysis of the throw distribution showed more variations than previously suggested. Throw contour plots seem to confirm a growth of the El Arish array faults by radial propagation. However, these faults do not exhibit striking triangular or C type vertical throw profile as expected for blind faults

but mostly M-type or hybrid throw profiles. These simpler blind faults are characterised by an absence of seismically resolvable folding due to fault slip.

- Throw profiles are greatly influenced by fault interaction with major lithological boundaries or other faults acting as mechanical barriers to fault propagation. The consequence of these interactions is an increase in throw gradients and throw values in the large proximity of the zone of interaction and is not only localised to the tip region.

- Comparing the simpler individual unrestricted blind fault with the other blind faults that interacted with a mechanical boundary or another structure suggests that the propagation and establishment of the dimensions of the faults preceded the accumulation of displacement on the El Arish faults. This has wide implications for existing fault growth models.

- Restricted blind faults are characterised by reverse folding of the strata offset by portions of faults that have accumulated higher displacement due to interaction with mechanical boundaries and exhibit C-type vertical throw profiles. The extent of the near field deformation surrounding those faults seems to be typically ¼ of the maximum length of the fault, which is half of the maximum distance predicted by previous studies (Barnett et al. 1987).

- Reverse folding is generally asymmetric and greater in the lower part of the hanging wall strata in close proximity to the fault plane. Factors influencing the displacement in the volume surrounding the fault include the displacement distribution on the fault plane and the interaction with mechanical boundaries.

- Upper tip folding can span up to a third of the surface area of some of these faults. A systematic approach for measurements is recommended as including or omitting the tip folded zones for some faults can add a significant scatter in displacement-length relationship.

6.2 Small syn-sedimentary faults

- Coast parallel growth faults located on the shelf break of the Levant margin have been investigated in relation to the tectono-stratigraphic environment by using a high quality 3D seismic dataset. A detailed analysis of the 3D geometry and throw distribution on one particular fault (Fault G3) provided essential information on the kinematics of this fault. It also supplied fundamental insights into the transition from a blind stage to a growth stage and the consequences for fault growth behaviour in general.

- This study provided an exceptional example of a fault interpreted as resulting from the combination of radial propagation of the fault plane, hard linkage of individual blind segments and vertical bifurcations of the fault plane followed by a common growth history.

- T-z plots for this fault exhibit M-type profiles at the lateral tip regions and skewed M-type on the central portions. The skewed M-type profile consists of an upper part characterised by high positive throw gradients. This zone is characterised by stratigraphic growth packages and reverse drag folding of a roll-over type in the hanging wall of the fault plane. Constant low negative throw gradients are observed beneath the point of maximum throw value. This corresponds to a pre-kinematic sequence characterised by normal folding of the strata at close proximity of the fault plane.

- This research provided a unique example of a fault that underwent the transition from being a blind fault to a syn-sedimentary fault. This is based on two main indications: (i) similarity between the throw profiles in the lateral tip region of Fault G3 with those of blind faults, assuming that lateral segments can reflect the same process of propagation as central segments during the early stage of development of the fault and (ii) interpretation of the central portion of the T-z plots as a relict of the blind fault stage.

- Stratal folding due to fault slip is generally greater in the hanging wall than in the footwall. However, the distribution of zones of higher displacement on the fault plane seems to control the wavelength, amplitude and frequency of folding. A change in kinematics, such as the transition from a blind fault to a syn-sedimentary fault, also influences greatly the ductile deformation in the volume adjacent to the fault plane.

- The interaction of the fault plane with the free surface changes the position of the point of maximum displacement as well as the complete vertical distribution of throw values. The amount of displacement added on the fault plane after interaction with the free surface decreases downwards and away from the maximum displacement with almost a constant gradient.

- As a result of the above, most of the dimension of the fault was accumulated by post-sedimentary process and most of the displacement has been added afterwards by syn-sedimentary faulting. Although it lies within the interval predicted by scaling laws, this behaviour suggests an extremely step like growth trajectory.

- A significant overlap is observed between the throw gradients measured from syn-sedimentary faults and post-sedimentary parts that grew by blind propagation. The previously published maximum blind gradients might therefore be misleading in assessing accurately the kinematics of faults in general.

6.3 Reactivated faults

- The kinematics of small crestal collapse faults offsetting Cenozoic clastic sediments that overlie Cretaceous anticlines was investigated using high quality 3D seismic data from offshore Brazil. Some faults show evidence of reactivation in an extensional manner.

- An analysis of the 3D geometry of the fault network with respect to the different stratigraphic units, the Cretaceous anticlines and the salt tectonic evolution associated with detailed measurements of the throw distribution allowed the fault kinematics to be reconstructed.

- The reactivated faults are part of a network resulting from the uplift of a semi-elliptical dome of the Cretaceous sequence during Early Cenozoic deformation with very little simultaneous extension.

- Two different modes of reactivation have been recognised from this dataset. The main mode is a typical reactivation by upward propagation of pre-existing structures. The alternative mode of reactivation is termed reactivation by dip linkage. It involves the propagation of an individual fault initiated within the upper Units 2 and 3 during a second phase of faulting. Further propagation of this fault results in hard-linkage in the dip direction with the pre-existing faults.

- Reactivated faults are characterised by typical stepped profiles with a major break in throw gradients corresponding to the Eocene-Oligocene boundary. The throw profiles and contour plots exhibit a regular decrease in throw values and gradients up to the upper tip point for reactivated faults by upward propagation. Throw minima separate the upper parts from the pre-existing fault in the cases of reactivation by dip-linkage.

- For both modes, reactivation processes are selective and only occur on some portions of a number of faults. The factors that control or influence the preferential reactivation of some segments include: (i) preferential orientation of the pre-existing faults at 90 to 110 ° relative to the estimated principal stresses resulting in faulting phase 1, (ii) segmentation of the pre-existing network, (iii) maximum dimensions and throw values of pre-existing faults and (iv) basal tip line geometry associated with a detachment.

- The absence of stratal folding on closely spaced faults suggests that the spacing of neighbouring faults controls the development of folding immediately adjacent to the main fault. Proximity of neighbouring faults might be an important factor inhibiting the development of stratal folding in the ductile deformation field in the rock volume surrounding an extensional fault.

6.4 Implications and further work

This study explored the propagation and early evolution of small normal faults using high quality 3D seismic data. The conclusions drawn from this research have wide implications for the understanding of fault growth in general. A further comprehension of these processes and of the timing of fault activity gives insights into different fault growth models previously published. Improvement of our knowledge concerning fault initiation, propagation and reactivation can also have direct applicability to petroleum systems.

The more general applicability of this research could be greatly improved with the investigation of more 3D seismic datasets that have better well control, in order to investigate the effect of lithological variations on fault propagation in further detail. This would allow an analysis of the throw distribution at finest increment and relate precisely to the sedimentology. The knowledge gained from such a study should be tested in the field where fine variations in the sedimentology can be analysed. Small changes in fault characteristics such as dip, thickness of the fault zone, vertical throw distribution and stratal folding within the rock volume surrounding the fault plane could then be related to various fault propagation modes at small scale. Characteristics of fault propagation would therefore be tested in different lithologies. In particular, an analysis from the field of faults that underwent a transition from blind to syn-sedimentary growth would greatly improve our understanding of normal fault kinematics and behaviour during propagation.

References

7 REFERENCES

A

Anders, M. H. & Schlische, R. W. 1994. Overlapping faults, intrabasins highs, and the growth of normal faults. *Journal of Geology* 102, 165-180.

Armijo, R., Meyer, B., King, G. C. P., Rigo, A. & Papanastassiou, D. 1996. Quaternary evolution of the Corinth Rift and its implications for the Late Cenozoic evolution of the Aegean. *Geophysical Journal International* 126, 11-53.

Atkinson, B. K. 1987. Fracture mechanics of rocks. In: *Academic Press Geology Series* Chapter 1. Academic Press, London.

Austin, J. A. & Uchupi, E. 1982. Continental-Oceanic Crustal Transition Off Southwest Africa. *American Association of Petroleum Geologists Bulletin* 66(9), 1328 - 1347.

B

Back, S., Hocker, C., Brundiers, M. B. & Kukla, P. A. 2006. Three-dimensional-seismic coherency signature of Niger Delta growth faults: integrating sedimentology and tectonics. *Basin Research* 18(3), 323-337.

Badley, M. E. 1985. *Practical seismic interpretation.* International Human Resources Development Corporation, Boston. 266p.

Barnett, J. A. M., Mortimer, J., Rippon, J. H., Walsh, J. J. & Watterson, J. 1987. Displacement geometry in the volume containing a single normal fault. *American Association of Petroleum Geologists Bulletin* 71(8), 925-937.

Baudon, C. & Cartwright, J. A. in review. 3D seismic characterisation of an array of blind normal faults in the Levant Basin, Eastern Mediterranean. *Journal of Structural Geology.*

Beach, A. 1984. Structural evolution of the Witch Ground Graben. *Journal of the Geological Society London* 141, 621-628.

Bellahsen, N. & Daniel, J. M. 2005. Fault reactivation control on normal fault growth: an experimental study. *Journal of Structural Geology* 27(4), 769-780.

Bertoni, C. & Cartwright, J. A. 2006. Controls on the basinwide architecture of late Miocene (Messinian) evaporites on the Levant margin (Eastern Mediterranean). *Sedimentary Geology* 188-189, 93-114.

Bischke, R. E. 1994. Interpreting sedimentary growth structures from well log and seismic data (with examples). *American Association of Petroleum Geologists Bulletin* 78(6), 873-892.

Blair, T. C. & Bilodeau, W. L. 1988. Development of tectonic cyclothems in rift, pull-apart, and foreland basins: Sedimentary response to episodic tectonism. *Geology* 16(6), 517-520.

Blenkinsop, T. G. & Rutter, E. H. 1986. Cataclastic deformation of quartzite in the Moine thrust zone. *Journal of Structural Geology* 8(6), 669-681.

Bouroullec, R. 2001. Synsedimentary Fault Kinematics and Stratigraphic Response-Thesis. Unpublished CD thesis, Imperial College.

Brewer, J. A. & Smythe, D. K. 1984. MOIST and the continuity of crustal reflector geometry along the Caledonian-Appalachian orogen. *Journal of the Geological Society* 141, 105-120.

Bruce, C. H. 1973. Pressured Shale and Related Sediment Deformation: Mechanism for Development of Regional Contemporaneous Faults. *American Association of Petroleum Geologists Bulletin* 57(5), 878 - 886.

Burgmann, R., Pollard, D. D. & Martel, S. J. 1994. Slip distributions on faults: effects of stress gradients, inelastic deformation, heterogeneous host-rock stiffness, and fault interaction. *Journal of Structural Geology* 16(12), 1675-1690.

Butler, R. W. H., Holdsworth, R. E. & Lloyd, G. E. 1997. The role of basement reactivation in continental deformation. *Journal of the Geological Society London* 154(1), 69-71.

C

Carter, K. E. & Winter, C. L. 1995. Fractal nature and scaling of normal faults in the Espanola Basin, Rio Grande rift, New Mexico: implications for fault growth and brittle strain. *Journal of Structural Geology* 17(6), 863-873.

Cartwright, J. A., Bouroullec, R., James, D. & Johnson, H. D. 1998. Polycyclic motion history of some Gulf Coast growth faults from high-resolution displacement analysis. *Geology* 26(9), 819-822.

Cartwright, J. A. & Mansfield, C. S. 1998. Lateral displacement variation and lateral tip geometry of normal faults in the Canyonlands National Park, Utah. *Journal of Structural Geology* 20(1), 3-19.

Cartwright, J. A., Mansfield, C. S. & Trudgill, B. D. 1996. The growth of normal faults by segment linkage. In: *Modern Developments in Structural Interpretation, Validation and Modelling* (edited by

Buchanan, P. G. & Nieuwland, D. A.) 99. Geological Society Special Publication, 163-177.

Cartwright, J. A., Truddgill, B. D. & Mansfield, C. S. 1995. Fault growth by segment linkage: an explanation for scatter in maximum displacement and trace length data from the Canyonlands Grabens of SE Utah. *Journal of Structural Geology* 17(9), 1319-1326.

Castelltort, S., Pochat, S. & Van Den Driessche, J. 2004. Using T-Z plots as a graphical method to infer lithological variations from growth strata. *Journal of Structural Geology* 26(8), 1425-1432.

Chang, H. K., Kowsmann, R. O., Figueiredo, A. M. F. & Bender, A. A. 1992. Tectonics and stratigraphy of the East Brazil Rift system: an overview. *Tectonophysics* 213(1-2), 97-138.

Chapman, T. J. & Williams, G. 1984. Displacement-distance methods in the analysis of fold-thrust structures and linked-fault systems. *Journal of the Geological Society, London* 141, 121-128.

Childs, C., Easton, S. J., Vendeville, B. C., Jackson, M. P. A., Lin, S. T., Walsh, J. J. & Watterson, J. 1993. Kinematic analysis of faults in a physical model of growth faulting above a visous salt analogue. *Tectonophysics* 228, 313-329.

Childs, C., Nicol, A., Walsh, J. J. & Watterson, J. 1996a. Growth of vertically segmented normal faults. *Journal of Structural Geology* 18(12), 1389-1397.

Childs, C., Nicol, A., Walsh, J. J. & Watterson, J. 2003. The growth and propagation of synsedimentary faults. *Journal of Structural Geology* 25, 633-648.

Childs, C., Watterson, J. & Walsh, J. J. 1995. Fault overlap zones within developing normal fault systems. *Journal of the Geological Society, London* 152(3), 535-549.

Childs, C., Watterson, J. & Walsh, J. J. 1996b. A model for the structure and development of fault zones. *Journal of the Geological Society, London* 153(3), 337-340.

Clark, R. M. & Cox, S. J. D. 1996. A modern regression approach to determining fault displacement-length scaling relationships. *Journal of Structural Geology* 18(2-3), 147-152.

Cloos, E. 1955. Experimental analysis of fracture patterns. *Geological Society of America Bulletin* 66(3), 241-256.

Cloos, E. 1968. Experimental Analysis of Gulf Coast Fracture Patterns. *American Association of Petroleum Geologists Bulletin* 52(3), 420 - 444.

Cobbold, P. R., Meisling, K. E. & Mount, V. S. 2001. Reactivation of an obliquely rifted margin, Campos and Santos basins, southeastern Brazil. *American Association of Petroleum Geologists Bulletin* 85(11), 1925-1944.

Cohen, H. A. & McClay, K. 1996. Sedimentation and shale tectonics of the northwestern Niger Delta front. *Marine and Petroleum Geology* 13(3), 313-328.

Cowie, P. A. 1998. A healing-reloading feedback control on the growth rate of seismogenic faults. *Journal of Structural Geology* 20(8), 1075-1087.

Cowie, P. A. & Scholz, C. H. 1992a. Displacement-length scaling relationship for faults: data synthesis and discussion. *Journal of Structural Geology* 14(10), 1149-1156.

Cowie, P. A. & Scholz, C. H. 1992b. Growth of faults by accumulation of seismic slip. *Journal of Geophysical Research* 97(B7), 11 085-11 095.

Cowie, P. A. & Scholz, C. H. 1992c. Physical explanation for the displacement -length relationship of faults using a post-yield fracture mechanics model. *Journal of Structural Geology* 14(10), 1133-1148.

Cowie, P. A. & Shipton, Z. K. 1998. Fault tip displacement gradients and process zone dimensions. *Journal of Structural Geology* 20(8), 983-997.

Crans, W., Mandl, G. & Haremboure, J. 1980. On the theory of growth faulting: a geomechanical delta model based on gravity sliding. *Journal of Petroleum Geology* 2(3), 265-307.

Crook, A. J. L., Willson, S. M., Yu, J. G. & Owen, D. R. J. 2006. Predictive modelling of structure evolution in sandbox experiments. *Journal of Structural Geology* 28(5), 729-744.

D

Dawers, N. H. & Anders, M. H. 1995. Displacement-length scaling and fault linkage. *Journal of Structural Geology* 17(5), 607-614.

Dawers, N. H., Anders, M. H. & Scholz, C. H. 1993. Growth of normal faults: Displacement-length scaling. *Geology* 21, 1107-1110.

Demercian, S., Szatmari, P. & Cobbold, P. R. 1993. Style and pattern of salt diapirs due to thin-skinned gravitational gliding, Campos and Santos basins, offshore Brazil. *Tectonophysics* 228(3-4), 393-433.

Druckman, Y., Buchbinder, B., Martinotti, G. M., Tov, R. S. & Aharon, P. 1995. The buried Afiq Canyon (eastern Mediterranean, Israel): a case study of a Tertiary submarine canyon exposed in Late Messinian times. *Marine Geology* 123(3-4), 167-185.

Dugdale, D. S. 1960. Yielding of steel sheets containing slits. *Journal of the Mechanics and Physics of Solids* 8, 100-104.

Duval, B., Cramez, C. & Jackson, M. P. A. 1992. Raft tectonics in the Kwanza Basin, Angola. *Marine and Petroleum Geology* 9(4), 389-404.

E

Ebrom, D., Li, X. & McDonald, J. 1995. Bin spacing in land 3-D seismic surveys and horizontal resolution in time slices. *The Leading Edge* 1, 37-40.

Edwards, M. B. 1995. Differencial subsidence and preservation potential of shallow-water Tertiary sequences, northern Gulf Coast Bain, USA. In: *Sedimentary facies analysis: International Association of Sedimentologists Special Publication* (edited by Plint, A. G.) 22, 265-281.

Elliott, T. 1976. The energy balance and deformation mechanisms of thrust sheets. *Philosophical Transactions of the Royal Society of London* A283, 289-312.

Ellis, M. A. & Dunlap, W. J. 1988. Displacement variation along thrust faults: implications for the development of large faults. *Journal of Structural Geology* 10(2), 183-192.

Enfield, M. A. & Coward, M. P. 1987. The Structure of the West Orkney Basin, northern Scotland. *Journal of the Geological Society* 144, 871-884.

Evans, J. P. 1990. Thickness-displacement relationships for the fault zones. *Journal of Structural Geology* 12(8), 1061-1065.

F

Fiduk, J. C., Brush, E. R., Anderson, L. E., Gibbs, P. B. & Rowan, M. G. 2004. Salt deformation, magmatism, and hydrocarbon prospectivity in the Espirito Santo Basin, offshore Brazil. In: *Salt-sediment interactions and hydrocarbon prospectivity: Concepts, applications, and case studies for the 21st century, GCSSEPM 24th Annual Research Conference* (edited by Post, P. J., Olson, D. L., Lyons, K. T., Palmes, S. L., Harison, P. F. & Rosen, N. C.), 370-392.

Frey Martinez, J., Cartwright, J. A. & Hall, B. 2005. 3D seismic interpretation of slump complexes: examples from the continental margin of Israel. *Basin Research* 17, 83-108.

G

Garfunkel, Z. 1998. Constrains on the origin and history of the Eastern Mediterranean basin. *Tectonophysics* 298(1-3), 5-35.

Garfunkel, Z. & Almagor, G. 1985. Geology and structure of the continental margin off northern Israel and the adjacent part of the Levantine basin. *Marine Geology* 62, 105-131.

Garfunkel, Z. & Almagor, G. 1987. Active salt dome development in the Levant Basin, southest mediterranean. *Accad. Press. Orlando, Fl, US*, 263-300.

Garfunkel, Z., Arad, A., Bugge, T. & Almagor, G. 1979. The Palmahim disturbance and its regional setting. *Geological Survey of Israel Bulletin* 72.

Gawthorpe, R. L. & Hurst, J. M. 1993. Transfert zones in extensional basins: their structural style and influence on drainage development and stratigraphy. *Journal of the Geological Society, London* 150(6), 1137-1152.

Gawthorpe, R. L., Sharp, I., Underhill, J. R. & Gupta, S. 1997. Linked sequence stratigraphic and structural evolution of propagating normal faults. *Geology* 25(9), 795–798.

Gibbs, A. D. 1983. Balanced cross-section construction from seismic sections in areas of extensional tectonics. *Journal of Structural Geology* 5(2), 153-160.

Gibson, J. R., Walsh, J. J. & Watterson, J. 1989. Modelling of bed contours and cross-sections adjacent to planar normal faults. *Journal of Structural Geology* 11(3), 317-328.

Gillespie, P. A., Walsh, J. J. & Watterson, J. 1992. Limitations of dimension and displacement data from single faults and the consequences for data analysis and interpretation. *Journal of Structural Geology* 14(10), 1157-1172.

Gradmann, S., Hubscher, C., Ben-Avraham, Z., Gajewski, D. & Netzeband, G. 2005. Salt tectonics off northern Israel. *Marine and Petroleum Geology* 22(5), 597-611.

Granier, T. 1985. Origin, damping, and pattern of development of faults in granite. *Tectonics* 4(7), 721-737.

Grasemann, B., Martel, S. & Passchier, C. 2005. Reverse and normal drag along a fault. *Journal of Structural Geology* 27(6), 999-1010.

Gross, M. R. 1995. Fracture partitioning: Failure mode as a function of lithology in the Monterey Formation of coastal California. *Geological Society of America Bulletin* 107(7), 779-792.

Gross, M. R., Gutierrez-Alonso, G., Bai, T., Wacker, M. A., Collinsworth, K. B. & Behl, R. J. 1997. Influence of mechanical

stratigraphy and kinematics on fault scaling relations. *Journal of Structural Geology* 19(2), 171-183.

Gudmundsson, A. 1987. Geometry, formation and development of tectonic fractures on the Reykjanes Peninsula, southwest Iceland. *Tectonophysics* 139, 295-308.

Gupta, A. & Scholz, C. H. 2000. A model of normal fault interaction based on observations and theory. *Journal of Structural Geology* 22, 865-879.

H

Hamblin, W. K. 1965. Origine of "reverse drag" on the downthrow side of normal faults. *Geological Society of American Bulletin* 76, 1145-1164.

Hancock, P. L. & Barka, A. A. 1987. Kinematic indicators on active normal faults in Western Turkey. *Journal of Structural Geology* 9(5-6), 573-584.

Hansen, D. M. & Cartwright, J. 2006. The three-dimensional geometry and growth of forced folds above saucer-shaped igneous sills. *Journal of Structural Geology* 28(8), 1520-1535.

Hardin, F. R. & Hardin, G. C. J. 1961. Contemporaneous normal faults of gulf coast and their relation to flexures. *Bulletin of the Association of American Petroleum Geology* 45(2), 238-246.

Hardy, S. & McClay, K. 1999. Kinematic modelling of extensional fault-propagation folding. *Journal of Structural Geology* 21(7), 695-702.

Higgs, W. G. & Williams, G. 1987. Displacement efficiency of faults and fractures. *Journal of Structural Geology* 9(3), 371-374.

Holdsworth, R. E., Butler, C. A. & Roberts, A. M. 1997. The recognition of reactivation during continental deformation. *Journal of the Geological Society London* 154, 73-78.

Hsü, K. J., Montadert, L., Bernoulli, D., Cita, M. B., Erickson, A., Garrison, R. E., Kidd, R. B., Mélière, F., Muller, C. & Wright, R. H. 1978. Initial Reports of the Deep Sea Drilling Project (edited by U.S. Government Printing Office, W. D. C.) 42, 1249.

Huggins, P., Watterson, J., Walsh, J. J. & Childs, C. 1995. Relay zone geometry and displacement transfer between normal faults recorded in coal-mine plans. *Journal of Structural Geology* 17(12), 1741-1755.

Hull, J. 1988. Thickness-displacement relationships for deformation zones. *Journal of Structural Geology* 10(4), 431-435.

Hull, J. 1989. Thickness-displacement relationships for deformation zones: Reply. *Journal of Structural Geology* 11(8), 1053-1054.

I

Imber, J., Tuckwell, G. W., Childs, C., Walsh, J. J., Manzocchi, T., Heath, A. E., Bonson, C. G. & Strand, J. 2004. Three-dimensional distinct element modelling of relay growth and breaching along normal faults. *Journal of Structural Geology* 26(10), 1897-1911.

J

Jackson, C. A. L., Gawthorpe, R. L. & Sharp, I. R. 2006. Style and sequence of deformation during extensional fault-propagation folding: examples from the Hammam Faraun and El-Qaa fault blocks, Suez Rift, Egypt. *Journal of Structural Geology* 28(3), 519-535.

Jackson, J. & Leeder, M. 1994. Drainage systems and the development of normal faults: an example from Pleasant Valley, Nevada. *Journal of Structural Geology* 16(8), 1041-1059.

Jackson, J. & McKenzie, D. 1983. The geometrical evolution of normal fault systems. *Journal of Structural Geology* 5(5), 471-482.

Jackson, J. A. 1980. Reactivation of basement faults and crustal shortening in orogenic belts. *Nature* 283(5745), 343-346.

Jackson, M. P. A. 1995. Retrospective salt tectonics. In: *Salt Tectonics, A Global Perspective* (edited by Jackson, M. P. A., Roberts, D. G. & Snelson, S.) 65. American Association of Petroleum Geologists Memoir, 1-28.

Jamison, W. R. & Stearns, D. W. 1982. Tectonic deformation of Wingate sandstone, Colorado national monument. *American Association of Petroleum Geologists. Bulletin* 66(12), 2584-2608.

K

Kelly, P. G., Peacock, D. C. P., Sanderson, D. J. & McGurk, A. C. 1999. Selective reverse-reactivation of normal faults, and deformation around reverse-reactivated faults in the Mesozoic of the Somerset coast. *Journal of Structural Geology* 21(5), 493-509.

Kim, Y.-S., Andrews, J. R. & Sanderson, D. J. 2001. Reactivated strike-slip faults: examples from north Cornwall, UK. *Tectonophysics* 340(3-4), 173-194.

Kim, Y.-S. & Sanderson, D. J. 2005. The relationship between displacement and length of faults: a review. *Earth-Science Reviews* 68(3-4), 317-334.

Knott, S. D. 1994. Fault zone thickness versus displacement in the Permo-Triassic sandstones of NW England. *Journal of the Geological Society, London* 151(1), 17-25.

Krantz, R. W. 1988. Multiple fault sets and three-dimensional strain: theory and application. *Journal of Structural Geology* 10(3), 225-237.

Krantz, R. W. 1991. Measurements of friction coefficients and cohesion for faulting and fault reactivation in laboratory models using sand and sand mixtures. *Tectonophysics* 188(1-2), 203-207.

Krueger, S. W. & Grant, N. T. 2006. Evolution of fault-related folds in the contrational toe of the deepwater Niger Delta. In: *April 9-12, AAPG 2006 Annual Convention Abstracts*, Houston, Texas.

L

Larsen, P. H. 1988. Relay structures in a Lower Permian basement-involved extension system, East Greenland. *Journal of Structural Geology* 10(1), 3-8.

Lisle, R. J. & Srivastava, D. C. 2004. Test of the frictional reactivation theory for faults and validity of fault-slip analysis. *Geology* 32(7), 569–572.

M

Maerten, L., Willemse, E. J. M., Pollard, D. D. & Rawnsley, K. 1999. Slip distributions on intersecting normal faults. *Journal of Structural Geology* 21, 259-271.

Manighetti, I., King, G. C. P., Gaudemer, Y., Scholz, C. H. & Doubre, C. 2001. Slip accumulation and lateral propagation of active normal faults in Afar. *Journal of Geophysical Research* 106(B7), 13667-13696.

Mansfield, C. S. 1996. Fault growth by segment linkage. PhD thesis, University of London.

Mansfield, C. S. & Cartwright, J. A. 1996. High resolution fault displacement mapping from three-dimensional seismic data: evidence for dip linkage during fault growth. *Journal of Structural Geology* 18(2/3), 249-263.

Mansfield, C. S. & Cartwright, J. A. 2000. Stratal fold patterns adjacent to normal faults: observations from the Gulf of Mexico. In: *Forced folds and fractures* (edited by Cosgrove, J. W. & Ameen, M. S.) 169. The Geological Society of London.

Mansfield, C. S. & Cartwright, J. A. 2001. Fault growth by linkage: observations and implications from analogue models. *Journal of Structural Geology* 23, 745-763.

Marchal, D., Guiraud, M. & Rives, T. 2003. Geometric and morphologic evolution of normal fault planes and traces from 2D to 4D data. *Journal of Structural Geology* 25(1), 135-158.

Marrett, R. & Allmendinger, R. W. 1991. Estimates of strain due to brittle faulting: sampling of fault populations. *Journal of Structural Geology* 13(6), 735-738.

Marrett, R. & Allmendinger, R. W. 1992. Amount of extension on "small" faults: an exemple from the Viking graben. *Geology* 20, 47-50.

Martel, S. J., Pollard, D. D. & Segall, P. 1988. Development of simple strike-slip fault zones, Mount Abbot quadrangle, Sierra Nevada, California. *Geological Society of American Bulletin* 100(9), 1451-1465.

McClay, K. R. 1990. Extensional fault systems in sedimentary basins: a review of analogue model studies. *Marine and Petroleum Geology* 7(3), 206-233.

McCulloh, R. P. 1988. Differencial Fault-Related Early Miocene Sedimentation, Bayou Hebert Area, Southwestern Louisiana. *American Association of Petroleum Geologists Bulletin* 72(4), 477-492.

Meisling, K. E., Cobbold, P. R. & Mount, V. S. 2001. Segmentation of an obliquely rifted margin, Campos and Santos basins, southeastern Brazil. *American Association of Petroleum Geologists Bulletin* 85(11), 1903-1924.

Meyer, V., Nicol, A., Childs, C., Walsh, J. J. & Watterson, J. 2002. Progressive localisation of strain during the evolution of a normal fault population. *Journal of Structural Geology* 24(8), 1215-1231.

Mohriak, W. U., Palagi, P. R. & Mello, M. R. 1998. Tectonic Evolution of South Atlantic Salt Basins. *American Association of Petroleum Geologists Bulletin* 82(10), 1945.

Morewood, N. C. & Roberts, G. P. 1999. Lateral propagation of the surface trace of the South Alkyonides normal fault segment, central Greece: its impact on models of fault growth and displacement-length relationships. *Journal of Structural Geology* 21(6), 635-652.

Morley, C. K. 1999. How successful are analogue models in addressing the influence of pre-existing fabrics on rift structure? *Journal of Structural Geology* 21(8-9), 1267-1274.

Morley, C. K., Nelson, R. A., Patton, T. L. & Munn, S. G. 1990. Transfert zones in the east african rift system and their relevance to hydrocarbon exploration in rifts. *American Association of Petroleum Geologists Bulletin* 74(8), 1234-1253.

Muir Wood, R. & Mallard, D. J. 1992. When is a fault 'extinct'? *Journal of the Geological Society London* 149(2), 251-256.

Muraoka, H. & Kamata, H. 1983. Displacement distribution along minor fault traces. *Journal of Structural Geology* 5(5), 483-495.

N

Nelson, M. 2007. 3D geometry and kinematics of non-colinear fault intersections. Unpublished manuscript thesis, Cardiff University.

Netzeband, G. L., Hubscher, C. P. & Gajewski, D. 2006. The structural evolution of the Messinian evaporites in the Levantine Basin. *Marine Geology* 230(3-4), 249-273.

Nicol, A., Gillespie, P. A., Childs, C. & Walsh, J. J. 2002. Relay zones between mesoscopic thrust faults in layered sedimentary sequences. *Journal of Structural Geology* 24(4), 709-727.

Nicol, A., Walsh, J., Berryman, K. & Nodder, S. 2005. Growth of a normal fault by the accumulation of slip over millions of years. *Journal of Structural Geology* 27(2), 327-342.

Nicol, A., Walsh, J. J., Watterson, J. & Gillespie, P. A. 1996a. Fault size distributions- are they really power-law? *Journal of Structural Geology* 18(2/3), 191-197.

Nicol, A., Walsh, J. J., Watterson, J. & Underhill, J. R. 1997. Displacement rates of normal faults. *Nature* 390, 157-159.

Nicol, A., Watterson, J., Walsh, J. J. & Childs, C. 1996b. The shapes, major axis orientations and displacement patterns of fault surfaces. *Journal of Structural Geology* 18(2/3), 235-248.

O

Ocamb, R. D. 1961. Growth faults of south Louisiana. *Transactions- Gulf coast association of geological societies* 11, 139-175.

Ojeda, H. A. O. 1982. Structural Framework, Stratigraphy, and Evolution of Brazilian Marginal Basins. *American Association of Petroleum Geologists Bulletin* 66(6), 732-749.

Opheim, J. A. & Gudmundsson, A. 1989. Formation and geometry of fractures, and related volcanism, of the Krafla fissures swarm, northeast Iceland. *Geological Society of America Bulletin* 101, 1608-1622.

Otsuki, K. 1978. On the relationship between the width of shear zone and the displacement along fault. *Journal of the Geological Society of Japan* 84, 661-669.

P

Parker, T. J. & McDowell, A. N. 1951. Scale models as guide to interpretation of salt-dome faulting. *American Association of Petroleum Geologists Bulletin* 35, 2076-2086.

Patton, T. L., Logan, J. M. & Friedman, M. 1998. Experimentally generated normal faults in single-layer and multilayer limestone specimens at confining pressure. *Tectonophysics* 295(1-2), 53-77.

Peacock, D. C. P. 1991. Displacements and segment linkage in strike-slip fault zones. *Journal of Structural Geology* 13(9), 1025-1035.

Peacock, D. C. P., Knipe, R. J. & Sanderson, D. J. 2000. Glossary of normal faults. *Journal of Structural Geology* 22, 291-305.

Peacock, D. C. P. & Parfitt, E. A. 2002. Active relay ramps and normal fault propagation on Kilauea Volcano, Hawaii. *Journal of Structural Geology* 24, 729-742.

Peacock, D. C. P. & Sanderson, D. J. 1991. Displacements, segment linkage and relay ramps in normal fault zones. *Journal of Structural Geology* 13(6), 721-733.

Peacock, D. C. P. & Sanderson, D. J. 1994. Geometry and development of relay ramps in normal fault systems. *AAPG* 78(2).

Peacock, D. C. P. & Sanderson, D. J. 1996. Effects of propagation rate on displacement variations along faults. *Journal of Structural Geology* 18(2/3), 311-320.

Peacock, D. C. P. & Zhang, X. 1994. Field examples and numerical modelling of oversteps and bends along normal faults in cross-section. *Tectonophysics* 234, 147-167.

Petersen, K., Clausen, O. R. & Korstgard, J. A. 1992. Evolution of a salt-related listric growth fault near the d-1 well, block 5605, danish north sea: displacement history and salt kinematics. *Journal of Structural Geology* 14(5), 565-577.

Pollard, D. D. & Aydin, A. 1984. Propagation and linkage of oceanic ridge segments. *Journal of Geophysical Research* 89(B12), 10 017-10 028.

Pollard, D. D. & Segall, P. 1987. Theoretical displacements and stresses near fractures in rock: with applications to faults, joints, veins,

dykes and solution surfaces. In: *Fracture Mechanics of Rock* (edited by Atkinson, B.). Academic Press, London, 277-349.

Poulimenos, G. 2000. Scaling properties of normal fault populations in the western Corinth Graben, Greece: implications for fault growth in large strain settings. *Journal of Structural Geology* 22(3), 307-322.

Q

R

Ramsay, J. G. & Huber, M. I. 1987. *The techniques of modern structural geology. Volume 2: Folds and fractures*. Academic press, London.

Reches, Z. & Eidelman, A. 1995. Drag along faults. *Tectonophysics* 247, 145-156.

Reches, Z. & Lockner, D. A. 1994. Nucleation and growth of faults in brittle rocks. *Journal of Geophysical Research* 99(B9), 18 159-18 173.

Richard, P. & Krantz, R. W. 1991. Experiments on fault reactivation in strike-slip mode. *Tectonophysics* 188(1-2), 117-131.

Rippon, J. H. 1985. Contoured patterns of the throw and hade of normal faults in the Coal Measures (Wesphalian) of the north-east Derbyshire. *Proceedings of the yorkshire geological society* 45(3), 147-161.

Rodger, M., Watts, A. B., Greenroyd, C. J., Peirce, C. & Hobbs, R. W. 2006. Gravity anomalies, crustal structure, and flexure at the NE Brazil rifted continental margin. In: *Geophysical Research Abstract* 8, p. 07260.

Rowan, M. G., Hart, B. S., Nelson, S., Flemings, P. B. & Trudgill, B. D. 1998. Three-dimensional geometry and evolution of a salt-related growth-fault array: Eugene Island 330 field, offshore Louisiana, Gulf of Mexico. *Marine and Petroleum Geology* 15(4), 309-328.

Rowan, M. G., Peel, F. J. & Vendeville, B. C. 2004. Gravity-driven foldbelts on passive margins. In: *Thrust tectonics and hydrocarbon systems: AAPG Memoir 82* (edited by McClay, K. R.), 157-182.

Rykkelid, E. & Fossen, H. 2002. Layer rotation around vertical fault overlap zones: observations from seismic data, field examples, and physical experiments. *Marine and Petroleum Geology* 19(2), 181-192.

S

Schlische, R. W. 1991. Half-graben basin filling models: new constraints on continental extensional basin development. *Basin Research* 3, 123-141.

Schlische, R. W. 1995. Geometry and origin of fault-related folds in extensional settings. *American Association of Petroleum Geologists. Bulletin* 79(11), 1661-1678.

Schlische, R. W., Young, S. S., Ackermann, R. V. & Gupta, A. 1996. Geometry and scaling relations of a population of very small rift-related normal faults. *Geology* 24(8), 683-686.

Scholz, C. H. 1987. Wear and gouge formation in brittle faulting. *Geology* 15, 495-497.

Scholz, C. H. & Cowie, P. A. 1990. Determination of total strain from faulting using slip measurements. *Nature* 346, 837-839.

Scholz, C. H., Dawers, N. H., Yu, J.-Z., Anders, M. H. & Cowie, P. A. 1993. Fault growth and fault scaling laws: preliminary results. *Journal of Geophysical Research* 98(B12), 21951-21961.

Schultz, R. A. 2000. Fault-population statistics at the Valles Marineris Extensional Province, Mars: implications for segment linkage, crustal strains, and its geodynamical development. *Tectonophysics* 316(1-2), 169-193.

Scott, D. R., Marone, C. J. & Sammis, C. G. 1994. The apparent friction of granular fault gouge in sheared layers. *Journal of Geophysical Research* 99(B4), 7231-7246.

Segall, P. & Pollard, D. D. 1980. Mechanics of discontinuous Faults. *Journal of Geophysical Research* 85(B8), 4337-4350.

Segall, P. & Pollard, D. D. 1983. Nucleation and growth of strike-slip faults in granite. *Journal of Geophysical Research* 88, 555-568.

Sibson, R. H. 1985. A note on fault reactivation. *Journal of Structural Geology* 7(6), 751-754.

T

Tearpock, D. & Bischke, R. E. 1991. *Applied subsurface geological mapping.* Prentice Hall, New York.

Thorsen, C. E. 1963. Age of growth faulting in the southeast Louisiana. *Transactions- Gulf coast association of geological societies* 13, 103-110.

Tibor, G. & Ben-Avraham, Z. 1992. Late Tertiary seismic facies and structures of the levant passive margin off central Israel, eastern Mediterranean. *Marine Geology* 105, 253-273.

Tibor, G. & Ben-Avraham, Z. 2005. Late Tertiary paleodepth reconstruction of the Levant margin off Israel. *Marine Geology* 221(1-4), 331-347.

Trudgill, B. D. & Cartwright, J. A. 1994. Relay ramp forms and normal fault linkages, Canyonlands National Park, Utah. *Bulletin of the Geological Society of America* 106, 1143-1157.

Twiss, R. J. & Moore, E. M. 1992. *Structural geology*. Freeman, New York.

U

V

Vendeville, B. C. & Jackson, M. P. A. 1992a. The fall of diapirs during thin-skinned extension. *Marine and Petroleum Geology* 9(4), 354-371.

Vendeville, B. C. & Jackson, M. P. A. 1992b. The rise of diapirs during thin-skinned extension. *Marine and Petroleum Geology* 9(4), 331-354.

Vetel, W., Le Gall, B. & Walsh, J. J. 2005. Geometry and growth of an inner rift fault pattern: the Kino Sogo Fault Belt, Turkana Rift (North Kenya). *Journal of Structural Geology* 27(12), 2204-2222.

Villemin, T. & Sunwoo, C. 1987. Distribution logarithmique self-similaire des rejets et longueurs de failles: exemple du Bassin Houiller Lorrain. *Comptes Rendus de l'Academie des Sciences Paris* Serie II, 1309-1312.

W

Wadsworth, J. A. H. 1953. Percentage of thinning chart-new technique in subsurface geology. *American Association of Petroleum Geologists Bulletin* 37(1), 158-162.

Walsh, J. J., Bailey, W. R., Childs, C., Nicol, A. & Bonson, C. G. 2003. Formation of segmented normal faults: a 3-D perspective. *Journal of Structural Geology* 25, 1251-1262.

Walsh, J. J., Nicol, A. & Childs, C. 2002a. An alternative model for the growth of faults. *Journal of Structural Geology* 24, 1669-1675.

Walsh, J. J., Nicol, A. & Childs, C. 2002b. A new model for the growth of faults. *EAGE 64th Conference & Exhibition_ Florence, Italie.*

Walsh, J. J. & Watterson, J. 1987. Distributions of cumulative displacement and seismic slip on a single normal fault surface. *Journal of Structural Geology* 9(8), 1039-1046.

Walsh, J. J. & Watterson, J. 1988. Analysis of the relationship between displacements and dimensions of faults. *Journal of Structural Geology* 10(3), 239-247.

Walsh, J. J. & Watterson, J. 1989. Displacement gradients on fault surfaces. *Journal of Structural Geology* 11(3), 307-316.

Walsh, J. J. & Watterson, J. 1990. New methods of fault projection for coalmine planning. *Proceedings of the yorkshire geological society* 48(2), 209-219.

Walsh, J. J. & Watterson, J. 1991. Geometric and kinematic coherence and scale effects in normal fault systems. In: *The Geometry of Normal Faults* (edited by Roberts, A. M., Yielding, G. & Freeman, B.). Geological Society of London, Special Publication 56, 193-203.

Walsh, J. J., Watterson, J., Bailey, W. R. & Childs, C. 1999. Fault relays, bends and branch-lines. *Journal of Structural Geology* 21(8-9), 1019-1026.

Walsh, J. J., Watterson, J., Childs, C. & Nicol, A. 1996. Ductile strain effects in the analysis of seismic interpretations of normal fault systems. In: *Modern Developments in Structural Interpretation, Validation and Modelling* (edited by Buchanan, P. G. & Nieuwland, D. A.) 99. Geological Society Special Publication, 27-40.

Watterson, J. 1986. Fault dimensions, displacements and growth. *Pure and Applied Geophysics* 124(1/2), 365-373.

Weber, K. J. 1987. Hydrocarbon distribution patterns in Nigerian growth fault structures controlled by structural style and stratigraphy. *Journal of Petroleum Science and Engineering* 1(2), 91-104.

Wendlandt, E. A., Shelby, T. H. & Bell, J. S. 1946. Hawkins field, Wood County, Texas. *American Association of Petroleum Geologists Bulletin* 30, 1830-1856.

Wernicke, B. & Burchfiel, B. C. 1982. Modes of extensional tectonics. *Journal of Structural Geology* 4(2), 105-115.

White, S. H., Bretan, P. G. & Rutter, E. H. 1986. Fault-zone reactivation: kinematics and mechanisms. *Philosophical Transactions of the Royal Society of London* A317, 81-97.

White, S. H. & Green, P. F. 1986. Tectonic development of the Alpine fault zone, New Zealand: A fission-track study. *Geology* 14(2), 124-127.

Wilkins, S. J. & Gross, M. R. 2002. Normal fault growth in layered rocks at Split Mountain, Utah: influence of mechanical stratigraphy on

dip linkage, fault restriction and fault scaling. *Journal of Structural Geology* 24(9), 1413-1429.

Willemse, E. J. M., Pollard, D. D. & Aydin, A. 1996. Three-dimensional analyses of slip distributions on normal fault arrays with consequences for fault scaling. *Journal of Structural Geology* 18(2/3), 295-309.

Williams, G. & Chapman, T. J. 1983. Strains developed in the hangingwalls of thrusts due to their slip/propagation rate: a dislocation model. *Journal of Structural Geology* 5(6), 563-571.

Withjack, M. O. & Callaway, S. 2000. Active normal faulting beneath a salt layer: an experimental study of deformation patterns in the cover sequence. *American Association of Petroleum Geologists Bulletin* 84(5), 627 - 651.

Withjack, M. O. & Scheiner, C. 1982. Fault patterns associated with domes- An experimental and analytical study. *American Association of Petroleum Geologists Bulletin* 66(3), 302-316.

Wojtal, S. F. 1994. Fault scaling laws and the temporal evolution of fault systems. *Journal of Structural Geology* 16(4), 603-612.

Wojtal, S. F. 1996. Changes in fault displacement populations correlated to linkage between faults. *Journal of Structural Geology* 18(2-3), 265-279.

Woodward, N. B., Wojtal, S., Paul, J. B. & Zadins, Z. Z. 1988. Partitioning of deformation within several external thrust zones of the appalachian orogen. *Journal of Geology* 96, 351-361.

X

Xiao, H.-B. & Suppe, J. 1992. Origine of rollover. *American Association of Petroleum Geologists. Bulletin* 76(4), 509-529.

Y

Z

Appendices

8 APPENDICES

This section aims to present additional maps and results appended to Chapters 2, 3 and 4. Time structure and dip maps of key horizons help to visualise the 3D geometry of the fault network that characterise the 3D seismic surveys located in the Levant and Espirito Santo Basins. The additional throw distribution plots presented in this section were not included in the results chapters for reasons of brevity. Only the T-z plots are included in this appendices chapter for the same reasons. However, the measurements that led to the construction of all T-z plots in this thesis are displayed in an electronic version provided by a CD attached to the thesis.

8.1 Maps

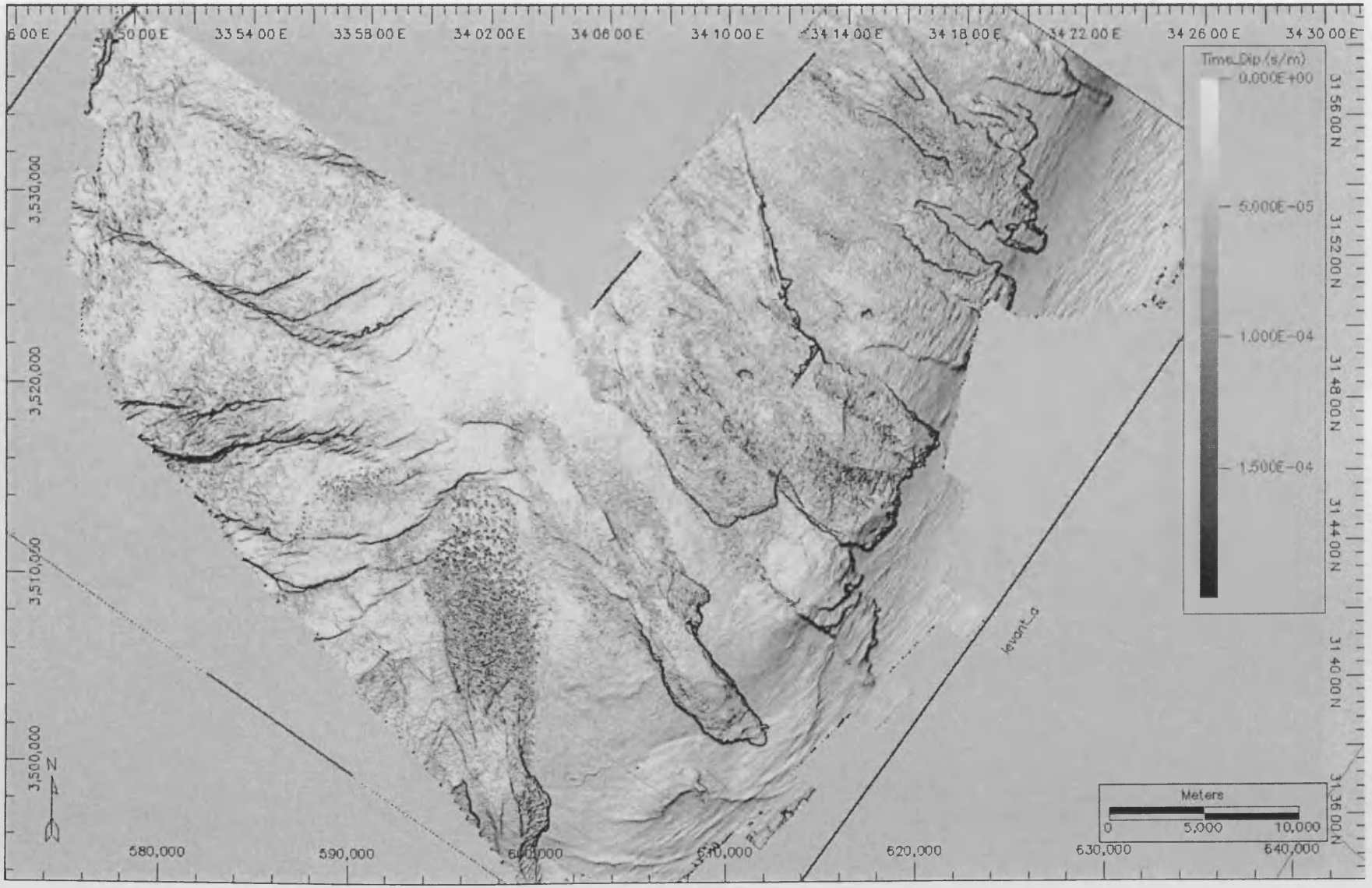

Fig. 8.1: Levant survey. Dip map of the Seabed horizon

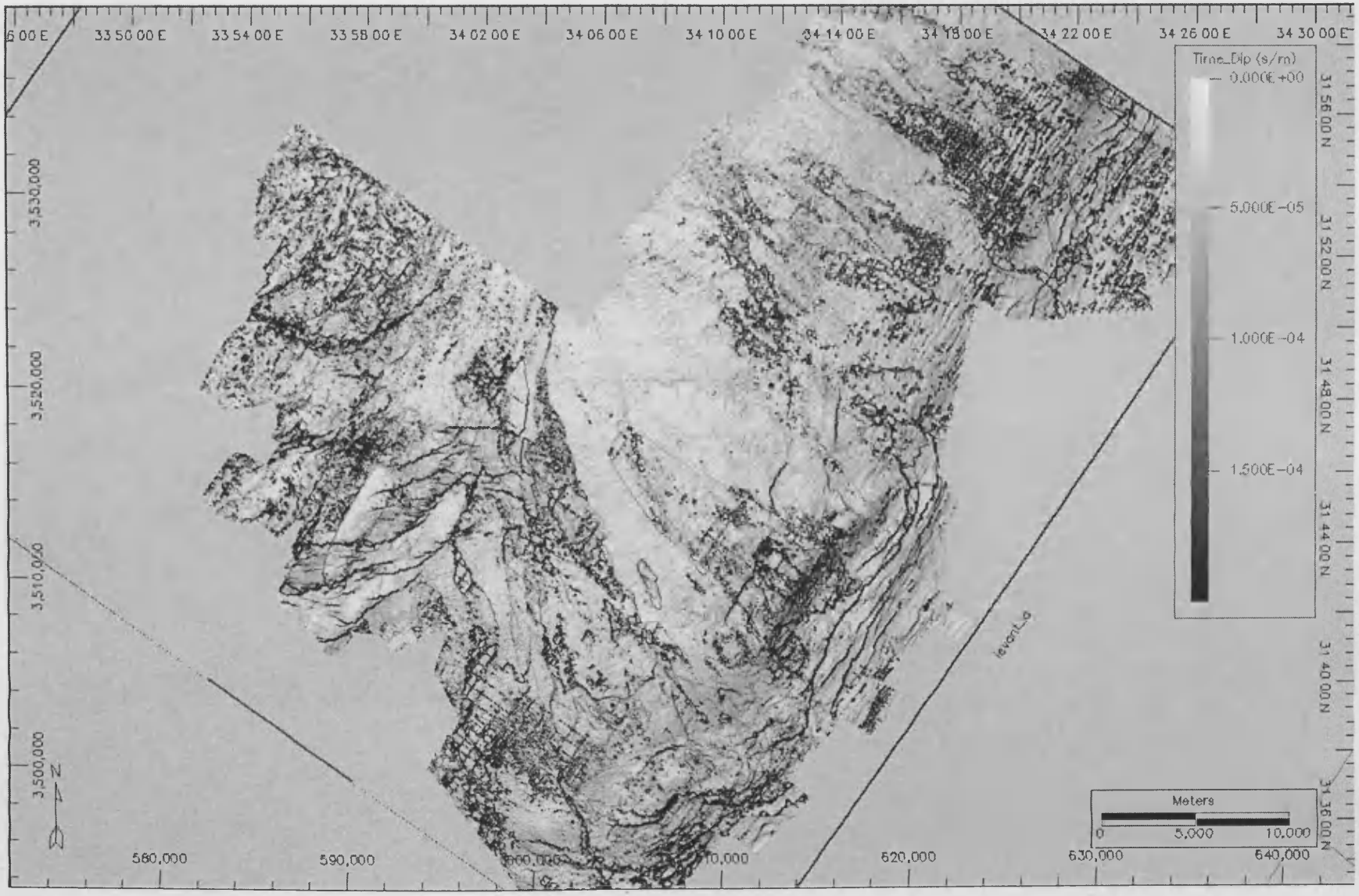

Fig. 8.2: Levant survey. Dip map of Horizon A

Fig. 8.3: Levant survey. Dip map of Horizon B

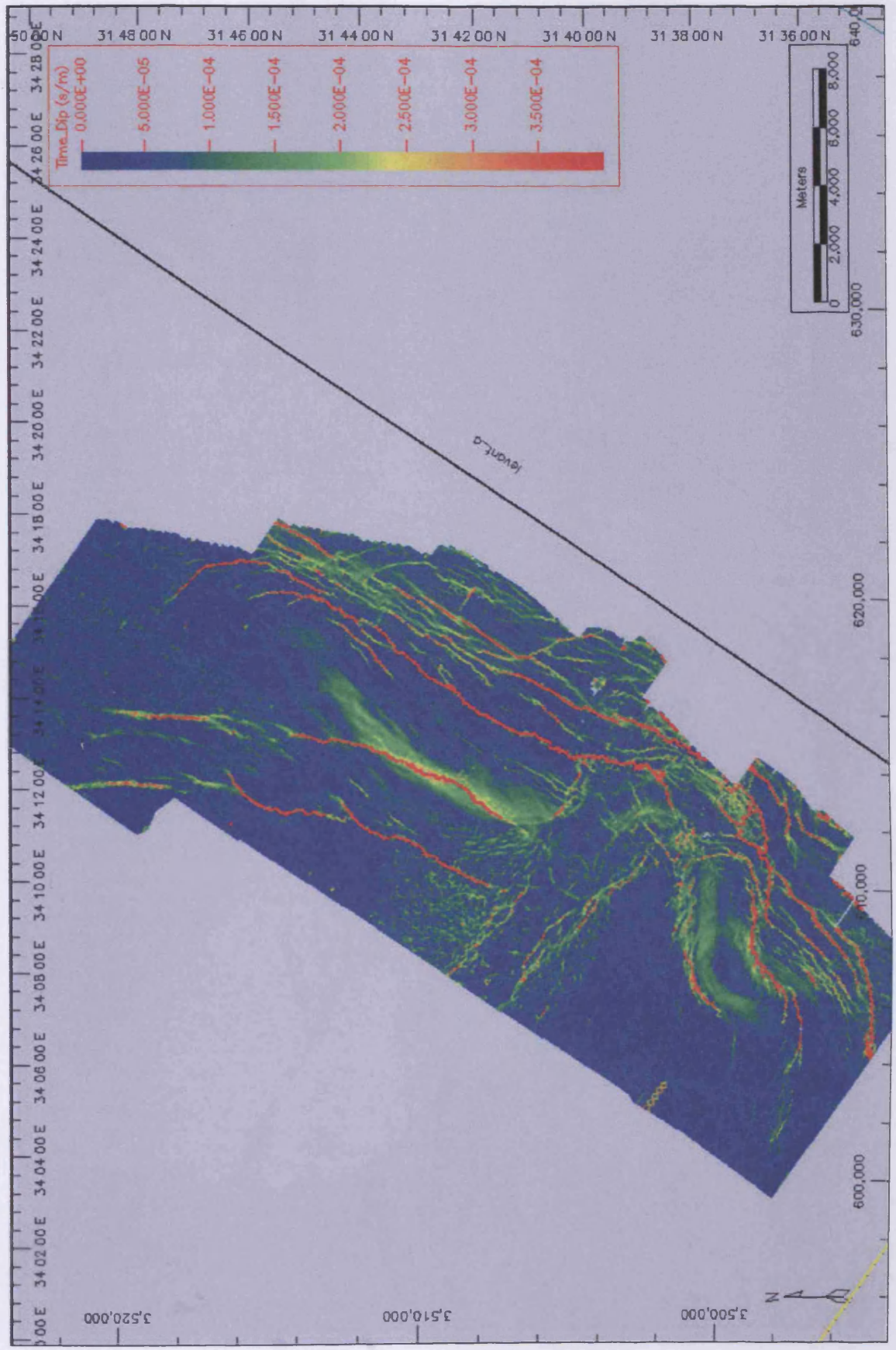

Fig. 8.4: Levant survey. Dip map of Horizon Ba (Close up)

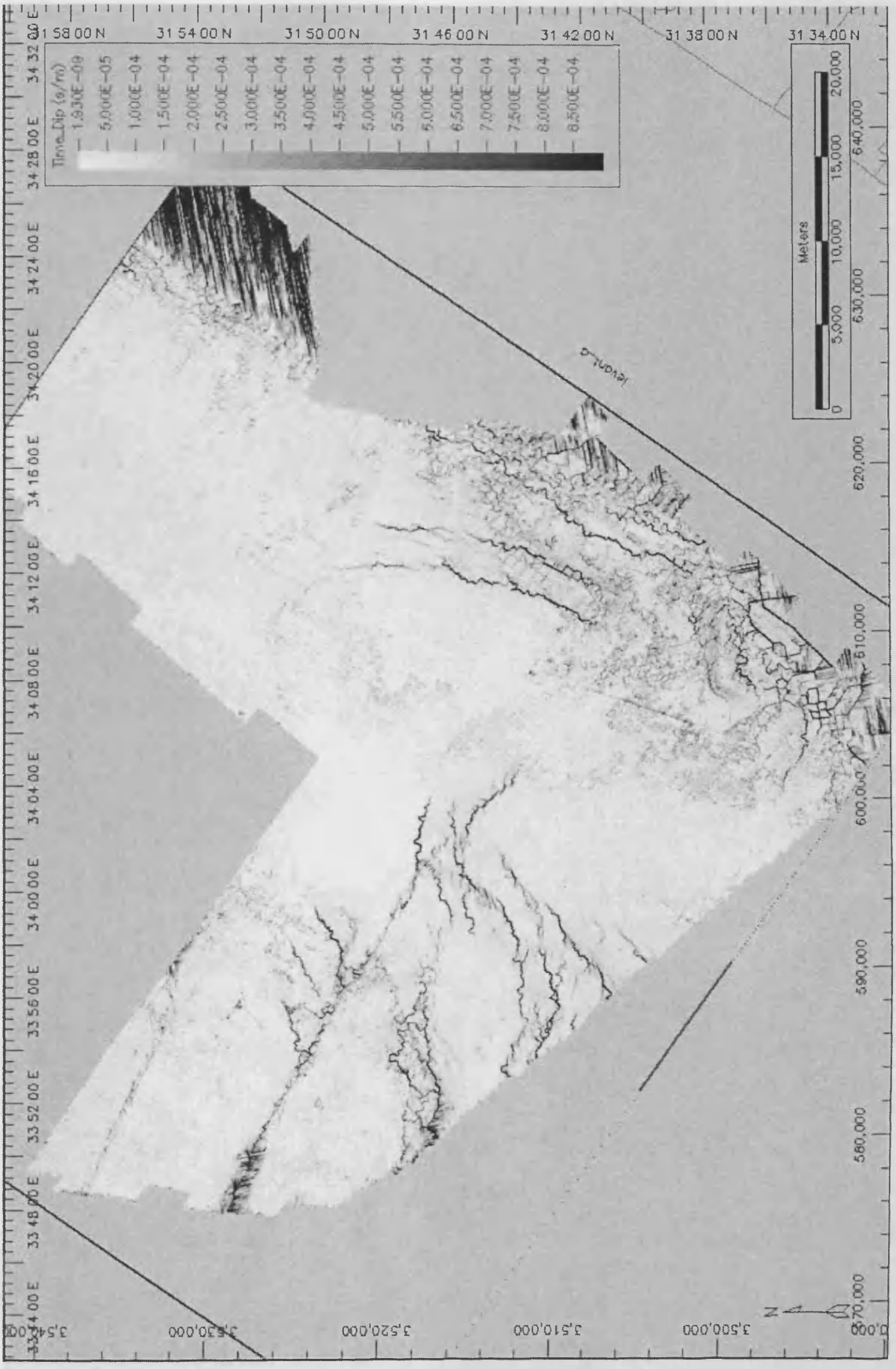

Fig. 8.5: Levant survey. Dip map of Horizon C

Fig. 8.6: Levant survey. Dip map of Horizon D

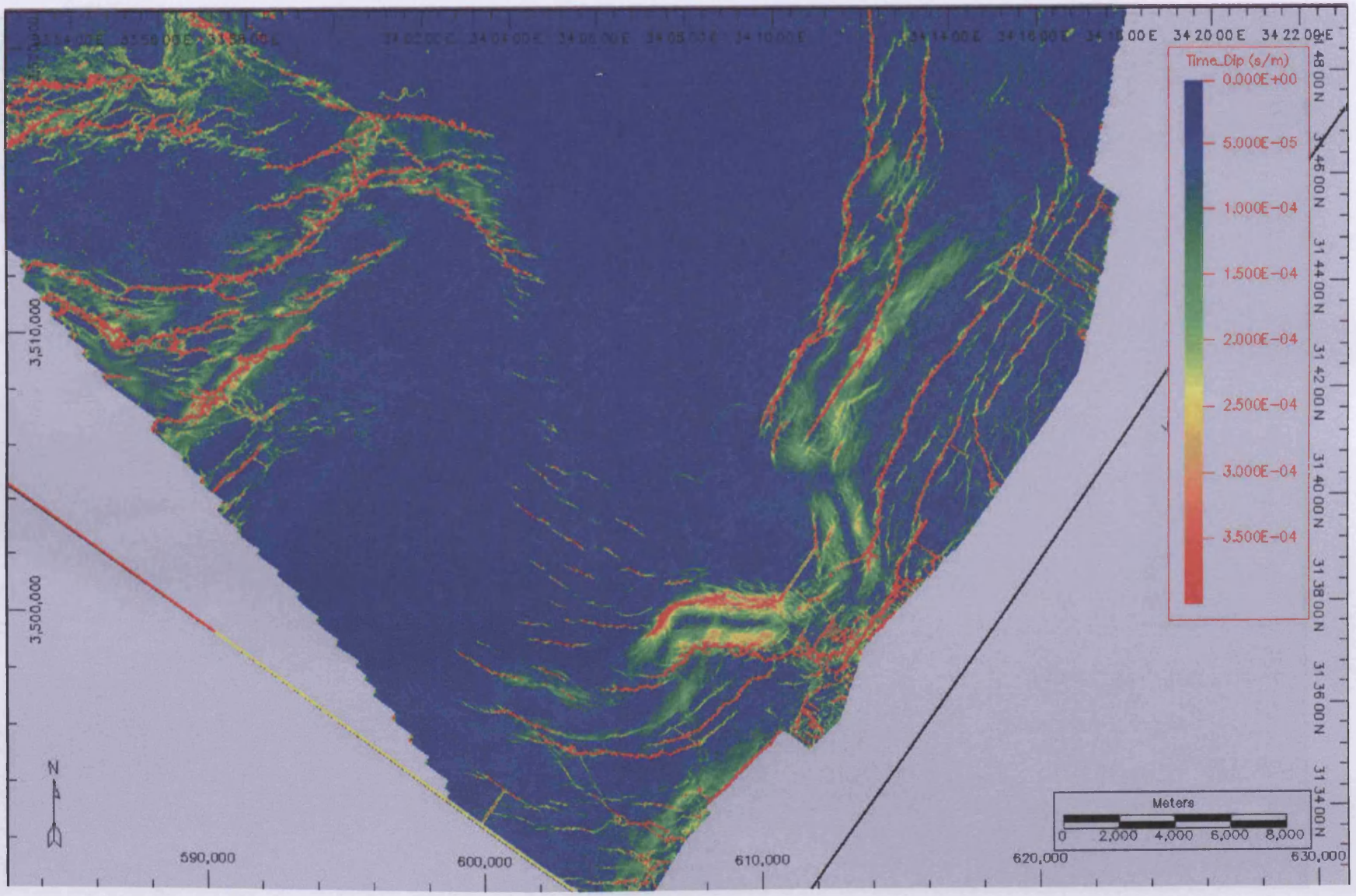

Fig. 8.7: Levant survey. Dip map of Horizon D (close up).

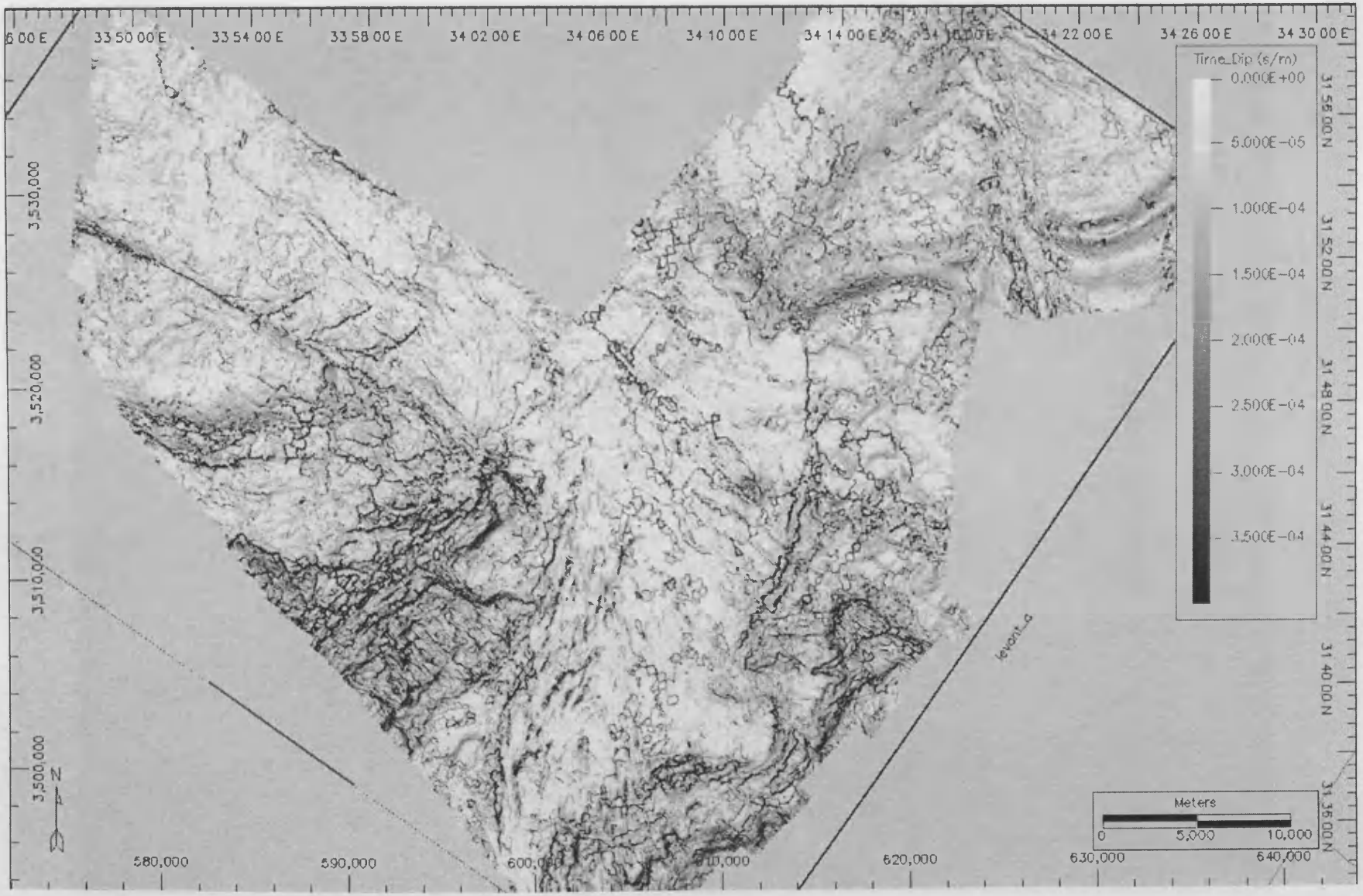

Fig. 8.8: Levant survey. Dip map of Horizon M

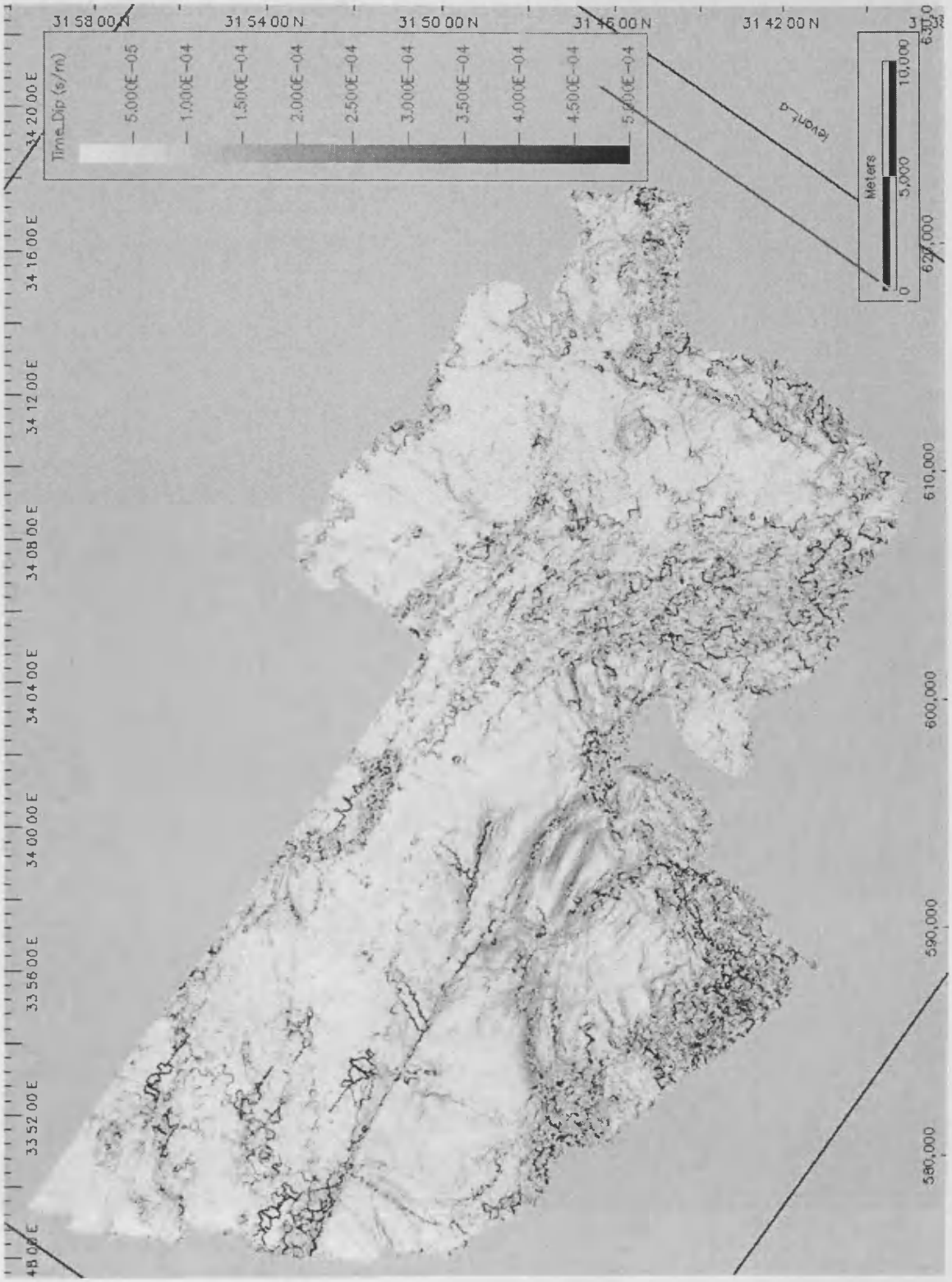

Fig. 8.9: Levant survey. Dip map of Horizon N

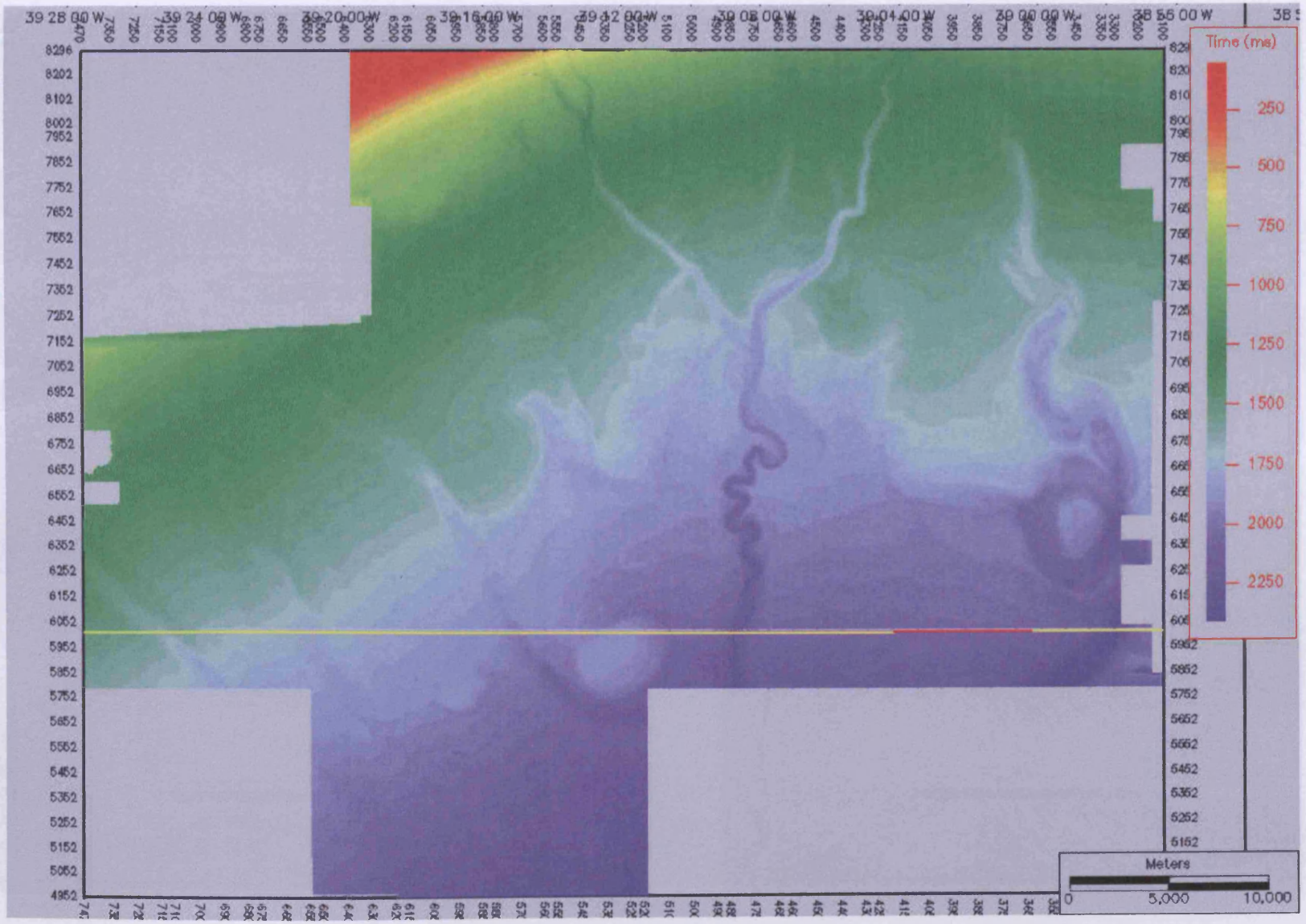

Fig. 8.10: BES2 survey. Time structure map of the seabed.

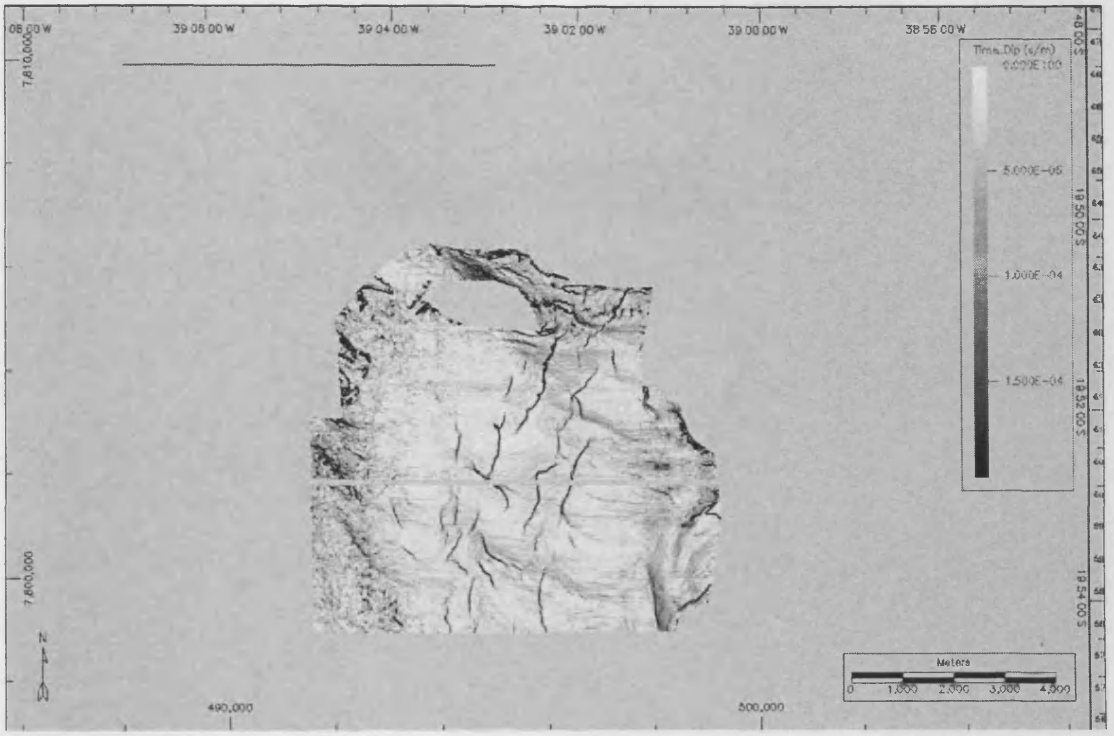

Fig. 8.11: BES2 survey. Dip map of Horizon C10 in Set 3.

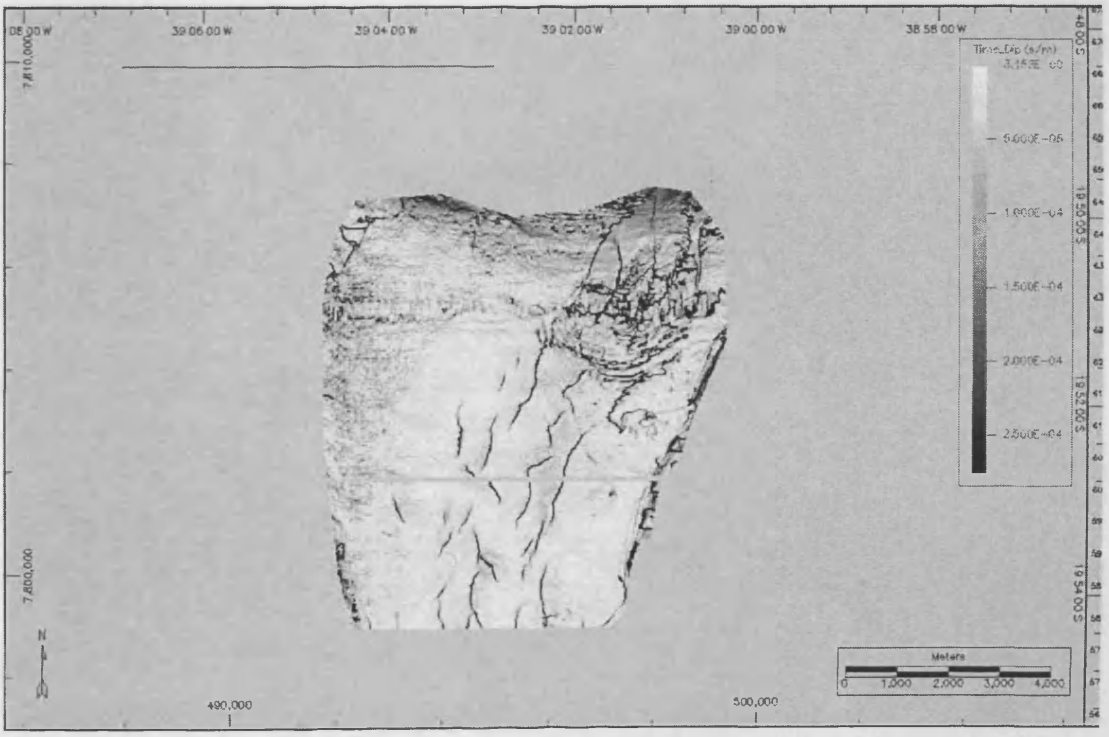

Fig. 8.12: BES2 survey. Dip map of Horizon C20 in Set 3.

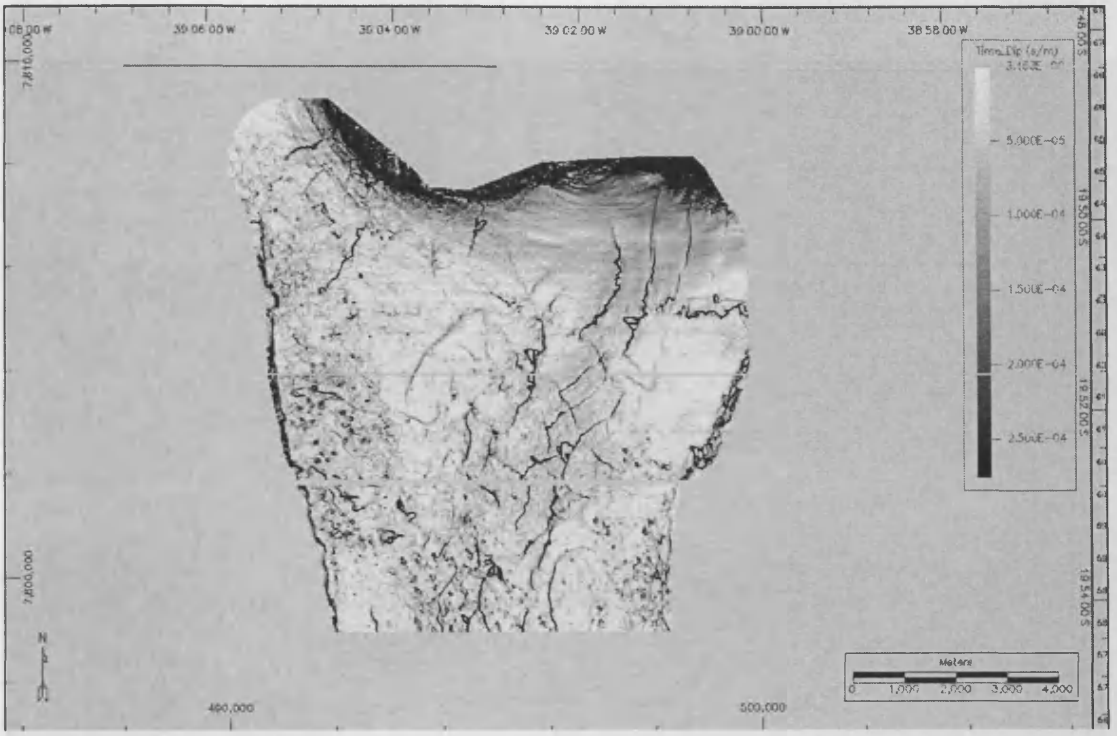

Fig. 8.13: BES2 survey. Dip map of Horizon C30 in Set 3.

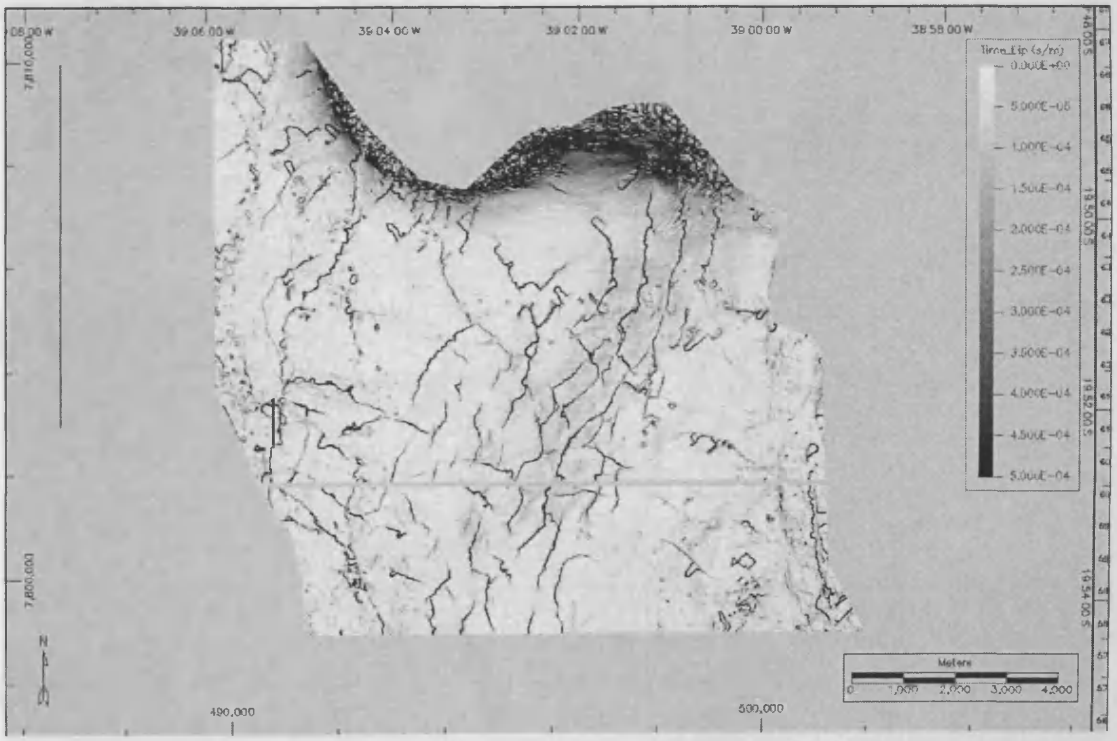

Fig. 8.15: BES2 survey. Dip map of Horizon C40 in Set 3.

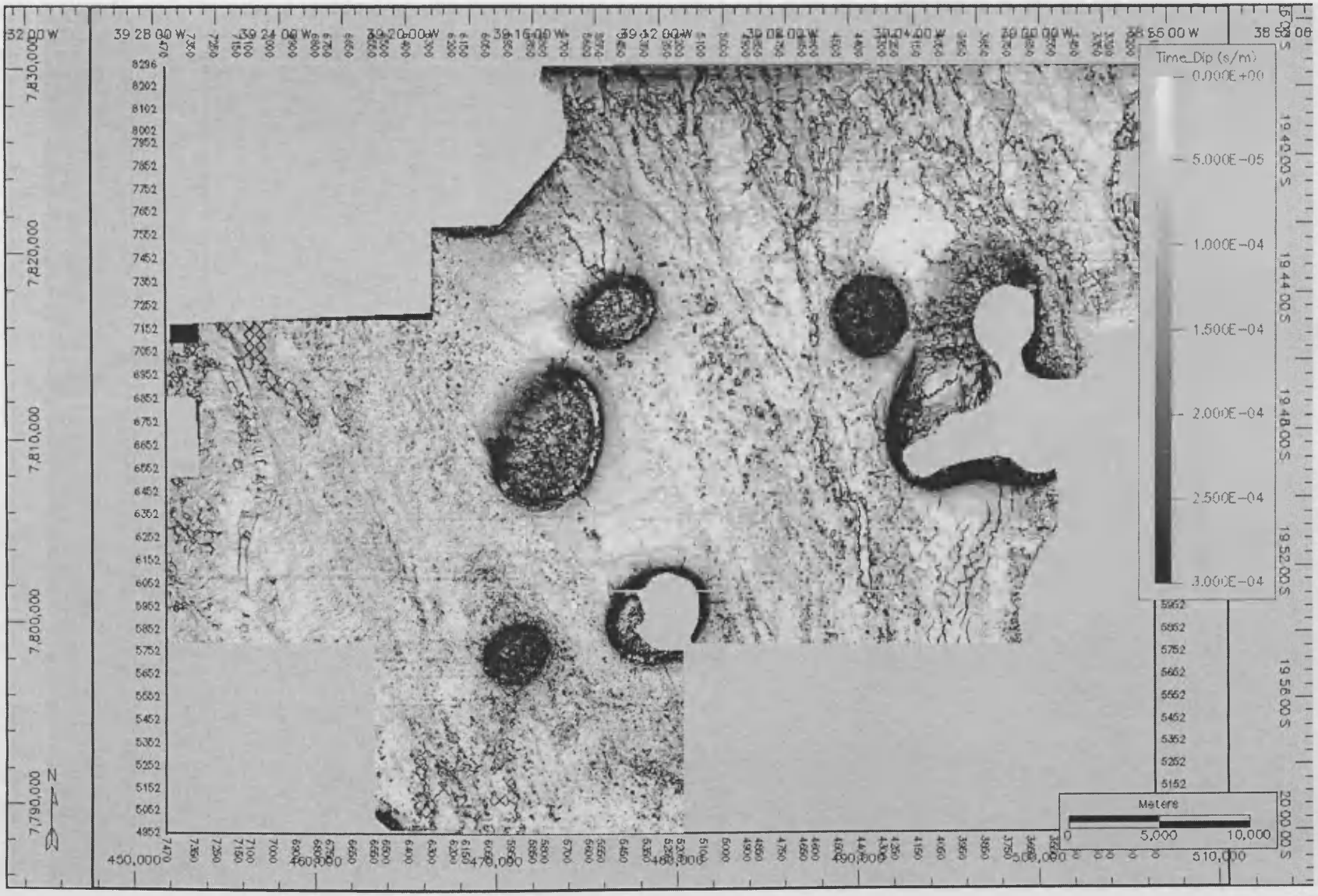

Fig. 8.14: BES2 survey. Dip map of Horizon C35.

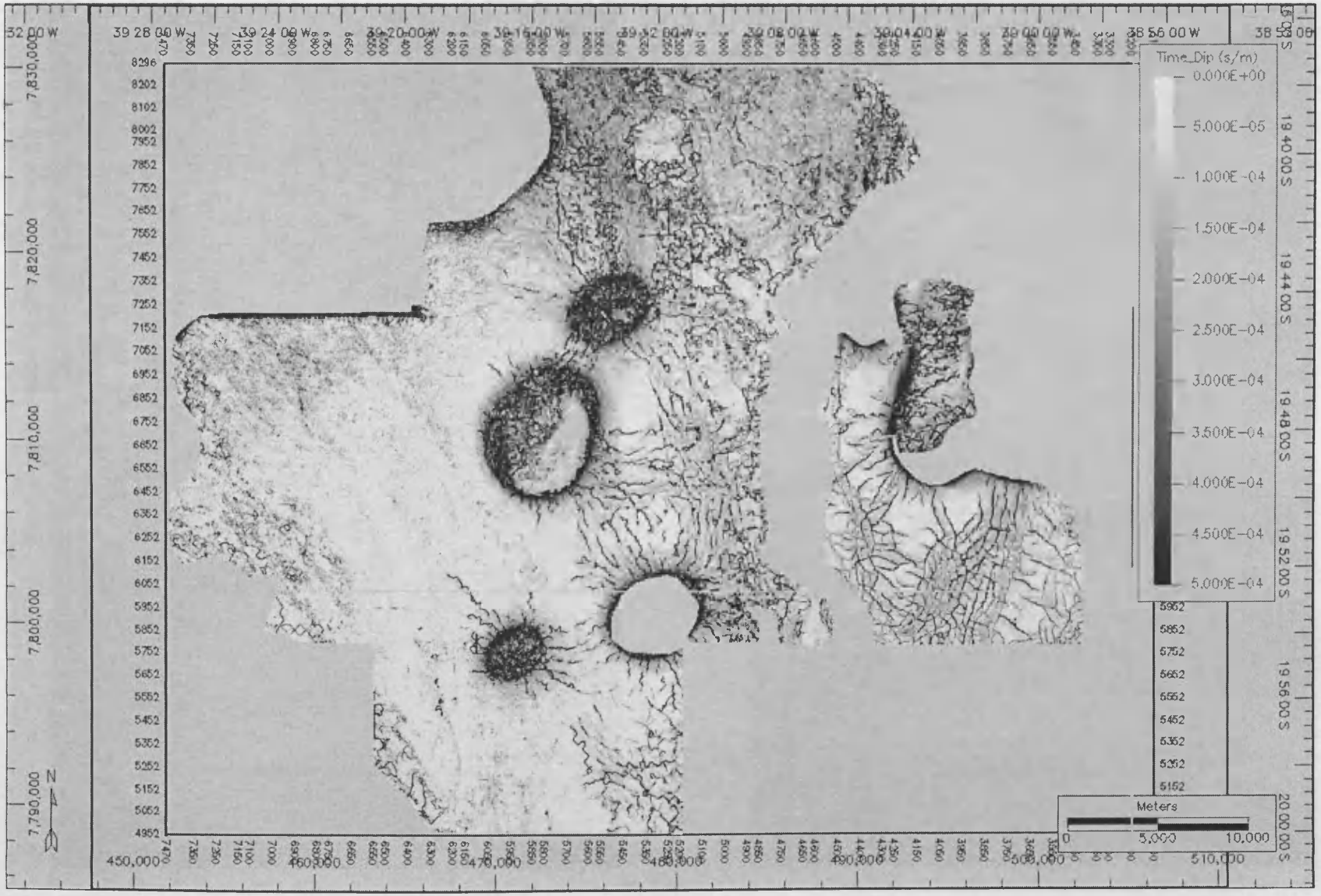

Fig. 8.16: BES2 survey. Dip map of Horizon C50.

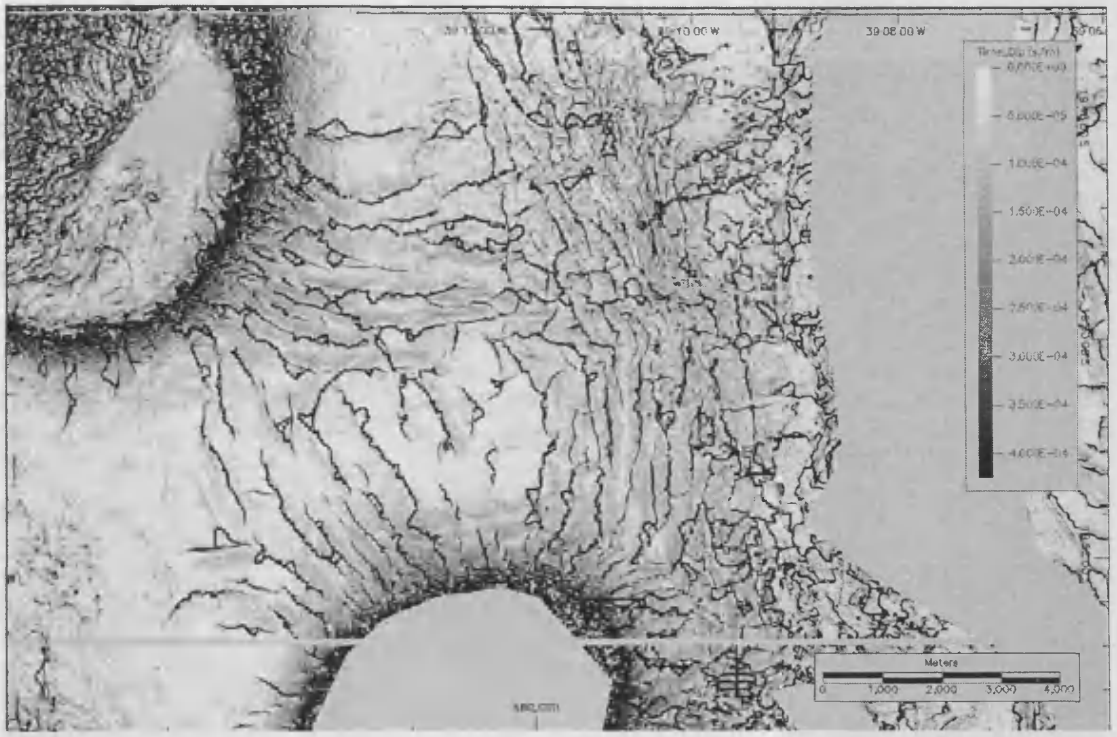

Fig. 8.17: BES2 survey. Dip map of Horizon C50 in Set 1.

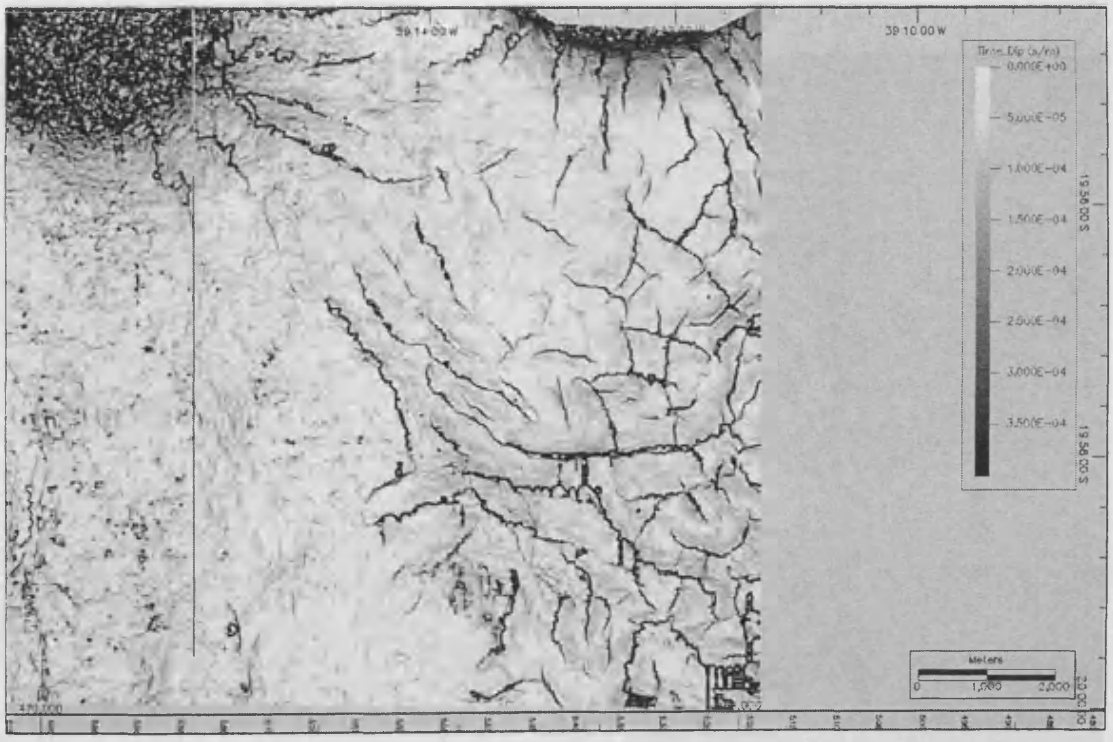

Fig. 8.18: BES2 survey. Dip map of Horizon C50 in Set 2.

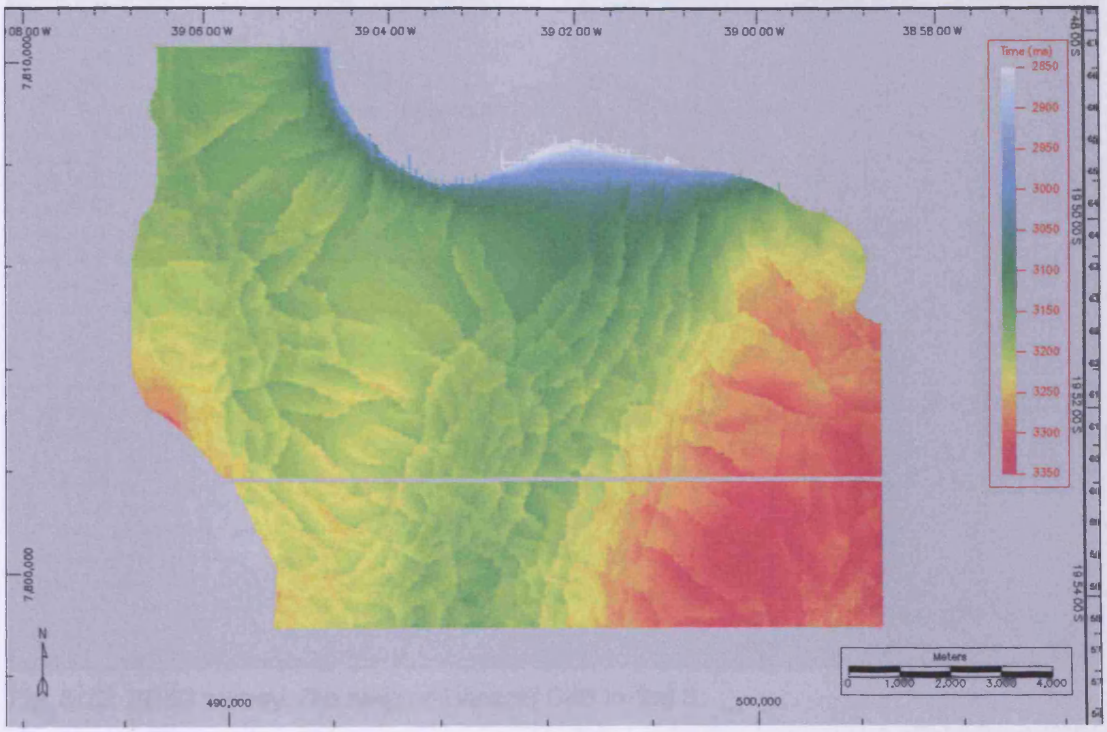

Fig. 8.19a: BES2 survey. Time structure map of Horizon C50 in Set 3.

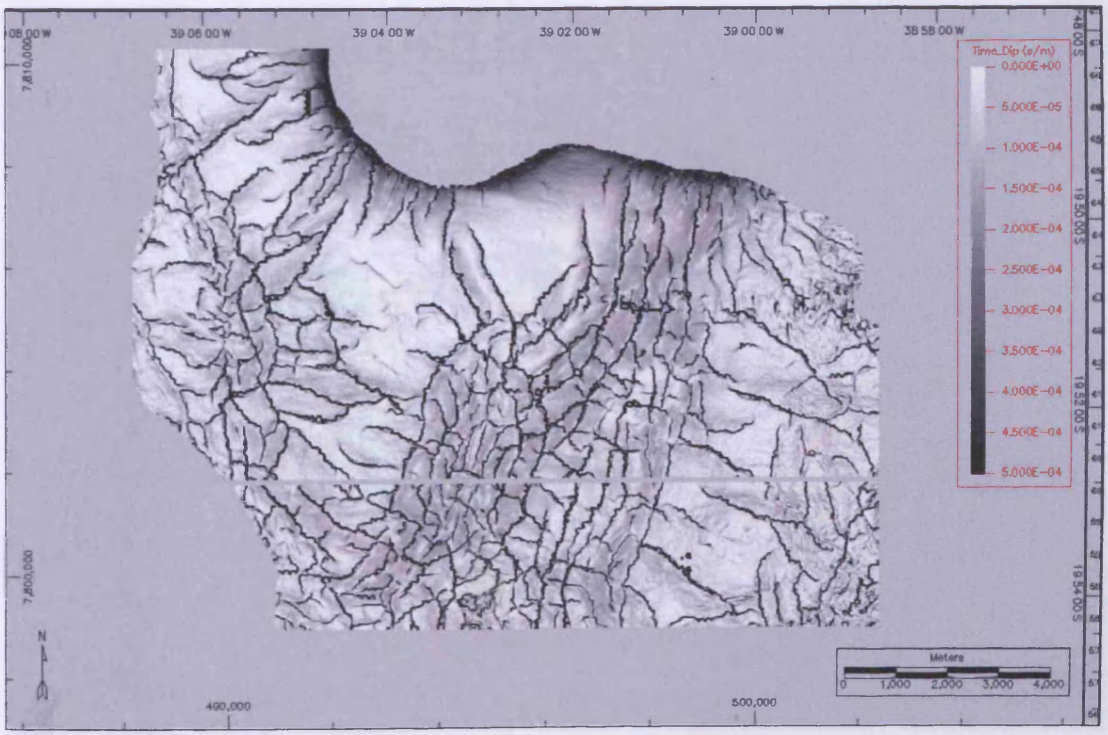

Fig. 8.19b: BES2 survey. Dip map of Horizon C50 in Set 3.

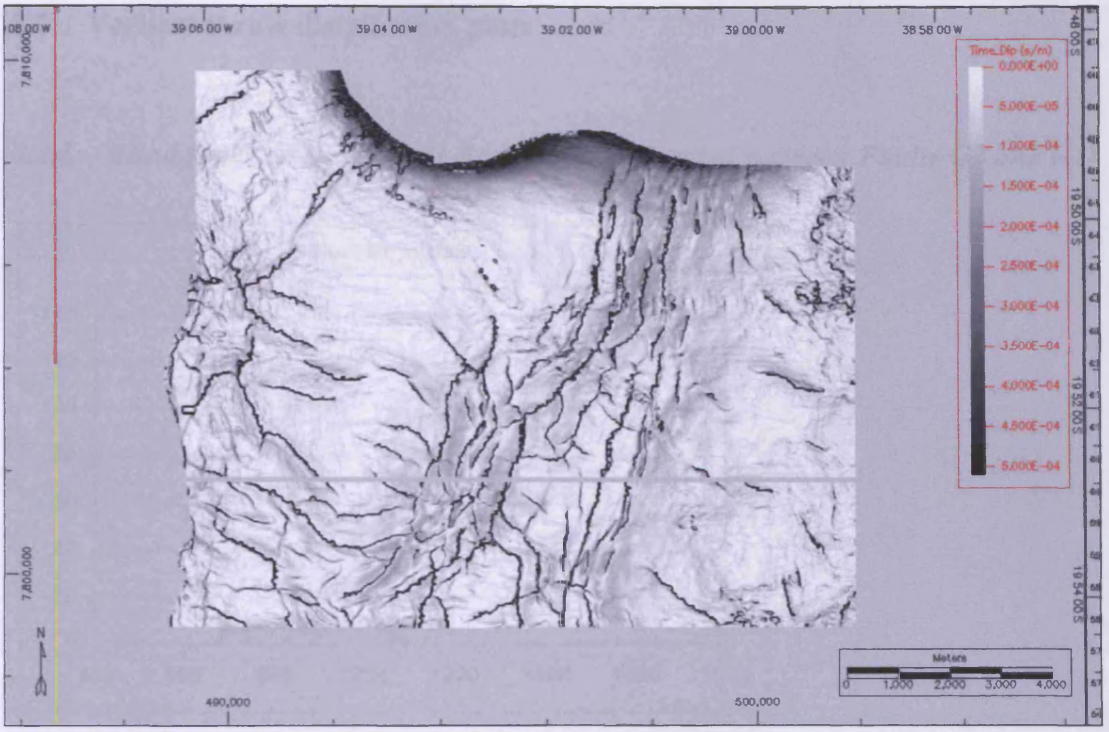

Fig. 8.20: BES2 survey. Dip map of Horizon C60 in Set 3.

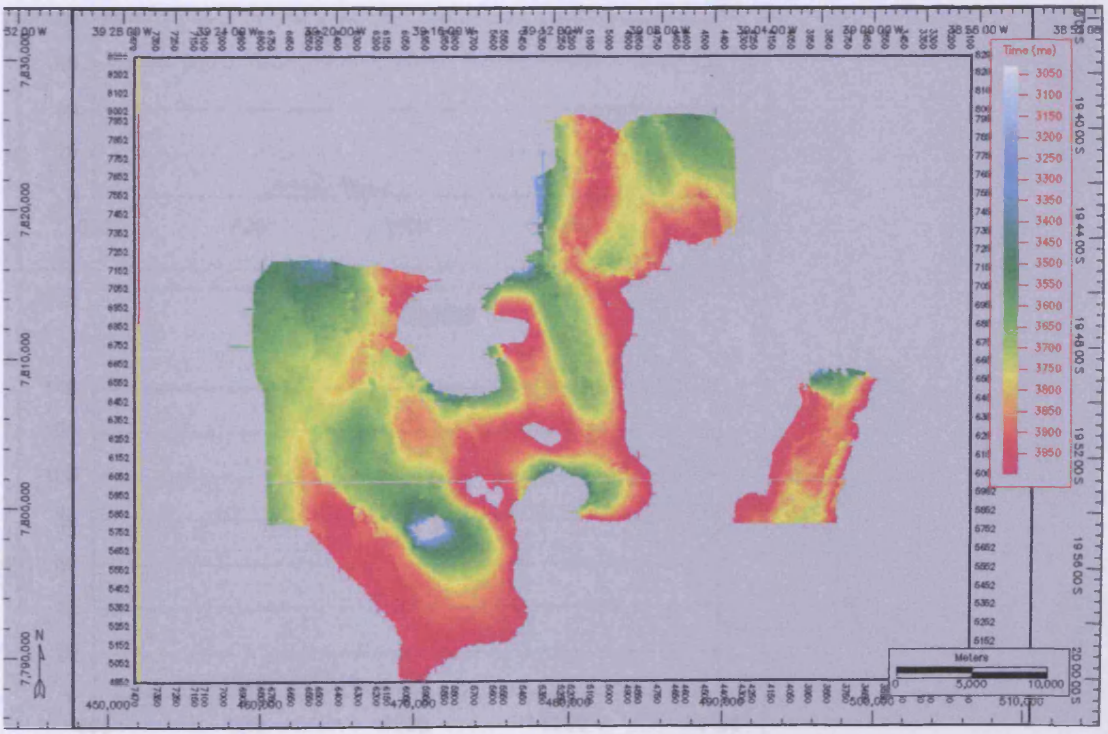

Fig. 8.21: BES2 survey. Time structure map of the Top Cretaceous Horizon.

8.2 Vertical throw distribution plots

8.2.1 Blind faults in the Levant Basin survey (located between Faults G2 and G3)

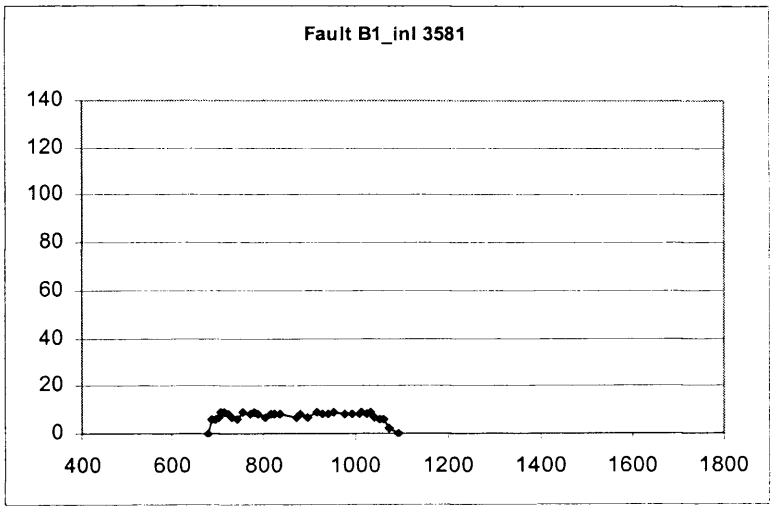

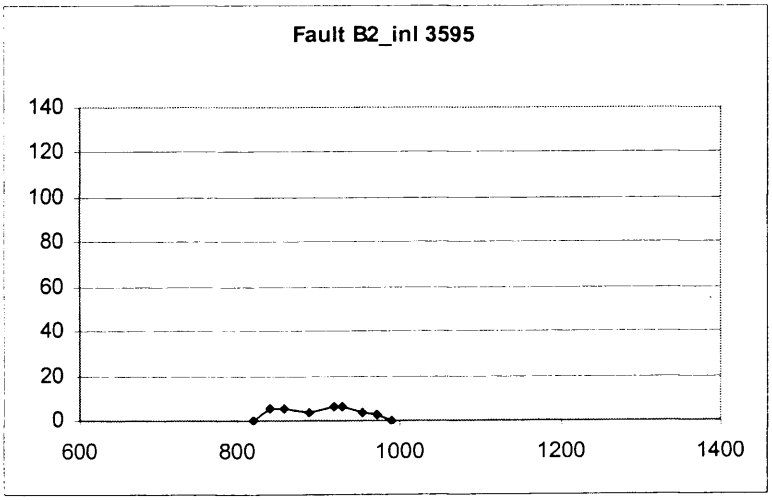

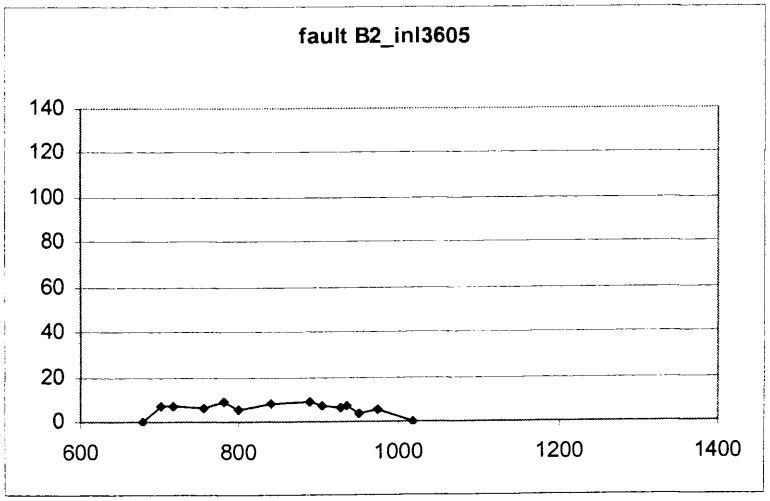

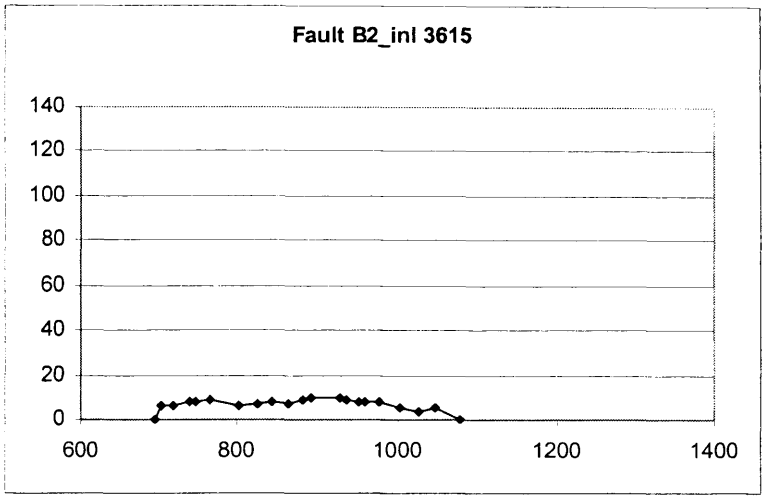
Fault B2_inl 3615
140
120
100
80
60
40
20
0
600
800
1000
1200
1400

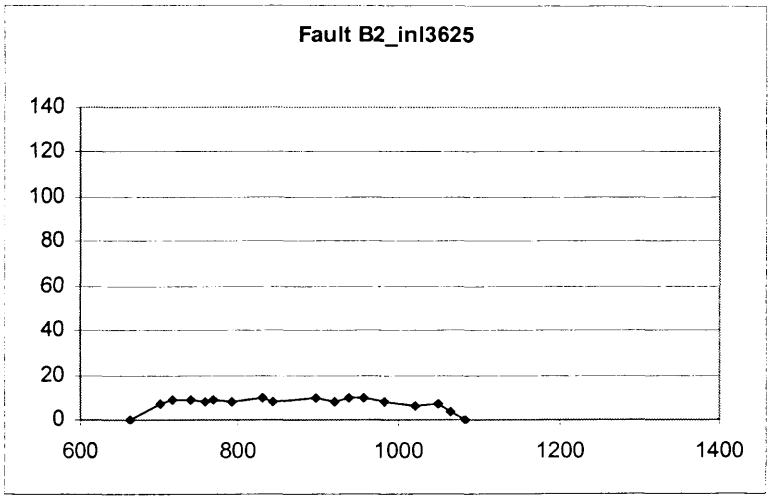
Fault B2_inl3625
140
120
100
80
60
40
20
0
600
800
1000
1200
1400

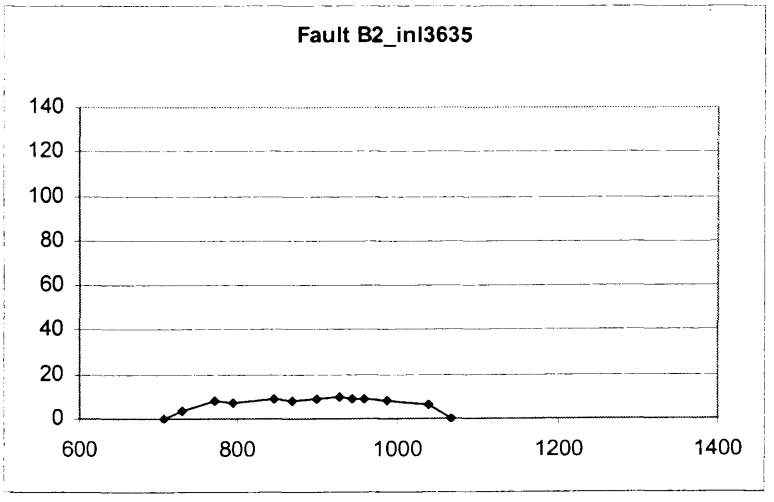
Fault B2_inl3635
140
120
100
80
60
40
20
0
600
800
1000
1200
1400

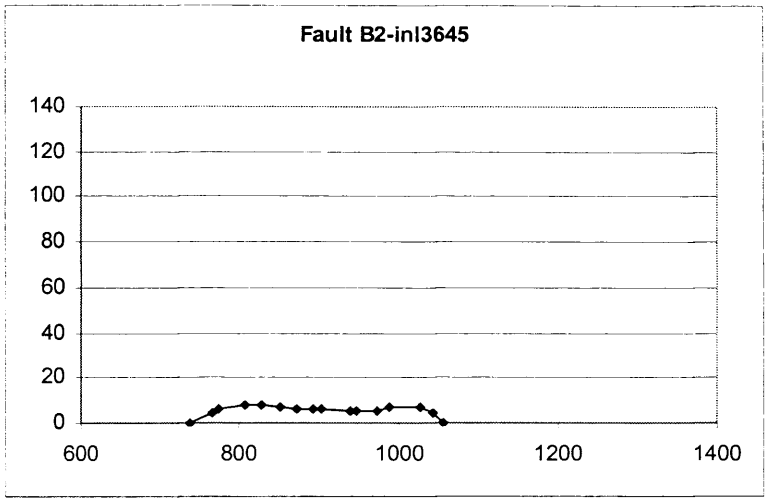
Fault B2-inl3645
140
120
100
80
60
40
20
0
600
800
1000
1200
1400

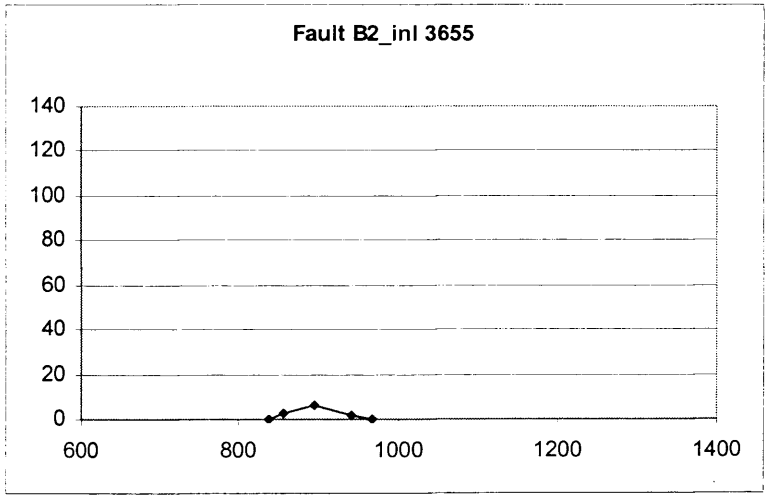
Fault B2_inl 3655
140
120
100
80
60
40
20
0
600
800
1000
1200
1400

8.2.2 Coast parallel faults in the Levant Basin survey

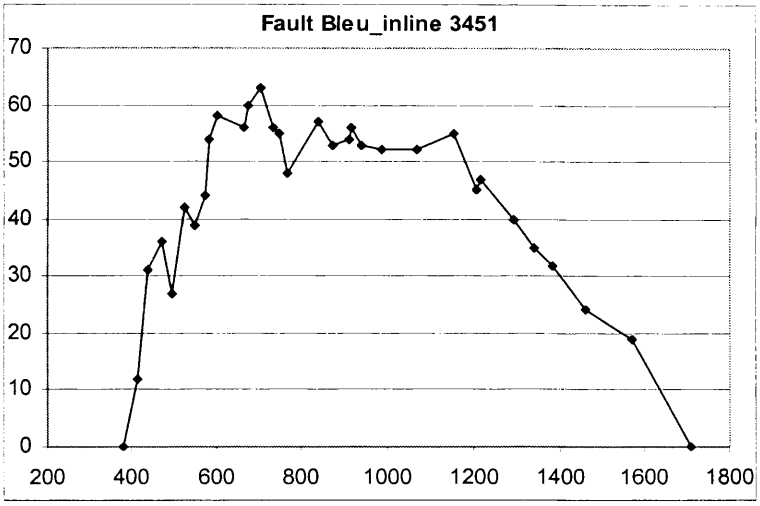

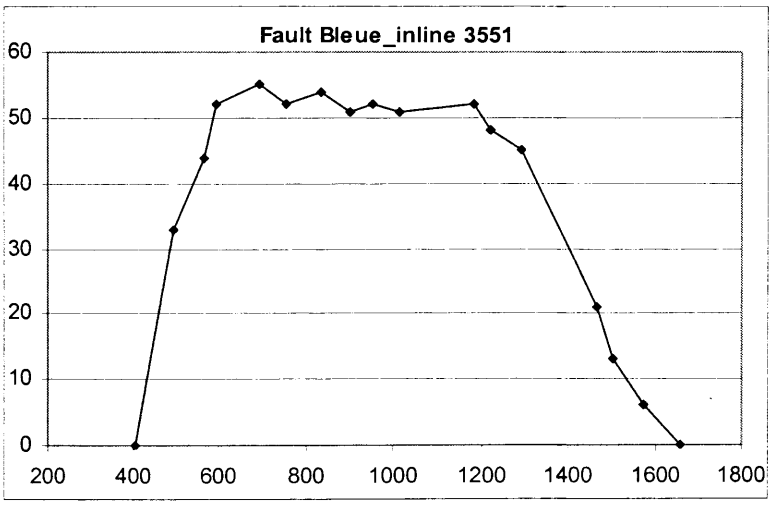

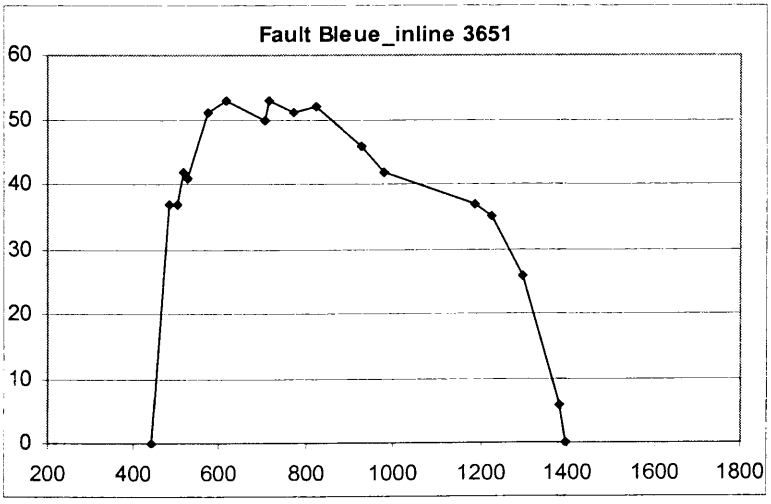

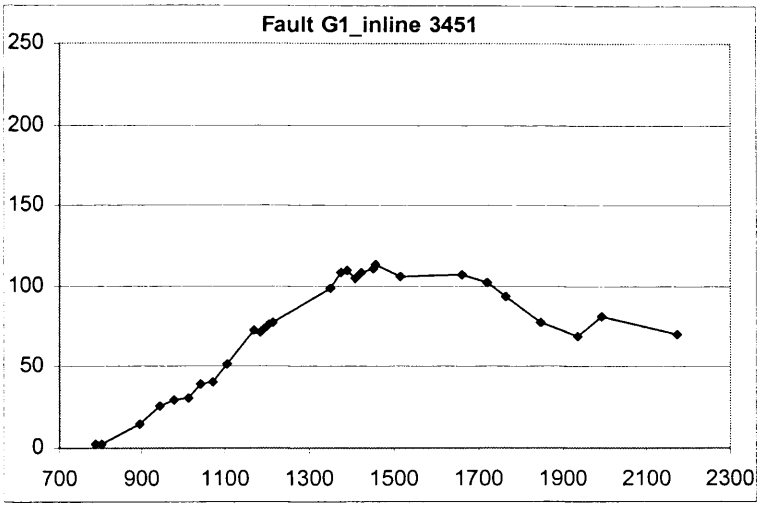
Fault G1_inline 3451
250
200
150
100
50
0
700
900
1100
1300
1500
1700
1900
2100
2300

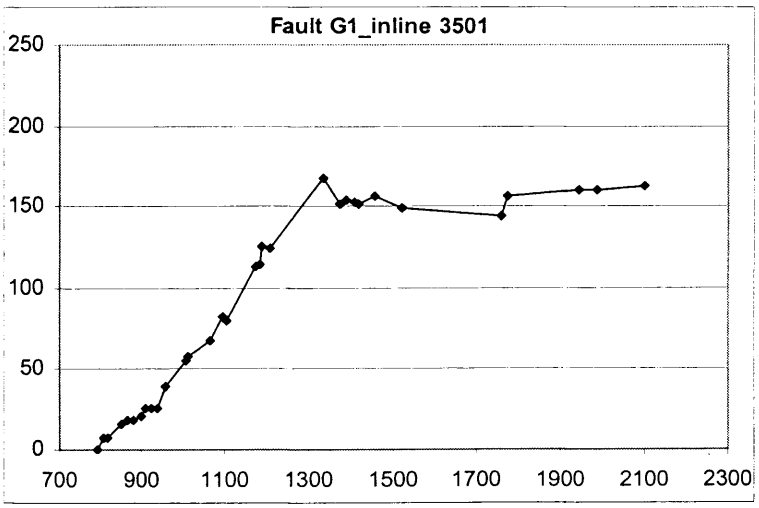
Fault G1_inline 3501
250
200
150
100
50
0
700
900
1100
1300
1500
1700
1900
2100
2300

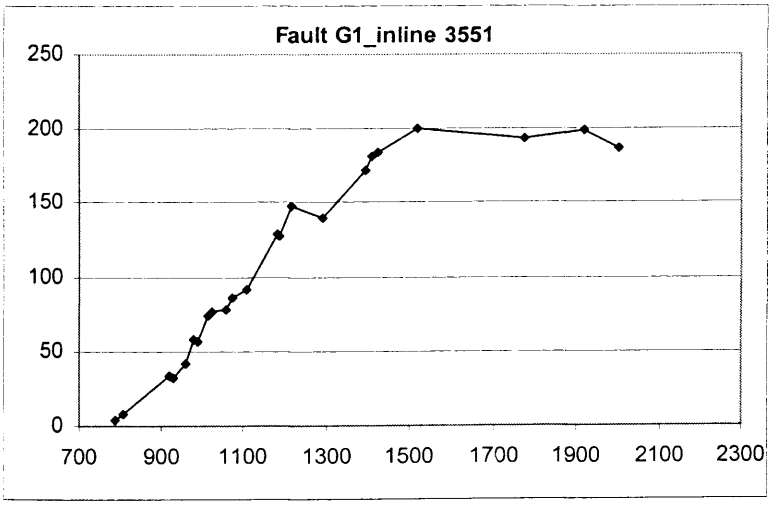
Fault G1_inline 3551
250
200
150
100
50
0
700
900
1100
1300
1500
1700
1900
2100
2300

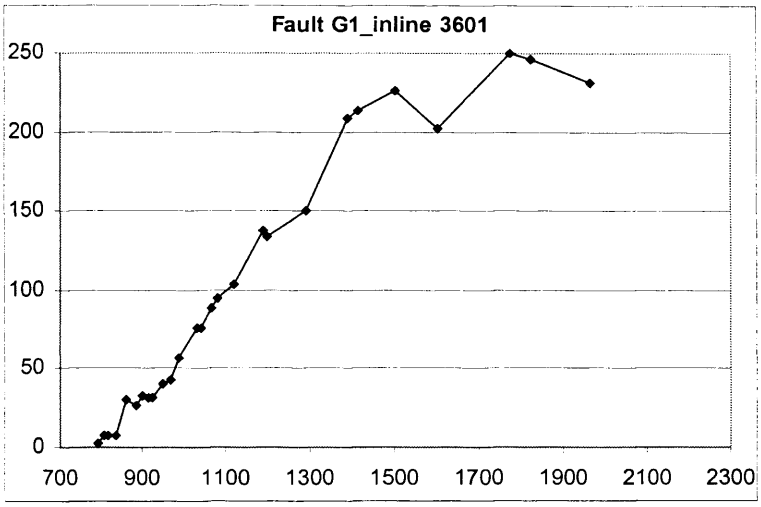
Fault G1_inline 3601
250
200
150
100
50
0
700
900
1100
1300
1500
1700
1900
2100
2300

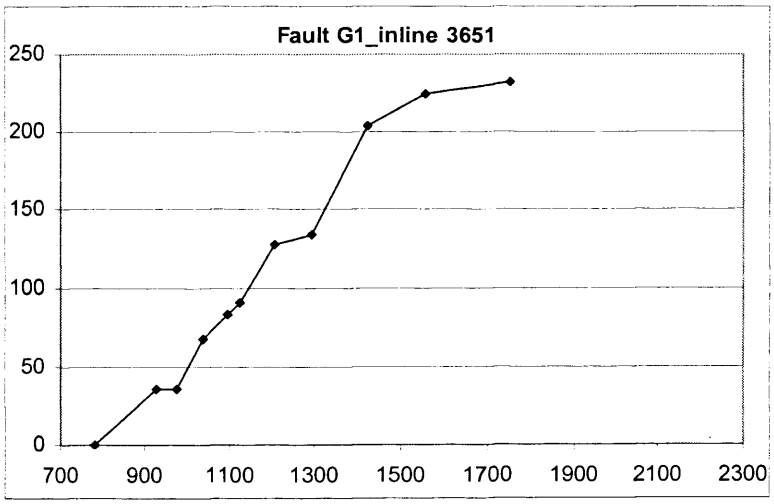
Fault G1_inline 3651
250
200
150
100
50
0
700
900
1100
1300
1500
1700
1900
2100
2300

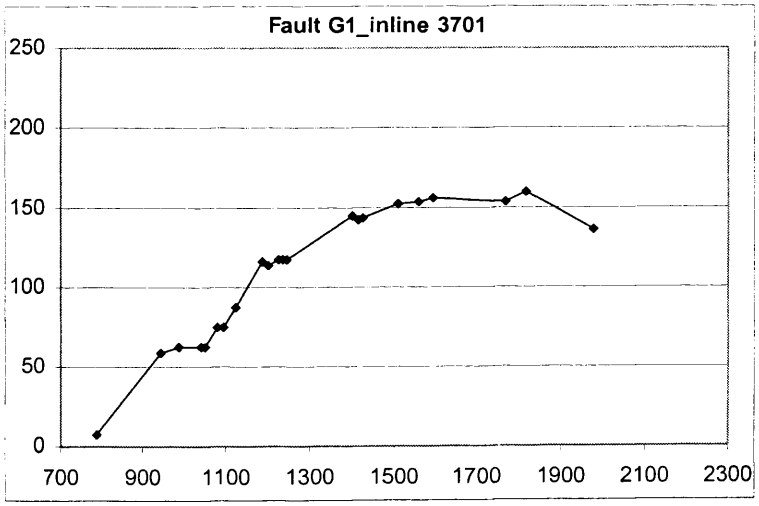
Fault G1_inline 3701
250
200
150
100
50
0
700
900
1100
1300
1500
1700
1900
2100
2300

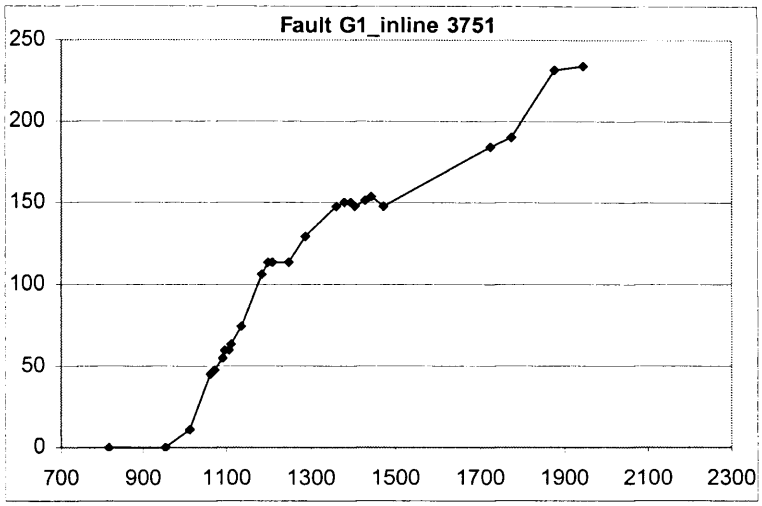
Fault G1_inline 3751
250
200
150
100
50
0
700
900
1100
1300
1500
1700
1900
2100
2300

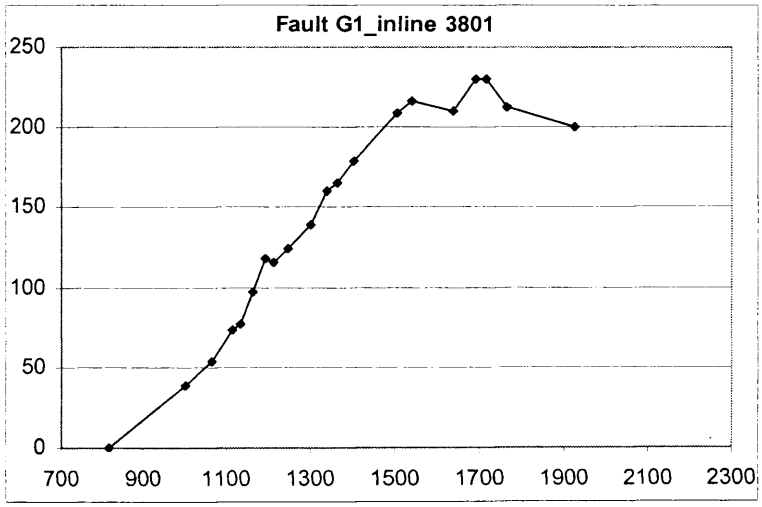
Fault G1_inline 3801
250
200
150
100
50
0
700
900
1100
1300
1500
1700
1900
2100
2300

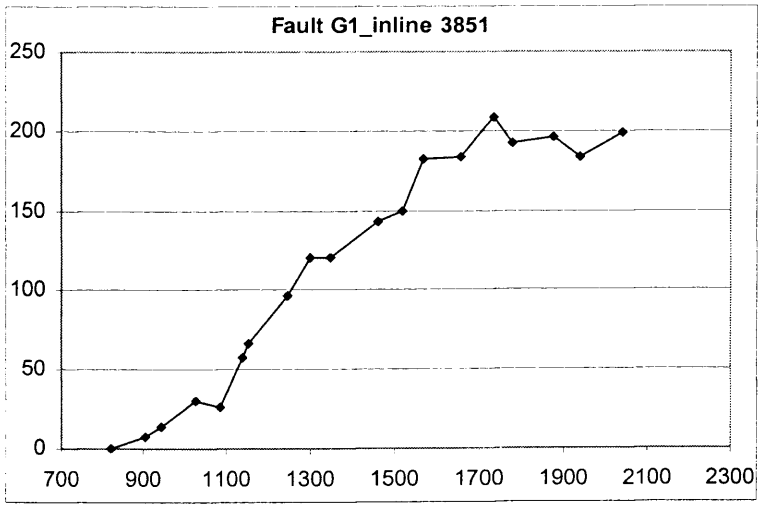
Fault G1_inline 3851
250
200
150
100
50
0
700
900
1100
1300
1500
1700
1900
2100
2300

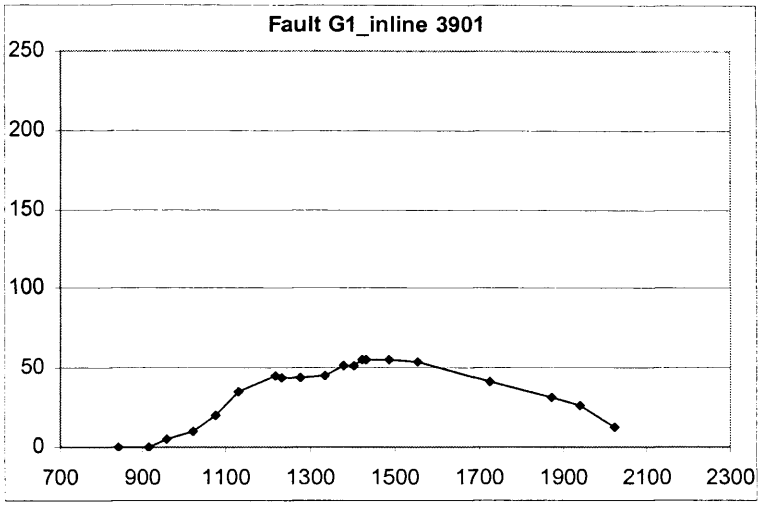
Fault G1_inline 3901
250
200
150
100
50
0
700
900
1100
1300
1500
1700
1900
2100
2300

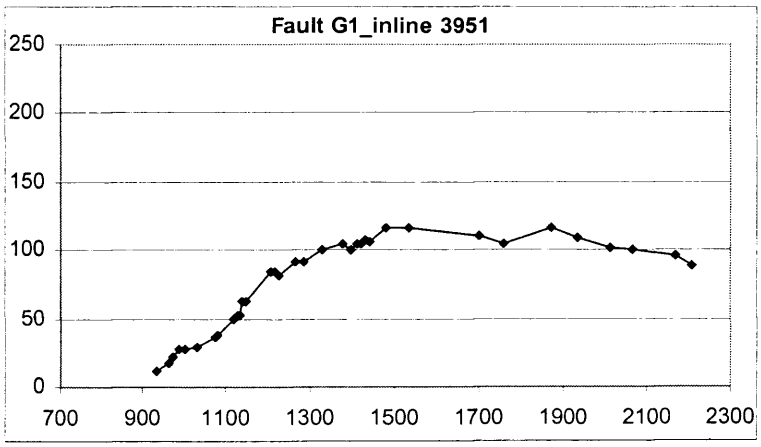
Fault G1_inline 3951
250
200
150
100
50
0
700
900
1100
1300
1500
1700
1900
2100
2300

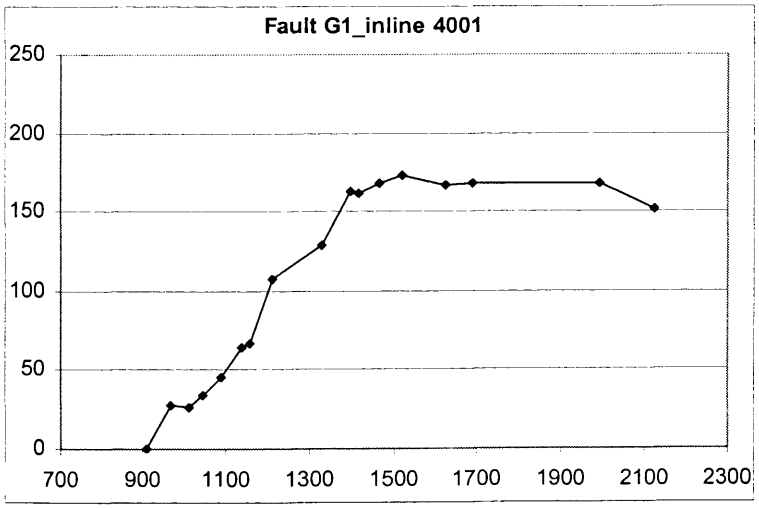
Fault G1_inline 4001
250
200
150
100
50
0
700
900
1100
1300
1500
1700
1900
2100
2300

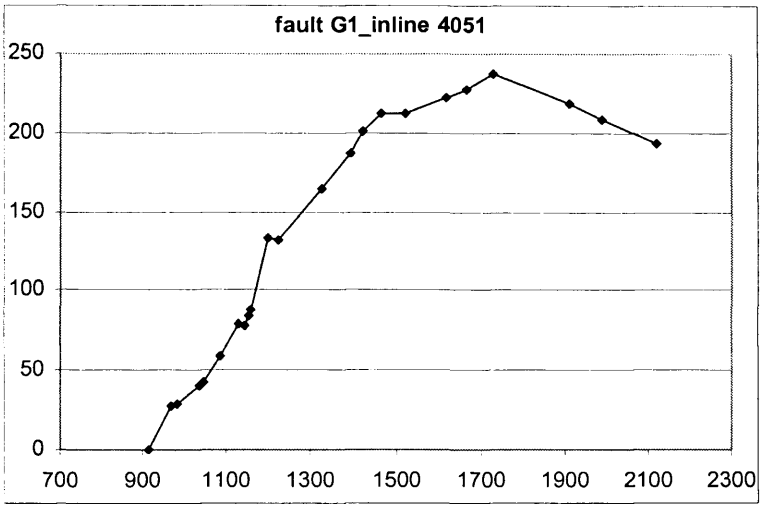
fault G1_inline 4051
250
200
150
100
50
0
700
900
1100
1300
1500
1700
1900
2100
2300

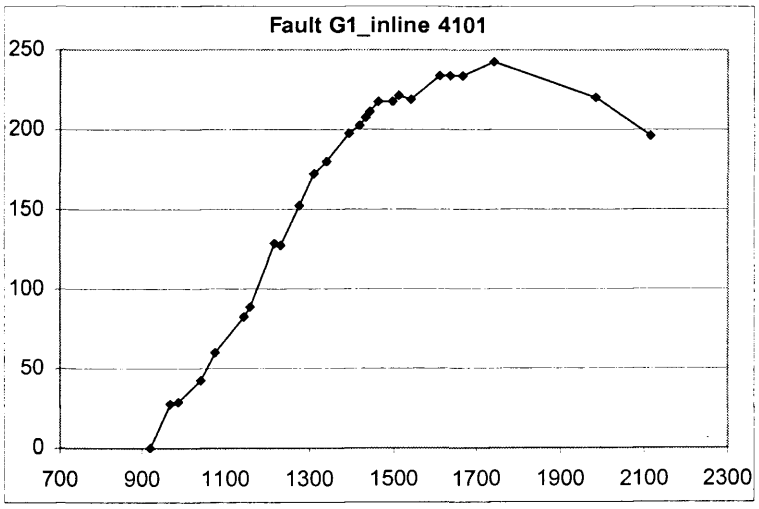
Fault G1_inline 4101
250
200
150
100
50
0
700
900
1100
1300
1500
1700
1900
2100
2300

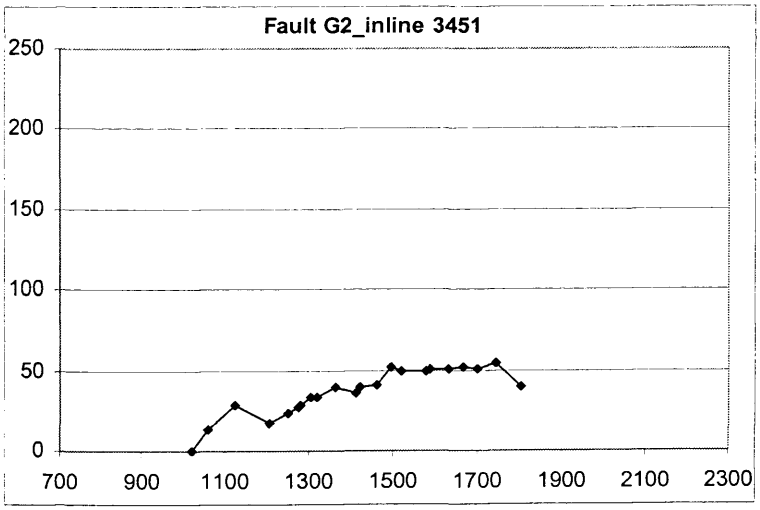
Fault G2_inline 3451
250
200
150
100
50
0
700
900
1100
1300
1500
1700
1900
2100
2300

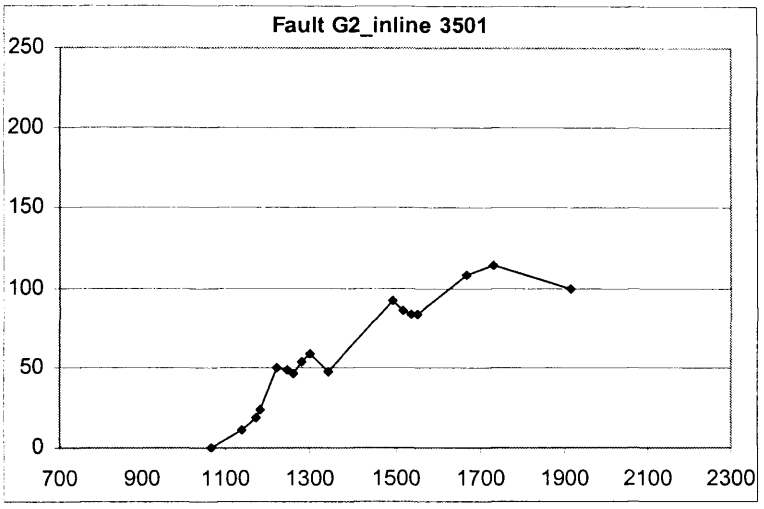
Fault G2_inline 3501
250
200
150
100
50
0
700
900
1100
1300
1500
1700
1900
2100
2300

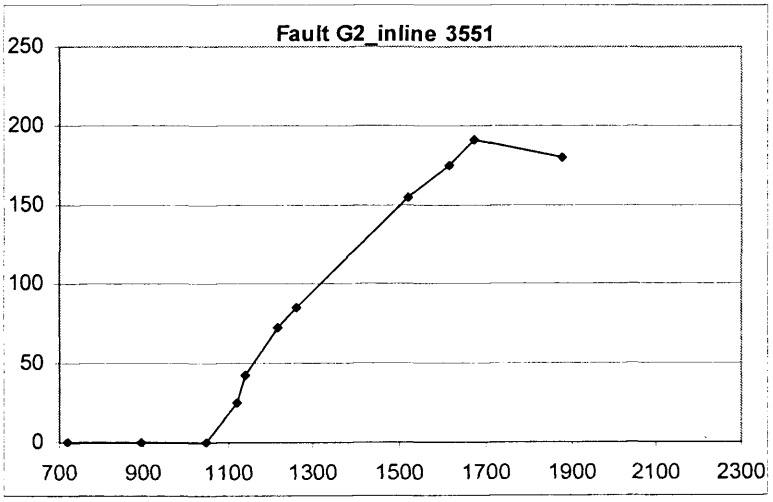
Fault G2_inline 3551
250
200
150
100
50
0
700
900
1100
1300
1500
1700
1900
2100
2300

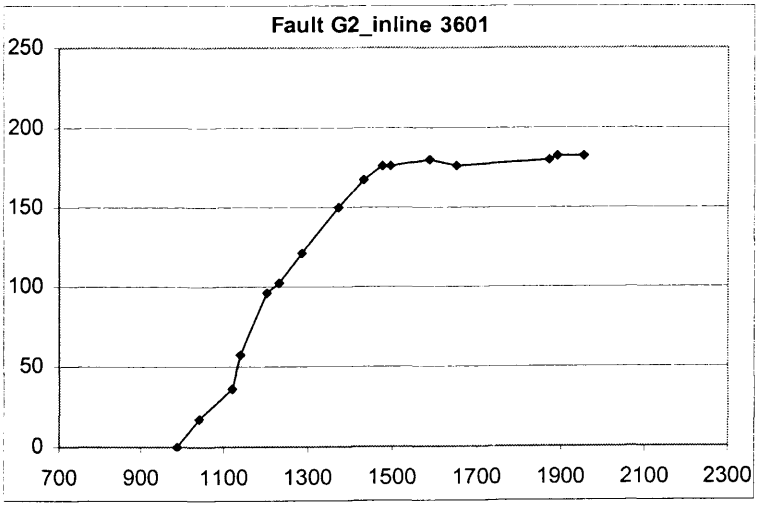
Fault G2_inline 3601
250
200
150
100
50
0
700
900
1100
1300
1500
1700
1900
2100
2300

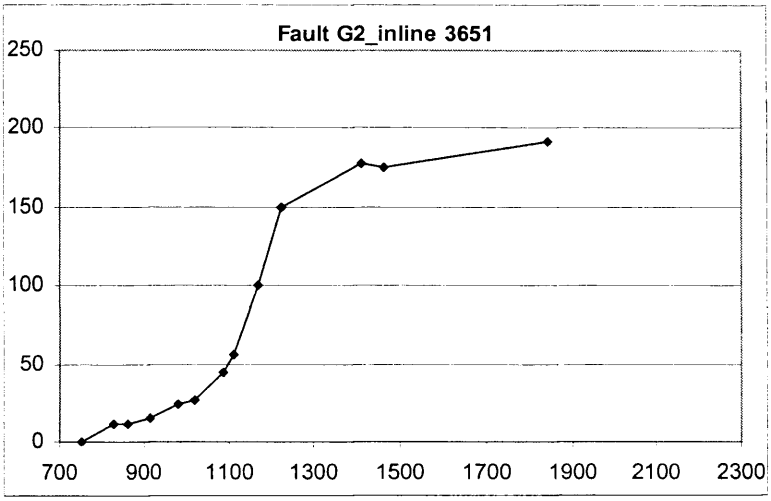
Fault G2_inline 3651
250
200
150
100
50
0
700
900
1100
1300
1500
1700
1900
2100
2300

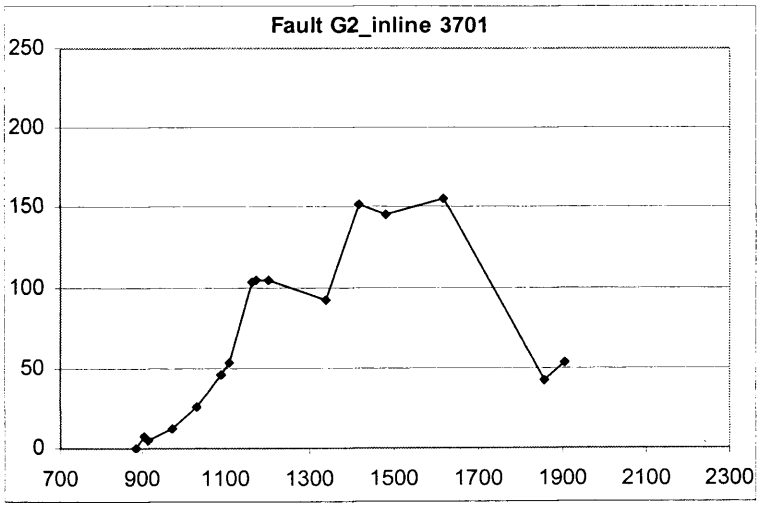
Fault G2_inline 3701
250
200
150
100
50
0
700
900
1100
1300
1500
1700
1900
2100
2300

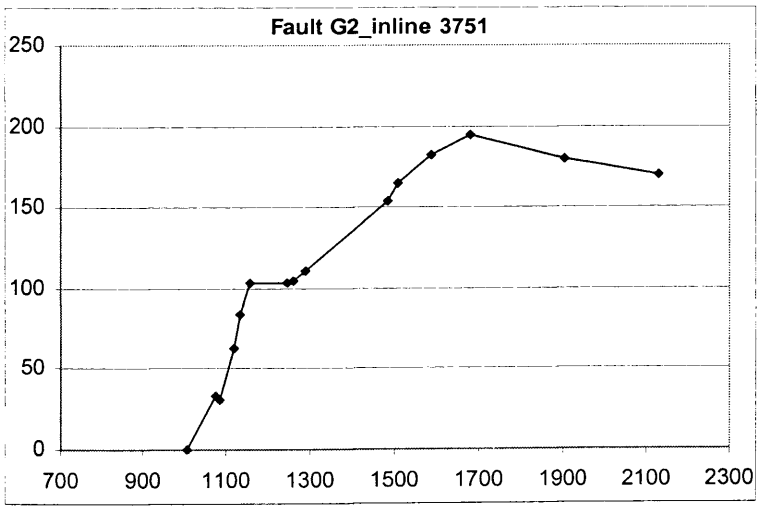
Fault G2_inline 3751
250
200
150
100
50
0
700
900
1100
1300
1500
1700
1900
2100
2300

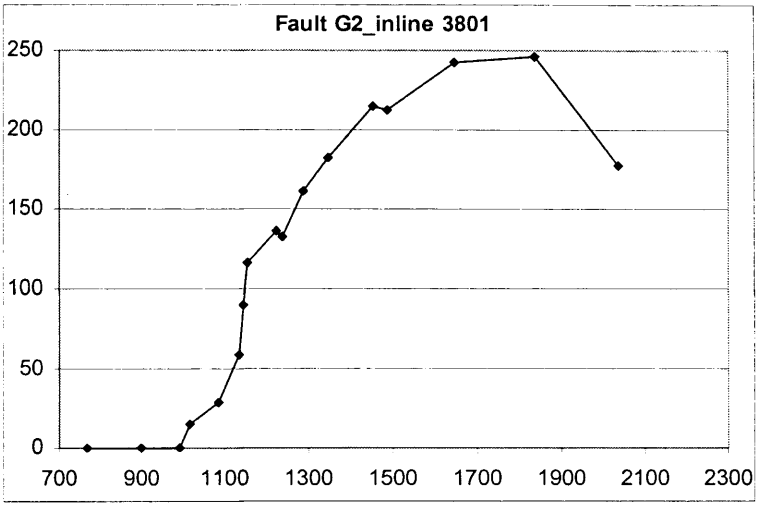
Fault G2_inline 3801
250
200
150
100
50
0
700
900
1100
1300
1500
1700
1900
2100
2300

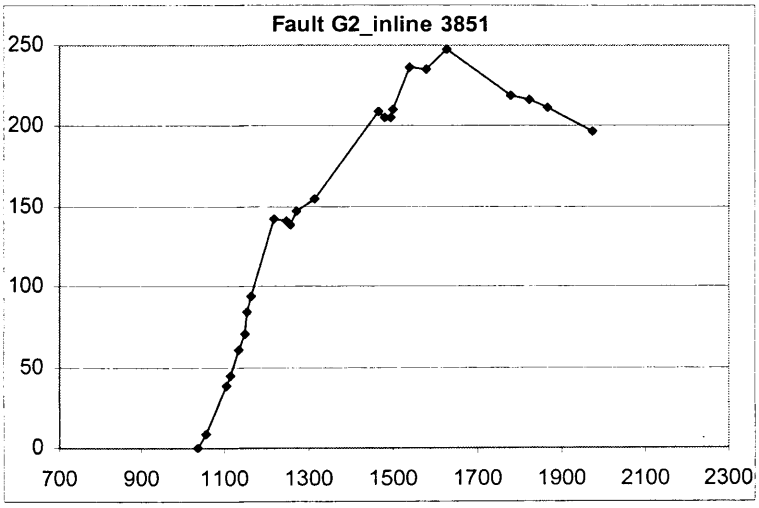
Fault G2_inline 3851
250
200
150
100
50
0
700
900
1100
1300
1500
1700
1900
2100
2300

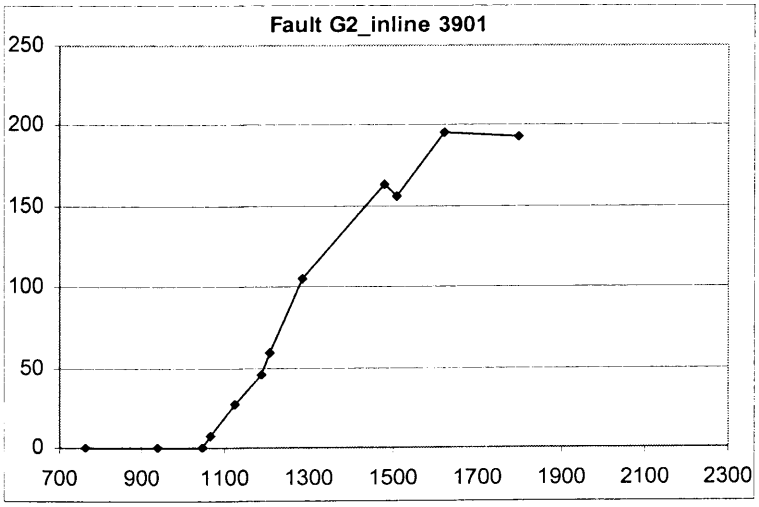
Fault G2_inline 3901
250
200
150
100
50
0
700
900
1100
1300
1500
1700
1900
2100
2300

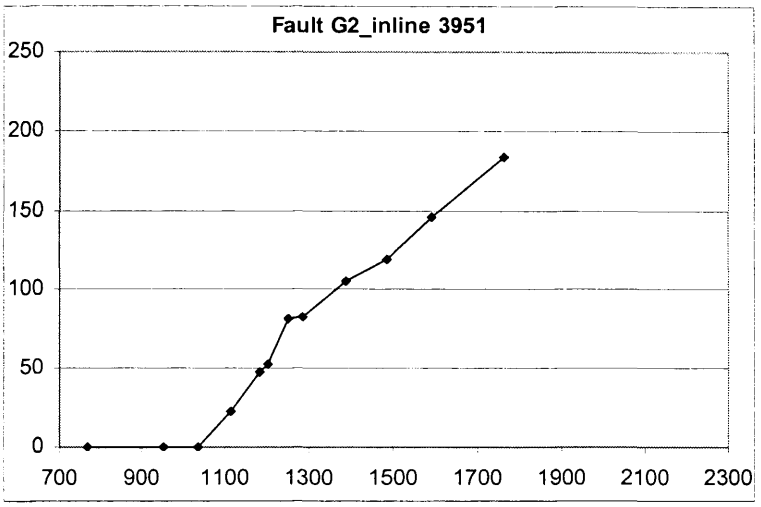
Fault G2_inline 3951
250
200
150
100
50
0
700
900
1100
1300
1500
1700
1900
2100
2300

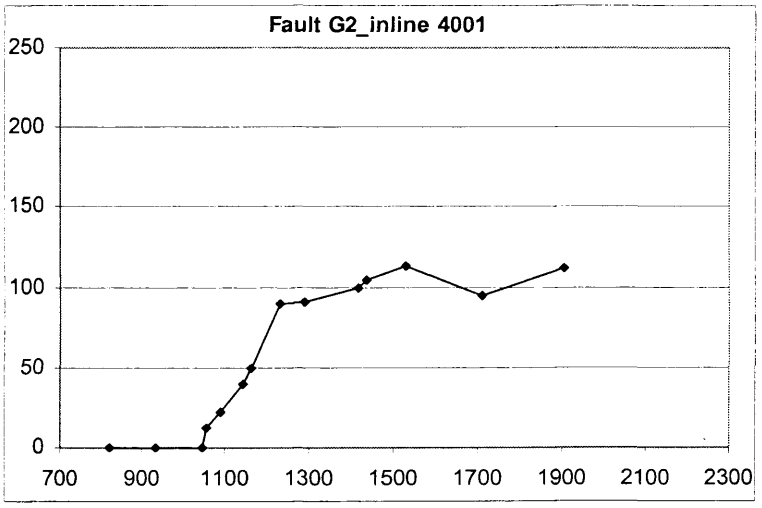
Fault G2_inline 4001
250
200
150
100
50
0
700
900
1100
1300
1500
1700
1900
2100
2300

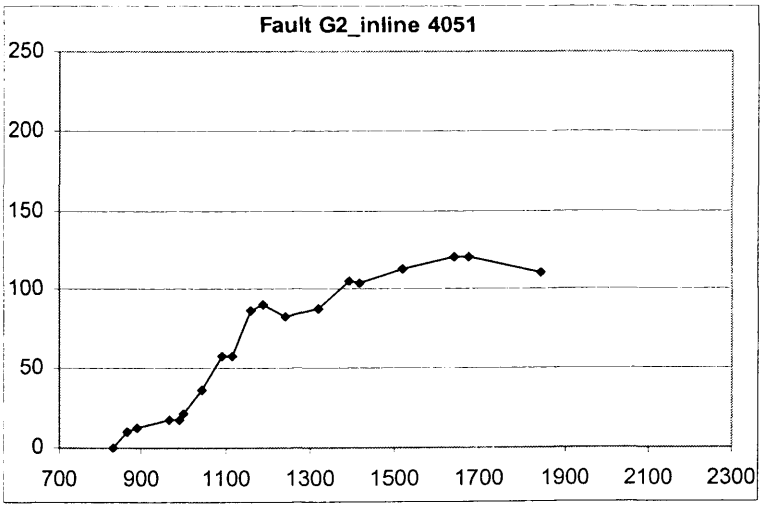
Fault G2_inline 4051
250
200
150
100
50
0
700
900
1100
1300
1500
1700
1900
2100
2300

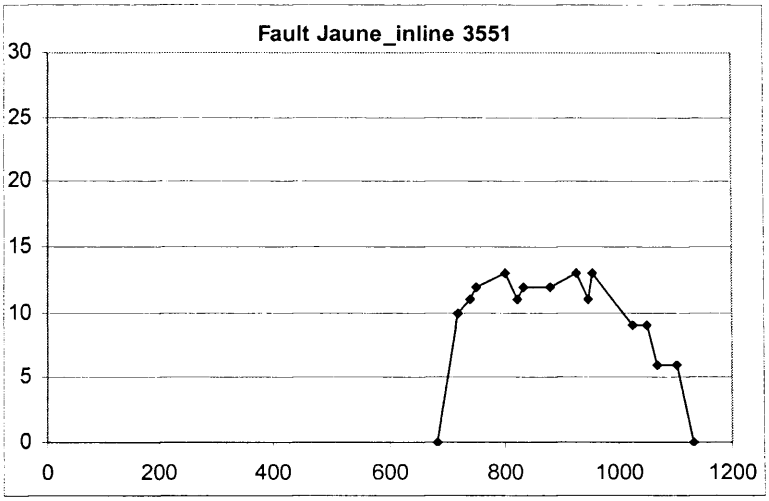
Fault Jaune_inline 3551
30
25
20
15
10
5
0
0
200
400
600
800
1000
1200

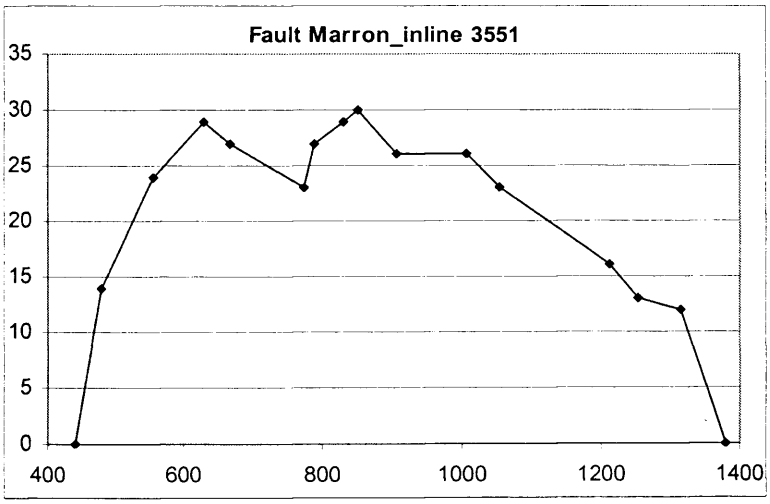
Fault Marron_inline 3551
35
30
25
20
15
10
5
0
400
600
800
1000
1200
1400

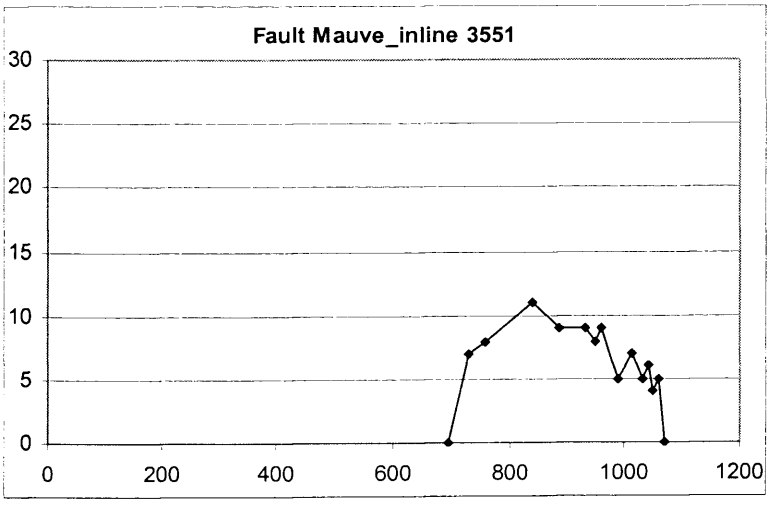
Fault Mauve_inline 3551
30
25
20
15
10
5
0
0
200
400
600
800
1000
1200

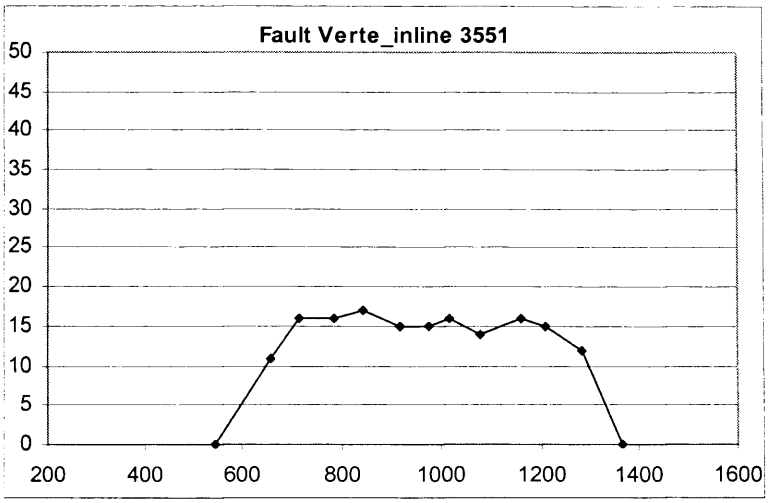
Fault Verte_inline 3551
50
45
40
35
30
25
20
15
10
5
0
200
400
600
800
1000
1200
1400
1600

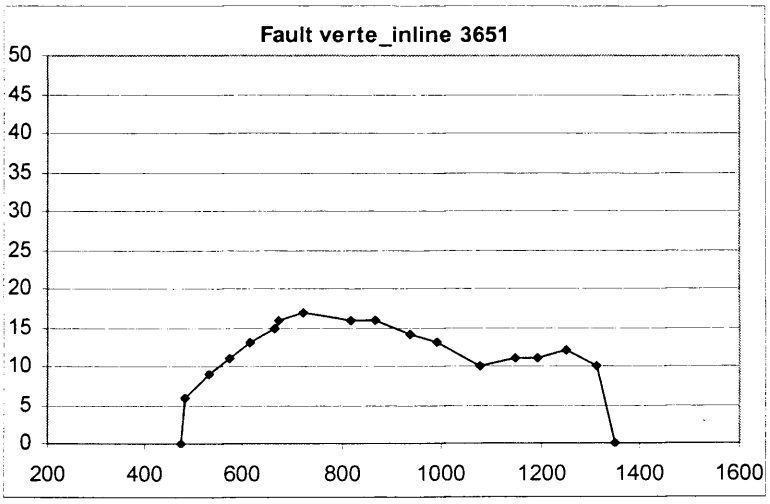
Fault verte_inline 3651
50
45
40
35
30
25
20
15
10
5
0
200
400
600
800
1000
1200
1400
1600

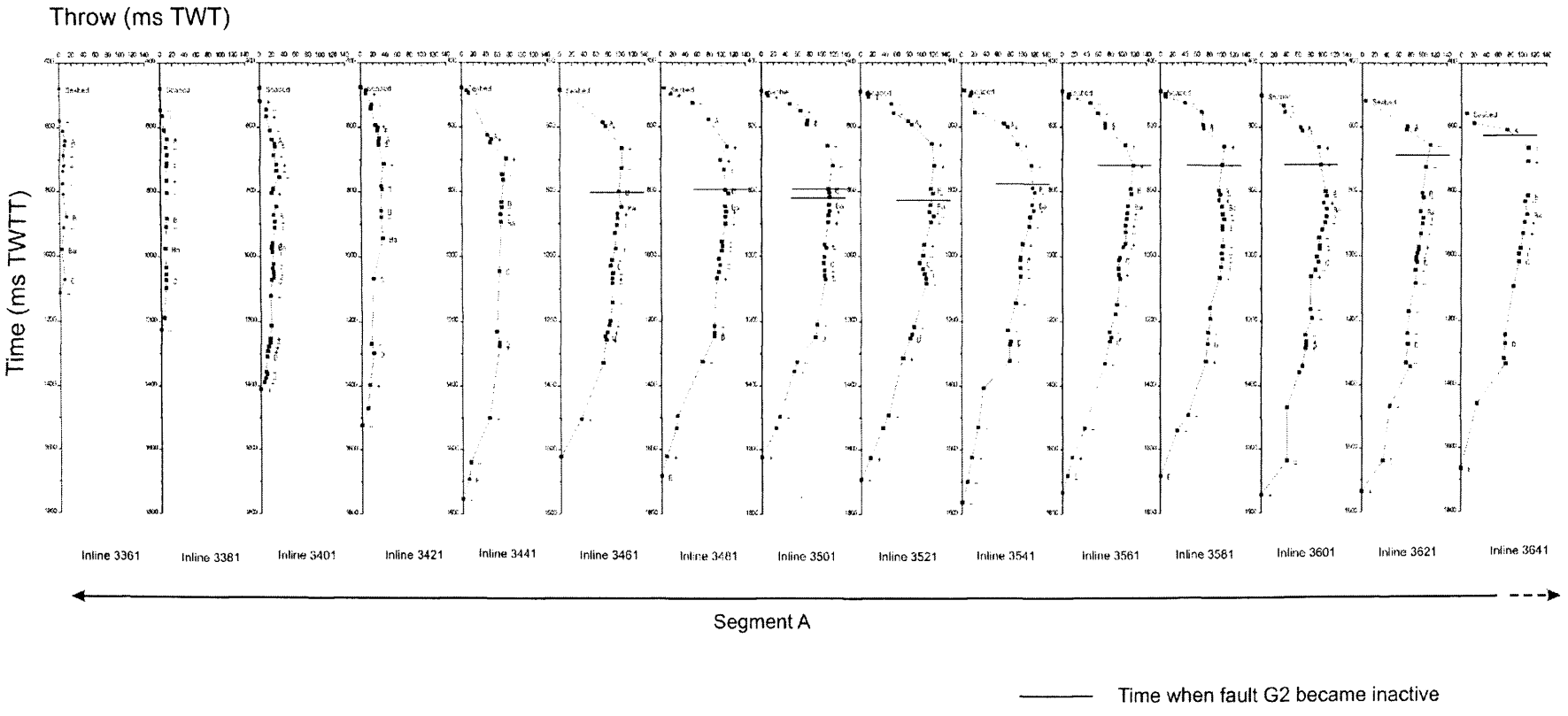

Fig. 8.22: T-z plots obtained for Fault G3_ inlines 3361 to 3641.

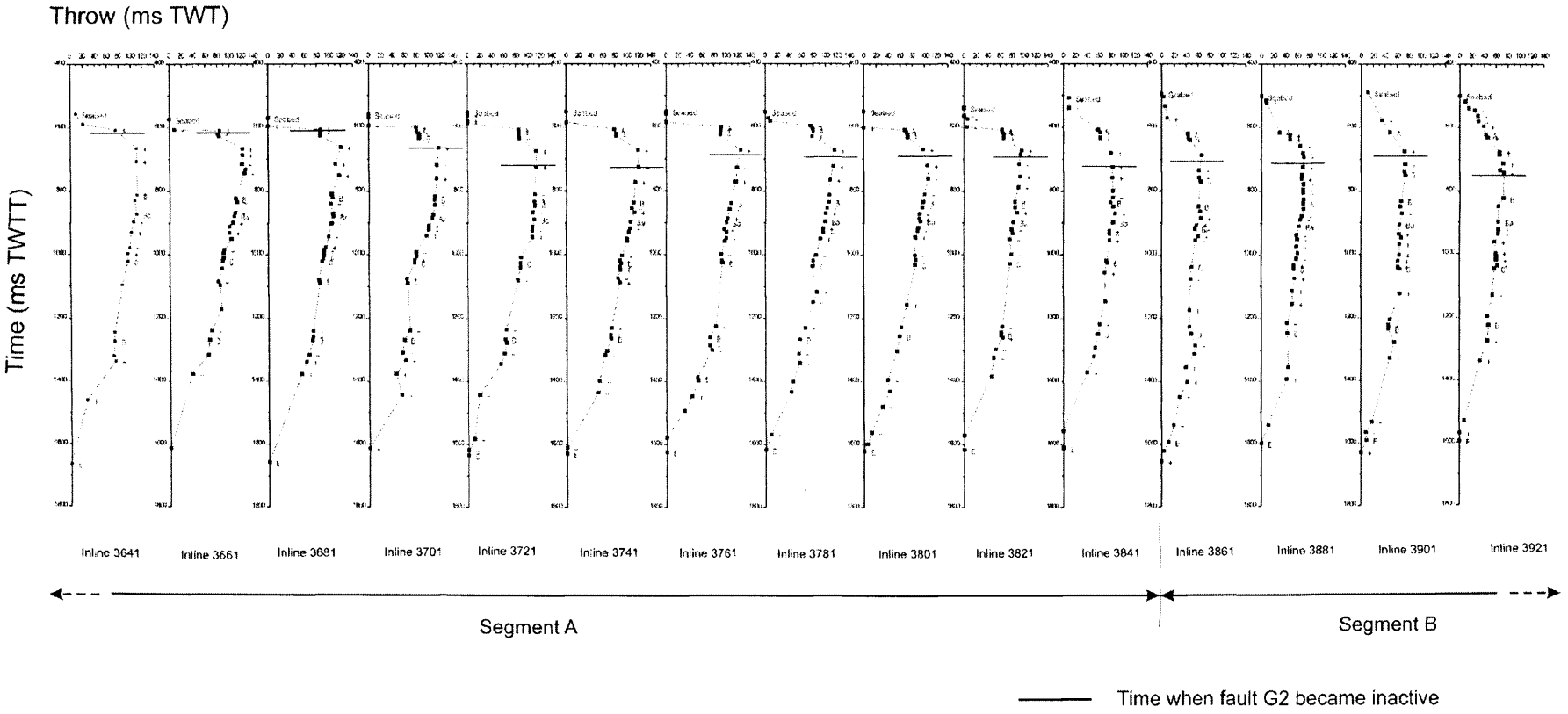

Fig. 8.23: T-z plots obtained for Fault G3_ inlines 3641 to 3921.

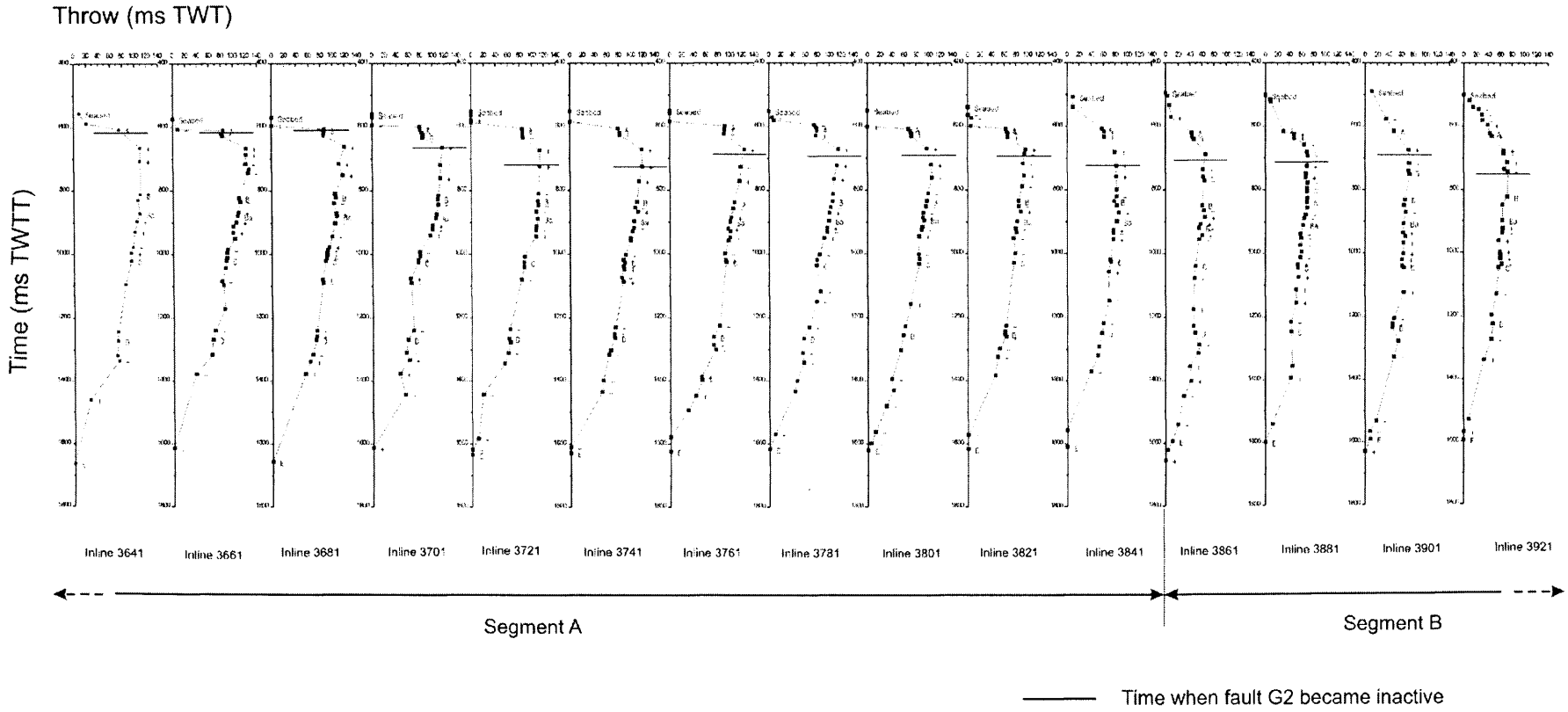

Fig. 8.23: T-z plots obtained for Fault G3_ inlines 3641 to 3921.

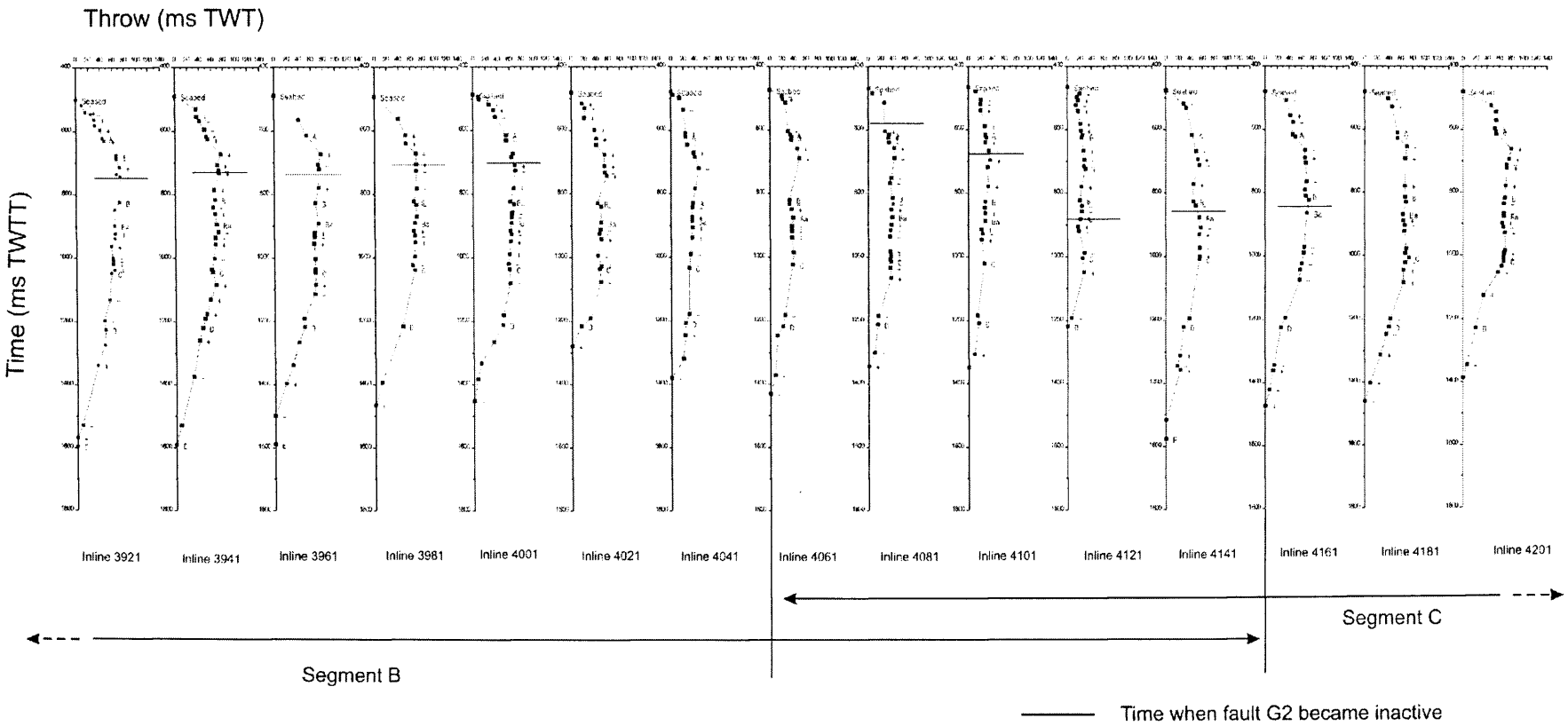

Fig. 8.24: T-z plots obtained for Fault G3 inlines 3921 to 4201

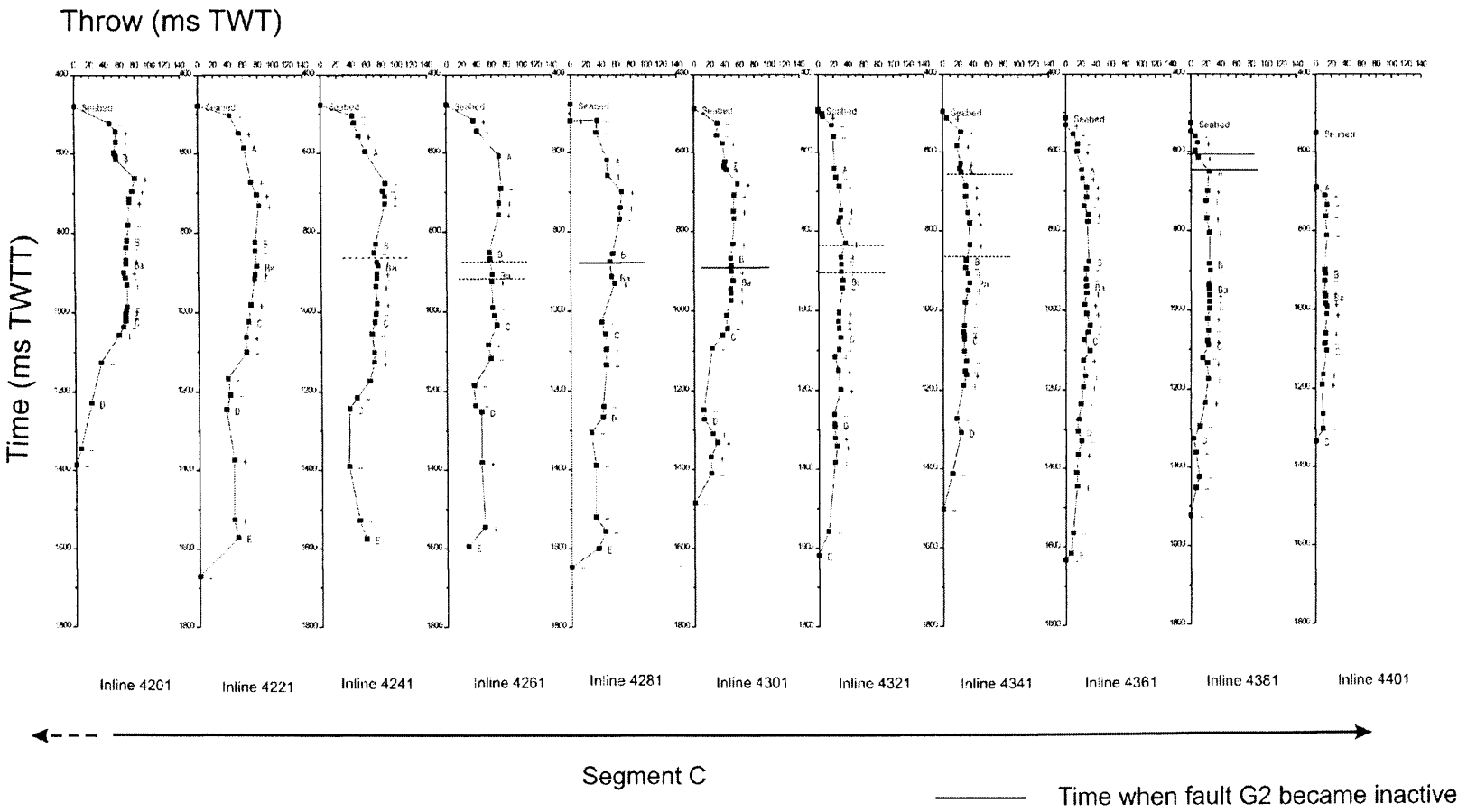

Fig. 8.25: T-z plots obtained for Fault G3 inlines 4201 to 4401.

8.2.3 Faults located in the Espirito Santo Basin

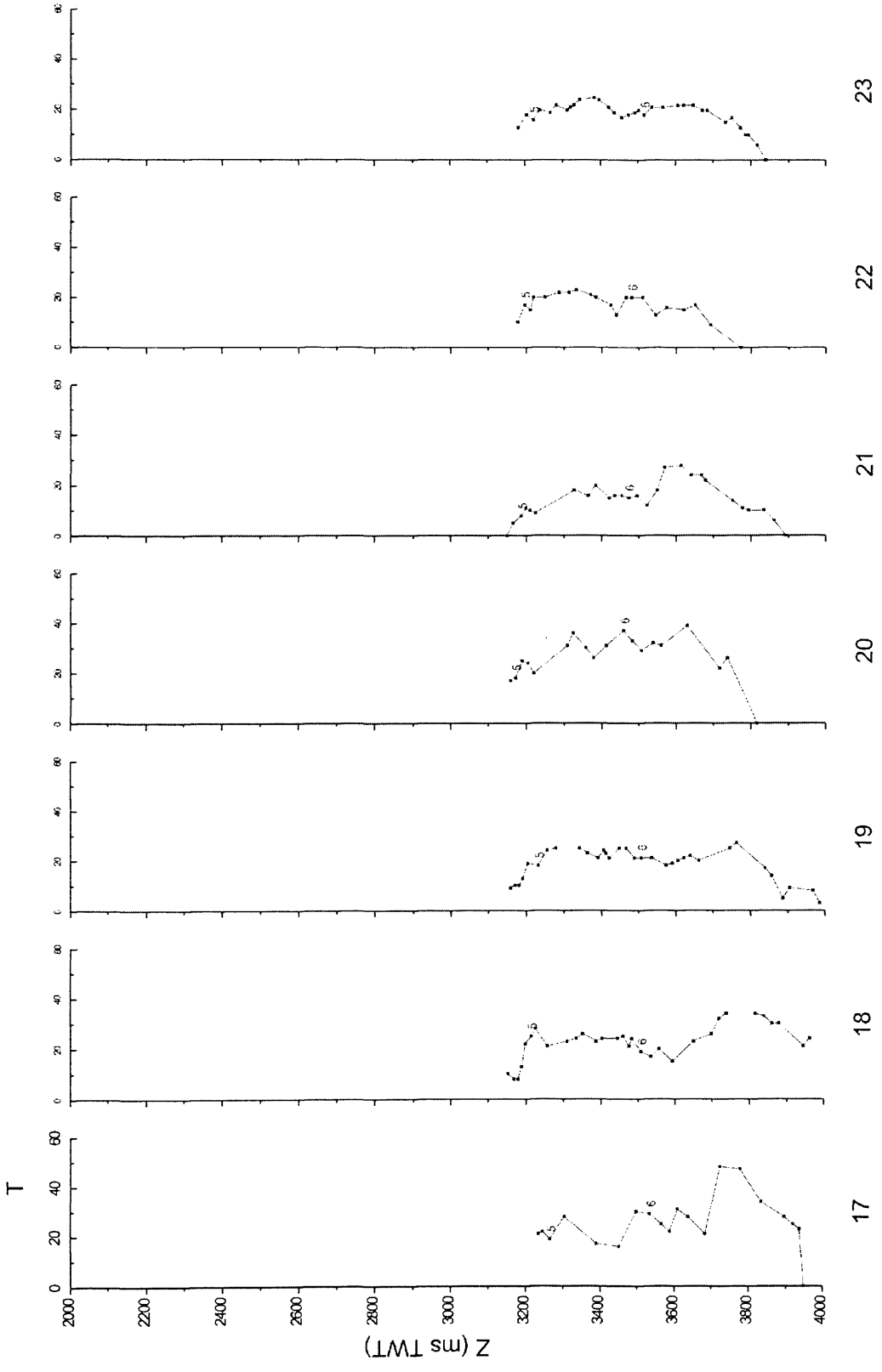

Fig. 8.26. T-z plots for Faults 17 to 23 in Set 2.

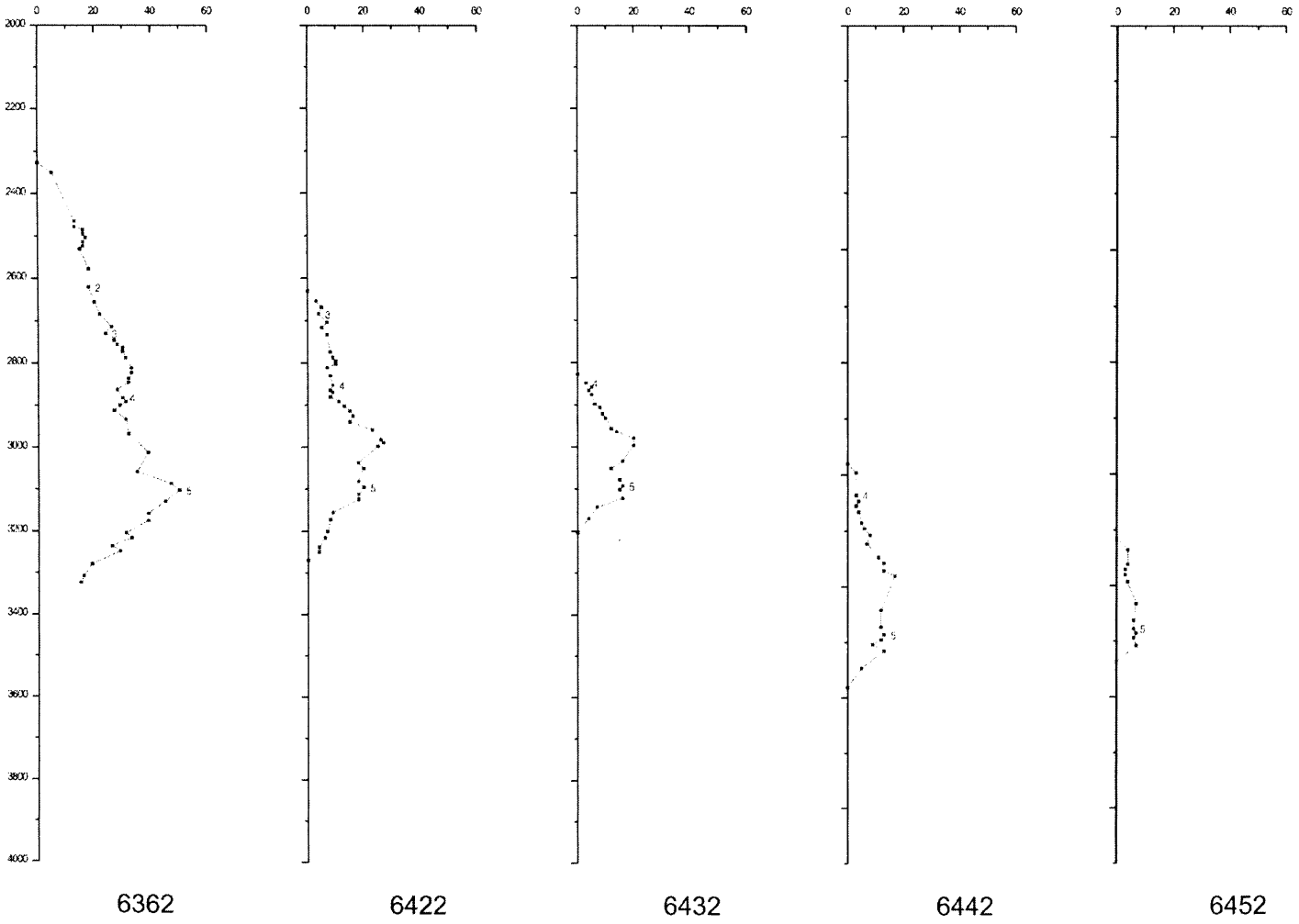

Fig. 8.27: T-z plots for Fault N4 in Set 3.

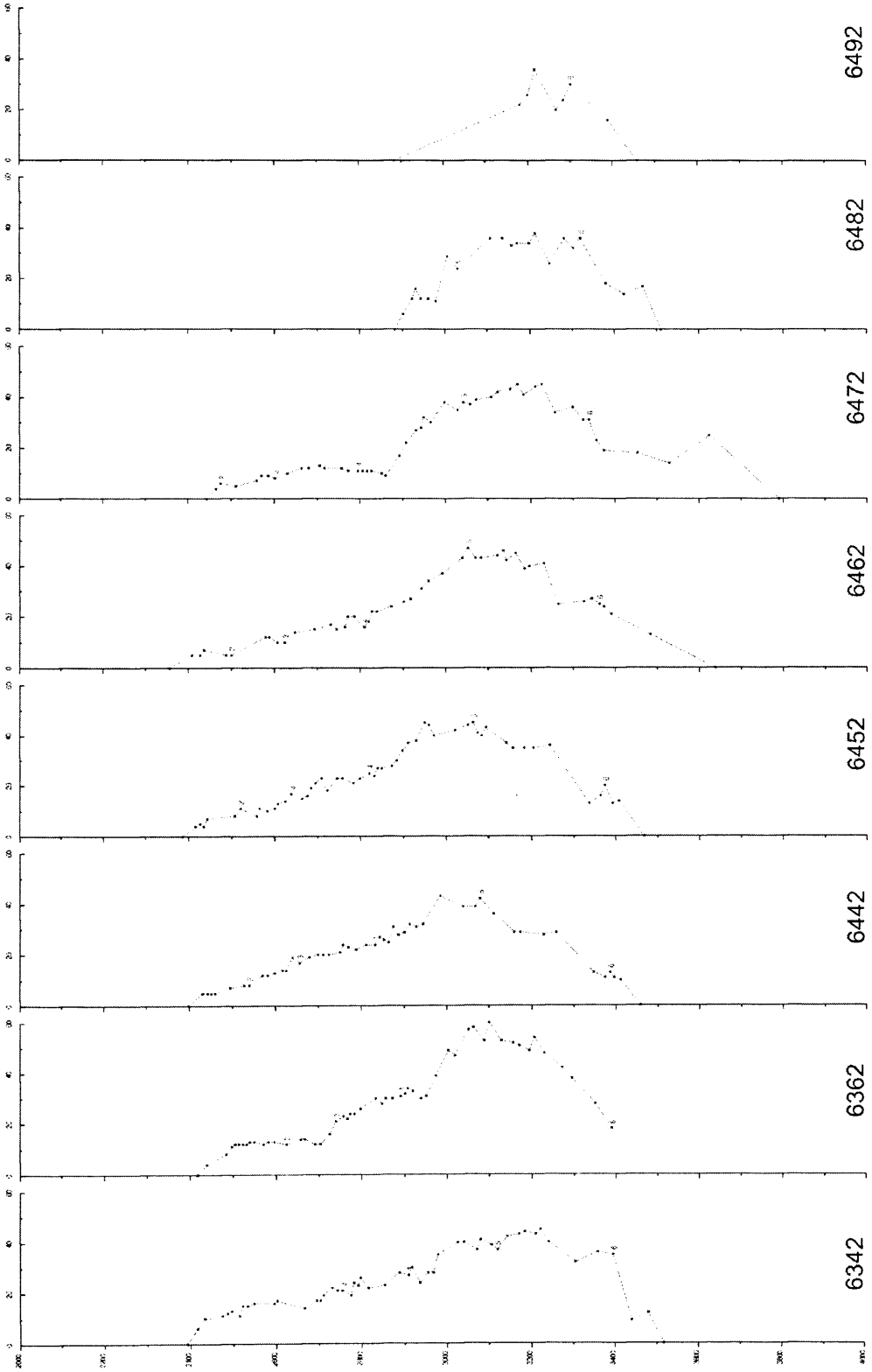

Fig. 8.28: T-z plots for Fault N6 in Set 3.

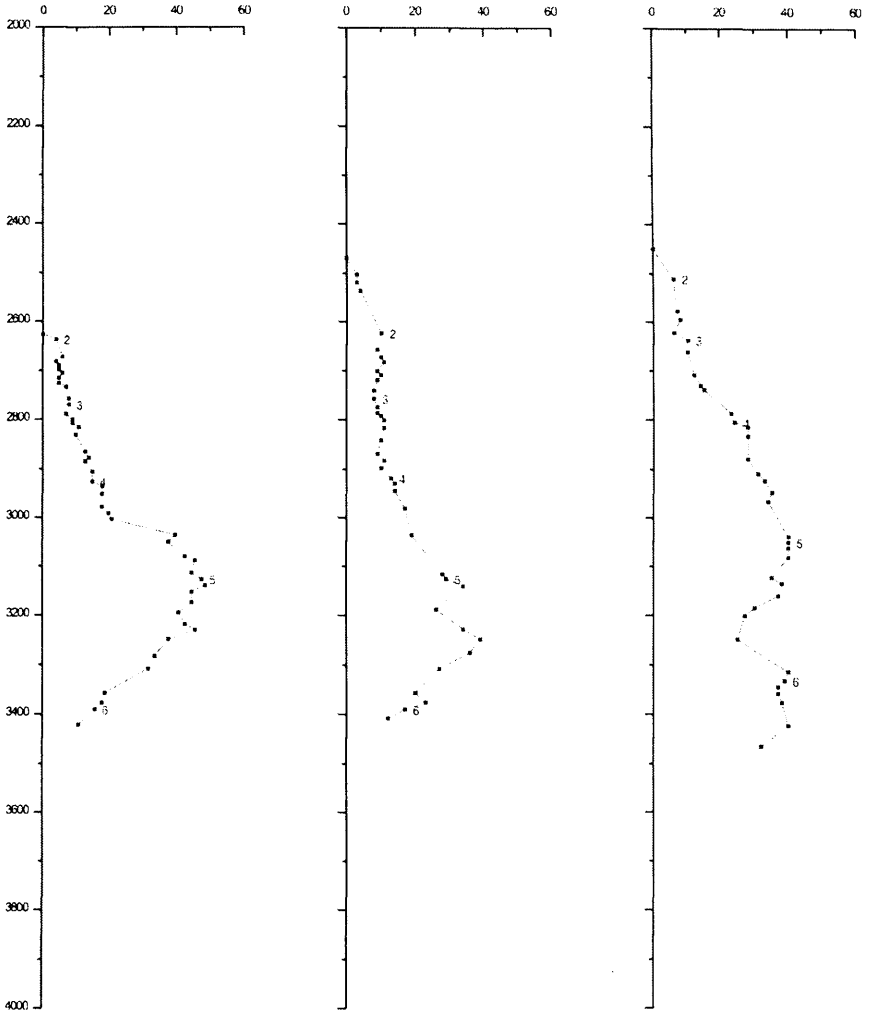

Fig. 8.29: T-z plots for Fault N8 in Set 3.

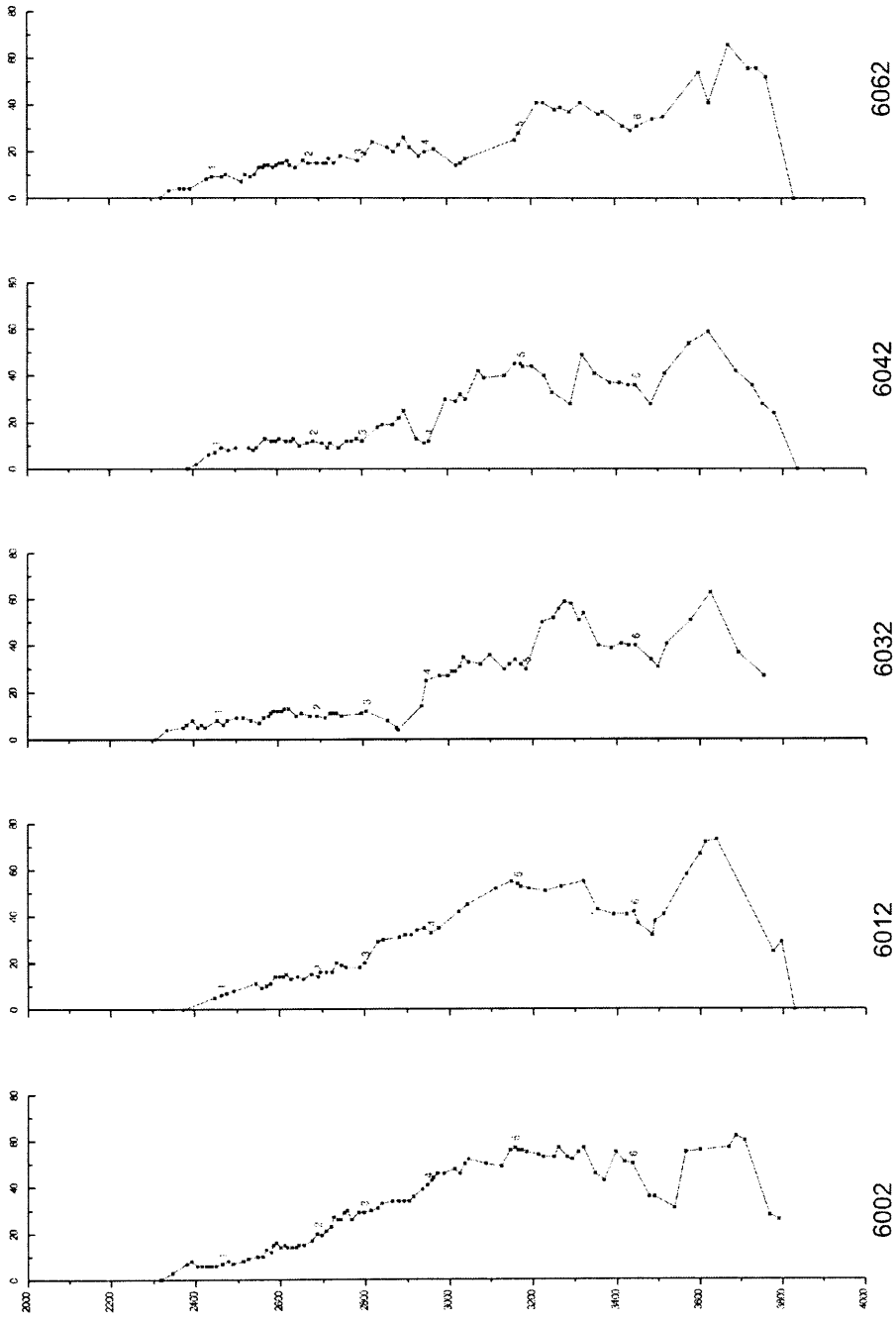

Fig. 8.30: T-z plots for Fault N25 in Set 3.

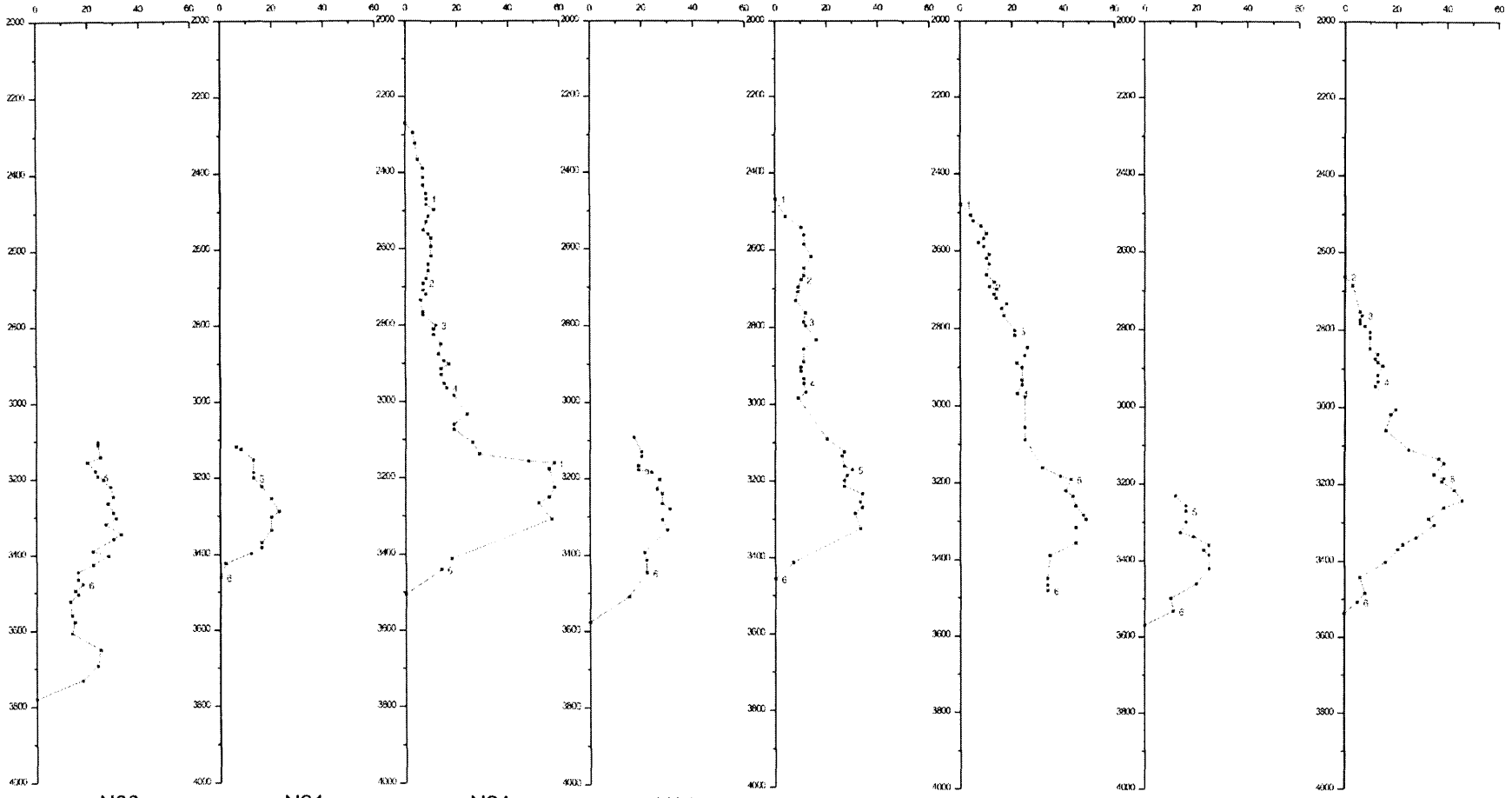

Fig. 8.31: T-z plots for various faults in Set 3.

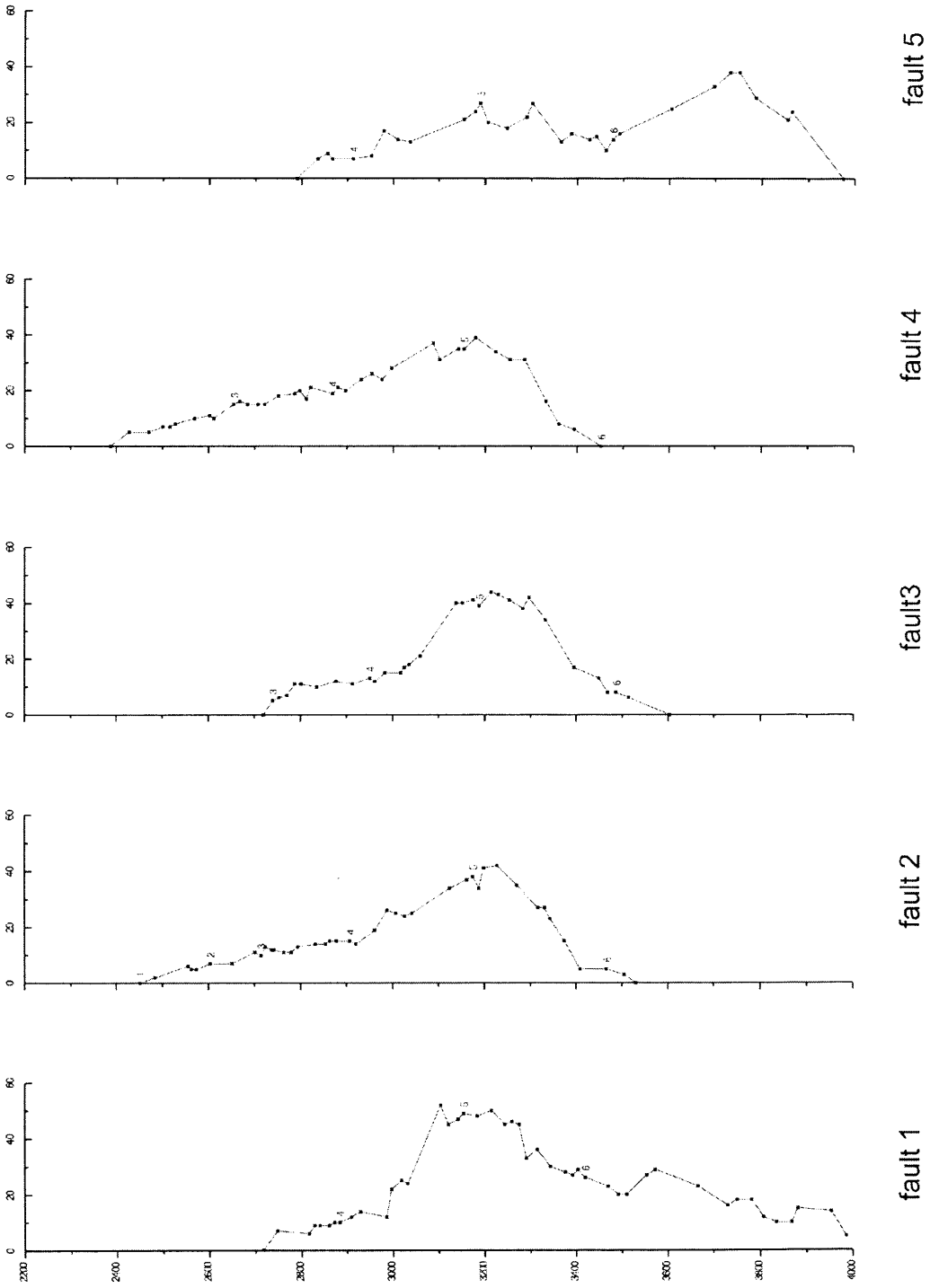

Fig. 8.32: T-z plots for faults in Set 4.